Faculty of Engineering

Department of Mechanical, materials, manufacturing Engineering

Dislocation Density-Based Finite Element Models for Viscoplasticity and Creep of High-Temperature Materials

Hiydar Kireem Musraa Al-Abedy

B.Sc., M.Sc.

A thesis submitted to the University of Nottingham
for the degree of Doctor of Philosophy

August 2019

ABSTRACT

High strength materials that are used in modern power generation plants have now received much more attention because of being exposed to significant thermal gradients due to the fluctuation of demand in daily operation. However, the nature of these materials is complex and several aspects of the evolution of the microstructure still need investigation. Thus, time-dependent plasticity and creep models are appropriate for modelling the P91 steel behaviour under thermomechanical loading. This thesis reports the findings of finite element (FE) analyses and experimental investigations of uniaxial tensile, conventional creep, small punch creep (SPCT) and small tensile test (SPTT) carried out with objective of enhancing the understanding of various microstructural features which describe the creep and viscoplastic behaviours of the specimen. It also aims to develop macro-scale material models, which can predict the creep and viscoplastic behaviours under high-temperature conditions, based on microstructural variables including dislocation density and various other parameters which specify the material structure.

A creep model was developed based on the initial microstructural variables of dislocation density at high-temperature conditions. This model is used to simulate the small punch creep behaviour of the P91 steel at 600°C. Finite element simulations of a small punch creep tests are carried out using ABAQUS software coupled with a UMAT material subroutine. The effect of friction behaviour of the contact between punch and specimen was investigated for SPCTs for a range of

levels of applied stress. The FE results observed that could utilize the microstructure properties to predict the creep behaviour for P91 steel at elevated temperatures.

A unified, Kocks-Mecking-Estrin (KME), viscoplasticity model, which includes isotropic hardening with a viscoplastic flow rule for time-dependent effects by growth and annihilation of dislocations, was used to model the uniaxial tensile and conventional creep behaviour of P91 steel at 600℃. This model was also used in the finite element simulations using a UMAT subroutine within the ABAQUS software. The prediction of the model was improved by including the nonlinear isotropic hardening in order to obtain better stress-strain behaviour in the necking and fracture phase. The prediction of necking and fracture shows good agreement in comparison with experimental testing. The results also show that flow stress at elevated temperatures can be well-characterized by the KME model with the dislocation hardening term.

The experimental tests on all specimens in the study were performed using the Tinius Olsen H5KS single column material testing machine with loading accuracy of ± 0.5% of the applied load within isothermal conditions of 600℃. The small punch tensile behaviour of the P91 steel was further studied by analysing data for force vs. punch displacement at 600°C and by performing microstructural investigations. Physical characterisation of the deformed specimens was conducted via scanning electron microscopy (SEM), coupled with energy dispersive X-ray spectroscopy (EDS), and electron backscatter diffraction (EBSD) to investigate bulk deformation, microstructural evolution, grain structure

change and the crack initiation of the P91 at different stages within all tests. The results show that the bulk deformation behaviour during SPTT indicates to six deformation reigns. The evolution of microstructure occurs after maximum load due to void nucleation resulting in significant necking and thinning at the edge of contact between specimen and punch. The grains exhibit elongation along plastic flow direction.

A visco-plastic model is then developed, based on the microstructural variables of dislocation density, PAGs size and martensitic lath width at high temperature conditions. The developed model was also used in the finite element simulations using the ABAQUS software coupled with a UMAT material subroutine. The finite element simulation was used to validate the performance of the model under multiaxial stress states. FE simulation results were compared with the isothermal small punch tensile tests data of the P91 steel at 600℃. The results of the FE simulation showed that the friction coefficient varies over the contact surface between punch and specimen, and this impacts on the small punch tensile results. The results of FE simulation also showed that the initial of micro-structural variables play an influential role on the small punch tensile results. Dislocation densities, the PAGs size and lath martensitic width and the friction coefficient can interact and have a strong effect on the macroscopic degradation of the material at high stress and elevated temperature conditions. The obtained results have also shown the model's versatility and good predictive capabilities for representing the viscoplastic behaviours of the P91 steel at 600 °C.

LIST OF PUBLICATIONS

1. H. K. Al-Abedy, I.A. Jones and W. Sun. FE modelling of small punch creep test using Kocks-Mecking-Estrin model. SSTT International Conference, 10-12 July 2018, Swansea, UK.

2. H. K. Al-Abedy, I.A. Jones and W. Sun. Small punch creep property evaluation by finite element of Kocks-Mecking-Estrin model for P91 at elevated temperature. Theoretical and Applied Fracture Mechanics, 98, 244-254, 2018.

3. H. Chen, H. K. Al-Abedy, H. Li, R. Yang, W. Sun, and I. A. Jones. On the deformation and fracture mechanism of the P91 steel during small punch tensile testing at elevated temperature. Materials Characterization, An International Journal on Materials Structure and Behaviour, (under review).

4. H. K. Al-Abedy, I.A. Jones and W. Sun. Dislocation density based viscoplastic modelling for high temperature behaviour of the P91 steel. (to be submitted).

ACKNOWLEDGEMENTS

I would like to take this opportunity to express my gratitude to my supervisors, Professor Arthur Jones and Professor Wei Sun, for their expertise, continued support and valuable advice during my PhD study. Also, I would like to thank Dr Si Thu Kyaw for his supervision during the first year of my research.

I also would like to express my special thanks to my wife and my children kids for their love and support during my study in Nottingham. Also, I thank my family back home, especially my Mum (Ummy), my Dad (Aby), my brothers and my sisters, for their prayers and for being behind me at all times.

I wish to thank the technical staffs from the Department of Mechanical, Materials and Manufacturing Engineering of the University of Nottingham, particularly Mr Shane Maskill for his help with the experimental aspects of this work. Thank you to Dr Nigel Neate and Mr Martin Roe, for the training in handling the SEM and TEM equipment. Also, I thank my fellow researchers in the Structural Integrity and Dynamics group for their friendship and knowledge sharing.

Most importantly, I would like to thank Dr Hao Chen from the Faculty of Science and Engineering, University of Nottingham, Ningbo, China and Dr Hezong Li from School of Mechanical and Equipment Engineering, Hebei University of Engineering, Handan, China for their valuable advice and continued help throughout my PhD.

Finally, I must thank Wasit University and Ministry of Higher Education and Scientific Research-Iraq for financial support through the PhD program, which enables me to study at the University of Nottingham.

Without their support, reaching this point would have been considerably harder.

ABBREVIATIONS

Al	Aluminium
B	Boron
BCC	Body Centred Cubic Centre Cube
C	Carbon
CEN	European Committee for Standardisation
CDR	Constant Displacement Rate
Co	Cobalt
Cr	Chromium
EBSD	Electron Backscatter Diffraction
EDS	Energy Dispersive X-Ray Spectroscopy
FE	Finite Element
Fe	Iron
GBDPZ	Grain Boundary Phase of Dislocation Pile-up Zone
GNDs	Geometrically necessary dislocations
GI	Grain Interior Phase
KME	Kocks Mecking Estrin
LVDT	Linear Variable Differential Transformer Transducers
MDBT	Miniature Disc Bend Test
Mn	Manganese
Mo	Molybdenum
N	Nitrogen
Nb	Niobium
Ni	Nickel
ORNL	Oak Ridge National Laboratory
P	Phosphorus
PAG	Prior Austenite Grain
S	Sulphur
SEM	Scanning Electron Microscopy
Si	Silicon
SPCT	Small Punch Creep Test
SPTT	Small Punch Tensile Test
Ta	Tantalum
TEM	Transmission electron microscope
Ti	Titanium
UMAT	User Material Subroutine
V	Vanadium
W	Tungsten
WEDM	Wire Electrical Discharge Machining

NOMENCLATURE

a	Unit cell constant
b	The magnitude of dislocation Burgers vector
C_{ijkl}	Stiffness matrix tensor
C^{e}_{ijkl}	Elastic stiffness matrix tensor
C^{cr}_{ijkl}	Creep stiffness matrix tensor
d	Punch diameter
d_{dip}	Dipole formation
d_e	Critical distance for loss of mobile dislocation
d_{lock}	Locked configurations
D	Receiving hole diameter
f	Yield function
f_w	Volume fracture
k_b	Boltzmann constant
k_1	Dislocation storage constant
k_2	Recovery coefficient
k_{20}	Initial recovery constant
L_e	Mean free path
m	The exponent of stress sensitivity
M	Taylor factor
m_{cl}	Rate of climb dislocation movement
n	Dynamic recovery exponent
n_o	Number of dislocation constant
$\mathbb{N}_{ij}$	Flow direction tensor
p	Creep exponent
$P1$	Punch load magnitude
$P2$	Punch clamp force magnitude
r	Corner radius of holder and support
R	Gas constant
S	Diameter of small punch specimen
S_{ij}	Deviatoric stress tensor
t	Time
t_f	Failure time
t_s	Thickness of small punch specimen
t_w	Wall thickness
T	Temperature
T_m	Absolute melting temperature
S^{cr}_{ijkl}	Creep compliance matrix
α	Constant
μ	Shear modulus
μ_f	Friction coefficient
ε^p, $\dot{\varepsilon}^p$, $\dot{\varepsilon}^c$	Plastic strain, plastic and creep strain rates
$\dot{\bar{\varepsilon}}^p$	Effective plastic strain rate

$\dot{\varepsilon}_{ij}, \dot{\varepsilon}^{e}_{ij}, \dot{\varepsilon}^{c}_{ij}$	Total, elastic and creep strain rate tensors
$\dot{\tilde{\varepsilon}}^{c}$	Effective creep strain rate
$\dot{\varepsilon}_{min}$	Minimum strain rate
$\dot{\varepsilon}_{o}$	Reference strain rate
$\dot{\varepsilon}_{s}$	Steady-state strain rate
$\Delta\varepsilon_{ij}, \Delta\varepsilon^{c}_{ij}$	Total and creep strain tensor increments
$\Delta\tilde{\varepsilon}^{c}$	Effective creep strain increment
ρ	Dislocation density
ρ_{f}	Mobile dislocation
ρ_{m}	Immobile dislocation at PAGs
ρ_{w}	Immobile dislocation at lath boundary
σ_{b}	Back stress
σ_{d}	Stress dependent on the dislocation density
σ_{f}	Flow stress
σ_{H}	Hydrostatic stress
σ_{s}	Saturation stress
σ_{y}	Initial yield stress
σ^{*}	Friction stress
$\tilde{\sigma}$	Effective stress
σ_{ij}	Stress Tensor
$\hat{\sigma}_{so}$	The saturation value of flow stress
σ^{tr}_{ij}	Elastic predictor stress tensor
θ_{o}	The initial strain hardening at the second stage.
δ	Martensitic lath width
$\delta\tilde{\varepsilon}^{c}$	Accumulated creep strain
δ_{ij}	Kronecker delta tensor
$\dot{\gamma}^{pl}$	Shear slip rate
ζ_{D}	Static PAG growth size
ζ_{δ}	Static lath growth size
Q_{D}	Activation energy for PAG growth
Q_{δ}	Activation energy for lath growth
α_{D}	Material Parameter
α_{δ}	Material Parameter
ω	Time interpolation parameter
ω_{δ}	Dynamic lath growth constant
Λ	Strain hardening constant

CONTENTS

ABSTRACT ii

LIST OF PUBLICATIONS iv

ACKNOWLEDGEMENTS v

ABBREVIATIONS vii

NOMENCLATURES viii

CONTENTS x

LIST OF FIGURES xvi

CHAPTER 1: INTRODUCTION **1**

1.1 OVERVIEW 1

1.2 RESEARCH AIM AND OBJECTIVE 3

1.3 ORGANIZATION OF THE THESIS 4

CHAPTER 2: LITERATURE REVIEW **7**

2.1 INTRODUCTION 7

2.2 CREEP 8

2.2.1 Primary and Secondary Creep 12

2.2.2 Tertiary Creep and Rupture 18

2.2.3 Creep Mechanisms 20

2.3 THE VISCO-PLASTIC CONSTITUTIVE MODELS 22
2.3.1 Yield Surface and Flow Rule 22
2.3.2 Internal Variables and Hardening 25
2.3.2.1 Isotropic Hardening 25
2.3.2.2 Kinematic Hardening 27
2.3.3 Uncoupled Elastoplasticity-Creep 30
2.3.4 Unified Viscoplasticity Model 31
2.4 PHYSICALLY BASED MODELS 35
2.5 SMALL PUNCH CREEP TEST (SPCT) 39
2.5.1 Experimental Displacement-Time Behaviour 40
2.5.2 Finite Element modelling of SPCT 41
2.6 SMALL PUNCH TENSILE TEST (SPTT) 46
2.6.1 Experimental Load-Displacement Behaviour 47
2.6.2 Finite Element modelling of SPTT 48
2.7 HIGH-TEMPERATURE MATERIALS 51
2.8 SUMMARY AND KNOWLEDGE GAPS 58

CHAPTER 3: FINITE ELEMENT CREEP MODELLING 60
3.1 INTRODUCTION 60
3.2 THE KME MODEL AND UMAT DEVELOPMENT 61
3.2.1 The Kocks-Mecking-Estrin Model 61
3.2.2 The Multi-Axial Formulation 62
3.2.3 The UMAT Coding and Implementation 64
3.2.4 Material Jacobian Matrix 68
3.3 UNIAXIAL CREEP TESTS 69
3.4 FE UNIAXIAL CREEP MODEL 69

3.5 MODELLING OF SMALL PUNCH CREEP TESTS 73
3.5.1 FE Model 73
3.5.2 Displacement-Time Curves 78
3.5.3 Contours of Displacement, von Mises Stress and Strain 83
3.6 CONCLUSIONS 90

CHAPTER 4: FE VISCO-PLASTICITY MODELLING BASED UPON DISLOCATION DENSITY 91

4.1 INTRODUCTION 91
4.2 KME MODEL FRAMEWORK 92
4.3 USER MATERIAL SUBROUTINE UMAT DEVELOPMENT 95
4.3.1 The Multiaxial Extension of the Constitutive Model 95
4.3.2 Implicit numerical implementation of the dislocation-based model. 99
4.4 MATERIAL AND CRYSTAL MAP OF THE P91 STEEL 104
4.5 APPLICATION OF THE UMAT TO FINITE ELEMENT MODEL 104
4.5.1 Structural Finite Element 105
4.6 MODEL IMPLEMENTATION ABILITIES AND DISCUSSION 106
4.6.1 Uniaxial Tensile Behaviour 106
4.6.2 Uniaxial Creep Behaviour 111
4.7 CONCLUDING REMARKS 118

CHAPTER 5: HIGH TEMPERATURE DEFORMATION AND FRACTURE PROCESS DURING SPT TESTS 119

5.1 INTRODUCTION 119
5.2 MATERIAL AND EXPERIMENTAL PROCEDURE 121
5.2.1 The P91 Steel 121

5.2.2 The Small Punch Tensile Testing....123
5.2.3 Microstructural Characterisation....125
5.3 MECHANICAL BEHAVIOUR....126
5.3.1 Load-Displacement Curves and Macroscopic Interrupted Patterns....126
5.3.2 Bulk Deformation Behaviour....134
5.4 PHYSICAL CHARACTERIZATION OF THE DEFORMATION PROCESS IN SPTT....143
5.4.1 Microstructural Evolution....143
5.4.2 Grain Structure Evolution....152
5.5 DISCUSSION....159
5.5.1 Deformation Regimes and Plasticity Energy....159
5.5.2 Deformation and Fracture Mechanisms....163
5.6 CONCLUSIONS....166

CHAPTER 6: FE MODELLING OF DISLOCATION DENSITY AND GRAIN SIZE EFFECT ON SPTT....168

6.1 INTRODUCTION....168
6.2 DEVELOPMENT OF CONSTITUTIVE MODEL....168
6.2.1 Model Formulation....169
6.2.2 Evolution of Dislocation Density....171
6.2.3 Growth of the PAG Size and Lath Microstructure....175
6.3 UMAT IMPLEMENTATION....175
6.4 DETERMINATION OF MATERIAL PARAMETERS....179
6.5 RESULTS AND DISCUSSION....182
6.5.1 FE Simulation of the SPTT....182

6.5.1.1 The Evolution of Microstructure....194
6.5.1.2 Bulk Deformation....198
6.5.2 Small Punch Tensile Curves....201
6.6 CONCLUSION....205

CHAPTER 7: CONCLUSIONS AND FUTURE WORK.... 207
7.1 CONCLUSIONS....207
7.2 FUTURE WORK....210

REFERENCES 206

APPENDIX A: MATERIAL JACOBIAN MATRIX CALCULATION 225

LIST OF FIGURES

Figure 2-1. Typical punch displacement (vertical deflection) versus time curve for a small punch creep test under constant load..... 9

Figure 2-2. General form of creep behaviour in pure metals 9

Figure 2-3. Recovery creep 10

Figure 2-4. Influence of temperature, T, on creep behaviour 11

Figure 2-5. Influence of stress on creep behaviour 11

Figure 2-6. A typical variation of creep strain rate versus time under constant stress 15

Figure 2-7. Schematic of isotropic hardening 23

Figure 2-8. Schematic of kinematic hardening 23

Figure 2-9. Isotropic hardening, (a) yield surface and (b) the corresponding uniaxial stress-strain curve 27

Figure 2-10. Reversed loading with kinematic hardening (a) the translation of the yield surface and (b) stress-strain curve which shows the Bauschinger effect 28

Figure 2-11. Non-linear kinematic hardening (a) the yield surface and (b) stress strain curve 30

Figure 2-12. (a) the von Mises yield surface with linear isotropic hardening and (b) the decompositions of corresponding stress 32

Figure 2-13. Chakrabarty's membrane stretch model 42

Figure 2-14. View of the FE meshes 45

Figure 2-15. Standard geometry of the small punch (SP) test 47

Figure 2-16. Small punch simulation for Ti-6Al-4V at (a and b) 20℃ and (c and d) 400℃ 50

Figure 2-17. Schematic illustration and photographs of a fossil-fired boiler and typical materials.....53

Figure 2-18. Stress versus temperature for various alloys 57

Figure 3-1. Flowchart of the implementation of the UMAT for creep model. 67

Figure 3-2. Uniaxial test specimen, all dimensions in mm. 69

Figure 3-3. FE axis-symmetric uniaxial creep specimen. 71

Figure 3-4. Experimental and calculated uniaxial creep curves for stresses at 140 and 150MPa. 72

Figure 3-5. Experimental and calculated uniaxial creep curves for stresses at 160 and 170MPa. 72

Figure 3-6. Experimental and calculated uniaxial creep curves for stresses at 180MPa. 73

Figure 3-7. Schematic three-dimensional of rig for small punch creep testing. ..75

Figure 3-8. Schematic representation of a FE model for small punch creep testing analysis (D=4mm, S=8mm, d=2.08mm, r=0.25mm, t_s=0.5mm).
(a) Schematic two-dimensional of rig for small punch creep testing. 76

Figure 3-9. FE mesh used for SPCT specimen. 77

Figure 3-10. Calculated SPCT curve at the variation of the friction coefficient for punch load of 30Kg. 79

Figure 3-11. Calculated SPCT curve at the variation of the friction coefficient for punch load of 34Kg. 79

Figure 3-12. The experimental and calculated SPCT curves at punch load of 25Kg 80

Figure 3-13. The experimental and calculated SPCT curves at punch load of 28Kg 81

Figure 3-14. The experimental and calculated SPCT curves at punch load of 30Kg 81

Figure 3-15. The experimental and calculated SPCT curves at punch load of 34Kg 82

Figure 3-16. The experimental and calculated SPCT curves at punch load of 40Kg 82

Figure 3-17. Contour plot of punch direction deformation of SPCT at punch load 25Kg.....83

Figure 3-18. Contour plot of punch direction deformation of SPCT at punch load 30Kg.....84

Figure 3-19. Contour plot of the equivalent stress with the SPCT at a punch load of 34Kg.....85

Figure 3-20. Contour plot of the equivalent stress with the SPCT at a punch load of 40kg. 85

Figure 3-21. Contour plot of strain and SEM images of SPCT at punch load 25Kg for P91 steel at 600ºC.....86

Figure 3-22. Contour plot of a strain of SPCT at punch load 34Kg. 87

Figure 3-23. Contour plot of a strain of SPCT at punch load 40kg.....88

Figure 4-1. Flowchart of the implementation of the UMAT for the KME model. 103

Figure 4-2. FE mesh and boundary conditions of the uniaxial tensile and creep specimen. 106

Figure 4-3. The comparison results between the simulated true stress-strain curves and the corresponding published data of Cu at RT with different strain rate 107

Figure 4-4. Contour plot of the effective plastic strain at failure for the P91 steel at 600ºC. 109

Figure 4-5. Contour plot of the flow stress at failure for the P91 steel at 600ºC. 109

Figure 4-6. Contour plot of the total dislocation density at failure for the P91 steel at 600ºC.....110

Figure 4-7. Experimental and numerical stress-strain curves for the P91 steel at 600ºC.....110

Figure 4-8. Total of dislocation density along with effective plastic strain for the P91 steel at 600℃. 111

Figure 4-9. Experimental and calculated uniaxial creep curves for stresses at 160, 170 and 180MPa. 112

Figure 4-10. Experimental and calculated uniaxial creep curves for stresses at 140 and 150MPa. 113

Figure 4-11. Influence of applied stress on dislocation density for constant stress tests at 160, 170 and 180MPa. 113

Figure 4-12. Influence of applied stress on dislocation density for constant stress tests at 140 and 150MPa. 114

Figure 4-13. Variation of minimum strain rate versus applied stress. 115

Figure 4-14. Variation of strain rate versus applied stress. 116

Figure 4-15. Variation of time to failure versus applied stress. 117

Figure 5-1. Scheme of the microstructural of the P91 steel. 123

Figure 5-2. The small punch testing machine with the furnace. 124

Figure 5-3. Detailed drawing of the rig, the part numbers are as follows: 125

Figure 5-4. Schematic diagram of the SPTT load-displacement curve. 127

Figure 5-5. The punch load-displacement curves of the whole stroke till material failure. 128

Figure 5-6. Interrupted stroke at 0.26 mm and whole stroke. 129

Figure 5-7. Interrupted stroke at 0.6 mm and whole stroke. 130

Figure 5-8. Interrupted stroke at 1.0 mm and whole stroke. 130

Figure 5-9. Interrupted stroke at 1.25 mm and whole stroke. 131

Figure 5-10. Interrupted stroke at 1.50 mm and whole stroke. 131

Figure 5-11. Interrupted stroke at 1.65 mm and whole stroke. 132

Figure 5-12. Interrupted stroke at 1.74 mm and whole stroke. 132

Figure 5-13. Tensile surfaces of The P91 steel following interrupted and fracture SPTT testing at 600℃. 133

Figure 5-14. The morphology of the deformed P91 specimens at 0.26 mm shown in (a) low magnification image, (b) high magnification image. 135

Figure 5-15. The morphology of the deformed P91 specimens at 0.6 mm shown in (a) low magnification image, (b) high magnification image. 136

Figure 5-16. The morphology of the deformed P91 specimens at 1.0 mm shown in (a) low magnification image, (b) high magnification image. 137

Figure 5-17. The morphology of the deformed P91 specimens at 1.25 mm shown in (a) low magnification image, (b) high magnification image. 138

Figure 5-18. The morphology of the deformed P91 specimens at 1.5 mm shown in (a) low magnification image, (b) and (c) high magnification image. 140

Figure 5-19. The morphology of the deformed P91 specimens at 1.65 mm shown in (a) low magnification image, (b) and (c) high magnification image. 141

Figure 5-20. The morphology of the deformed P91 specimens at 1.74 mm shown in (a) low magnification image, (b) and (c) high magnification image. 142

Figure 5-21. (a) The cross-sectional microstructure of the P91 specimen at interrupted displacements of 0.26 mm, where the black box outline the area shown in the higher magnification image (b). 145

Figure 5-22. (a) The cross-sectional microstructure of the P91 specimen at interrupted displacements of 0.6 mm, where the black box outline the area shown in the higher magnification image (b). 146

Figure 5-23. (a) The cross-sectional microstructure of the P91 specimen at interrupted displacements of 1.0 mm, where the black box outline the area shown in the higher magnification image (b). 147

Figure 5-24. (a) The cross-sectional microstructure of the P91 specimen at interrupted displacements of 1.25 mm, where the black box outline the area shown in the higher magnification image (b). 148

Figure 5-25. (a) The cross-sectional microstructure of the P91 specimen at interrupted displacements of 1.5 mm, where the black box outline the area shown in the higher magnification image (b). 149

Figure 5-26. (a) The cross-sectional microstructure of the P91 specimen at interrupted displacements of 1.65 mm, where the black box outline the area shown in the higher magnification image (b). 150

Figure 5-27. (a) The cross-sectional microstructure of the P91 specimen at interrupted displacements of 1.74 mm, where the black box outline the area shown in the higher magnification image (b). 151

Figure 5-28. EBSD mappings of the as-received of the P91 steel. 152

Figure 5-29. EBSD mappings of regions near the edge of contact for displacements of (a) 0.26 mm and (b) 0.6 mm. 155

Figure 5-30. EBSD mappings of regions near the edge of contact for displacements of (a) 1.0 mm and (b) 1.25 mm. 156

Figure 5-31. The grain structure at the edge of contact for SPTT displacements of (a) 1.5 mm, (b) 1.65 mm and (c) 1.74 mm. 157

Figure 5-32. The cross-sectional microstructure at the fracture point. 158

Figure 5-33. The deformation energy in different stages of the SPTT load-displacement curve for P91 at 600°C. 161

Figure 5-34. The evolution of specimen thickness at the edge of contact against displacements. 161

Figure 5-35. The schematic diagram of deformation mechanism of P91 in SPTT at different stages. 162

Figure 5-36. The schematic diagram of microstructure evolution and fracture mechanism of P91 during SPTT. (a) the as-received structure prior to SPTT, (b) the grain alignment, (c) the elongation of grains and voids and (d) the void coalescence that leads to fracture. 165

Figure 6-1. Flow chart describing the main processes in the UMAT user material subroutine. 178

Figure 6-2. Maximum principal strains at a Puncher displacements of 0.26, 1.0 and 1.25mm. 183

Figure 6-3. Maximum principal strains at a Puncher displacements of 1.5, 1.65 and 1.74mm. 184

Figure 6-4. The evolution of dislocation densities (SDV4) at a Puncher displacements of 0.26, 1.0 and 1.25mm. 187

Figure 6-5. The evolution of dislocation densities (SDV4) at a Puncher displacements of 1.5, 1.65 and 1.74mm. 188

Figure 6-6. Mises stresses at a Puncher displacements of 0.26, 1.0 and 1.25mm. 190

Figure 6-7. Mises stresses at a Puncher displacements of 1.5, 1.65 and 1.74mm. 191

Figure 6-8. The x-axis (U1) displacement at a Puncher displacements of 0.26, 1.0 and 1.25mm. 192

Figure 6-9. The x-axis (U1) displacement at a Puncher displacements of 1.5, 1.65 and 1.74mm. 193

Figure 6-10. Contour plot of strain and SEM images of SPTT at interrupted displacements of 1.0 and 1.25mm for the P91 steel at 600℃. 196

Figure 6-11. Contour plot of strain and SEM images of SPTT at interrupted displacements of 1.5 and 1.65mm for the P91 steel at 600℃. 197

Figure 6-12. The comparison between FE result and the dome-shaped deformed P91 specimen for punch displacement of 1.25mm. 199

Figure 6-13. The comparison between FE result and the dome-shaped deformed P91 specimen for punch displacement of 1.5mm. 199

Figure 6-14. The comparison between FE result and the dome-shaped deformed P91 specimen for punch displacement of 1.65mm. 200

Figure 6-15. The comparison between FE result and the dome-shaped deformed P91 specimen for punch displacement of 1.74mm. 200

Figure 6-16. Comparison of FE model with experimental data. 203

Figure 6-17. Plot of punch force versus punch displacement for various initial PAGs size and lath width.....203

Figure 6-18. Plot of dislocation density versus plastic strain for various initial PAGs size and lath width.....204

Figure 6-19. Plot of punch force versus punch displacement for various friction coefficient.....204

Figure 6-20. Plot of dislocation density versus plastic strain for various friction coefficient.....205

CHAPTER 1:
INTRODUCTION

1.1 Overview

The efficiency of power plants relies critically upon the resistance to high operating temperature and stresses of their components [1]. Creep occurs in materials of components due to elevated temperatures and stresses in power plants, chemical plant and aero-engines [2]. Many investigations have taken place regards 9-12%Cr martensitic steels materials due to their increasing use to improve the thermal efficiency of power plant components [3]. The study of these materials has included their creep strength, as a result of their application at high temperature. However, insight into the thermomechanical behaviour of materials that are used under highly tough operating conditions has become more significant as this material undergoes plasticity and creep, making the understanding of thermomechanical viscoplastic problems ever more critical. The concern of researchers on viscoplastic behaviour has increased due to the required high thermal operation of the power plant. The rapid change in temperature and the high thermal gradients associated with rapid on-off cycling of the plant may lead to high levels of stress [4]. For example, internal cracks have been found in components of the power plant as a result of thermo-mechanical loading [5]. Shibli,

2008 has been suggested utilising high creep strength alloy steels in the pressure vessel components as one of the keys to prevent initiation of cracks [6] so that the thickness of components in the power plant can be decreased. However, a better understanding of the stress-strain behaviour of steel alloys materials in the power plant components requires to be recognised first. This limitation can be estimated by the finite element simulation as formerly modelled by Hyde et al. for pipe weldments under creep states at elevated temperature [7]. The simulation of power plant components requires an appropriate constitutive material model which can exactly predict the thermo-mechanical behaviour and the failure of life. The majority of the earliest research on power plant materials has been connected with their bulk creep behaviour under constant load operation. For instance, a creep constitutive equation incorporates damage has been presented for the P91 steel [8]. Similar studies have also been presented for the parent, heat-affected zone (HAZ) and weld materials of Cr-Mo-V steel welds in the range 565-640˚C [9]. The extension of these creep constitutive models has led to a wider understanding of the material behaviour in such applications as modelling of failure prediction, for example, work by Hayhurst et al. and Yaghi et al. [10, 11]. A commonly used model is the unified viscoplasticity model developed by Chaboche and Rousselier [12]. This viscoplasticity model has been used in many studies, involving research into aero-engine materials such as nickel-based alloys [13].

In contrast to the above applications, constitutive creep models which contain micromechanical details have had relatively little attention. Thus, a model which can include microstructural effects is required.

1.2 Research Aim and Objective

Considering the above motivations, the aim of this thesis is to investigate how the mechanical properties of the P91 steel at high temperatures are influenced by the evolution of dislocation density, grain growth and initial microstructural parameters such as the magnitude of the dislocation Burgers vector and the Taylor factor. The thesis will also examine the applicability of the developed microstructural models using a small pinch test rig through experimentation and finite element-based simulation. These aims will be fulfilled by realising the following objectives:

1- Develop a creep model with consideration of initial microstructural parameters for the P91 steel to evaluate creep behaviour of uniaxial and multiaxial creep applications at elevated temperatures environments.

2- Implement the developed creep model in a commercial finite element software and simulate the creep strain behaviour of the P91 steel under isothermal and constant loading conditions.

3- Obtain quality stress-strain data from the P91 steel under plasticity and creep conditions in isothermal tests using available testing machine systems in the University of Nottingham.

4- Conduct a comprehensive study to investigate the microstructural evolution and physical fracture mechanisms of the P91 steel during small punch tensile tests.

5- Develop a viscoplastic model based on dislocation and grain growth for the P91 steel to simulate the plasticity behaviour of multiaxial small punch tensile rig tool at high temperatures environments.

6- Implement the developed physical-based viscoplastic model in a commercial finite element software and simulate the plastic behaviour of the P91 steel under isothermal and constant strain rate conditions.

1.3 Organization of the thesis

This thesis is organised into eight chapters with content summarised as follows:

The first chapter introduces the general background of the constitutive material models with particular attention paid to the research aims and objectives of the research and the organisation of the thesis.

Chapter 2 presents a literature review on the material constitutive models, which involves creep models, small punch creep test, small punch tensile test and viscoplasticity models. Examples of previous work on material creep modelling under mechanical loading conditions are detailed. Experimental and finite element simulation of punch creep has been reviewed to describe the displacement-time behaviour of high thermal components. Small punch tensile experimental and its finite element simulation examples have also been provided for the case of high temperature applications. Particular attention has been given to the viscoplasticity model, which includes typical plasticity components, such as

kinematic and isotropic hardening in addition to a viscoplasticity model. Examples of previous work on material behaviour modelling under thermo-mechanical conditions are also presented. The developments of high-temperature materials used in the power plant applications are briefly introduced.

Chapter 3 presents the development of the creep model based on initial material parameters for the P91 steels using the isothermal constant load conditions. The procedures for determining the initial material constants are described. Then, a finite element model to simulate uniaxial and small punch creep is described, and the mathematical calculations and model implementation are also presented. The microstructural creep model has been also implemented in ABAQUS software via a UMAT user subroutine. Simulation results of an axisymmetric small punch model under isothermal conditions subjected to various load ranges and an axisymmetric model under isothermal stress-controlled conditions are compared to experimental data to validate the prediction capability of the microstructural creep model.

The fundamental theory and key practical considerations in using FE to simulate uniaxial tensile and creep are described in Chapter 4; these include the microstructural based viscoplastic constitutive model and non-linear FE solution methods. The constitutive microstructural model has been implemented in ABAQUS software via a UMAT user subroutine. Simulation results of an axisymmetric model under isothermal conditions at various strain ranges and an axisymmetric model under isothermal stress-controlled conditions are compared

to experimental data to validate the prediction capability of the microstructural model.

Chapter 5 presents the experimental small punch tensile whole and interrupted tests data, particularly for the P91 steel at 600°C, which further analysed in order to understand the physical characterisation and fracture process under constant loading conditions. The results of microstructure investigation of the tested steel specimens at different punch displacement of the tests using scanning electron microscopes, backscattered electron, energy dispersive X-ray spectroscopy and electron backscattered diffraction are also presented.

In chapter 6, a modified microstructural model is developed with consideration of the evolution of dislocation density and grain growth to predict viscoplastic behaviour in the small punch process. The modified microstructural constitutive model has been also implemented in ABAQUS software via a UMAT user subroutine. Simulation results of an axisymmetric small punch model under isothermal conditions at various strain ranges are compared to experimental data to validate the prediction ability of the developed microstructural model.

Chapter 7 summarises the main research work conclusions based on the results gained in the above sections. Suggestions for possible further work are also outlined.

CHAPTER 2:
LITERATURE REVIEW

2.1 Introduction

As a step towards the development of a new microstructurally based mechanical model for creep and viscoplasticity, a literature review of current modelling techniques in relation to the steels is presented here, namely the P91 steel. As the material deforms under thermomechanical loading conditions, plastic and creep behaviours become significant and model of strain hardening behaviour such as isotropic and kinematic hardening are presented in the literature review. This chapter also reviews finite element modelling of the small punch creep tests and small punch tensile tests, which have been carried out to predict the plastic and creep behaviour and compare to the experimental data. This chapter also contains information on the improved P91 steels, which have been found in power plant applications, to give new steel components with acceptable mechanical behaviour at high temperature.

2.2 Creep

Creep is the time-dependent plasticity of material under relatively high temperature (usually above $0.4T_m$ for most materials where T_m is the absolute melting temperature) and constant stress. The creep strain (ε^c) is controlled by time, stress, and temperature and therefore, the lifetime of the engineering components can be defined as a function of these factors as follow:

$$\varepsilon^c = f(t, \sigma, T) \tag{2-1}$$

where $t, \sigma,$ and T are time, stress and temperature, respectively [14].

The new microstructural method used to investigate creep resistance and to realize the constant material parameters involve applying a constant load on small discs and cylindrical uniaxial specimens at high temperature respectively. The test results, for the small punch creep tests are normally presented as a graph of punch displacement versus time as shown in Figure 2-1 and then for uniaxial creep tests as a graph of creep strain versus time curve, shown in Figure 2-2. The inelastic deformation behaviour under these conditions is divided into three distinct regions, primary creep, secondary creep and tertiary creep, as depicted in Figure 2-2. These stages are connected with transient, steady-state, and rapidly-accelerating creep strain rate, respectively [15].

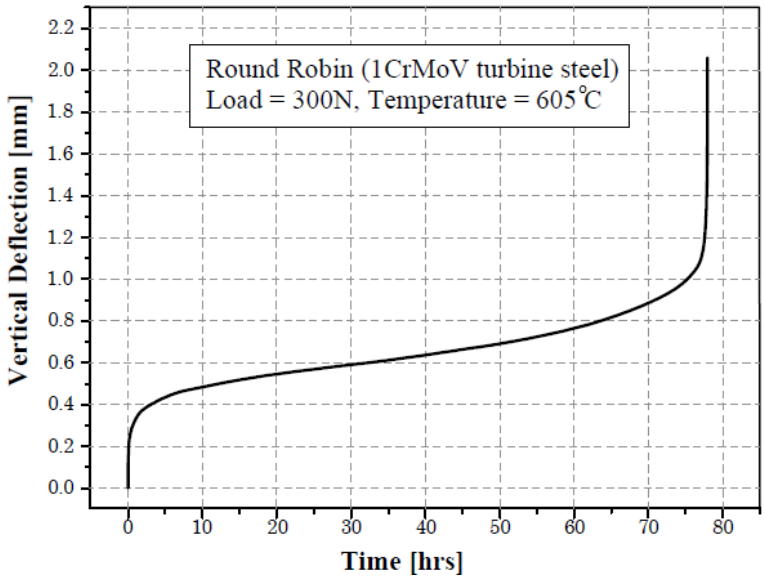


Figure 2-1. Typical punch displacement (vertical deflection) versus time curve for a small punch creep test under constant load [16].

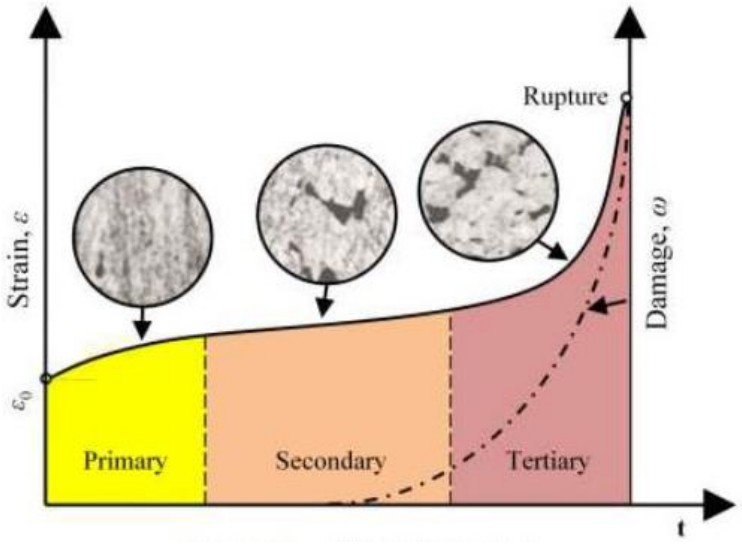


Figure 2-2. General form of creep behaviour in pure metals [17].

A specific material may not necessarily display all the regions of creep for applied testing conditions. In Figure 2-3, OA is the stage involving transient creep rate, which develops instantly after the full testing load has been used. It is termed the inhibiting creep rate where work-hardening actions increase and act to prevent the dislocation motion. The next stage, AB, is usually observed as the largest portion of the creep curve and corresponds to a period of constant creep rate due to a balance between work-hardening and thermally activated recovery (softening) actions. Usually, if the applied creep load is eliminated part way through a test, the strain drops by approximately the elastic strain value. Then a small proportion of the creep strain is later recovered over a period of time, leading a permanent (irrecoverable) strain. The final stage, BC, corresponds with the accelerating creep rate, which leads up to damage. This stage can be caused by several factors which include the increase of stress during a constant load creep test, development of necking, and the formation of voids and cracks.

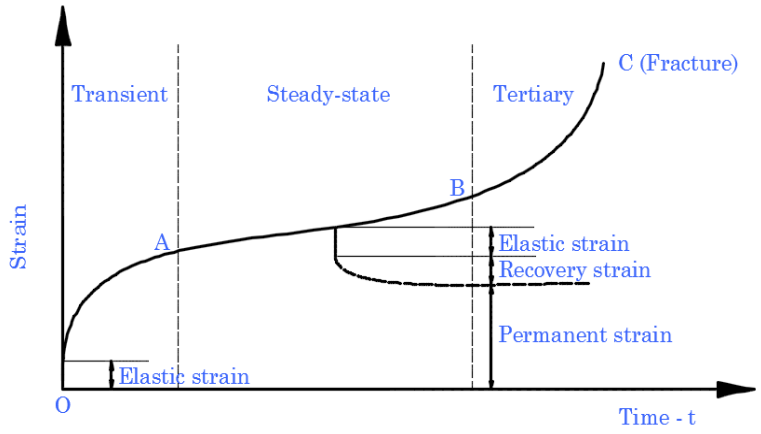


Figure 2-3. Recovery creep [18].

For most polycrystalline materials, a group of creep strain-time curves can be plotted, as shown in Figure 2-4 for tests conducted at constant stress and different temperatures. a similar trend is obtained when the creep tests are performed at different stresses and a constant temperature, as shown in Figure 2-5 [18].

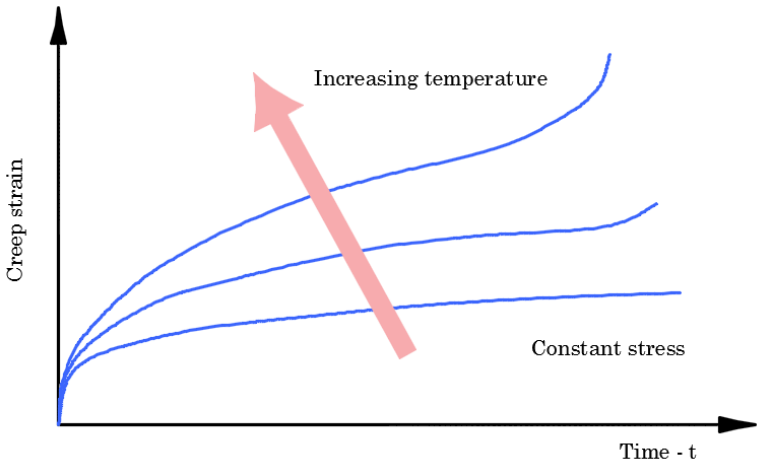


Figure 2-4. Influence of temperature, T, on creep behaviour [19].

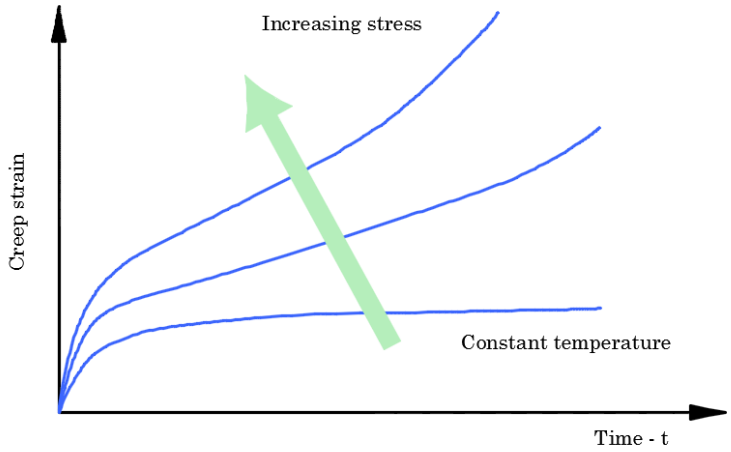


Figure 2-5. Influence of stress on creep behaviour [19].

2.2.1 Primary and Secondary Creep

Primary creep occurs after a relatively small elastic deformation, and strain rate trends to be relatively high at the beginning of the primary region. Many constitutive models of primary creep have been studied. Andrade's model for primary creep is one of the most popular creep models which assumes dependence only on time.

$$\varepsilon^c = At^{1/m} \tag{2-2}$$

where ε^c is a transient creep, A is a creep coefficient, t is time and m is a dimensionless creep exponent.

In most materials, the experimental tests have been observed that the constant m taken a value of 3 [20]. The stress dependence has been incorporated into the primary creep Equation (2-2) to give the following widely used equation.

$$\dot{\varepsilon}_c = A\sigma^n t^m \tag{2-3}$$

where σ (MPa) is effective stress, A ($MPa^{-n}hr^{-m}$), and n and m are temperature-dependent primary creep constants [17]. A list of the earliest and most popular primary creep models are presented in Table 2-1.

Table 2-1. Primary creep constitutive models [14]

Source	Creep Law
Andrade, 1910	$\varepsilon_{cr} = \left(1 + At^{1/m}\right)\exp(kt) - 1$ $\varepsilon_{cr} = At^{1/m}(t \to 0, k \to 0)$
Bailey, 1935	$\varepsilon_{cr} = Ft^{n} \quad \left(\frac{1}{3} \le n \le \frac{1}{2}\right)$
McVetty, 1943	$\varepsilon_{cr} = G(1 - e^{-qt}) + Ht$
Graham and Walles, 1955	$\varepsilon_{cr} = \sum_{i} a_i t^{n_i}$
Garofalo, 1965	$\varepsilon_{cr} = \theta_1\left(1 - e^{-\theta_2 t}\right) + \dot{\varepsilon}_s t$

If the stress σ is assumed to be constant then the time hardening primary creep rate $\dot{\varepsilon}_c$ is given by the relation

$$\dot{\varepsilon}_c = \frac{d\varepsilon_c}{dt} = Am\sigma^{n}t^{m-1} \tag{2-4}$$

where the units of A modify to $(MPa^{-n}hr^{-(m-1)})$. This constitutive equation can be expressed in terms of the multiaxial state of stress using the normal direction tensor theory [21]

$$d\varepsilon_{ij} = \frac{3}{2}A\sigma^{n-1}S_{ij}t^{m-1}dt\ , \tag{2-5}$$

where $d\varepsilon_{ij}$ are the deformation tensor components and S_{ij} is the deviatoric stress. Inserting the time t from Equation 2-3 into 2-4 leads to a strain-hardening primary creep rate equation

$$\dot{\varepsilon}_c = \frac{d\varepsilon_c}{dt} = A^{1/m} m\sigma^{n/m}\varepsilon_c^{(m-1)/m} \quad (2\text{-}6)$$

In general, the solution of strain hardening predicts slightly lower creep strain rates than time hardening. The strain hardening equation, 2-6, involves stress and strain as variables while the time hardening equation, 2-4, includes stress and time as variables. Many examples of research have demonstrated in experiments that the prediction of creep behaviour of materials using strain hardening theory is better than those using the time hardening theory [15].

Many attempts have been made to combine time and strain hardening theories to produce an equation taking account of both phenomena, and becoming in the following form

$$\dot{\varepsilon}_c = \frac{d\varepsilon_c}{dt} = C\sigma^{\delta}\varepsilon_c^{\beta}t^{\gamma} \ , \quad (2\text{-}7)$$

where $C\ (1/\text{MPa})^{-\delta}(1/\text{hr})^{-\gamma}$, δ, β, and γ are constants.

In the secondary creep stage, creep behaviour within this region is characterised by the minimum creep strain rate $\dot{\varepsilon}_{min}$ during constant load tests. The creep strain rate is almost constant, as depicted in Figure 2-6 [2]. Creep lifetimes of the secondary regime are, for most engineering components, usually large and the creep deformations are identical aspect with plastic deformations behaviour. Therefore, such secondary creep behaviour is the most widely modelled aspect of creep behaviour. The constant steady-state creep strain rate results from the balance between the strain hardening (athermal) and thermal softening (annealing).

Many examples of research have presented a direct relationship between minimum creep strain rate and the stress. One of the most popular steady-state models is the classical Norton power law.

$$\dot{\varepsilon}_c = \frac{d\varepsilon_c}{dt} = A\sigma_e^n , \tag{2-8}$$

where σ_e is an equivalent stress, and A and n are the steady state creep constants. Various stress-dependent creep constitutive models have been developed. The secondary creep constants, A and n both exhibit temperature dependency. Applied stress presents a major contribution to the secondary creep strain rate where the secondary creep constant, n, is utilised as an exponent of stress [17].

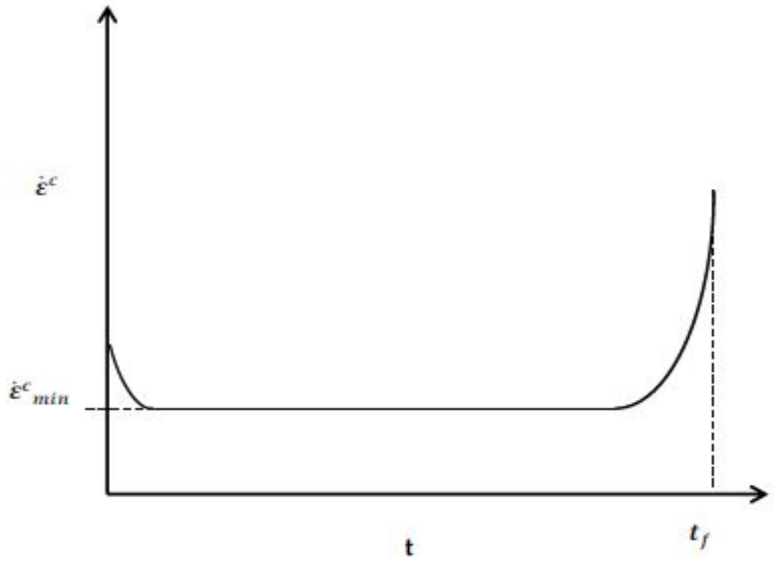


Figure 2-6. A typical variation of creep strain rate versus time under constant stress [2].

The popularity of this constitutive equation arises from the ease of its application and the retention of functional shape in spite of stress magnitude. This leads that the change of stress distribution is not affected by the increase of the proportional load in the Norton creep law. By contrast, most other steady-state creep models subject to change of functional shape, which leads to redistribution of stress when the load is increasing. A list of the fundamental and most suitable secondary creep models are shown in Table 2-2. Both kinds of steady-state creep models make use of the classic von Mises equivalent stress

$$\sigma_{von} = \sqrt{\frac{3}{2} S_{ij} S_{ij}} \tag{2-9}$$

$$S_{ij} = \sigma_{ij} - \sigma_H, \quad \sigma_H = \frac{1}{3}\sigma_{kk}\delta_{ij} \ , \tag{2-10}$$

where S_{ij} is the deviatoric stress tensor, σ_H is the pressure (hydrostatic) stress, σ_{kk} is the trace of a second-order stress tensor, σ_{ij}, and δ_{ij} is the Kronecker delta tensor.

Dorn proposed that the Arrhenius equation can be used instead of the creep constant, A, to account the dependence upon temperature [22].

$$A(T) = B\exp\left(\frac{-Q}{RT}\right) \tag{2-11}$$

where B is the pre-exponential factor in units ($MPa^{-1}hr^{-1}$), Q is the activation energy for creep behaviour in units ($J\,mol^{-1}$), R is the universal gas constant which equals 8.314 $J\,mol^{-1}\,K$, and T is the temperature in Kelvin.

Substituting Equation 2-11 into Equation 2-8 gives

$$\dot{\varepsilon}_c = \frac{d\varepsilon_c}{dt} = B\sigma_e^n \exp\left(\frac{-Q}{RT}\right) \quad (2\text{-}12)$$

The secondary creep constants, B, n and Q, exhibit stress dependence, within the experimental tests, when comparing constants obtained from lower stress (low strain rate) with those at high stress (high creep strain rate) [17]. A modification of Equation (2-12) to describe the secondary creep strain rate within high-stress applications was proposed by Garofalo as follows [23]

$$\dot{\varepsilon}_c = \frac{d\varepsilon_c}{dt} = B \exp(\varphi\sigma)\exp\left(\frac{-Q}{RT}\right) \quad (2\text{-}13)$$

where φ is a further secondary creep constant. Garofalo also inserted the creep constant φ in the Equation 2-13 into Equation 2-12 to give [23]

$$\dot{\varepsilon}_c = \frac{d\varepsilon_c}{dt} = B(\sinh\gamma\sigma)^n \exp\left(\frac{-Q}{RT}\right) \quad (2\text{-}14)$$

According to Webster and Ainsworth, the model employs the Equation 2-12 when $\gamma\sigma < 0.8$ and employs the Equation 2-13 when $\gamma\sigma > 1.2$ provided that $\varphi = \gamma n$ [18].

Table 2-2. Secondary creep constitutive models [14].

Source	Creep Law
Norton, 1929	$\dot{\varepsilon}_{cr} = A\left(\frac{\sigma}{\sigma_o}\right)^n$
Soderberg, 1936	$\dot{\varepsilon}_{cr} = A\left(\exp\left(\frac{\sigma}{\sigma_o}\right) - 1\right)$
McVetty, 1943	$\dot{\varepsilon}_{cr} = A\sinh\left(\frac{\sigma}{\sigma_o}\right)$
Dorn, 1955	$\dot{\varepsilon}_{cr} = A\exp\left(\frac{\sigma}{\sigma_o}\right)$
Johnson, Henderson and Kahn, 1963	$\dot{\varepsilon}_{cr} = A_1\left(\frac{\sigma}{\sigma_o}\right)^{n_1} + A_2\left(\frac{\sigma}{\sigma_o}\right)^{n_2}$
Garofalo,1965	$\dot{\varepsilon}_{cr} = A\left(\sinh\left(\frac{\sigma}{\sigma_o}\right)\right)^n$

2.2.2 Tertiary Creep and Rupture

The final creep regime is termed the tertiary stage. In the creep tests, with constant applied load and temperature, the tertiary creep strain rate trends to increase during the tertiary regime and eventually leads to a rupture, as indicated in Figure 2-3. The rapture results from several factors which combine to give reduced load-bearing area increased local stress and hence significantly increased strain rates, such as necking, void formation and cracking [18].

Many mixed creep constitutive models have been proposed, in order to develop a mathematical model capable of representing some or all of the complete creep

strain curve. A list most popular mixed regime models are provided in Table 2-3. Kachanov made the earliest attempt to analyse the entire creep strain–time curve using the damage parameter, w, where $0 < w < 1$ [24].

Andrade presented a new creep strain equation to describe the steady-state and tertiary creep strain as follows [25, 20].

$$\varepsilon = \varepsilon_i\left(1 + \beta t^{1/3}\right)\exp(kt) \tag{2-15}$$

where ε_i is initial creep strain, t is a time , and β and k are material parameters.

Garofalo extended equation 2-15 to include the transient creep strain and hence achieved a good fit with the corresponding creep data;

$$\varepsilon = \varepsilon_i + \varepsilon_p^c(1 - \exp(-rt)) + \dot{\varepsilon}_s^c t \tag{2-16}$$

where ε_p^c is the primary (transient) creep strain, $\dot{\varepsilon}_s^c$ is the secondary creep strain rate and r is the ratio of transient creep strain rate to the transient creep strain at a given time, i.e., $r = \dot{\varepsilon}_p^c/\varepsilon_p^c$, where $\dot{\varepsilon}_p^c$ and ε_p^c are the transient creep strain rate and the transient creep strain respectively [25].

Table 2-3 Mixed regions creep constitutive equations [26-29].

Source	Creep Law	Creep Regions
Kachanov-Rabotnov, 1967-69	$\dot{\varepsilon}_{cr} = A\left(\frac{\sigma_e}{1-w}\right)^n$, $\dot{w} = \frac{M\sigma^{\chi}}{(1-w)^{\phi}}$	Secondary Tertiary
Evans-Wilshire (Theta Projection), 1984	$\varepsilon = \theta_1\left(1-\exp(-\theta_2 t)\right) + \theta_3(\exp(\theta_4 t)-1)$	Primary Secondary Tertiary
Prager, M. (Omega Method), 1995	$\dot{\varepsilon}_{cr} = \dot{\varepsilon}_o \exp(\beta_p \varepsilon)$	Secondary Tertiary

2.2.3 Creep Mechanisms

The creep mechanisms depend upon a material's grain size and alloying additions and the applied stress and temperature conditions that it is subjected to. In general, the creep deformation of a range of engineering alloys exhibit identical characteristics at identical fractions of their absolute melting temperature T_m. When the material's absolute temperature is greater than about $0.5T_m$, creep mechanisms can be divided into two processes: diffusion (bulk-self and grain boundary diffusion) and dislocation creep [30, 31]. Atoms in solid materials have a high frequency of vibration about their mean locations. A high magnitude of vibration is sufficient to allow the atom to move from its current position into a nearby site. This process is called solid-state diffusion, which is a thermally activated movement. The necessary activation energy, yields by thermal energy, required to overcome the potential energy barrier which prevents atomic movements. Therefore, the elevated temperature is responsible for activating the

solid-state diffusion mechanism [28, 3]. The creep resistance can be improved by creating obstacles to prevent the movement of atoms inside grains. Moreover, the grain boundaries also act as barriers to dislocation climb or travel from one grain into another. The pileup of dislocations on the grain boundary contributes to the strengthening of the grain boundary in addition to that providing by changing orientations and size of grains. Since developments of microstructural rearrangement directly affect atomic displacement, it is then reasonable to assume that creep mechanisms will be directly connected to the diffusion mechanism, especially, at the elevated temperature [32, 33]. Small grain size materials tend to be harder than those with coarse grains, and hence have high creep resistance because it can be shown for solids that fine grain size allows only a short distance for atom's movement inside the grain. The relation between flow stress and an average value of grain size is defined mathematically by the Hall-Petch equation as follows

$$\sigma_f = \sigma_i + \frac{K}{\sqrt{D}} \tag{2-17}$$

where σ_i is the initial friction stress, K is a material constant and D is the average grain diameter [34]. However, for both extremely fine-grained and very large-grained polycrystalline materials, equation (2-17) is not valid. The solidification rate directly controls the number and size of the grains. High solidification rates generate fine-grained materials, whereas on the other hand, slow solidification rates lead to coarse-grained materials. Therefore, the solidification rate is a significant factor in the mechanical properties of a material, including its creep properties [35, 25, 36, 37].

2.3 The Visco-Plastic Constitutive Models

Monotonic loading of engineering components at elevated temperature may result in both plasticity and creep deformation. Viscoplastic constitutive models involve three main components: a yield criterion, a flow rule, and a hardening rule. Viscoplastic materials also demonstrate strain hardening/softening where strain rate contributes the obvious yield strength. Generally, visco-plastic properties of crystalline materials exhibit rate-dependent or time-dependent deformation in which the total strain rate value involves both the plastic strain rate and the creep strain rate.

2.3.1 Yield Surface and Flow Rule

The yield criterion indicates the beginning of plastic deformation based on the stress tensor, expressed in terms of equivalent stress. There are many yield criteria including those of von Mises and Tresca for yielding materials and the Gurson model for porous materials. The yield criterion and yield stress define a surface in the stress space giving the threshold between elastic behaviour inside the boundary of the region and inelastic deformation outside the boundary of the yield surface [38]. The mechanisms underlying isotropic and kinematic hardening are described in Figures 2-7 and 2-8, respectively [39].

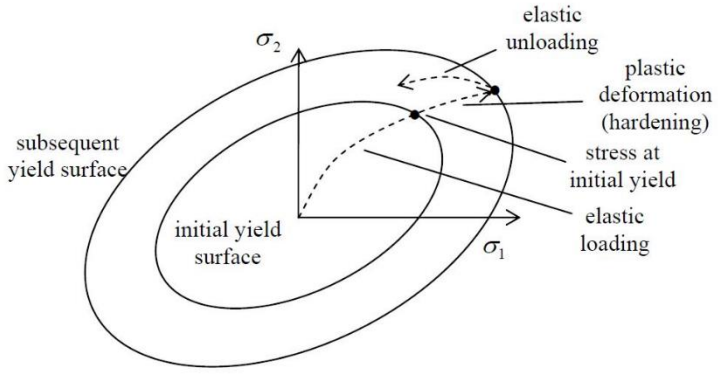


Figure 2-7. Schematic of isotropic hardening [40].

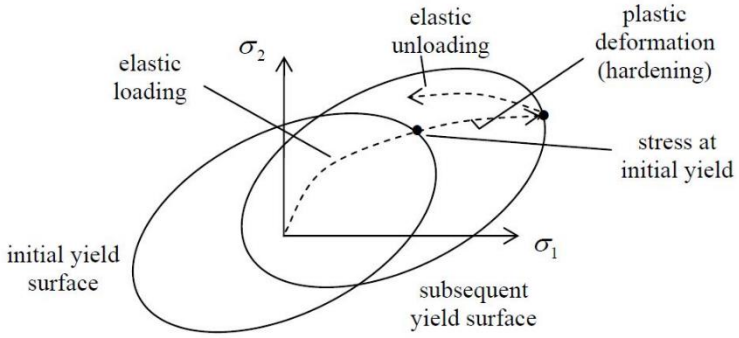


Figure 2-8. Schematic of kinematic hardening [40].

The flow rule provides a relation between stress and plastic strain increment (or rates). In the isotropic hardening behaviour, it is reasonable to assume that the principal plastic strain increments $d\varepsilon_i^p$ are proportional to the principal deviatoric stresses S_i:

$$\frac{d\varepsilon_1^p}{S_1} = \frac{d\varepsilon_2^p}{S_2} = \frac{d\varepsilon_3^p}{S_3} = d\lambda \geq 0 \tag{2-18}$$

The positive scalar λ , which knowns as the plastic multiplier, gives the ratios of the plastic strain increments to the deviatoric stresses. The Equation 2-18 is often expressed in the general alternative form

$$d\varepsilon_{ij}^{p} = d\lambda S_{ij} \tag{2-19}$$

or, in the rating form, dividing by dt, one has

$$\dot{\varepsilon}_{ij}^{p} = \dot{\lambda} S_{ij} \tag{2-20}$$

In terms of the actual stresses, the Levy-Mises equation has

$$\dot{\varepsilon}_{ij}^{p} = \dot{\lambda}\left(\sigma_{ij} - \frac{1}{3}\sigma_{kk}\delta_{ij}\right) \tag{2-21}$$

where σ_{kk} is the hydrostatic stress and δ_{ij} is Kronecker delta tensor [41, 42].This plastic stress-strain relationship is known as flow stress. Instead of the particular flow rule, Equation 2-20, the plastic multiplier can be defined from the hardening rule

$$\dot{\varepsilon}_{ij}^{p} = \dot{\lambda} G_{ij} \tag{2-22}$$

where G_{ij} is the function of stresses and maybe other hardening parameters [40]. The general form of the flow rule can be used to model the wide class of material behaviour

$$\dot{\varepsilon}_{ij}^{p} = \dot{\lambda}\frac{\partial g}{\partial \sigma_{ij}} \tag{2-23}$$

Here, g is a scalar function known as the plastic potential that, when differentiated with respect to the stress, gives the plastic strains. The flow rule in

the Equation 2-23 is known as a non-associated flow rule. Further materials whose plastic potential is the yield function, $g = f$, the plastic deformation may be expressed as [43]:

$$\dot{\varepsilon}_{ij}^{p} = \dot{\lambda}\frac{\partial f}{\partial \sigma_{ij}} \tag{2-24}$$

This form is known as the associated flow rule because the flow rule is associated with a given yield criterion [44].

2.3.2 Internal Variables and Hardening

Strain hardening is the increase in yield strength of materials which are subjected to inelastic deformation under external loading. It is also known as work hardening, and occurs due to dislocation movements and dislocation accumulation at the grain boundary, within the structure of materials undergoing plastic strain. Three rules have been proposed for modelling work hardening of materials: isotropic hardening; kinematic hardening and combined isotropic/kinematic hardening.

2.3.2.1 Isotropic Hardening

Isotropic hardening depicts the way that the yield surface giving the value of equivalent stress which results in further yield expands uniformly in all directions as accumulated plastic strain increments. The yield surface constantly expands in all direction, which means the flow stress increases in all principal stress directions once the material has undergone plastic strain. A simplified description of the isotropic hardening is shown in Figure 2-9.

A number of investigators have proposed hardening equations to perform various mechanisms to describe both hardening and recovery processes [45]. The changing size of yield stress during the isotropic hardening is described by an internal hardening variable, R, and also called as drag stress. The common one rate evolution of drag stress that is presented by Chaboche and Rousselier [12]

$$\dot{R} = b(Q - R)\dot{\varepsilon}^p \tag{2-25}$$

where b is the speed at which the saturation value is approached, Q is the asymptotic value of R and $\dot{\varepsilon}^p$ is the accumulated plastic strain rate.

The integration of Equation 2-25 with respect to time leads to the following relation

$$R = Q\left(1 - \exp(-b\bar{\varepsilon}^p)\right) \tag{2-20}$$

With the isotropic strain hardening applied to the von Mises criterion, the hardening variable as a function of plastic strain can be written [38]

$$R = R(\bar{\varepsilon}^p) \tag{2-26}$$

The accumulated plastic strain, $\bar{\varepsilon}^p$, expressed in the form

$$\bar{\varepsilon}^p = \int_0^t \sqrt{\frac{2}{3}\dot{\varepsilon}^p : \dot{\varepsilon}^p \, dt} \tag{2-27}$$

and the yield criterion is given in the following form

$$f = \sqrt{\frac{3}{2}S_{ij}S_{ij}} - \mathrm{R} - \sigma_y \tag{2-28}$$

where σ_y is the yield stress.

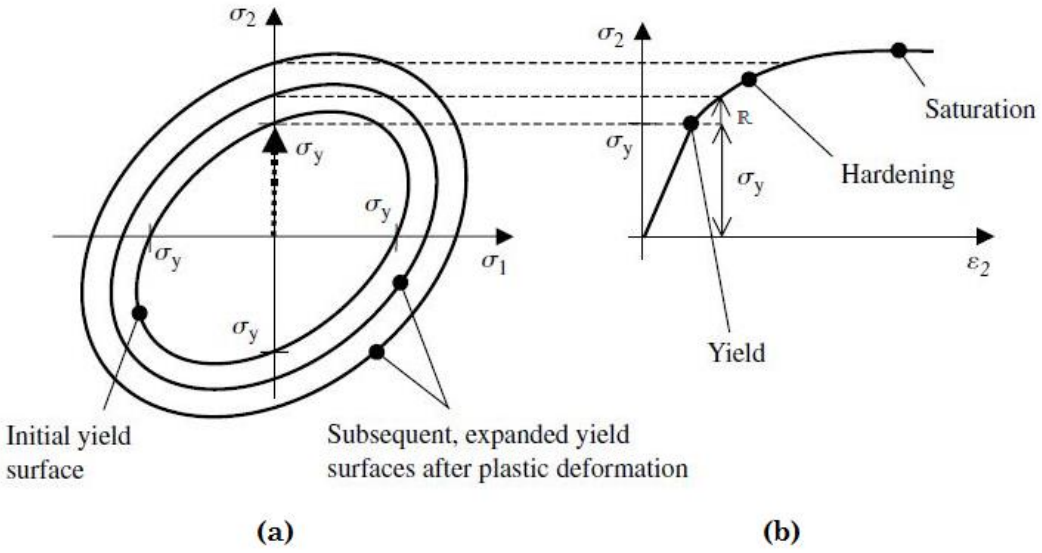


Figure 2-9. Isotropic hardening, (a) yield surface and (b) the corresponding uniaxial stress-strain curve [38].

2.3.2.2 Kinematic Hardening

Kinematic hardening occurs when the yield surface merely translates through the stress space while retaining its original shape and size, as shown in Figure 2-10. In practice, for most materials, it is observed that if these materials are subjected to external uniaxial loading, either tension or compression, they show reduced strength to inelastic deformation in the reverse direction. For instance, in the case

of a tension-compression test, it is normally observed that the yield stress in tension is higher than that in compression if the test is accomplished in tension first. This phenomenon is frequently referred to the Bauschinger effect and formulated numerically via kinematic hardening [46]. Several of constitutive models have been proposed to define elastic-plastic behaviour dependent on cyclic loading conditions [47-50].

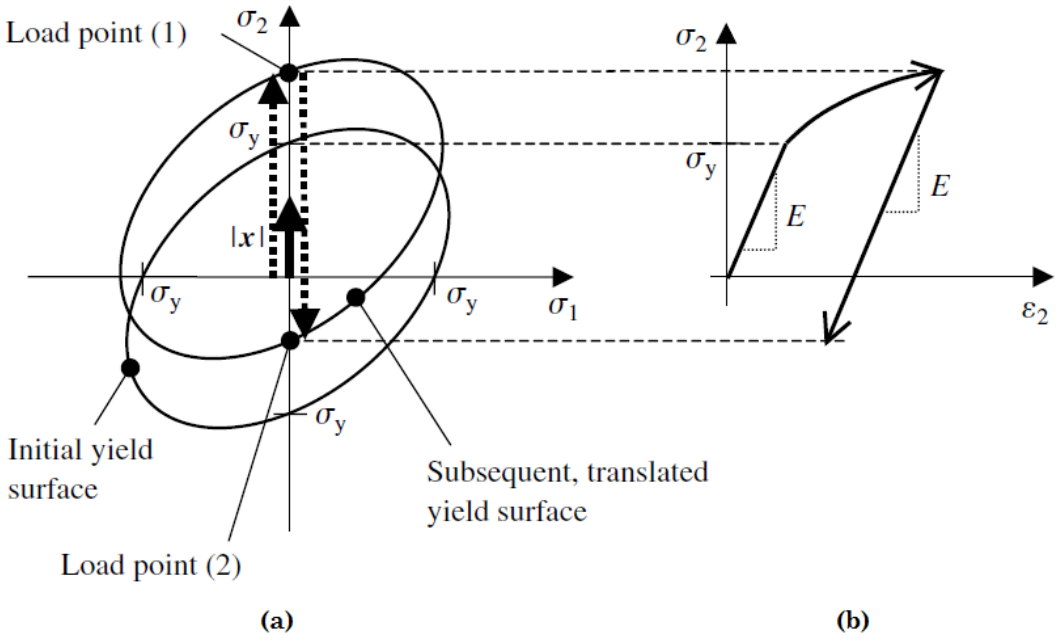


Figure 2-10. Reversed loading with kinematic hardening (a) the translation of the yield surface and (b) stress-strain curve, which shows the Bauschinger effect [38].

In the uniaxial form, the yield function for the kinematic hardening model is given by the following expression

$$f = \sqrt{\frac{3}{2}(S_{ij} - \chi)(S_{ij} - \chi)} - \sigma_y \,, \tag{2-29}$$

where χ is the hardening parameter and is normally known as the back stress.

The linear hardening kinematic model is developed by Prager which is given by the following form [51]

$$\dot{\chi} = \frac{2}{3} c\dot{\varepsilon}^p \tag{2-30}$$

where c is the material constant, representing the gradient of the linear hardening graph [52]. In general, a non-linear kinematic hardening model is widely used to represent the stress-strain for cyclic loading tests. This model utilizes a dynamic recovery behaviour term, also known as a recall term, which is given by [53]

$$\dot{\chi} = \frac{2}{3} c\dot{\varepsilon}^p - \gamma\chi\dot{p} \tag{2-31}$$

where γ is a material constant.

For the non-linear kinematic hardening plasticity model, the value of saturation stress can be determined by the value of c/γ in the plastic deformation regime. The maximum stress value for independent plasticity tests can be determined by the combination of c/γ and initial yield stress σ_y for the plasticity tests [38]. The saturation stress is shown, schematically, in Figure 2-11.

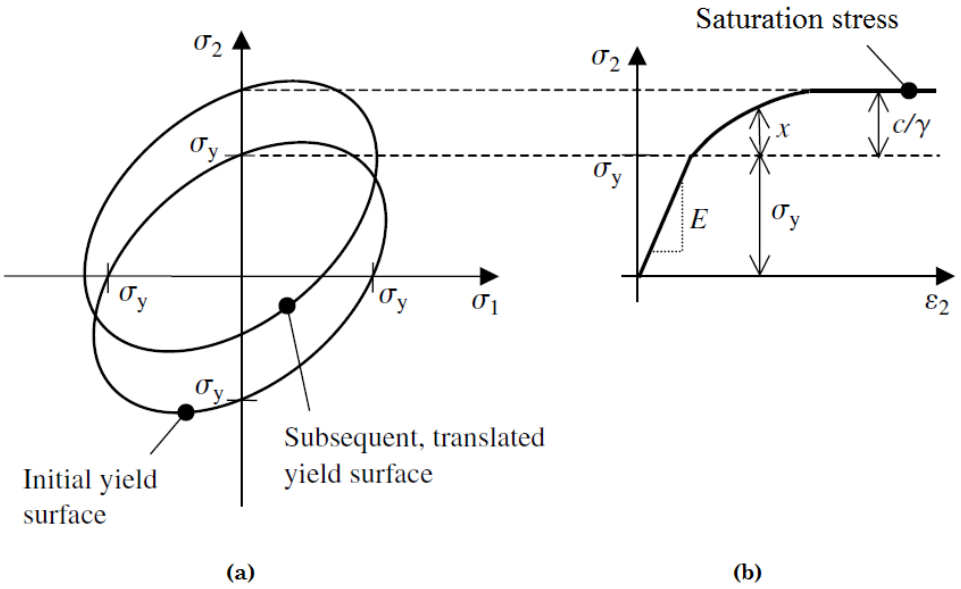


Figure 2-11. Non-linear kinematic hardening (a) the yield surface and (b) stress-strain curve [38].

2.3.3 Uncoupled Elastoplasticity-Creep

Uncoupled elastic-plasticity-creep models, typically called non-unified models, conventionally consist of time-dependent creep and time-independent plasticity deformation which are combined in order to analyse both of these behaviours in the same model. One of the most popular creep models is the Norton power law to represent time-dependent properties and one of the isotropic and/or kinematic hardening models to exhibit time-independent properties. Shang et al. [54] used a non-unified model to exhibit the stress-strain behaviour of superplastic forming dies. The entire set of material constants for creep and plastic models are obtained by utilizing a constant loading test and cyclic loading tests, respectively. It is also assumed that the constants of the creep model are not correlated with those in

the plastic model [54]. Krempl's model was a combination of the creep and plastic constitutive equations. However, when compared with corresponding experimental results, it has been found that an uncoupled elastic-plasticity-creep model gives unsatisfactory results [55]. Therefore, visco-plasticity models have been used more widely than the non-unified models to determine time-dependent plasticity behaviour at elevated temperature.

2.3.4 Unified Viscoplasticity Model

Time-dependent effects in the plastic domain can be modelled using `viscoplasticity laws which incorporate various functions to represent the time dependency [56]. One of the well-known unified viscoplastic models is that suggested by Chaboche and Rousselier [12]. There are two reasons why the model is known as "unified". Firstly, one strain parameter, called viscoplastic strain simultaneously represents both the creep and the plastic strains. Therefore, for different kinds of loading, the viscoplastic strain does not lead to a discontinuity in the representation. Secondly, the same hardening mechanisms, expressed in terms of effective plastic strain, are used in both the time-dependent constitutive model and the independent model [57].

For the isotropic hardening case, the total stress, σ, is made up of the yield stress, σ_y, together with stress causing from by the isotropic hardening, R, and viscous stress, σ_v as shown in Figure 2-12 [38].

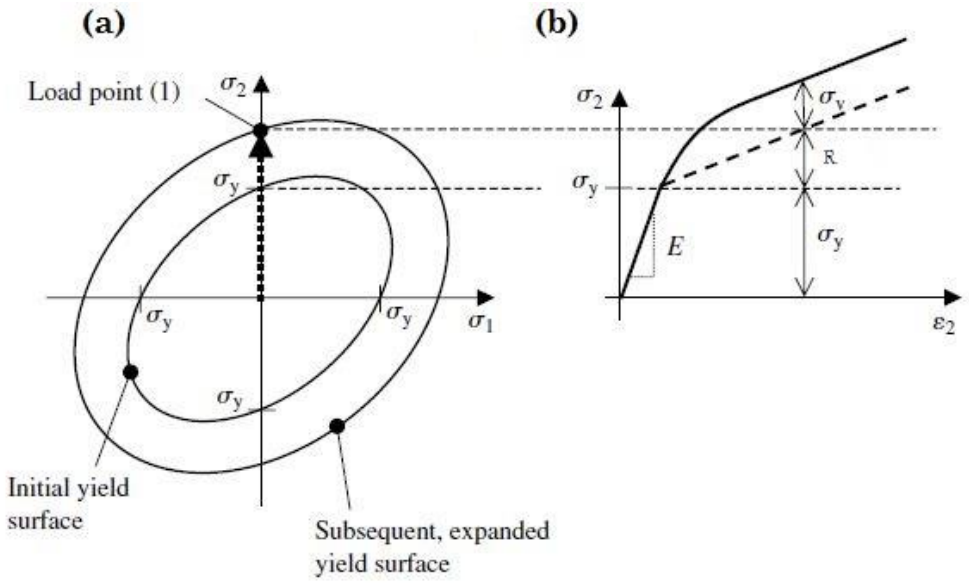


Figure 2-12. (a) the von Mises yield surface with linear isotropic hardening and (b) the decompositions of corresponding stress [38].

From Figure 2-12, the stress-strain curve which contains the time dependence of stress is given by the following an equation

$$\sigma = \sigma_y + R + \sigma_v \tag{2-32}$$

There are numerous forms of equations used to describe the viscous stress, in which the time depending is present; however, they are usually dependent upon the effective plastic strain rate, $\dot{p}$, typically expressed in a power-law form

$$\sigma_v = K\dot{p}^{1/n} \quad , \tag{2-33}$$

where K and n are material constants.

Substituting Equation 2-33 into Equation 2-32 gives

$$\sigma = \sigma_y + R + K\dot{p}^{1/n} \tag{2-34}$$

Equation 2-34 can be rearranged to give the isotropic viscoplastic strain rate as follows [38]

$$\dot{p} = \left\langle \frac{\sigma - \sigma_y - R}{K} \right\rangle^{1/n} \tag{2-30}$$

For this case, isotropic hardening, the yield function,f, is given by

$$f = \sigma - R - \sigma_y \tag{2-35}$$

Kinematic hardening also occurs in addition to the contribution from the isotropic hardening, Equation 2-30 then becomes

$$\dot{p} = \left\langle \frac{f}{K} \right\rangle^{1/n} \mathrm{sgn}(\sigma - \chi) \tag{2-36}$$

where

$$\mathrm{sgn}(x) = \begin{cases} 1 & x > 0 \\ 0 & x = 0 \\ -1 & x < 0 \end{cases} \quad \text{and} \quad x = \begin{cases} x & x \geq 0 \\ 0 & x < 0 \end{cases} \tag{2-37}$$

$$f = |\sigma - \chi| - R - \sigma_y \tag{2-38}$$

where χ is the kinematic hardening stress which sometimes called backstress [38].

The viscous functions used with several popular viscoplastic constitutive models are presented in Table 2-1, along with the hardening parameters used in these expressions.

Table 2-4. Viscoplasticity constitutive models [17].

Source	Viscous Function	Hardening Variable
Bodner, 1975	$\dot{p} = \dot{p}_o \, e^{\left(\left(\frac{Z}{\sigma_{eq}}\right)^{2n}\right)}$	$Z = K + D'$
Miller, 1976	$\dot{p} = \theta(T) \left(\sinh\left(\frac{\frac{\sigma}{E} - R}{D} \right)^{1.5} \right)^n$	D, R
Chaboche, 1977	$\dot{p} = \left\langle \frac{\lVert\sigma - X\rVert - R}{D} \right\rangle^n$	D, R, X
Krempl, 1980	$\dot{p} = \frac{\sigma}{E \emptyset \sigma}$, $\sigma = \lVert\sigma - g\rVert$	g
Walker, 1981	$\dot{p} = \dot{p}_o \left\langle \frac{\lVert\sigma - X\rVert}{D(p)} \right\rangle^n$	D, X
Delobelle,1988	$\dot{p} = \dot{p}_o \sinh\left(\frac{\sigma}{D(p,T)}\right)^n$, $\sigma = \lVert\sigma - X\rVert$	D, X

K - isotropic hardening variable
D′ - kinematic hardening variable
D - drag stress (isotropic hardening)
R - rest stress (kinematic hardening)
X -back stress (kinematic hardening)
g - overstress (kinematic hardening)

2.4 Physically Based Models

During the 1970s, dislocation based constitutive models were developed by Kocks [58], and then developed by Mecking and Kocks [59] and later were developed by Estrin and Mecking [60] and Estrin [61]. These models are a consequence of the fact that the work hardening is due to strain produced, at the internal crystalline grain, caused by some friction of mobile dislocation. This assumption is based on two phenomena to describe behaviour relating to growth and annihilation of dislocations: a mobile (storage) dislocation $\left(k_1\sqrt{\rho}\right)$ and an immobile (dynamic recovery) dislocation $(k_2\rho)$. These models concentrate on the change rate of dislocation density as the key to representing visco-plastic deformation. The dislocations stored inside the crystals interact with other dislocations to create new obstacles to continued slip. These dislocations do not climb out of the grain boundary, do not annihilate each other, and are not absorbed into the grain boundaries [61]. An equation of simple exponential form to describe the stress-strain relation was first suggested in 1948 by Voce [62, 63] to describe the upper range of the real stress-strain curves of polycrystalline aluminium, copper, and stainless steel. The stress-strain curves were measured at constant strain rates. Voce's model assumed the existence of saturation stress to be an essential characteristic of work hardening behaviour. Two kinds of tests were represented: dynamic tests were carried out at constant strain, and the stress varied smoothly; creep tests were carried out at constant stress, and the strain rate was varied moderately.

Domkin [64] made the first attempt to use a simple dislocation density model to describe the isotropic non-linear hardening within the forming of a circular cup. This model was implemented in the ABAQUS user-defined material subroutine UMAT, using an implicit return-map algorithm for anisotropic rate-independent plasticity in the large deformation context. A further dislocation model has been developed to include non-linear kinematic hardening and strain-rate dependency. The developed model was implemented in the Matlab software. The material parameters have been identified via an optimisation procedure using this toolbox, in order to fit the dislocation model to the experimental data for fully reversed strain-controlled cyclic tests. Both observations have concluded that physically based models can be employed to simulate a wider range of strains and strain rates at a variety of temperatures comparing with bulk mechanical models. The dislocation density models represent a connection between the micro-level phenomena and macro-level continuum quantities [64].

Dunlop et al. [65] presented an extension of the Kocks-Mecking-Estrin model to cover creep behaviour of HCP alloys. The basic KME model has been extended by introducing the effects of solute on the mechanical threshold stress as a second internal variable. In order to represent the reference strain rate, further modification has been made, which takes into account an initial transient strain. They compared the model predictions and the experimental data for the cold working stress of Zircaloy-4. The results showed that the model could be used for other HCP materials. The results have made use of the fact that model parameters could be calculated from constant strain rate and strain rate jump tests to predict creep behaviour.

Estrin [61] extended the elastic-viscoplastic constitutive dislocation density model to incorporate the two internal variables, solute concentration and grain size of second phase particles, into the micromechanical behaviour model for aluminium. The reaction between mobile dislocations is already included in the two-internal variable model. The simulated monotonic compression test results have been compared with actual experimental data. This comparison, showing that model prediction for large deformation gives less satisfactory results because of a number of effects have not been included in the simulation.

Barlat et al. [66] described a simple KME dislocation model to represent the stress-strain behaviour during the forming processes of aluminium alloys at room temperature. Their model used three variables to describe the evolution of dislocation density which are average forest dislocation (ρ_f), mobile dislocation density (ρ_m) and the mean free path of dislocation (l) described using the Kalidini model [67]. Experimental single stress-strain curve data have been used to determine the evolution of the state variables. The simulated mean free path results have been compared against experimental measurements, at a strain of about 0.5, of inter-dislocation spacing for some of the investigated aluminium alloys. The results showed the predicted mean free path was 3 to 4 times higher than the experimental mean free path. The reason for this deviation was because the predicted value has been obtained from a dislocation model whose material coefficients were only obtained from data for a stress–strain curve.

Capolungo et al. [68] applied a dislocation model to describe the effect of grain size on the flow stress in nanocrystal materials which are made up of two phases.

These phases were the grain core phase which was assumed to have elastic-viscoplastic properties and the grain boundary phase, which was assumed to have elastic-perfectly plastic behaviour. The strain rate and the grain size dependence of each phase have been employed in this model. The modelling results demonstrated that, for a grain size smaller than around 100 nm, the grain boundary phase dominated the grain core phase, and the deformation was no longer dominated by the dislocation glide mechanism. For a grain size greater than around 100 nm, the grain core phase becomes increasingly important, and the deformation was dominated by the dislocation glide mechanism.

Youyi et al. [69] evaluated the effect of high strain rate on the mechanical behaviour of nanocrystalline materials. Their constitutive model makes use of the evolution of dislocation density and strain gradient to describe the plastic deformation behaviour of strain rate and grain effect for grain interior (GI) phase and grain boundary phase of dislocation pile-up zone (GBDPZ) in nanocrystalline materials. The model assumed that the total dislocations were decomposed into two parts: statically stored dislocations within the grain interior, and geometrically necessary dislocations within the grain boundary pile up zone. Isotropic strain hardening and kinematic strain hardening were used in this model to describe the work hardening. A comparison was made between the calculated results and the corresponding experimental data, and strong strain rate dependent behaviours were observed in the prediction.

2.5 Small Punch Creep Test (SPCT)

In the last ten years, testing techniques using miniature samples have received increasing attention from the electricity generation industry companies for situations where the amount of material used in the test is limited. Published reviews for small specimen techniques have focused on their application to conventional and nuclear plants [70, 71]. The removal of small amounts of material that are required for miniature specimens testing may not affect the structural integrity of in-service components. Finite element (FE) modelling of small specimen tests can give an estimate of remnant life in the use of these tests for components of power plants [72, 73]. Many efforts have been made by various researchers using miniature samples for creep testing to characterise the creep properties of materials used in high-temperature power generation components. One of these tests is the small punch creep test (SPCT), with a recommended specimen diameter of 8 mm and a thickness of 0.5 mm. The SPCT involves the application of a constant load through a hemispherical end indenter on a small circular flat disk [74]. The ease of manufacture and testing of SPCT samples is one of the most important characteristics that distinguish it from other miniature testing techniques. SPCT has one more advantage over other miniature testing techniques, namely that the SPCT can be used to evaluate creep rupture [75]. Typically, the test technique has been used for testing materials such as P91, P92, CrMoV steels, 316LN stainless steel, and magnesium and aluminium alloys [76] within power plant applications (e.g. steam headers or steam pipes).

The SPCT method is still not universally accepted, due to limitations concerning test repeatability which relate to three main reasons: firstly, lack of standardisation of the test apparatus and specimen dimensions; secondly, concerns related to the procedure used to correlate SPCT data with the output of a uniaxial creep test; and thirdly, due to the complex deformation mechanisms (e.g. initial plasticity effect, which is material dependent). To overcome the first and second concerns, the European Committee for Standardisation (CEN) developed a draft code of practice (workshop agreement CWA 15627:20068) for the SPCT of metallic materials.

2.5.1 Experimental Displacement-Time Behaviour

The first small punch creep test (SPCT) introduced by Parker and James [77] , who concluded that the SPCT would be possible using a constant load upon the small punch specimen to evaluate the creep properties of a material. SPC methods have since been widely used to examine the creep properties effectively for a wide range of materials used in power generation and nuclear components [78, 79, 1]. The displacement-time curve for a small punch creep test is presented by Moreno and Chen [80, 81]. They demonstrated that the displacement-time curve is identical in shape to that of a uniaxial creep curve and involves three regions, a primary regime, a secondary steady-state regime, and a tertiary regime. However, the constant displacement rate in the SPC test is achieved when the strain is in the range 10-150% and thus would overlap with the tertiary regime in a conventional creep test [82]. In a conventional creep test, the considerable creep damage behaviour is basically connected with the tertiary region. Kobayashi et

al. [83] indicated that for super duralumin, the initiation of circumferential cracks could occur in SPC specimens as early as the primary creep stage, which indicates to that the creep mechanisms do not result from the displacement rate in the secondary deformation stage. Rouse et al. and Hyde et al. [73, 82] also found that the secondary stage in a SPC curve is caused by the balance between geometric stiffening and a decreasing in stiffness of the small punch creep specimen shape. Consequently, the secondary stage in a small punch creep test is closely connected with the tertiary creep region that controls the life of the small punch creep specimen. The complicated multiaxial stress state in a SPC specimen and the overlap of creep stages makes it hard to interpret the data from tests of SPC correctly. However, in order to address this, important analytical and numerical approaches have been presented and considerable development has occurred on the finite element modelling of the SPC test.

2.5.2 Finite Element modelling of SPCT

The stretched membrane model has been developed by Chakrabarty to examine the SPCTs [84]. The von Mises equivalent strain imposed through a hemispherical punch head is determined by using a formulation derived assuming only membrane strains. Yang and Wang [85] have modified a semi-empirical polynomial expression to investigate the maximum equivalent strain at the centre of a deformed disc specimen. A polynomial formulation has been developed by Li and Zhang [86] to determine the maximum equivalent strain for a hemispherical punch head using contact conditions between the punch and specimen as follows

$$\varepsilon = 0.20465\delta + 0.12026\delta^2 + 0.0095\delta^3 \,, \qquad (2\text{-}39)$$

where δ is the punch displacement at the specimen centre and the radius of the punch head equals 1mm.

An empirical solution has also been derived from Chakrabarty's membrane stretch model to determine the equivalent uniaxial stress from the SPC load. This solution has been presented in the European Committee for Standardisation workshop agreement as shown follows [87]

$$\frac{F}{\sigma} = 3.33 K_{sp} a_p^{-0.2} R_s^{1.2} t_o \tag{2-40}$$

where F is the punch load (N) and K_{sp} is a correction factor which used to connect uniaxial testing with the SPC work. R_s is the punch head radius, a_p is the radius of the receiving die and t_o is the thickness of the specimen as depicted in Figure 2-13. K_{sp} takes a value between 1.2 and 1.3.

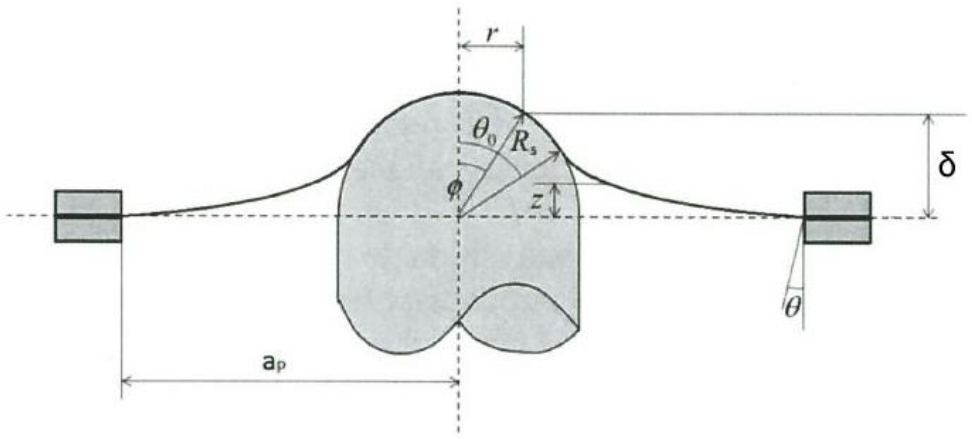


Figure 2-13. Chakrabarty's membrane stretch model [84].

During small punch creep tests, the specimen deformation is controlled by different interacting mechanisms and conditions such as nonlinear material behaviour, nonlinear contact conditions between the test rig components and the specimen, large deformation, large stresses and large strains [73, 82]. Therefore, in order to understand the distribution of complex stress-strain fields within a SPC specimen, it is necessary to examine mechanisms which take place during tests using finite element (FE) modelling. Generally, several finite element models have been developed which employed a difference of techniques and methods. FE has therefore been commonly used to obtain a detailed understanding of the mechanisms within small punch tests [88, 89]. FE models have also developed to study the large deformation process for small discs using the constitutive creep laws similar to that proposed by Kachanov [90]. Among the modelling approaches are the Kachanov-like laws developed initially by Li [91], which result in a set of displacement-time curves for given constant stresses values. Abendroth [92] used an FE approach but focused on the modelling guidelines: geometry of the SPT, convergence of the chosen mesh and the influence of friction coefficient on the load-deflection curve. Manahan et al. [93] have modified the plasticity approach to simulate creep curves and compare with corresponding experimental data by using a least-squares method to determine the parameters of the model by fitting them to the results of a uniaxial test. The creep and fracture behaviour in high-temperature components by FE modelling of the small punch specimens was also proposed by Shibli et al. [94]. The influence of friction on the displacement of a hemispherical punch is investigated. The von Mises equivalent strain and the continuum damage data showed the strain is raised up at the region located under the punch and the maximum damage occurs

on the bottom of the specimen. Evans and Evans [95] and Evans and Wang [96] have made use of an extended visco-plasticity model of SPCT to take into account the effect of surface morphology [95]. Account was taken of the sensitivity of the experiment to many of the parameters including specimen dimensions in order to optimise the method to obtain the best test results [96]. They found that the failure time was most sensitive to specimen thickness, support diameter, initial damage and the radius of the punch head but least sensitive to the specimen diameter and applied load.

The FE models usually represent the SP using two dimensions via the use of axisymmetric elements that have more computational cost efficiency compared with three-dimensional models [85, 73, 82, 78]. The interaction between the specimen and the rig components has been investigated using two different FE models of SPCT, shown in Figure 2-14. In the two-dimensional axisymmetric model, as shown in Figure 2-14a, the contact surfaces between the specimen and the dies have been described by constraining the degrees of freedom of the surfaces nodes using boundary conditions. The contact between the punch and the specimen has been represented by a uniformly distributed pressure load applied on the estimated contact surface [73]. In the three-dimensional model, see Figure 2-14b, the punch and the dies have been modelled by elastically deformable bodies contacting the specimen by a surface-to-surface contact model with a constant friction value as shown in Figure 2-14b [73, 97]. Even when no damage or hardening is considered in the applied material models, the second FEA model has the capability of simulating the primary, secondary and tertiary creep regimes of displacement-time curves. Necking of the specimen can also be

observed. Both models have been represented by creep power law and continuum damage material models. Uniform meshes have been used in implementation of material models [73]. Guan et al. [98] presented three-dimensional FE models of Q235A and Q345R steels using SP specimens. This research studied the effect of voids which were incorporated into the specimen mesh, on the elastic-plastic behaviour. The load-displacement curves obtained from the FE simulation have been compared with corresponding of experimental results for Q235A and Q345R steels. The results for Q235A have demonstrated that the load-displacement curves have a satisfactory agreement with each other just before P_{max} because the microdefects have a great effect on the ultimate strength while having no influence on the yield strength.

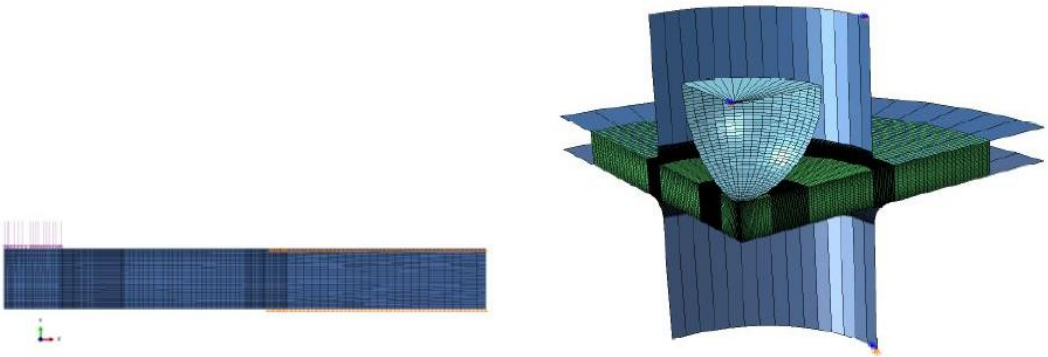


Figure 2-14. View of the FE meshes [73].

2.6 Small punch tensile test (SPTT)

A series of study has been made for small punch tensile testing that requires limited amounts of material. During the 1980s, the first investigation of the miniature disc bend test (MDBT) was reported by Huang et al. [99] and Manahan et al. [100] as an important part of ongoing efforts to realise miniature scale testing approaches. The miniature disc bend test (MDBT) is basically used to improve the small punch tensile (SPT) test in order to obtain load-punch displacement results using a 3mm diameter specimens. The typical geometry of the SPT test is shown in Figure 2-15. A sample is fastened between an upper and lower die and the load is applied to the specimen through a hemispherical punch head [1].

SPT tests carried out by Baik et al. [101] to study the effect of temperature on ductile-brittle transition behaviour of steel. They investigated that the cracking mode changes from brittle into ductile fracture when the test temperature increase. Lucas et al. [102] studied the small punch rig component dimensions, which include punch radius and receiving-hole radius, and thickness of the sample. They also carried out small punch testing by using a square sample measuring 10mm x 10mm which was clamped using the same rig components, upper and lower dies, while the test geometry relied on the unclamped central area of the specimen.

The influence of fixing the SP samples was considered by Li et al. who noted that unclamped specimens created uncertain results as a consequence of the difficulty in providing a well-defined contact zone over the supporting die [103].

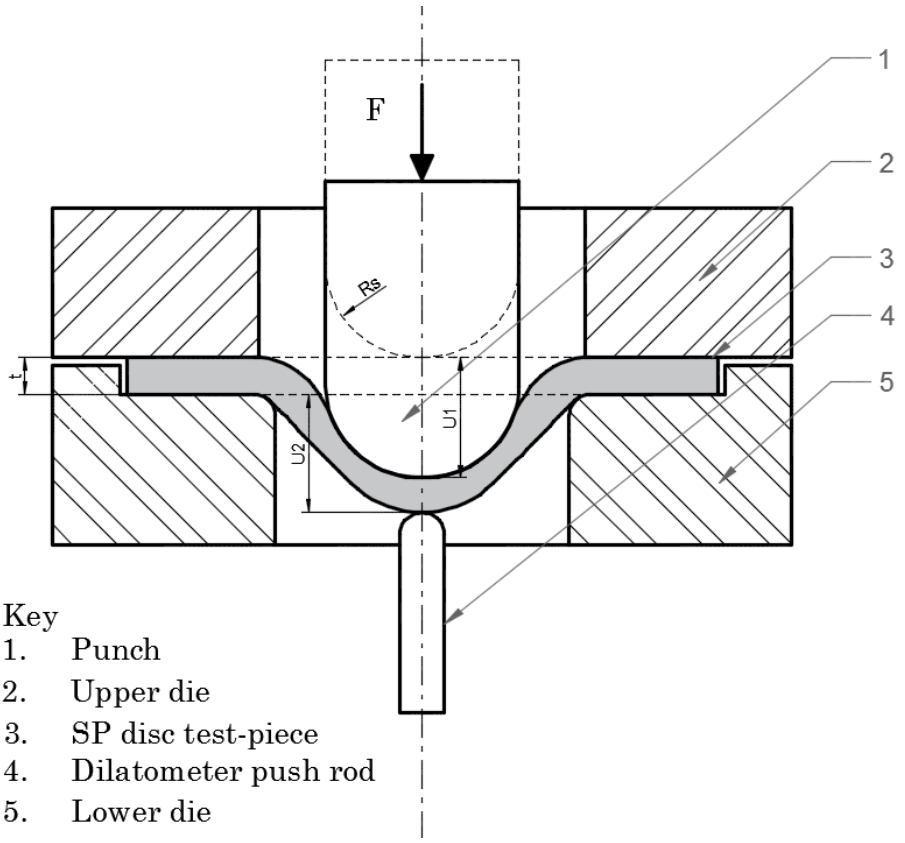


Figure 2-15. Standard geometry of the small punch (SP) test [1].

2.6.1 Experimental Load-Displacement Behaviour

The Small Punch Tensile Test (SPTT) is a popular miniature specimen test method that has been used to characterise the tensile mechanical properties for ductile metallic materials with specimens consisting of discs of ~ 10 mm diameter and ~ 0.5 mm thickness [104]. The punch load was applied to the disc at a given constant displacement rate (CDR). The very small size of the specimen implies that the SPTT can be considered as a limited volume and non-destructive method provide a real evaluation of mechanical properties when compared with the

conventional test [105-108]. Moreover, the SPTT specimen could be manufactured and evaluated directly from in-service components without significantly affecting their structural integrity [109]. Anisotropic, heterogeneous behaviour can also be examined using SPTT [110, 111]. A range of SPTT tests was conducted to evaluate fracture properties of austenitic steels [112-114], and in recent years even pre-cracked [115] or pre-notched specimen have been presented [116, 117].

2.6.2 Finite Element modelling of SPTT

The finite element (FE) modelling of the SPT test has made a considerable contribution to gaining an understanding of how strains and stresses develop in experimental SPT tests as plastic deformation and lead to damage and failure. Manahan et al. presented finite element modelling of SPT tests to describe the different regions in the load-displacement curves and investigated the plastic strains in experimental tests [118]. Many finite element models have been produced in order to clarify the interpretation of the results of SPT experiments by estimating the evolution of the stress and strain fields in the specimen [119-121]. A finite element model of the small punch tensile test has been analysed by Coleman et al. [119] to investigate the role of stress state on the local deformation. They correlated the load and displacement values from the small punch tensile tests to constitutive equations to evaluate tensile yield strength, ultimate yield strength and elongation data. The FE results showed that the model can predict the deformation mechanisms as punch displacement increases. It was also found that this type of modelling does have a limitation as it ignores the microstructural characteristics throughout the finite element simulations.

Chang et al. [120] employed two FE damage models to investigate methods of predicting ductile fracture resistance for two types of typical nuclear materials, namely low alloy steel and high Cr steel. The proposed mechanical, GTN and Rousselier, models have carried out by using SPTT specimens. The finite element analyses results showed that the two proposed models are useful models to predict the J-R curve of virgin materials at room temperature.

Lancaster et al. [122] employed fractographic investigations in the finite element modelling using deform software method to analyse specimen deformation through the testing of miniature disc specimens under punch displacement. The contour plots of maximum principal stresses in a SPT test specimen with respect to punch displacement are shown in Figure 2-16. It can be clearly seen that an area of high tensile stress exists when the punch displacement is small. A high compressive stress field is raised in the region of punch–specimen contact that leads to localised yield stress at both 20℃ and 400℃ [122].

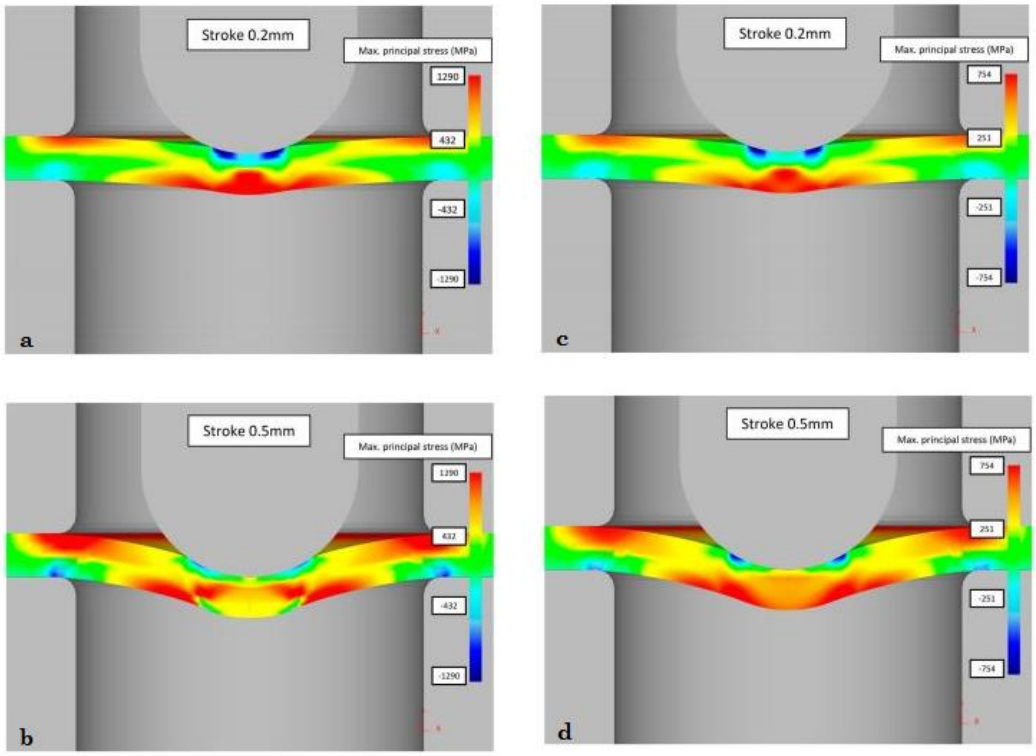


Figure 2-16. Small punch simulation for Ti-6Al-4V at (a and b) 20℃ and (c and d) 400℃ [122].

2.7 High-Temperature Materials

In the power generation industry, the operational efficiency of the power plant has been enhanced by improving new materials with better properties and developing the design of power generation structures. The deformation processes and fracture mechanisms of industrial power plant equipment have been of the major area of concern to researchers because the power generation components are subjected to high temperatures and loads for extended periods of time [123]. Therefore, engineering components within the power generation plants require higher creep and corrosion strength, in order to resist these more arduous operating conditions. In addition, the very big maintenance and repair costs of these plant parts make it necessary for these parts to be produced from materials that have a high creep and corrosion resistance at high-temperature conditions [18, 124, 125]. In order to achieve these high-temperature properties, a new composition of alloys developed incorporating a variety of elements [126].

One such nickel-based superalloy, known as Inconel, is widely used in aero-engine applications. There are many different types of this material, 600, 617, 625, 718 and X-750 that have slight variations in alloy compositions. For example, Table 2-5 shows the chemical composition of Inconel 718 that is widely used in aerospace components [127, 128]. However, for large components for use in high-temperature applications, steels known as P91 and P92 are available. These creep-resistant steels are usually used in the pipework, super-heater and reheated tubes of power plants and also in cooling systems of nuclear reactors as shown in Figure 2-17. Generally, the P91 steel formulation developed from 9Cr1Mo steel, and it consists

of 9% chromium and 1% molybdenum, which permits engineers to use a thin wall thickness to design pipes and tubes.

Table 2-5. Chemical compositions of Inconel 718 [127].

Element	Composition (W%)
Ni+Co	**50**
Cr	**17**
Nb+Ta	**5.5**
Mo	**1.0**
Si	**0.35**
Al	**0.7**
C	**0.02**
Mn	**0.35**
Ti	**1.15**
S	**0.015**
P	**0.015**
B	**0.002**
Fe	**Bal.**

In general, P92 steel is made through partial replacement of molybdenum, Mo, by tungsten,W, and therefore consists of 9% chromium, 0.5% molybdenum and 1.75% tungsten [129, 130]. The P92 steels exhibit high creep resistance, low thermal expansion value and good corrosion properties [131]. Table 2-6 gives the chemical composition of P92 steel [132].

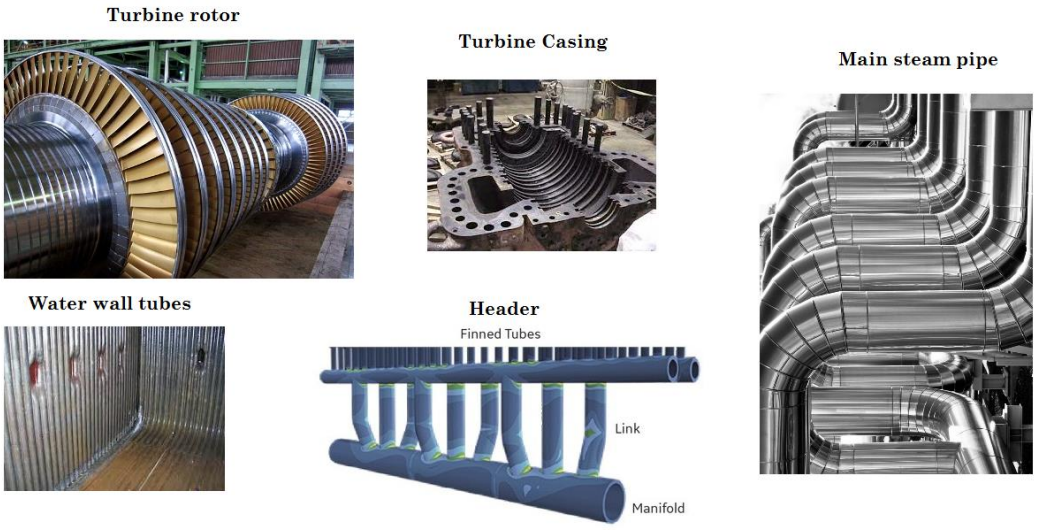


Figure 2-17. Schematic illustration and photographs of a fossil-fired boiler and typical materials.

Table 2-6. Chemical composition of P92 (W%) [132].

Element	Composition	
	Min. (W%)	Max. (W%)
C	**0.07**	**0.13**
Mn	**0.3**	**0.6**
P	**-**	**0.02**
S	**-**	**0.01**
Si	**-**	**0.5**
Cr	**8.5**	**9.5**
W	**1.5**	**2**
Mo	**0.3**	**0.6**
V	**0.15**	**0.25**
Nb	**0.04**	**0.09**
N	**0.03**	**0.07**
B	**0.001**	**0.006**
Al	**-**	**0.04**
Ni	**-**	**0.4**
Fe	**Bal.**	**Bal.**

The P91 and P92 steels both are ferritic/martensitic type steels which are part of the 9-12%Cr family of steels. The value of thermal expansion coefficient of austenitic steel is greater than that of ferritic steel, therefore ferritic steels tend to be more suitable for components subject to thermo-mechanical loading [3].

The increasing need for ferritic steels with higher creep resistance has led to the improvement of 9Cr martensitic steel [4]. One of the earliest attempts to develop Grade 91 steel, as a modification to 9Cr-1Mo steel, was undertaken by Oak Ridge National Laboratory (ORNL) [133]. Swindeman et al. also modified 9Cr-1Mo steel alloy by adding new elements from niobium, vanadium and nitrogen and decreasing in the content of chromium, carbon, phosphorus, silicon, sulphur and molybdenum [134]. Richard et al aimed to improve the properties of P91 steel by increasing the tungsten and boron content and reducing the molybdenum content [135].

Figure 2-18 presents the creep properties of many of the commonly-used engineering alloys. It clearly shows that enhancements in creep resistance can be gained by alloying additions to steel and why chromium base alloys are utilized for the elevated temperature components in, for instance, power generation plants [18].

Generally, several procedures contribute to microstructure development in 9-12%Cr steels in order to meet the requirements of the steel's specifications. The heat treatment procedures are usually carried out on the 9-12%Cr steels during their manufacturing processes that classify into an austenitizing and tempering procedure. Firstly, heating 9-12%Cr steels up to 1100℃ followed by cooling to

ambient temperature leads to the formation of a martensitic structure with a high dislocation density. Secondly, tempering treatment of 9-12%Cr steels can be carried out by reheating up to 750℃ which significantly contributes to improving the ductility and impact strength. During the tempering procedure, formation of dislocation networks and subgrains within the microstructure of 9-12%Cr steels [3, 136]. The different parameters used for the austenitizing and tempering processes can affect the microstructure of the steels. Various conditions can be used in the austenitizing and tempering processes that lead to change in the microstructure of the steels. For instance, utilizing high temperature in austenitizing procedure produces rapid expand in width of lath and rapid growth in grain size of prior austenite [3].

A number of material models based on the physical mechanisms of creep have been applied to 9–12Cr steels. Esposito et al. [137] have suggested a mechanism based model for primary creep assuming that the creep rate in the first region can be presented as a function of the secondary creep rate. The results showed that the assumed formulation does not depend on the steady state creep formulation. It has also been found that the model parameters seem to have a non-linear dependence upon stress. A Norton power law with the addition of back stresses has been examined by Magnusson and Sandstrom [138] to simulate the creep behaviour of the P91. Dislocations, in addition to precipitates, are used to simulate the back stress by taking evolution and annihilation of free dislocations into account at elevated temperature. The results showed that the model can predict only the primary and secondary creep regions, not the tertiary creep region. The classical creep power law has been also employed by Spigarelli and

Quadrini [139] to describe the minimum creep-rate dependence on applied stress for a welded steel joint at elevated temperature. However, the experimental investigations have revealed the effects of different grain structures on creep response of welds in P91 steel. A different microstructure based model has been proposed to assess the long-term creep strength for the P91 steel. The presence of precipitates and coarsening of grain is also employed in this model to predict the creep strength in the P91 steel. However, the model did not take into account the storage and annihilation of dislocations which occurs with a sufficiently long time of exposure [140].

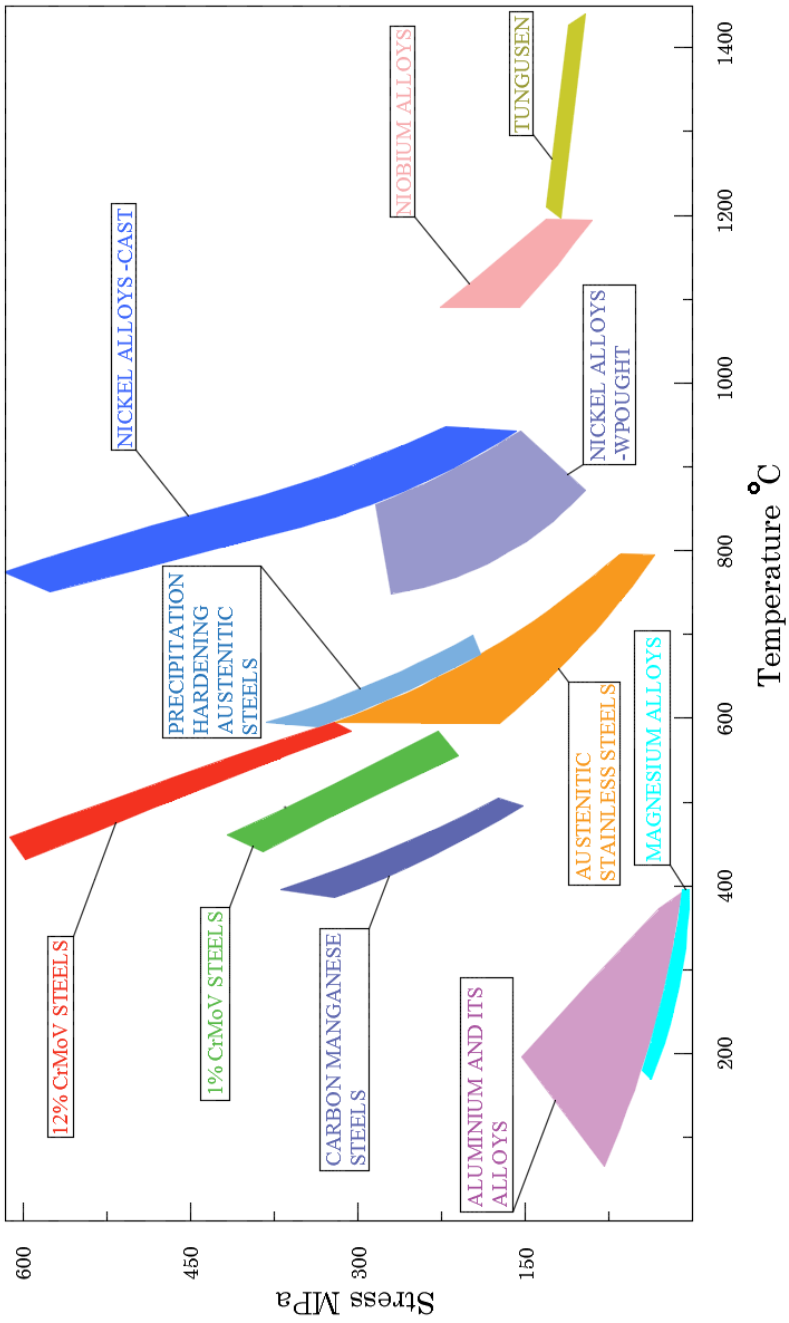


Figure 2-18. Flow stress versus temperature for various alloys [18].

2.8 Summary and Knowledge Gaps

As reviewed in this chapter, significant attempts have been made towards modelling the constitutive behaviour of materials experiencing viscoplasticity and creep under high-temperature conditions. However, these approaches are limited with respect to their prediction of the dislocation density and grain structural evolution, which are key to material and structural integrity for power plant applications.

As noted in many of the papers reviewed, routine characterisation of viscoplastic and creep behaviours of engineering materials usually involves full-size creep test specimens. However, due to their large dimensions, it is impractical to use these specimens where only small amounts of material are available for testing. In such situations, the testing of small disc specimens of the materials provides a useful alternative route for determining viscoplastic and creep properties.

It is also noticeable from this literature review that one material type used in the power plant components are the 9-12%Cr steels which have a good thermo-mechanical property and enough oxidation resistance. Specifically, the recently developed martensitic P91 is widely used for the replacement of conventional materials used in power plants. The P91 steel has been characterised reasonably well by the previous investigations. However, P91 is successfully investigated by using small specimen creep and tensile testing techniques, despite the considerable efforts and the continued attempts to understand the microstructure of P91 using these SP tests.

Therefore, major contributions of the work in this thesis relate to the development of physically-based viscoplastic and creep models in order to represent these phenomena under realistic conditions within the finite element modelling approach. Experimental small punch tensile tests are undertaken, involving the bulk deformation behaviour and the microstructure evolution during these tests of the P91 steel at 600ºC.

CHAPTER 3:
FINITE ELEMENT CREEP MODELLING

3.1 Introduction

Historically, more phenomenological creep models than physically based models have been obtained and used to model the creep of materials. One of the most popular and well-received models is the Kocks–Mecking–Estrin (KME) model for secondary creep which has been developed for a wide range of materials [58, 141]. The constitutive equation describes the viscous relation between von Mises equivalent stress and plastic strain rate quantities for a given microstructure. The microstructural aspects of material properties are well known to exhibit rate and temperature-dependent behaviour [66, 68, 65, 69].

This chapter is structured as follows: Section 3.2 presents a brief description of the constitutive equations of the Kocks-Mecking-Estrin (KME) model which are based on microstructural properties. The development of the user material subroutine (UMAT) is also detailed in this section. The implementation of the constitutive model, in the implicit finite element code ABAQUS/Standard, is also presented. Section 3.3 details the material and microstructure of the P91 steel. The uniaxial and small punch creep tests for the P91 steel at 600ºC for several loads are presented as well. Section 3.4 of this chapter is devoted to the application of the model by characterising the material using uniaxial creep and

small punch creep cases. These simulations are used to calibrate the accuracy of the UMAT by comparing the results from numerical modelling and corresponding experimental tests. Finally, conclusions are given in Section 3.5.

3.2 The KME Model and UMAT Development

In the present work, in an attempt to overcome some of the repeatability issues, the multi-axial KME viscoplastic model is developed and implemented without the need to carry out a uniaxial creep test. A user-defined material subroutine (UMAT) was developed. The results of the FE analysis for uniaxial creep and small punch creep tests using the KME model are compared with experimental results to investigate the capability of the numerical model to provide creep behaviour predictions for the small punch creep test.

3.2.1 The Kocks-Mecking-Estrin Model

The Kocks-Mecking-Estrin form is a unified elasto-viscoplastic constitutive model which is highly nonlinear and referred to as the kinetic equation by Kocks [58] and Mecking [59]. An appropriate mathematical formulation has been presented in Equation 3-1. The constitutive equations of this model can be integrated with the case of constant plastic strain rate [59] and with constant stress creep [60].

$$\frac{d\sigma}{d\varepsilon} = (\sigma/m)\frac{d\ \ln\dot{\varepsilon}}{d\varepsilon} + \left(\sigma/\hat{\sigma}\right)\frac{d\hat{\sigma}}{d\varepsilon} \qquad (3\text{-}1)$$

At the steady state, the evolution of $\hat{\sigma}$ does not change with the strain $\left(\frac{d\hat{\sigma}}{d\varepsilon} = 0\right)$, by arrange the Equation (3-1) may provide a simple description of deformation in creep as

$$\frac{d\ln\left(\frac{\dot{\varepsilon}}{\dot{\varepsilon}_s}\right)}{d\varepsilon} = \left(\frac{\theta_o m}{\hat{\sigma}}\right)\left[\left(\frac{\dot{\varepsilon}}{\dot{\varepsilon}_s}\right)^{-\frac{1}{n}-\frac{1}{m}} - 1\right], \tag{3-2}$$

where θ_o is the initial strain hardening within the second stage and $\dot{\varepsilon}_s$ is steady state strain rate. The steady-state strain rate, $\dot{\varepsilon}^c$, is used as a function of strain in creep tests at constant stress.

$$\dot{\varepsilon}^c = \dot{\varepsilon}_o^{m/(m+n)}\dot{\varepsilon}_o^{n/(m+n)}\left(\frac{\sigma}{\alpha b\mu M\left(\frac{k_1}{k_{20}}\right)}\right)^{mn/(m+n)}, \tag{3-3}$$

One can simplify Equation (4-3) to give

$$\dot{\varepsilon}^c = \dot{\varepsilon}_o\left(\frac{\sigma}{\alpha b\mu M\left(\frac{k_1}{k_{20}}\right)}\right)^{p}, \tag{3-4}$$

where $\frac{m}{(m+n)} + \frac{n}{(m+n)} = 1$ and $\frac{1}{p} = \frac{1}{m} + \frac{1}{n}$

3.2.2 The Multi-Axial Formulation

The one-dimensional constitutive equations for the Kocks-Mecking model have been derived by Estrin [142]. In this section, the significant aspects of the 3-dimensional version are discussed.

Since in most cases of experimental tests, the materials have shown nonlinear behaviour, the stress state, σ_{ij}, is assumed to be a nonlinear function of the strain

state, ε_{ij}. Thus, using Hooke's law in chain rule form, these can be re-expressed in direct notation to give

$$\dot{\sigma}_{ij} = C_{ijkl}\, \dot{\varepsilon}^{e}_{kl} \ , \tag{3-5}$$

where $\dot{\sigma}_{ij}$, $\dot{\varepsilon}^{e}_{kl}$ are the Cauchy stress rate and elastic strain rate tensor respectively (a superposed dot refers to the time derivative) while C_{ijkl} is the fourth order elastic stiffness matrix tensor which depends on the strain, but not on the strain rate.

$$C_{ijkl} \equiv \frac{\partial \Delta\sigma_{ij}}{\partial \Delta\varepsilon_{kl}}, \tag{3-6}$$

In elasto-viscoplasticity, it is usual to split the total strain rate tensor, $\dot{\varepsilon}_{ij}$, into two parts, namely an elastic strain rate, $\dot{\varepsilon}^{e}_{ij}$ and a creep strain rate tensor, $\dot{\varepsilon}^{c}_{ij}$, i.e.

$$\dot{\varepsilon}_{ij} = \dot{\varepsilon}^{e}_{ij} + \dot{\varepsilon}^{c}_{ij} \, . \tag{3-7}$$

The update of $\dot{\varepsilon}^{e}_{ij}$ is given by

$$\dot{\varepsilon}^{e}_{ij}\,\big|_{n+1} = \dot{\varepsilon}^{e}_{ij}\,\big|_{n} + \left(\Delta\varepsilon_{ij} - \Delta\varepsilon^{c}_{ij}\right), \tag{3-8}$$

The elastic strain rate tensor can be connected with the rate form of Hooke's law, Equation (4-7), to give:

$$\dot{\sigma}_{ij}\,\big|_{n+1} = C_{ijkl} : \left(\dot{\varepsilon}^{e}_{ij}\,\big|_{n} + \Delta\varepsilon_{ij} - \Delta\varepsilon^{c}_{ij}\right) , \tag{3-9}$$

To derive the incremental constitutive relationship, let us consider an integration over one step, Δt, from $t|_n$ to $t|_{n+1}$.

$$\sigma_{ij}\big|_{n+1} = \sigma_{ij}\big|_{n} + \ C_{ijkl}{:}\,\Delta\varepsilon_{ij} - \ C_{ijkl}{:}\,\Delta\varepsilon^{c}_{ij}\ \big|_{n+1}\ , \tag{3-10}$$

$$\sigma_{ij}\big|_{n+1} = \ \sigma^{tr}_{ij}\ - \ C_{ijkl}{:}\ \Delta\varepsilon^{c}_{ij}\ \big|_{n+1}\ , \tag{3-11}$$

where σ^{tr}_{ij} is an elastic predictor which is known and obtained by assuming the increment is entirely elastic, while $\Delta\varepsilon^{c}_{ij}$ are the creep strain increments [143].

We assume that the creep strain rate $\dot{\varepsilon}^{c}_{ij}$ is expressed using the Levy-von Mises equation as [45]:

$$\dot{\varepsilon}^{c}_{ij} = \dot{c}\ \mathbb{N}_{ij}\ ,\ \ \mathbb{N}_{ij} = \frac{3}{2}\ \frac{\mathcal{S}_{ij}}{\tilde{\sigma}} \tag{3-12}$$

where $\dot{c}$ is the effective creep strain rate, $\mathbb{N}_{ij}$ is the flow direction tensor, and S_{ij} denotes the deviatoric stress tensor, while the quantities in Equation (3-13) indicate the equivalent stress and equivalent creep strain rate respectively.

$$\tilde{\sigma} = \sqrt{\frac{3}{2}\mathcal{S}_{ij}{:}\,\mathcal{S}_{ij}}\ , \text{and}\ \dot{\tilde{\varepsilon}}^{c} = \sqrt{\frac{2}{3}\dot{\varepsilon}^{c}_{ij}{:}\,\dot{\varepsilon}^{c}_{ij}}\ , \tag{3-13}$$

3.2.3 The UMAT Coding and Implementation

The FE software ABAQUS permits the addition and implementation of various constitutive models into the ABAQUS library by using user material subroutines (UMATs) [144]. In the present study, the Kocks-Mecking-Estrin constitutive model described above for constant stress creep is implemented into ABAQUS by UMAT for the P91 steel at 600℃.

We here presented the implicit backward Euler integration for the multiaxial case of equations in the previous section. According to Equation (3-4), the rate form of the constitutive equation may be written in iterative form as

$$\Delta c = \dot{\varepsilon}_o \left(\frac{\sigma}{\alpha b \mu M \left(\frac{k_1}{k_{20}} \right)} \right)^p \Delta t \,, \tag{3-14}$$

and thus may be expressed in a form suitable for Newton-Raphson iterative solution as [38]

$$\mathcal{R}(\Delta c) = \dot{\varepsilon}_o \left(\frac{\sigma}{\alpha b \mu M \left(\frac{k_1}{k_{20}} \right)} \right)^p \Delta t - \Delta c = 0 \,. \tag{3-15}$$

Using Newton's method, one has

$$\mathcal{R} + \frac{\partial \mathcal{R}}{\partial \Delta \varepsilon^c} \delta \Delta c + \cdots = 0 \,, \tag{3-16}$$

In this method, an additional iteration step i is introduced to calculate the increment in accumulated creep strain that gives $\mathcal{R}(\Delta c) = 0$

The first step, i = 0 (initial) $\Delta c = 0$

$$\mathcal{R}_0 = \mathcal{R}(\Delta c_0) \,, \tag{3-17}$$

and at the next step, (i) is replaced with (i + 1), so Equation (3-16) becomes [38]

$$\delta \Delta c \,\big|_{i+1} = \frac{\mathcal{R}\,\big|_i - \frac{\Delta c}{\Delta t}}{\frac{1}{\Delta t} - \frac{\partial \mathcal{R}}{\partial \Delta c}\big|_{\delta \Delta c_i}} \,, \tag{3-18}$$

Now, the effective creep strain increment is updated by

$$\Delta c_{n+1} = \Delta c_n + \delta \Delta c \,\big|_{i+1} \,. \tag{3-19}$$

From Equation (3-12), the creep strain increment tensors are then determined as

$$\Delta\varepsilon_{ij}^{c} = \frac{3}{2}\Delta c\frac{S_{ij}}{\tilde{\sigma}} \tag{3-20}$$

The final step is to update the stress by

$$\sigma_{ij}\big|_{n+1} = \sigma_{ij}\big|_{n} + C_{ijkl}\colon \Delta\varepsilon_{ij}^{e}\big|_{n+1}. \tag{3-21}$$

The flow chart of the implementation of the UMAT for the creep model is shown in Figure 3-1.

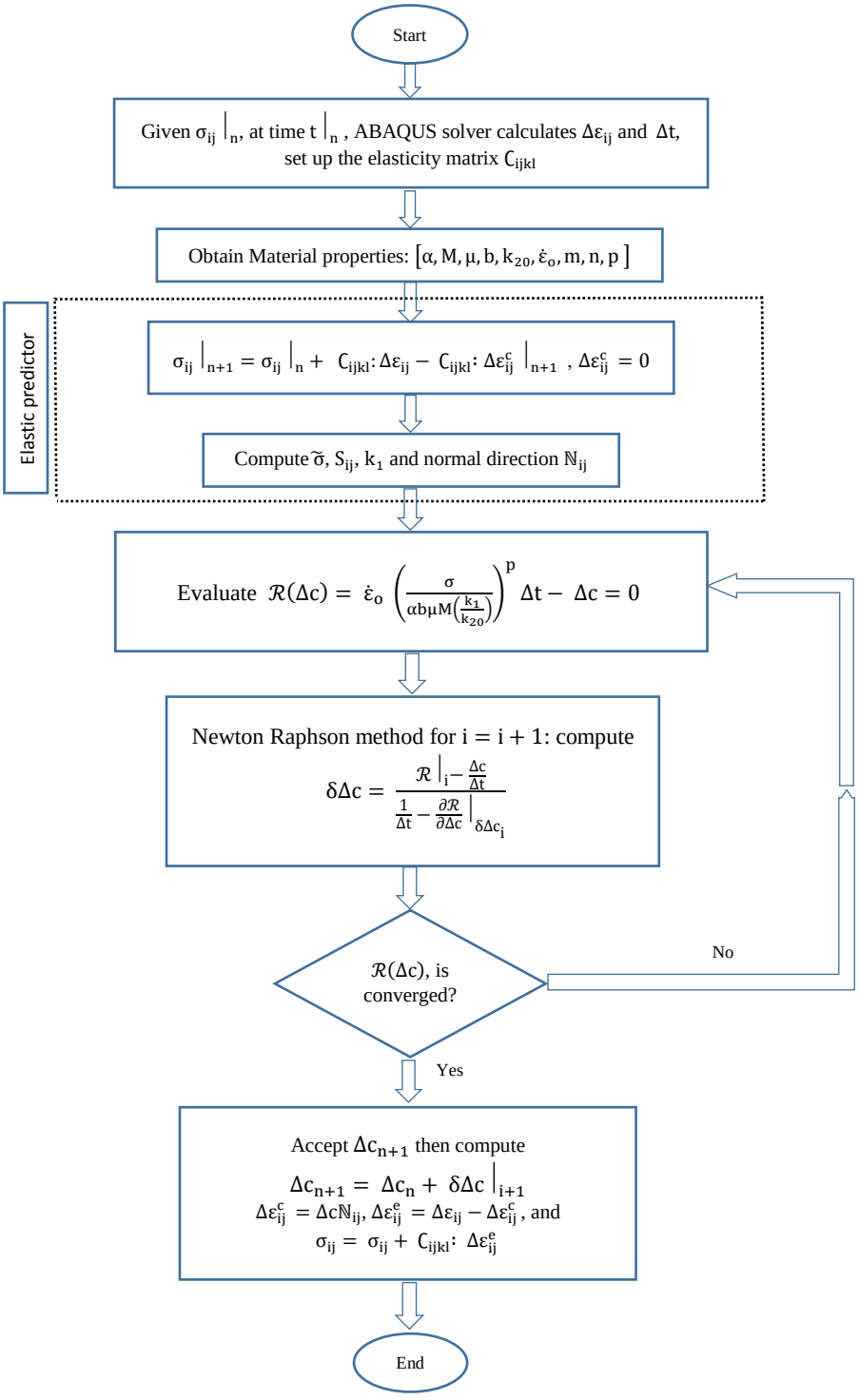


Figure 3-1. Flowchart of the implementation of the UMAT for creep model.

3.2.4 Material Jacobian Matrix

The material Jacobian can be described as a partial derivative

$$C_{ijkl} \equiv \frac{\partial \Delta\sigma_{ij}}{\partial \Delta\varepsilon_{kl}} = C^{e}_{ijkl} + C^{cr}_{ijkl}, \tag{3-22}$$

A closed-form solution to C^{e}_{ijkl} the elastic stiffness matrix is always known. A closed-form solution to C^{cr}_{ijkl} the creep stiffness matrix may or may not be known. Reversing the expression for creep stiffness matrix, C^{cr}_{ijkl}, will furnish the creep compliance matrix, S^{cr}_{ijkl}, as follows:

$$S^{cr}_{ijkl} = \frac{\partial \Delta\varepsilon^{cr}_{ij}}{\partial \Delta\sigma_{kl}}. \tag{3-23}$$

The matrix was simplified to the following

$$S^{cr}_{ijkl} = \frac{3}{2}\dot{\varepsilon}_o\, \widehat{\sigma}^{-p}_{so}\Delta t\left[(p-1)\tilde{\sigma}^{p-2}\frac{\partial \tilde{\sigma}}{\partial S_{pq}}S_{ij} + \tilde{\sigma}^{p-1}\delta_{ip}\delta_{jq}\right]\frac{\partial S_{pq}}{\partial \Delta\sigma_{kl}}. \tag{3-24}$$

The complete derivation of Equation (3-24) is explained in Appendix A.

To obtain the stiffness matrix the compliance tensor must be inverted

$$C^{cr}_{ijkl} = \left(S^{cr}_{ijkl}\right)^{-1} \tag{3-25}$$

3.3 Uniaxial Creep Tests

Experimental uniaxial creep and small punch creep tests were conducted on the P91 steel at 600ºC. The material chemical composition of the P91 steel used in the current work is given in Table 3-1. The conventional creep specimens were manufactured from a P91 pipe. The gauge length of the specimen is 50mm, and the diameter of the gauge length is 10mm. The dimensions of the uniaxial specimen are shown in Figure 3-2. Stress levels of 140, 150, 160, 170, 180MPa were used in uniaxial creep tests for the P91 steel at 600℃.

Table 3-1. Chemical of the P91 steel composition [145, 64].

Cr	Mo	C	Si	S	P	Al	V	Nb	N	W	Fe
8.60	1.02	0.12	0.34	0.002	0.017	0.007	0.24	0.070	0.060	0.030	Bal

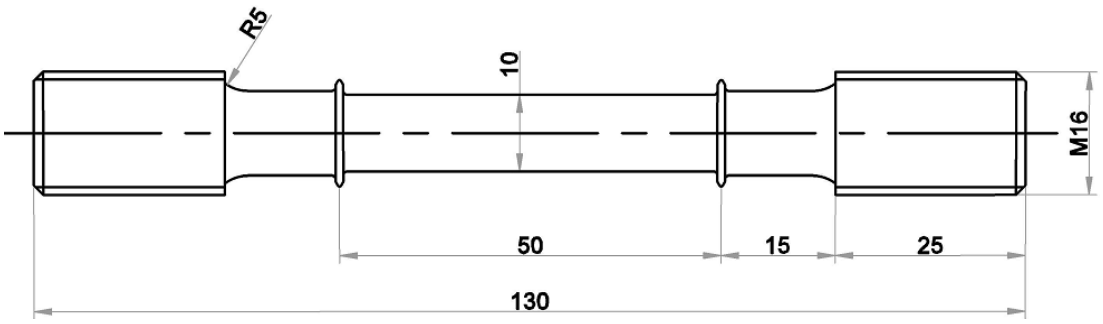


Figure 3-2. Uniaxial test specimen, all dimensions in mm.

3.4 FE Uniaxial Creep Model

The axisymmetric model represented the FE geometry of the uniaxial creep specimen. The implementation of the UMAT was carried out with load controlled condition in the Y-direction for five levels of stress, i.e., 140, 150, 160, 170,

180MPa. The fully boundary conditions were applied in X and Y directions of the specimen. Firstly, displacements were constrained to zero in the X-direction for all nodes located on the Y-axis. Secondly, movements were limited to zero in the Y-direction for all nodes situated on X-axis as shown in Figure 3-3. The fundamental objective of FE analysis of the uniaxial creep tests is to validate and display capability of creep aspects in the developed model. The material constant α, the magnitude of dislocation Burgers vector b, and Taylor factor M were taken from [64]; these and other material constants previously used in calculations for the P91 steel are listed in Table 3-2.

Table 3-2. Notation and material constants used in numerical FE for the P91 steel at 600°C [64, 61, 146].

Parameter	**Name**	**Value**
ρ_i	Initial Dislocation Density	1×10^{14} m^{-2}
E	Elastic modulus	145 GPa
v	Poisson's ratio	0.3
b	The magnitude of Burgers vector	2.5×10^{-10} m
m	The exponent of stress sensitivity	55.89
$\dot{\varepsilon}_o$	Reference strain rate	1 s^{-1}
k_{20}	Dynamic recovery	55
α	Constant	0.8
M	Taylor factor	3.06

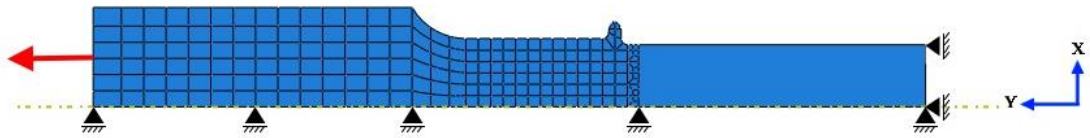


Figure 3-3. FE axis-symmetric uniaxial creep specimen.

The strain-time curves for uniaxial creep test of 140, 150, 160, 170, and 180MPa at 600ºC are shown in Figures 3-4 to 3-6. Uniaxial creep data at 600℃ was used to compare with the corresponding FE results. The results obtained show excellent agreement though the FE results for the 180MPa test predict a much shorter failure life. The unified mechanical model produces typical primary, secondary, and tertiary creep responses for all stress levels. The primary creep strain increases with stress. The minimum creep strain rate observed in the secondary creep regime increases as stress increases. The amount and rate of tertiary creep strain increase with stress.

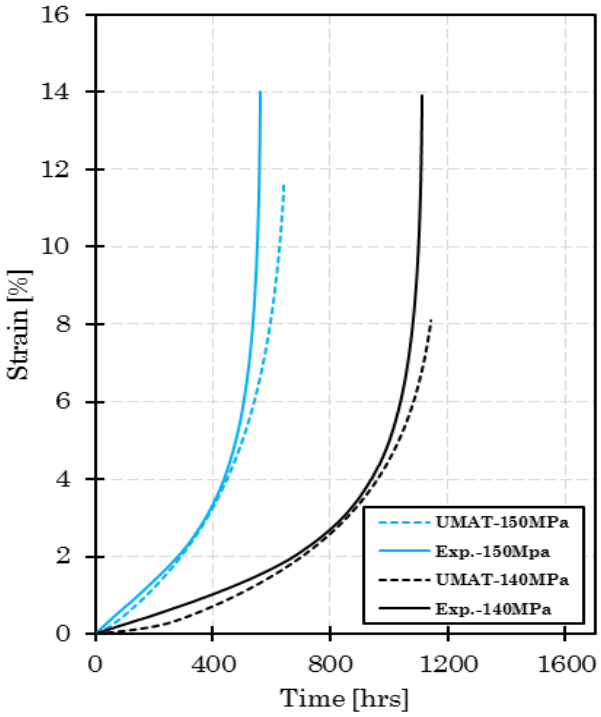


Figure 3-4. Experimental and calculated uniaxial creep curves for stresses at 140 and 150MPa.

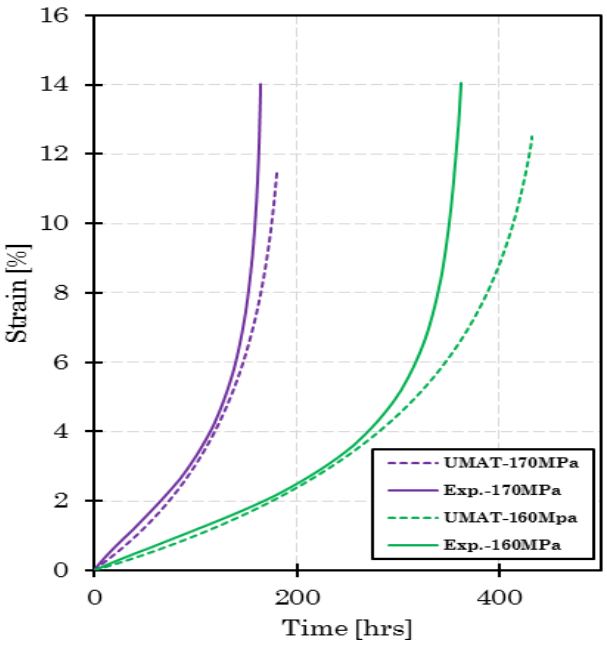


Figure 3-5. Experimental and calculated uniaxial creep curves for stresses at 160 and 170MPa.

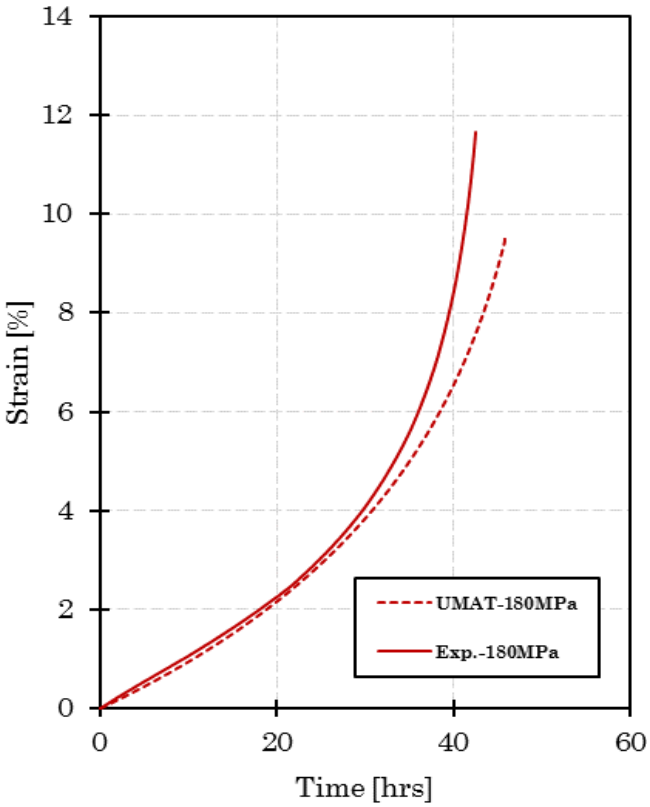


Figure 3-6. Experimental and calculated uniaxial creep curves for stresses at 180MPa.

3.5 Modelling of Small Punch Creep Tests

3.5.1 FE Model

Finite element modelling of small punch creep for P91 steel at 600℃ was carried with five levels of punch loads P1= 25, 28, 30, 34 and 40 kg using the UMAT code. Figure 3-7 shows the Schematic three-dimensional of rig for small punch creep testing. An axisymmetric finite element model was used. Figure 3-8 shows the geometry of the FE model where the punch radius is 1.04mm, the holder and the support radius is 0.25mm, the thickness, and radius of the specimen are 0.5 and 4mm, respectively, the receiving hole radius is 2mm. The punch, the holder, and the support were modelled as rigid parts. Approximately half of the surface of the

bottom of the specimen is constrained by a support to simulate clamped surface to surface. The friction coefficient between these surfaces is assumed to be 0.8 [147]. The SPCT specimen was considered as a deformable part and was meshed with rectangular elements. The contacting interfaces between the top surface of the sample and the rigid punch were assigned as surface to surface contacts with a coefficient of friction assumed to have a value of 0.2. The simulation was carried out with three types of boundary conditions. Firstly, the axial movement and rotation around the axis of symmetry of the support were constrained entirely. Secondly, the horizontal movement and rotation of punch and holder were also restricted.

The complete displacement and rotation constraints were applied on the left side of the specimen in the X-direction for all nodes located on the Y-axis. The loads are directed in the Y direction and are applied to the reference point of for the punch which is assumed to be rigid, while a clamping load, 500N, is used on to the reference point of holder die. The FE mesh consists of 891 nodes and 800 bilinear axis-symmetric 4-nodes elements.

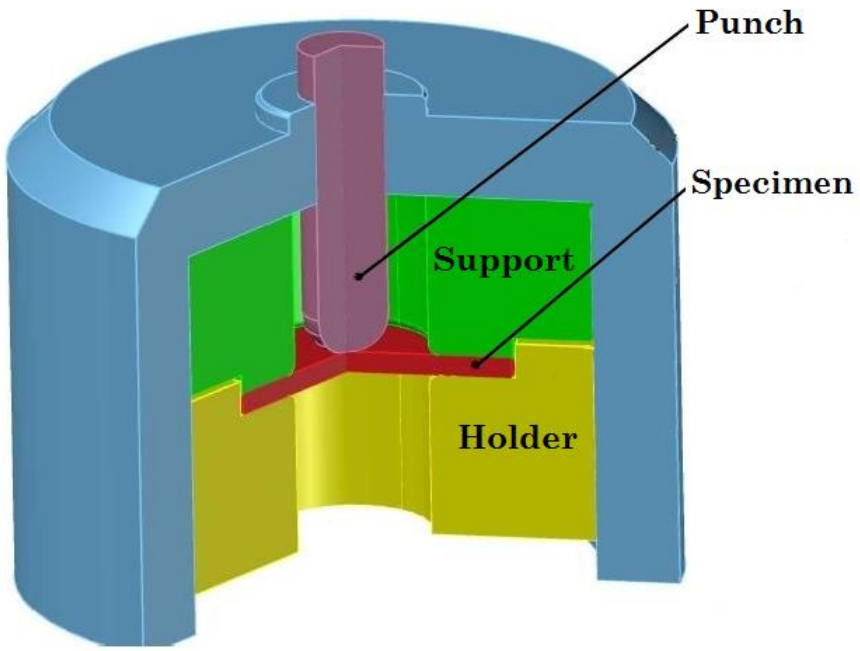


Figure 3-7. Schematic three-dimensional of rig for small punch creep testing.

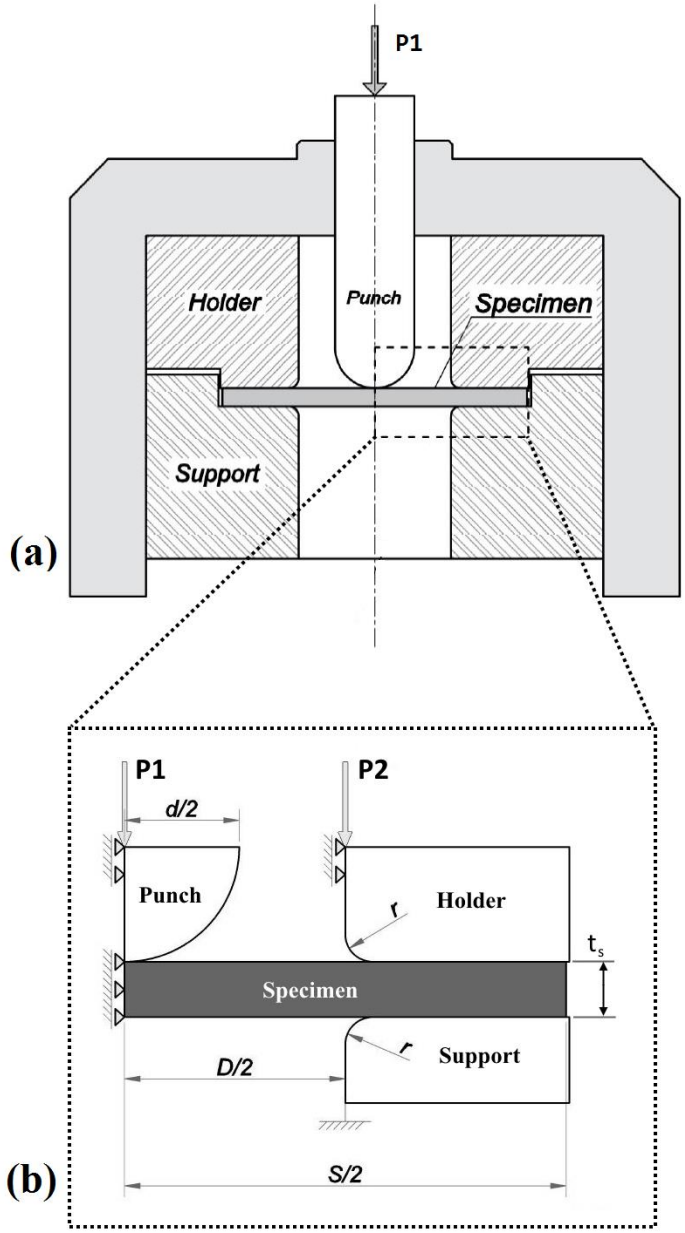


Figure 3-8. Schematic representation of a FE model for small punch creep testing analysis (D=4mm, S=8mm, d=2.08mm, r=0.25mm, t_s=0.5mm).
(a) Schematic two-dimensional of rig for small punch creep testing.
(b) Representation loads and boundary conditions of finite element modelled part.

The punch, holder and support dies were considered as rigid bodies. The specimen was implemented as a deformable body with two elements type groups. The first group consists of 1480 4-node bilinear axisymmetric quadrilateral, reduced integration elements, (CAX4R) while the second group involves 10 3-node linear axisymmetric triangle elements (CAX3). Figure 3-9 shows the mesh used for the SPCT analysis. The specimen was refined along the contact region between the punch and the specimen. The minimum element size, in the refined zone, is 0.025mm.

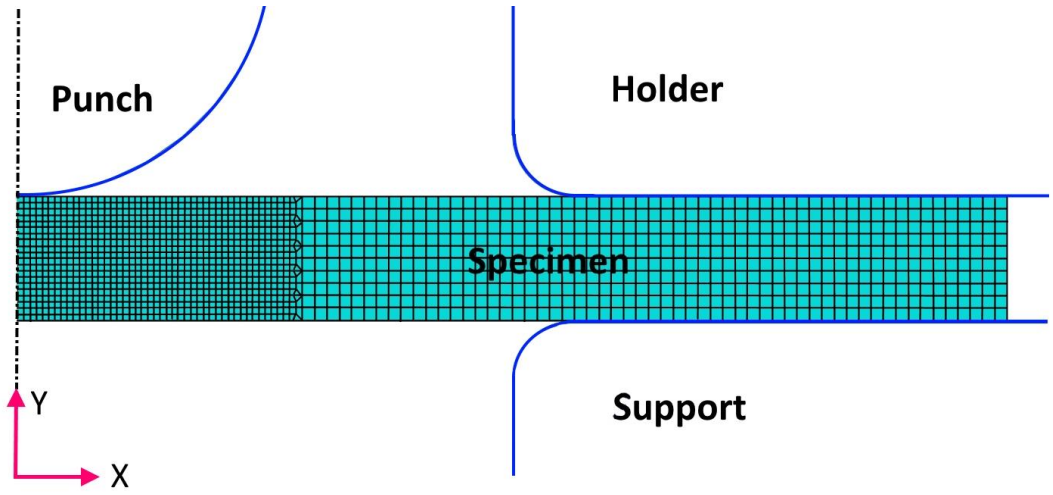


Figure 3-9. FE mesh used for SPCT specimen.

3.5.2 Displacement-Time Curves

The relationship between the coefficient of friction and the magnitude of the friction forces is directly proportional. A parametric study of the different friction coefficients between the specimen and punch is carried out. The contact between the sample and punch was modelled using surface to surface contact with various friction coefficients. Figures 3-10 and 3-11 show the effect of friction coefficient for three values ($\mu = 0.2$, 0.3 and, 0.4) each with two cases of loads, namely 34 and 40kg. From these results, it can be observed clearly that the effect of the coefficient of friction on the FE outputs is significant. For a given load level, when the friction coefficient increases, the minimum deflection rate will drop and the failure time will increase. From the above, one can conclude that the value of the friction coefficient of $\mu = 0.2$ gives the best approximation between modelling and practical data.

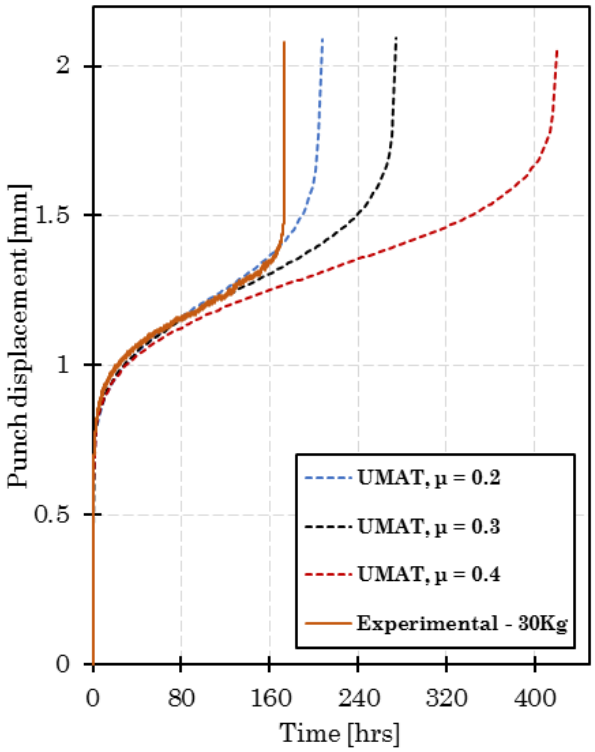


Figure 3-10. Calculated SPCT curve at the variation of the friction coefficient for punch load of 30Kg.

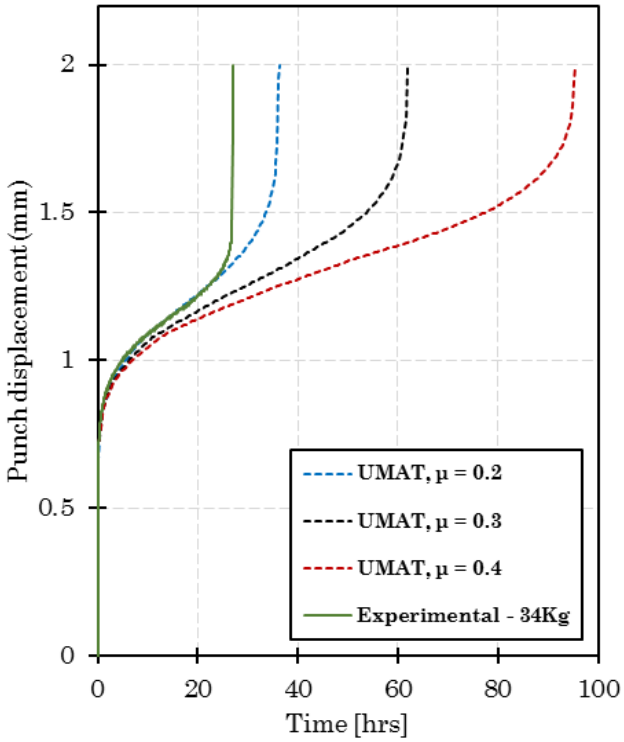


Figure 3-11. Calculated SPCT curve at the variation of the friction coefficient for punch load of 34Kg.

The experimental SPCT curves at five different load levels and the corresponding predicted curves are compared in Figures 3-12 to 3-16. The coefficient of friction between punch and specimen is assumed to be constant ($\mu = 0.2$) for all applied loads.

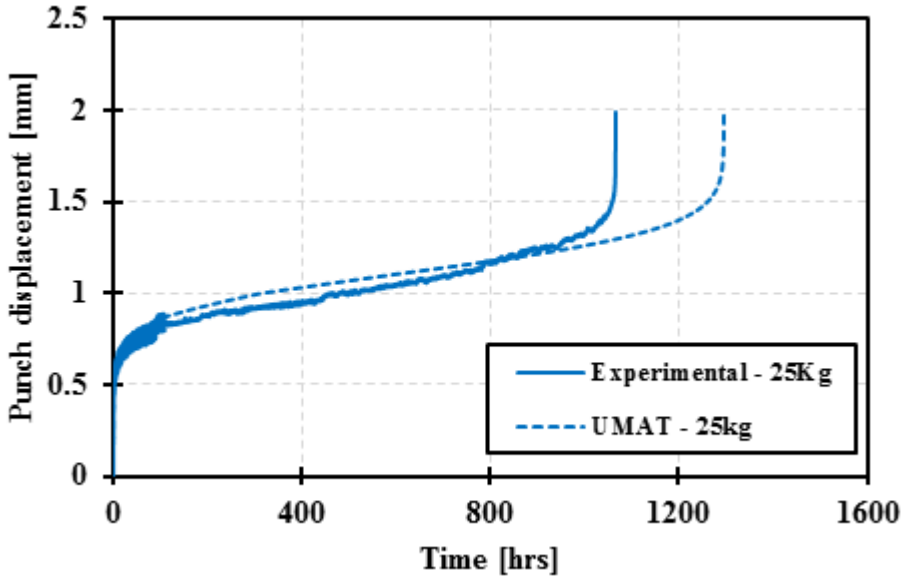


Figure 3-12. The experimental and calculated SPCT curves at punch load of 25Kg[74].

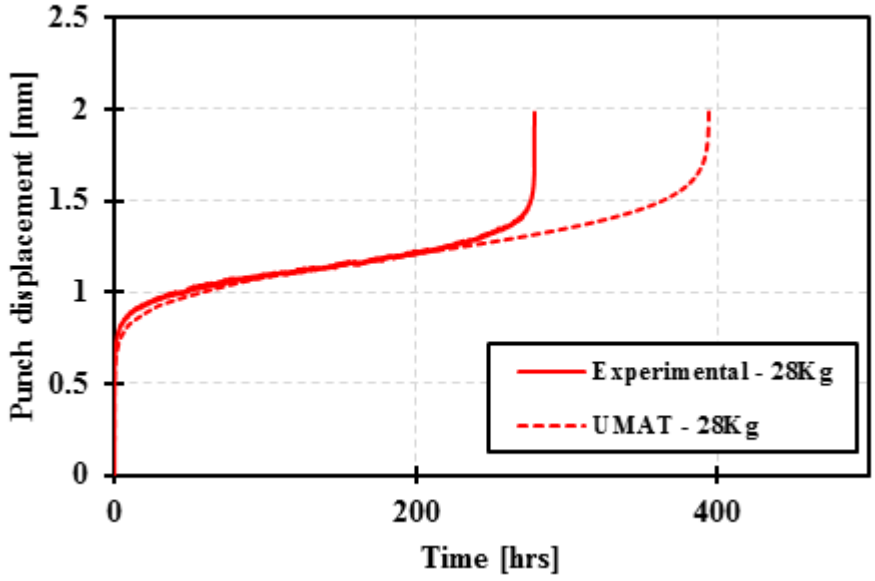


Figure 3-13. The experimental and calculated SPCT curves at punch load of 28Kg [74].

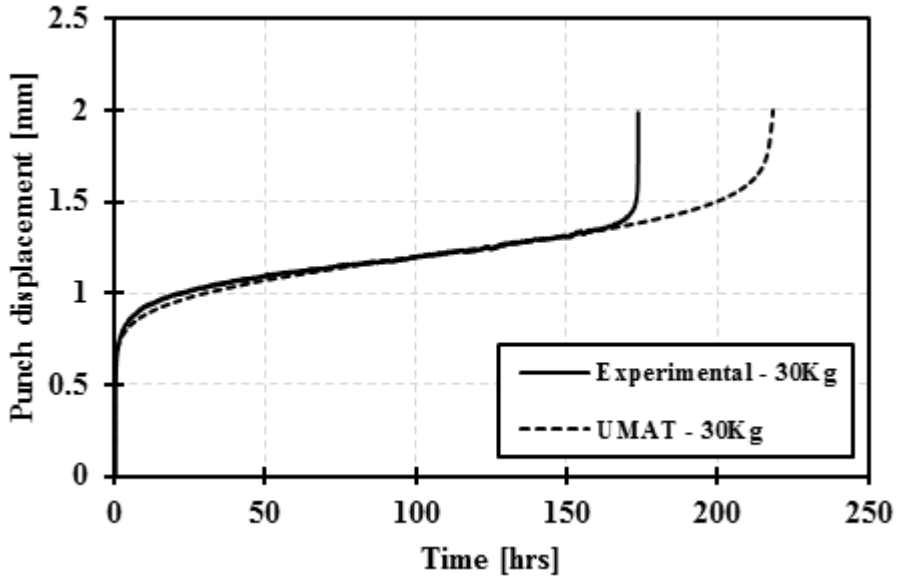


Figure 3-14. The experimental and calculated SPCT curves at punch load of 30Kg [74].

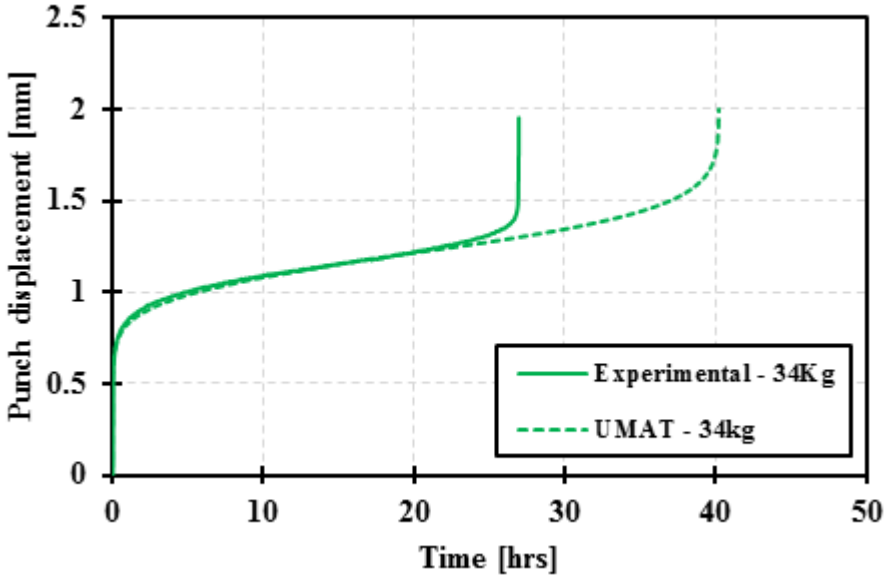


Figure 3-15. The experimental and calculated SPCT curves at punch load of 34Kg [74].

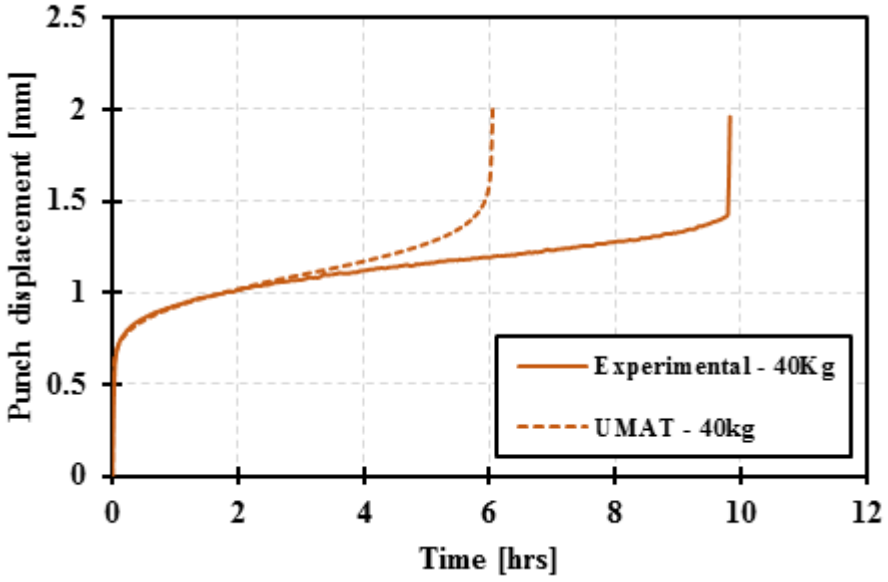


Figure 3-16. The experimental and calculated SPCT curves at punch load of 40Kg [74].

3.5.3 Contours of Displacement, von Mises Stress and Strain

The FE analysis of SPCTs was carried out using UMAT code through the ABAQUS package. Figures 3-17 and 3-18 show the results of punch deformation at loads 28 and 30Kg. The displacements of the punch range from 0.727mm for a load of 25kg up to 0.946mm for a load of 30kg at 5.2 hrs.

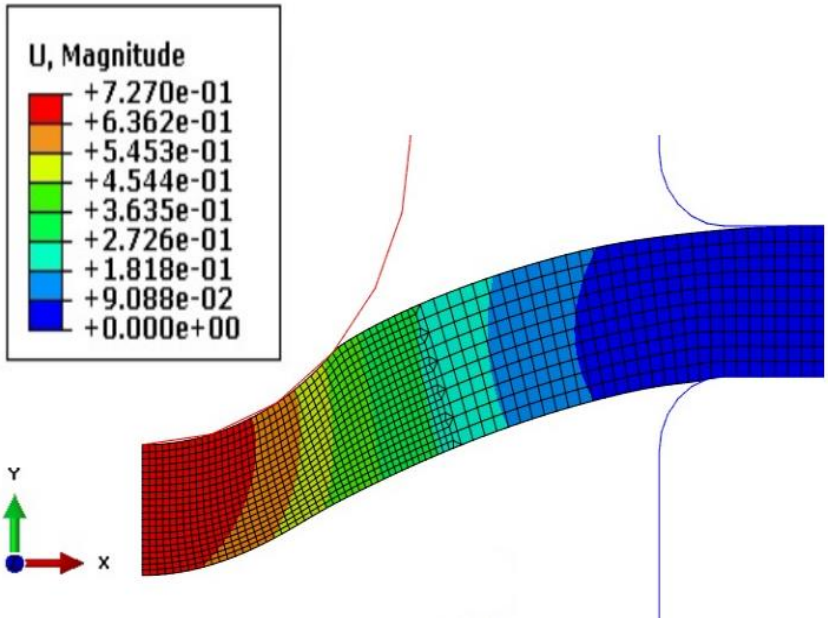


Figure 3-17. Contour plot of punch direction deformation of SPCT at punch load 25Kg.

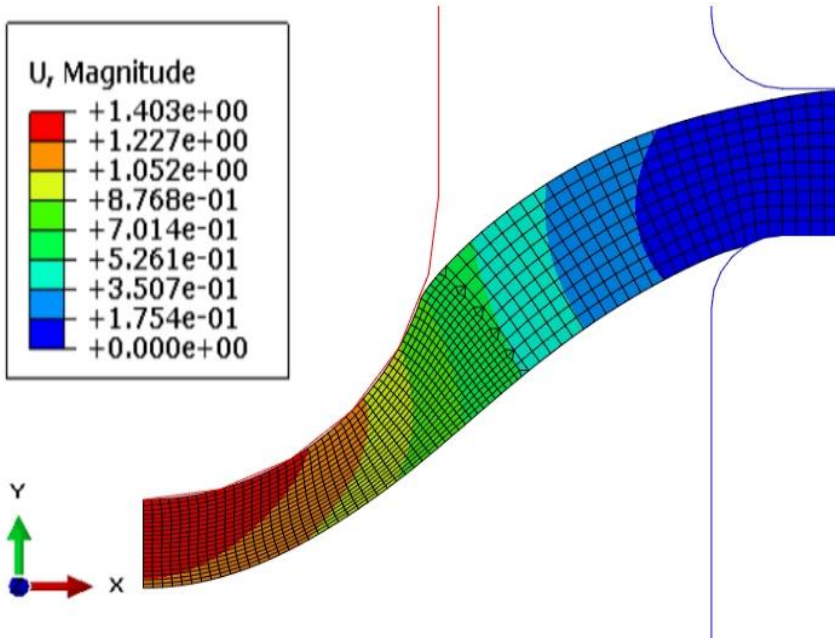


Figure 3-18. Contour plot of punch direction deformation of SPCT at punch load 30Kg.

Figures 3-19 and 3-20 show the distribution of stress at the cross-section of the specimen after 6 hours under a constant punch load of 34Kg and 40Kg respectively. The highest equivalent stress value is observed at a point located about 0.9 mm from the centre of the initial specimen at the start of SPC test (the black arrow in the figure indicates the location of the maximum stress value), while it drops down at the zone located at about 2.0mm from the centre of the specimen.

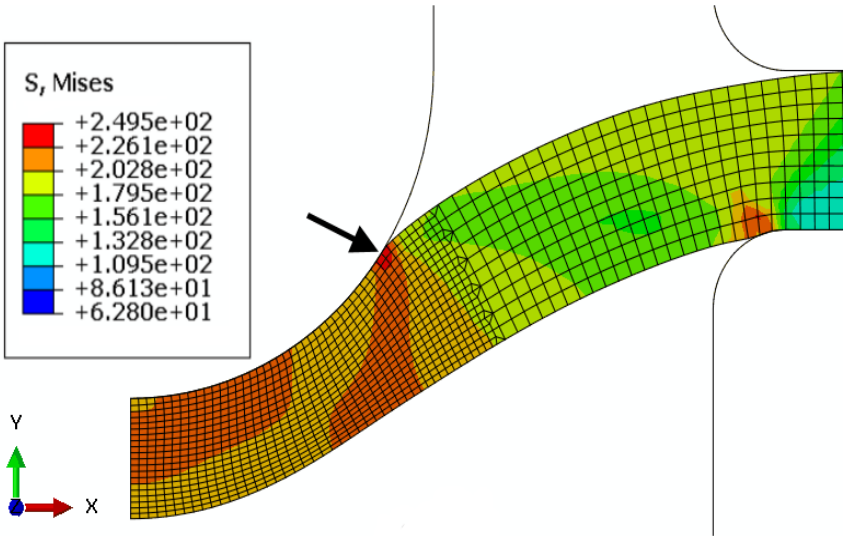


Figure 3-19. Contour plot of the equivalent stress with the SPCT at a punch load of 34Kg.

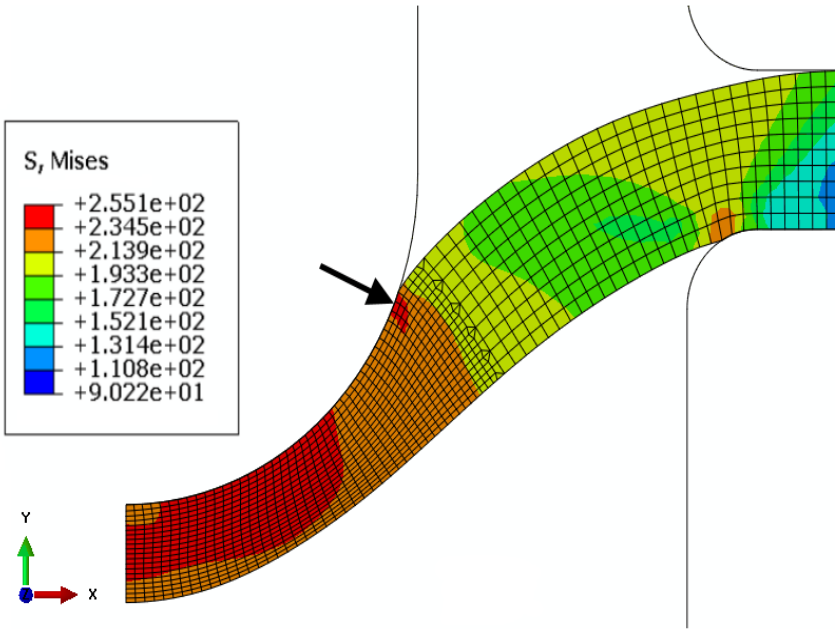


Figure 3-20. Contour plot of the equivalent stress with the SPCT at a punch load of 40kg.

Figure 3-21 shows SEM images of experimental SPC tests for punch load of P1= 25 kg which are suspended after (a) 2hrs, (b) 200hrs and, (c) 669hrs and the corresponding effective strain contour plots. The regions of local deformity were nearly identical to those of the experimental specimen tested.

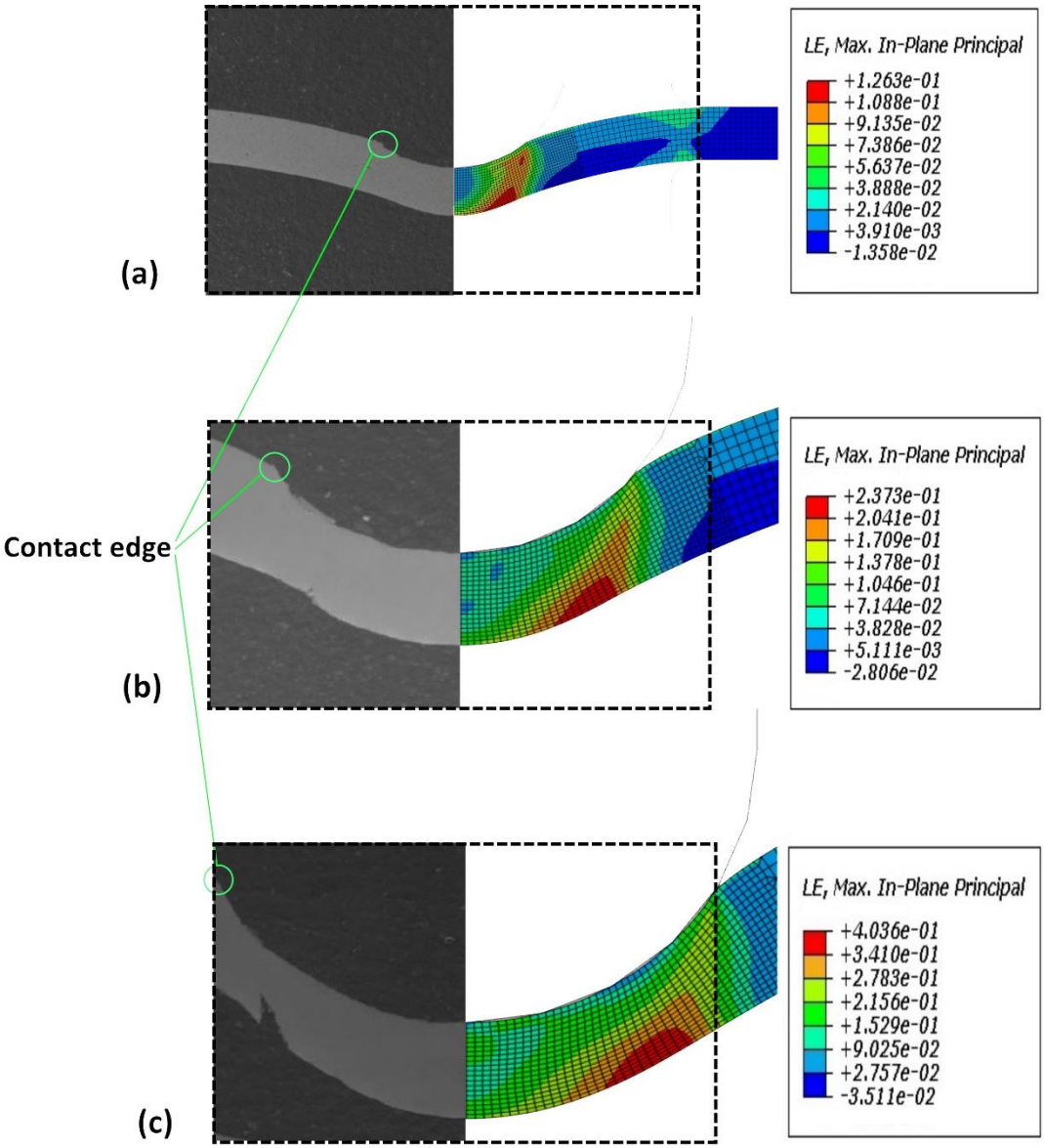


Figure 3-21. Contour plot of strain and SEM images of SPCT at punch load 25Kg for P91 steel at 600°C.

Figures 3-22 and 3-23 show the variations of equivalent strain under applied loads of 34 and 40kg. The directions and locations of the strain data are identified in both figures. Equivalent strains also suddenly increase at the region located at about 2.0 mm from the centre of the specimen. This deformation may be due to severe bending of specimen at the corner of lower die located at 2.0 mm from the centre of the sample. Except for this region, maximum equivalent strains occur identically at the location of about 0.7 mm. In addition, it is seen that the position of the maximum effective strains did not effected by the applied load.

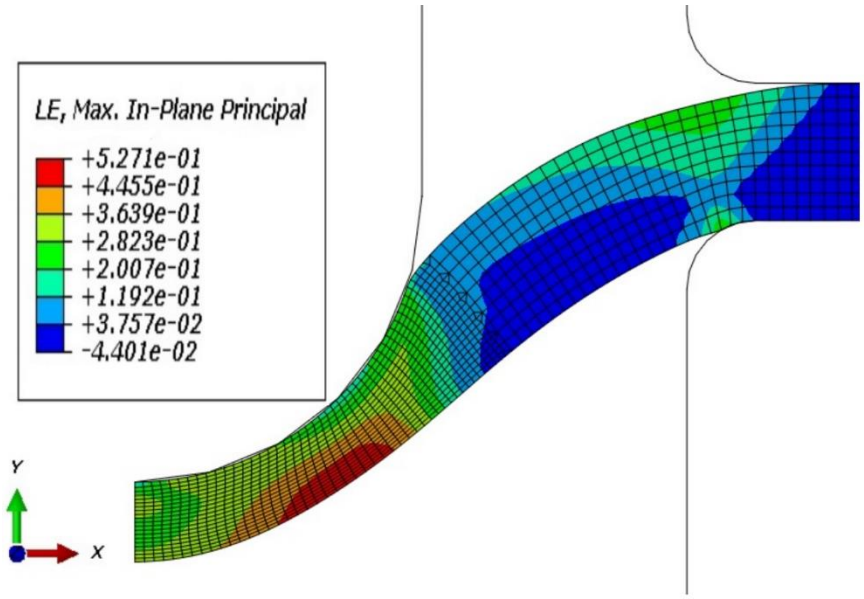


Figure 3-22. Contour plot of a strain of SPCT at punch load 34Kg.

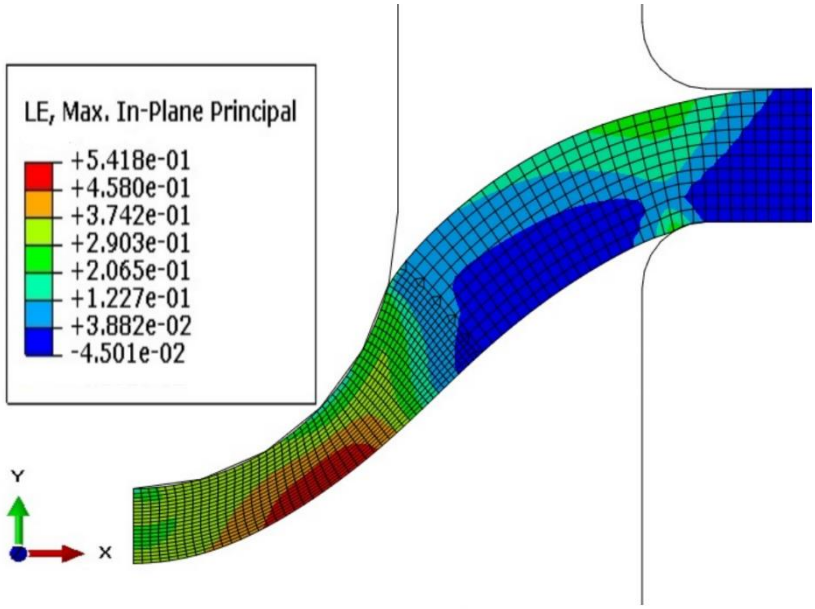


Figure 3-23. Contour plot of a strain of SPCT at punch load 40kg.

The mechanisms of the SPCT deformation contrast sharply with those in uniaxial creep tests. During the first SPCT regime, the specimen undergoes a severe development in shape. Change of the structure causes a decrease in the specimen's stiffness and a change in the deformation mechanism, from bending dominated to 'membrane stretching' dominated. In the second SPCT regime, the controlling mechanism is tensile stretching of the annular region around the contact edge between the punch and the specimen. Material creep damage is still observed to occur in the secondary SPCT region. The third SPCT region, symbolised by developing deformity rate, is governed by creep material degradation and specimen necking.

Although model formulations were based on the assumption of small deformations, the FE results indicate the existence of large strains (up to 60%) within the SPCT. Notwithstanding this apparent conflict, the UMATs that have

been discussed in the current chapter and in the following chapters 4 and 6 are still applicable to large deformation problems. This is because the necessary rigid body rotations have already been applied to the strain and stress quantities within the ABAQUS system before they are supplied to the UMAT subroutine.

3.6 Conclusions

The constitutive equations of the KME model rely on the basic physical microstructure and were implemented in the finite element modelling through the user material subroutine (UMAT) and evaluated in comparison with the experimental results. The testing procedure involved SPCT and uniaxial creep tests on the P91 steel at 600ºC.

- The KME model has been implemented into the finite element scheme ABAQUS using UMAT code. The predicted results of SPC and uniaxial creep simulations have a good agreement with the corresponding of experimental tests.

- The additional advantage of using the current model is the capability to determine the creep model parameters from utilizing microstructure information in addition to uniaxial creep data.

- The influence of friction behaviour of the contact between punch and specimen was considered for SPCTs at different levels of load. The failure time gradually increases with an increase of the friction coefficient.

- The maximum equivalent strain was observed within an annular zone on the underside of the specimen and this weakest location did not change even though the timescales to reach failure varied greatly across the different loading cases.

CHAPTER 4:
FINITE ELEMENT VISCO-PLASTICITY MODELLING BASED UPON DISLOCATION DENSITY

4.1 Introduction

One of the main strengthening mechanisms of the P91 steel comes from immobile dislocations where the strain hardening resulting from the rate of dislocation evolution/annihilation. So the finite element numerical modelling of the stress-strain relation, as a first step, is carried out using a dislocation-based material model of the P91 steel at a constant strain rate and at elevated temperature. The proposed approach follows the models of Kocks [58], Estrin and Mecking [60] in which the evolution of dislocation density plays a central role as the internal parameter exemplifying the microstructural behaviour of the material.

This chapter is structured as follows: Section 4.2 presents the KME model framework based on the evolution of dislocation density at several strains rates and temperatures. The development of the user material subroutine (UMAT) is detailed in Section 4.3, in which the implementation of the constitutive model, in the implicit finite element code ABAQUS/Standard, is also presented. Section 4.4 is devoted to the material used in this work. The application of the model to the

simulation of uniaxial tensile and creep is described in Section 4.5. These simulations are achieved for displacement controlled to give constant strain rate and for constant stress loading at elevated temperature. The comparison between the calculated FE results and experimental data is presented in Section 4.6. This part aims to demonstrate the capability of the implemented implicit model to be utilised for structural FE analysis. The influence of internal variables on the overall tensile and creep behaviour at different conditions is discussed. Finally, concluding remarks and future work are given in Section 4.7.

4.2 KME Model Framework

The core of the dislocation density model is the following particular power-law form which connects the equivalent plastic strain rate to the equivalent stress. The proposed mathematical structure for the viscoplastic constitutive model is a power law which suggested by Kocks[58].

$$\dot{\varepsilon}^{(vp)} = \dot{\varepsilon}_o \left(\frac{\sigma_{eq}}{\sigma_f}\right)^m, \tag{4-1}$$

where $\dot{\varepsilon}^{(vp)}$ is viscoplastic strain rate, $\dot{\varepsilon}_o$ is a reference strain rate, the σ_{eq} is effective stress, m is an exponent of stress sensitivity and the quantity of flow stress of the strained material, σ_f. The following microstructural constitutive relationship has frequently been observed between flow stress, an internal state variable, and dislocation density ρ [60].

$$\sigma_f = M\alpha bG\sqrt{\rho}\,. \tag{4-4-2}$$

Here α is a constant, b is the magnitude of the dislocation Burgers vector, μ is the shear modulus, and M is the Taylor factor. The P91 has a large initial dislocation density, with a range of primary states from $1.6 \times 10^{14}\,\mathrm{m}^{-2}$ to $7.5 \times 10^{14}\,\mathrm{m}^{-2}$ determined using TEM [3, 148]. The model assumed that the micromechanical strength of the material depends upon the pile-up of dislocation-dislocation interactions. All other reasons that act to prevent dislocation slip have been neglected. The evolution of dislocation density ρ, which is taken as a primary variable that describes work hardening, can be expressed as

$$\Delta\rho = M\left[k_1\sqrt{\rho} - k_2\rho\right]\Delta\varepsilon^{(vp)}, \tag{4-3}$$

The first term in the right hand side of Equation (4-3) represents an athermal process where k_1 is constant which accounts for the static recovery, and can be evaluated as

$$k_1 = 2\left(\frac{\theta_{II}}{\mu}\right)(\alpha b)^{-1}, \tag{4-4}$$

where Θ_{II} is strain hardening rate at the second stage which is given by the expression

$$\Theta_{II} = \frac{1}{2} M^2 \alpha\mu b k_1 \left(\frac{\dot{\varepsilon}^{(vp)}}{\dot{\varepsilon}_o}\right)^{1/m}. \tag{4-5}$$

or can be estimated to be of the order of $\frac{\mu}{20} - \frac{\mu}{30}$ [58].

The second term in the right side of Equation (4-3) relates to a dynamic recovery process that is controlled by the softening of stored dislocations within a

crystalline grain. The coefficient of dynamic recovery (k_2) represents a thermally-activated action of dynamic recovery by dislocation glide. Since the dynamic process is thermally activated, k_2 is a function of strain rate and temperature, $k_2 = k_2(\dot{\varepsilon}, T)$, and can be expressed as follows [61]:

$$k_2 = k_{20} \left(\frac{\dot{\varepsilon}^{(vp)}}{\dot{\varepsilon}_o}\right)^{-1/q}. \tag{4-4-6}$$

where k_{20} is a constant, $\dot{\varepsilon}^{(vp)}$ is the plastic strain rate, and q is the exponent of dynamic recovery which is given by [58]

$$q = \frac{\Lambda}{k_b T}\ , \tag{4-7}$$

where k_b is the Boltzmann constant, T is the temperature in Kelvin, and Λ is a constant. In the case of a coarse-grained single phase material for which the plastic strain rate is constant, the stress-strain behaviour can now be determined from the set of equations

$$\dot{\varepsilon}^{(vp)} = \dot{\varepsilon}_o \left(\frac{\sigma_{eq}}{\sigma_f}\right)^m,$$

$$\sigma_f = M\alpha b\mu\sqrt{\rho}\,,$$

$$\Delta\rho = M\left[k_1\sqrt{\rho} - k_2\rho\right]\Delta\varepsilon^{(vp)}, \tag{4-8 a-d}$$

$$k_2 = k_{20} \left(\frac{\dot{\varepsilon}^{(vp)}}{\dot{\varepsilon}_o}\right)^{-1/q}.$$

Equation set 4-8 can be solved numerically using a UMAT for the case of multiaxial deformation with constant plastic strain rate and temperature.

4.3 User Material Subroutine UMAT Development

UMAT is an interface that allows the user to implement a constitutive equation within the ABAQUS/Standard finite element framework. This interface is used when none of the existing material models included in the ABAQUS material library is appropriate. It also makes its possible to define complex constitutive models which be used with any mesh element type with the ABAQUS geometry. In the next section, the constitutive equations of the developed dislocation density-based model will be derived and implemented. The proposed computational algorithm features are fully implicit integration and return mapping based on a two-step elastic predictor/plastic corrector strategy.

4.3.1 The Multiaxial Extension of the Constitutive Model

The following equation defines Hooke's law for a multi-axial state regarding stress and strain tensors:

$$\sigma_{ij} = 2\mu\,\varepsilon_{ij}^{(e)} + \lambda\varepsilon_{kk}^{(e)}\delta_{ij}\,, \tag{4-9}$$

where μ denotes the shear modulus, λ the Lame constant, ε_{kk} is the trace of a second-order tensor, ε_{ij}, while δ_{ij} is the Kronecker delta tensor.

In the domain of elastoplasticity and viscoplasticity, the total strain tensor ε is commonly assumed to be split into two parts: elastic (recoverable) $\varepsilon^{(e)}$ and visco-plastic (irrecoverable) $\varepsilon^{(vp)}$ parts. In the following, we consider a time increment $\Delta t = t_{n+1} - t_n$. It is assumed that the elastic strains at the beginning

of the time step, t_n, and the value of the total strain increment $\Delta\varepsilon$ are known, and the aim is then to find the solution for the elastic strains at the end of the time step, t_{n+1}, as

$$\varepsilon_{ij}^{(e)(t_{n+1})} = \varepsilon_{ij}^{(e)(t_n)} + \left(\Delta\varepsilon_{ij}^{(t_{n+1})} - \Delta\varepsilon_{ij}^{(vp)(t_{n+1})}\right), \tag{4-10}$$

where $\Delta\varepsilon_{ij}^{(t_{n+1})}$ and $\Delta\varepsilon_{ij}^{(vp)(t_{n+1})}$ are total and plastic strain increments respectively

so that

$$\Delta\sigma_{ij}^{(t_{n+1})} = 2\mu\left(\varepsilon_{ij}^{(e)(t_n)} + \Delta\varepsilon_{ij}^{(t_{n+1})}\right) + \lambda\left(\varepsilon_{kk}^{(e)(t_n)} + \Delta\varepsilon_{kk}^{(t_{n+1})}\right)\delta_{ij} - 2\mu\left(\Delta\varepsilon_{ij}^{(vp)(t_{n+1})}\right), \tag{4-11}$$

since $\Delta\varepsilon_{kk}^{(vp)(t_{n+1})} = 0$

The procedure is split into two steps. In the first step, it is assumed that the inelastic strains do not evolve and that only elastic strains are generated. This step is called the elastic predictor. Then, in the second step, the total strain is assumed to be fixed, and the error in stress is corrected by developing inelastic strains. The latter step is called an inelastic corrector, $2\mu\left(\Delta\varepsilon_{ij}^{(vp)(t_{n+1})}\right)$.

The elastic predictor, or trial stress, is given by

$$\Delta\sigma_{ij}^{(trial)(t_{n+1})} = 2\mu\left(\varepsilon_{ij}^{(e)(t_n)} + \Delta\varepsilon_{ij}^{(t_{n+1})}\right) + \lambda\left(\varepsilon_{kk}^{(e)(t_n)} + \Delta\varepsilon_{kk}^{(t_{n+1})}\right)\delta_{ij}\ , \tag{4-12}$$

Thus, the numerical integration of the Hooke's law Equation (4-11) using a fully implicit backward Euler time discretisation methods leads to:

$$\Delta\sigma_{ij}^{(t_{n+1})} = \Delta\sigma_{ij}^{(trial)(t_{n+1})} - 2\mu\left(\Delta\varepsilon_{ij}^{(vp)(t_{n+1})}\right), \quad (4\text{-}13)$$

where $\Delta\sigma_{ij}^{(trial)(n+1)}$ is the increment in trial stress which is known, and obtained by assuming the increment is entirely elastic. The plastic strain tensor increments $\Delta\varepsilon_{ij}^{(vp)}$is defined using the Levy-Mises flow rules:

$$\Delta\varepsilon_{ij}^{(vp)(t_{n+1})} = \Delta p^{(t_{n+1})}\, \mathcal{N}_{ij}^{(t_{n+1})}, \quad (4\text{-}14)$$

$$\mathcal{N}_{ij}^{(t_{n+1})} = \frac{3}{2}\frac{\mathcal{S}_{ij}^{(t_{n+1})}}{\sigma_{eq}^{(t_{n+1})}}. \quad (4\text{-}15)$$

Where $\mathcal{N}_{ij}$ is the flow direction tensor, $\mathcal{S}_{ij}$ denotes the deviatoric stress tensor, while Δp is the increment in effective plastic strain which is solved iteratively as

$$\Delta p^{(n+1)(k+1)} = \Delta p^{(n+1)(k)} + \delta\Delta p^{(n+1)(k)}, \quad (4\text{-}16)$$

The deviatoric parts of the stress and strain are given, respectively, in the following form as

$$\mathcal{S}_{ij}^{(t_{n+1})} = \sigma_{ij}^{(t_{n+1})} - \frac{1}{3}\sigma_{kk}\delta_{ij}, \quad e_{ij}^{(t_{n+1})} = \varepsilon_{ij}^{(t_{n+1})} - \frac{1}{3}\varepsilon_{kk}\delta_{ij}. \quad (4\text{-}17)$$

Thus, using Equation (4-11),

$$\Delta\mathcal{S}_{ij}^{(t_{n+1})} = 2\mu\left(\Delta e_{ij}^{(t_{n+1})} - \Delta\varepsilon_{ij}^{(p)(t_{n+1})}\right), \quad \Delta\mathcal{S}_{ij}^{(trial)(t_{n+1})} = 2\mu\,\Delta e_{ij}^{(t_{n+1})} \quad (4\text{-}18)$$

Substituting into Equation (4-11) gives

$$\Delta\sigma_{ij}^{(t_{n+1})} = \Delta\mathcal{S}_{ij}^{(t_{n+1})} + \lambda\left(\varepsilon_{kk}^{(e)(t_n)} + \Delta\varepsilon_{kk}^{(t_{n+1})} - \Delta\varepsilon_{kk}^{(vp)(t_{n+1})}\right)\delta_{ij}\,, \qquad (4\text{-}19)$$

The increment in deviatoric stress at the end of the time step, t_{n+1}, may be written as

$$\Delta\mathcal{S}_{ij}^{(t_{n+1})} = \Delta\mathcal{S}_{ij}^{(trial)(t_{n+1})} - 2\mu\Delta p^{(t_{n+1})}\,\mathcal{N}_{ij}^{(t_{n+1})}\,, \qquad (4\text{-}20)$$

and therefore

$$\mathcal{S}_{ij}^{(t_{n+1})} = \mathcal{S}_{ij}^{(trial)(t_{n+1})} - 2\mu\Delta p^{(t_{n+1})}\,\mathcal{N}_{ij}^{(t_{n+1})}\,, \qquad (4\text{-}21)$$

which can be expressed, making use of the flow direction tensor, $\mathcal{N}_{ij}$, as

$$\frac{2}{3}\,\sigma_{eq}^{(t_{n+1})} = \frac{2}{3}\,\sigma_{eq}^{(trial)(t_{n+1})} - 2\mu\Delta p^{(t_{n+1})}\,, \qquad (4\text{-}22)$$

Finally, the following relationship links the predictor and the equivalent von Mises stress:

$$\sigma_{eq}^{(t_{n+1})} = \sigma_{eq}^{(trial)(t_{n+1})} - 3\mu\Delta p^{(t_{n+1})}\,. \qquad (4\text{-}23)$$

4.3.2 Implicit numerical implementation of the dislocation-based model

The essential equations for the KME visco-plastic prediction at the end of the time step, t_{n+1}, are written as

$$\Delta p^{(n+1)(k+1)} = \Delta p^{(n+1)(k)} + \delta\Delta p^{(n+1)(k)},$$

$$\Delta\varepsilon_{ij}^{(vp)(t_{n+1})} = \Delta p^{(t_{n+1})}\, \mathcal{N}_{ij}^{(t_{n+1})},$$

$$\Delta S_{ij}^{(t_{n+1})} = \mathcal{S}_{ij}^{(trial)(t_{n+1})} - 2\mu\left(\Delta e_{ij}^{(t_{n+1})} - \Delta\varepsilon_{ij}^{(vp)(t_{n+1})}\right), \qquad (4\text{-}24\ \text{a-d})$$

$$\Delta\sigma_{ij}^{(t_{n+1})} = \Delta\mathcal{S}_{ij}^{(t_{n+1})} + \lambda\left(\varepsilon_{kk}^{(e)(t_n)} + \Delta\varepsilon_{kk}^{(t_{n+1})} - \Delta\varepsilon_{kk}^{(vp)(t_{n+1})}\right)\delta_{ij}.$$

The trial quantities may be determined by solving the set of Equations 4-24 numerically.

$$\Delta\mathcal{S}_{ij}^{(trial)(t_{n+1})} = 2\mu\,\Delta e_{ij}^{(t_{n+1})}, \qquad (4\text{-}25)$$

$$\Delta\sigma_{ij}^{(trial)(t_{n+1})} = \Delta\mathcal{S}_{ij}^{(trial)(t_{n+1})} + \lambda\left(\varepsilon_{kk}^{(e)(t_n)} + \Delta\varepsilon_{kk}^{(t_{n+1})} - \Delta\varepsilon_{kk}^{(vp)(t_{n+1})}\right)\delta_{ij}, \qquad (4\text{-}26)$$

There are various types of constitutive equations used to represent the viscous stress, but they often contain the effective plastic strain rate dependent $(\dot{p})$, Equation (4-1) becomes

$$\dot{p} = \dot{\varepsilon}_o \left(\frac{\sigma_{eq}}{\sigma_f}\right)^m, \qquad (4\text{-}27)$$

Equation (4-27) is a constitutive equation relating plastic strain rate to stress, and which depends upon internal variable; the isotropic hardening of flow stress, σ_f. The constitutive equation, such as (4-27), is utilised within the

viscoplasticity FE model, which relates the effective plastic strain rate to the stress and internal hardening variables.

From Section 4-2, Equation (4-8 b), the hardening rate is given by

$$\dot{\sigma}_f = M\alpha b\mu\sqrt{\dot{\rho}}\,, \tag{4-28}$$

In this chapter, the evolution of mobile dislocation density rate ($\dot{\rho}$) is characterized in terms of the plastic deformation rate. From Section 4-2, Equation (4-8 c), the evolution of dislocation rate is given by

$$\dot{\rho} = M\left[k_1\sqrt{\rho} - k_2\rho\right]\dot{p}, \tag{4-29}$$

The fundamental equation for the numerical identification is defined by substituting Equation (4-23) into (4-27)

$$\dot{p} = \dot{\varepsilon}_o\left(\frac{\sigma_{eq}^{(trial)} - 3\mu\Delta p}{M\alpha b\mu\sqrt{\rho}}\right)^m, \tag{4-30}$$

where the effective trial stress is known.

From Equation (4-24 b), for a viscoplastic material, the plastic strain rate can be written as

$$\dot{\varepsilon}_{ij}^{(vp)} = \dot{p}\,\mathcal{N}_{ij}\,, \tag{4-31}$$

in which, for viscoplasticity, $\dot{p}$ is now characterize by a constitutive equation which, for isotropic hardening, can be written as

$$\dot{p} = \Phi\left(\sigma_{ij}, \sigma_f\right). \tag{4-32}$$

Implicit backward Euler integration will be used in this study for the multiaxial case of the viscoplastic constitutive equation. Equation (4-32) may be written in an incremental form, consider isotropic hardening, as

$$\Delta p = \Phi(\Delta p, \rho)\Delta t = \dot{\varepsilon}_o \left(\frac{\sigma_{eq}^{(trial)} - 3\mu\Delta p}{M\alpha b\mu\sqrt{\rho}}\right)^m \Delta t \tag{4-33}$$

This equation takes a non-linear form which may be solved iteratively using the Newton-Raphson method and we may write this in a form suitable for Newton's iterative solution, in order to solve for the unknown Δp, as

$$\psi(\Delta p, \rho) = \Delta p - \Phi(\Delta p, \rho)\Delta t = \Delta p - \dot{\varepsilon}_o \left(\frac{\sigma_{eq}^{(trial)} - 3\mu\Delta p}{M\alpha b\mu\sqrt{\rho}}\right)^m \Delta t = 0. \tag{4-34}$$

Using Newton's method, we have

$$\psi^{(n+1)(k)} + \left(\frac{\partial\psi}{\partial\Delta p}\right)^{(n+1)(k)} \delta\Delta p^{(n+1)(k+1)} + \left(\frac{\partial\psi}{\partial\rho}\frac{\partial\rho}{\partial\Delta p}\right)^{(n+1)(k)} \delta\Delta p^{(n+1)(k+1)} = 0. \tag{4-35}$$

In Equation (4-35), an additional incremental step (k) is introduced. Differentiating (4-34) and substituting into (4-35) gives

$$\Delta p - \dot{\varepsilon}_o \left(\frac{\sigma_{eq}^{(trial)} - 3\mu\Delta p}{M\alpha b\mu\sqrt{\rho}}\right)^m \Delta t + \left(1 - \left(\frac{\partial\psi}{\partial\Delta p}\right)^{(n+1)(k)} \Delta t\right) \delta\Delta p^{(n+1)(k+1)} - \left(\frac{\partial\psi}{\partial\rho}\frac{\partial\rho}{\partial\Delta p}\right)^{(n+1)(k)} \Delta t\, \delta\Delta p^{(n+1)(k+1)} = 0 \tag{4-36}$$

Rearranging (4-36) gives

$$\delta\Delta p^{(n+1)(k+1)} = \frac{\dot{\varepsilon}_o\left(\frac{\sigma_{eq}^{(trial)} - 3\mu\Delta p}{M\alpha b\mu\sqrt{\rho}}\right)^m - \frac{\Delta p}{\Delta t}}{\frac{1}{\Delta t} - \left(\frac{\partial\psi}{\partial\Delta p}\right)^{(n+1)(k)} - \left(\frac{\partial\psi}{\partial\rho}\frac{\partial\rho}{\partial\Delta p}\right)^{(n+1)(k)}}. \quad (4\text{-}37)$$

When the norm of ψ is less than a specified tolerance, the iterative Newton-Raphson schema ends. The scalar value of a given quantity of accumulated plastic deformation, Δp, is updated from the previous time step (t_n) to the current step (t_{n+1}), using Equation (4-24a). The plastic strain increment tensor, $\Delta\varepsilon_{ij}^{(vp)(t_{n+1})}$, is computed using Equation (4-24b). From Equations (4-24c) and (4-24d), the updated stress tensor can be computed from the relation:

$$\sigma_{ij}^{(t_{n+1})} = \sigma_{ij}^{(t_n)} + \Delta\sigma_{ij}^{(t_{n+1})}. \quad (4\text{-}38)$$

The flow chart of the implementation of the UMAT for the Kocks-Mecking-Estrin (KME) model is shown in Figure 4-1.

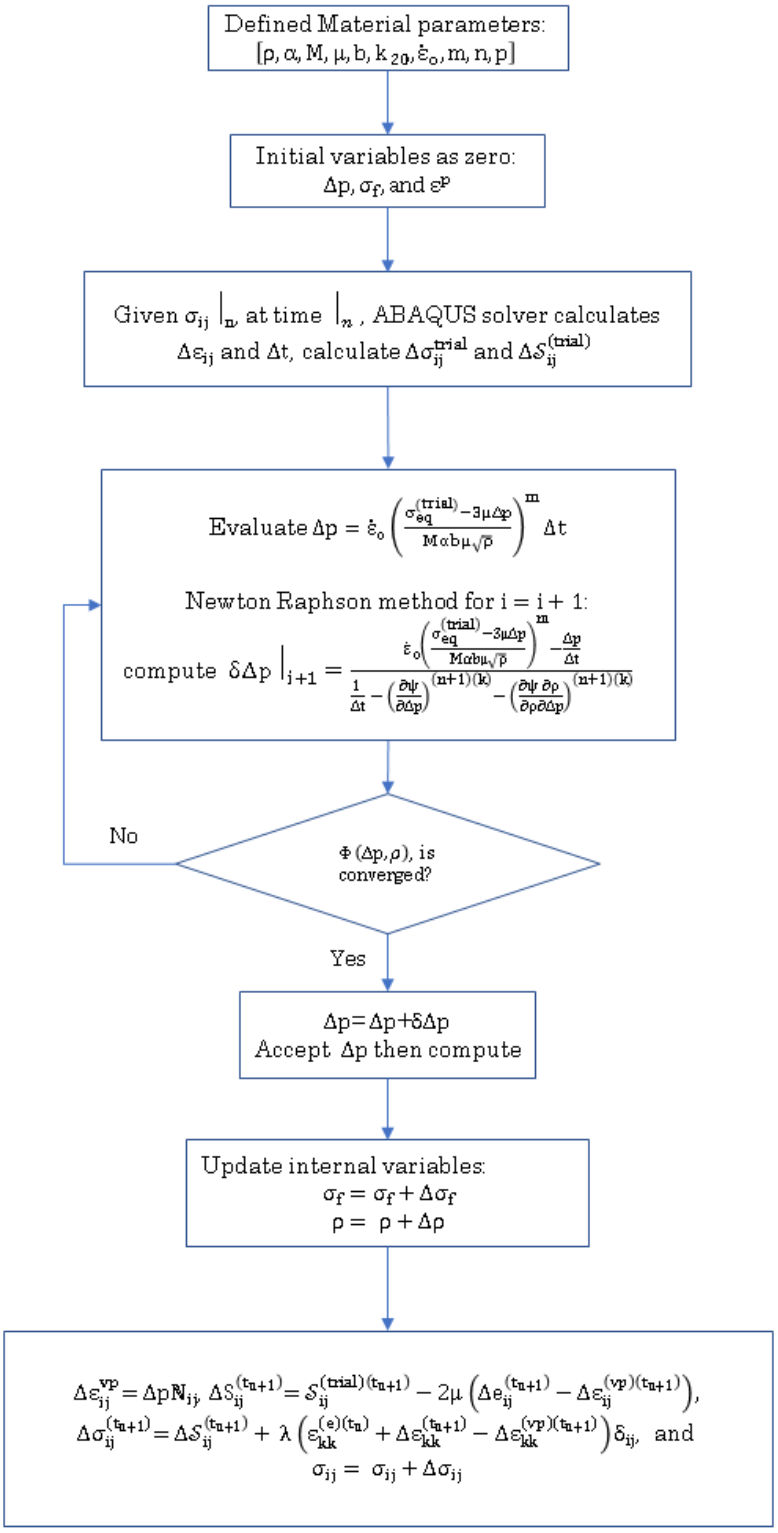


Figure 4-1. Flowchart of the implementation of the UMAT for the KME model.

4.4 Material and Crystal map of the P91 steel

In order to provide data for validation of the model described in Section 3.3, experimental tensile and uniaxial creep tests were conducted on the P91 steel at 600ºC. The material chemical composition of the P91 steel used in the current work is given in Table 3-1. The material parameters which are used in this determination shown in Table 4-1.

Table 4-1. Notation and material parameters used in numerical calculations for Cu and P91 steel.

Material properties	**Name**	**Cu [69]**	**P91 steel [64]**	**Units**
ρ_i	Initial Dislocation Density	3×10^{13}	1.37×10^{13}	m^{-2}
E	Elastic modulus	100	150	GPa
v	Poisson's ratio	0.33	0.3	unitless
b	Magnitude of Burgers vector	2.56×10^{-10}	2.56×10^{-10}	m
m	Exponent of Stress Sensitivity	232	55.9	unitless
$\dot{\varepsilon}_o$	Reference strain rate	1.0	1.0	s^{-1}
k_{20}	Dynamic recovery	30	55	unitless
q	Stress exponent coefficient	23	14.9	unitless
α	Constant	$0.2 - 0.5$	$0.8 - 1$	unitless
M	Taylor factor	$\sqrt{3} - 3.06$	$\sqrt{3} - 3.06$	unitless

4.5 Application of the UMAT to Finite Element Model

In the previous section, the principle of the user material subroutine UMAT is introduced, along with the implementation of the constitutive dislocation model via the UMAT developed the prototype Kocks-Mecking-Estrin constitutive model for constant strain rate is implemented into the finite element code ABAQUS in the form of a UMAT. The conventional uniaxial tensile and creep specimens were

manufactured from a P91 pipe. The gauge length of the specimen is 50mm and the diameter of the gauge length is 10mm.

4.5.1 Structural Finite Element

The suggested UMAT coding within ABAQUS standard is utilised to undertake FE modelling of the uniaxial tensile and creep tests to clarify the capability of the dislocation-based material model. Two examples of FE structural analysis are used to simulate the uniaxial behaviour, under tension and creep respectively of the P91 steel at 600ºC. The mesh and boundary conditions used are shown in Figure 4-2. The mesh consists of 673 axisymmetric quadrilateral elements. Only a quarter section was modelled due to symmetry. By using the geometrically non-linear (GNL) approach the uniaxial tensile specimen, the FE model can take into account the significant deformations and changes of section which occur for large engineering strains. The tensile model was subjected to a displacement-controlled condition with constant strain rate, while the creep model was run pressure controlled conditions for five levels of stress, i.e., 140, 150, 160, 170 and 180MPa at the top of specimen in the positive Y direction. Two boundary conditions were applied on X and Y directions of the specimen: complete displacement constraint in the X-direction for all nodes located on the Y-axis; and complete displacement constraint in the Y-direction for all nodes located on the X-axis.

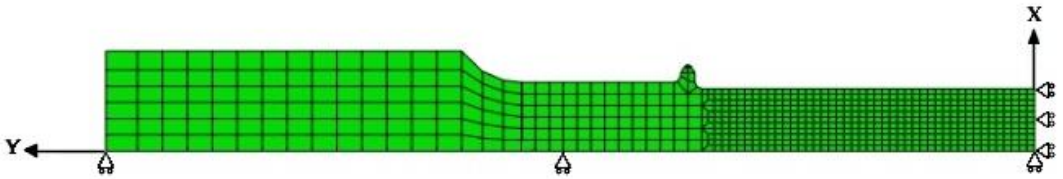


Figure 4-2. FE mesh and boundary conditions of the uniaxial tensile and creep specimen.

4.6 Model Implementation Abilities and Discussion

4.6.1 Uniaxial Tensile Behaviour

In order to investigate the influence of strain rate and temperature on the flow stress behaviour, contour shapes and two-dimensional plots of the state variable data are robust features to present and visualise the results. The radial return mapping algorithm presented above has been implemented in the finite element model. The predict stress-strain relationships of tensile behaviour were presented for Cu and the P91 steel at various strain rates and at different temperatures.

Figure 4-3 gives a comparison of various anticipated results of FE analysis stress-strain curves with the corresponding published experimental data [149] at room temperature with different strain rates for Cu, ranging from $10^{-4}\ s^{-1}$ to $10^{-2}\ s^{-1}$. It can be found out that a change in the strain has a directly proportional effect on the stress-strain relations. Therefore, according to the results obtained, the stress will increase instantly with increasing strain rate and vice versa.

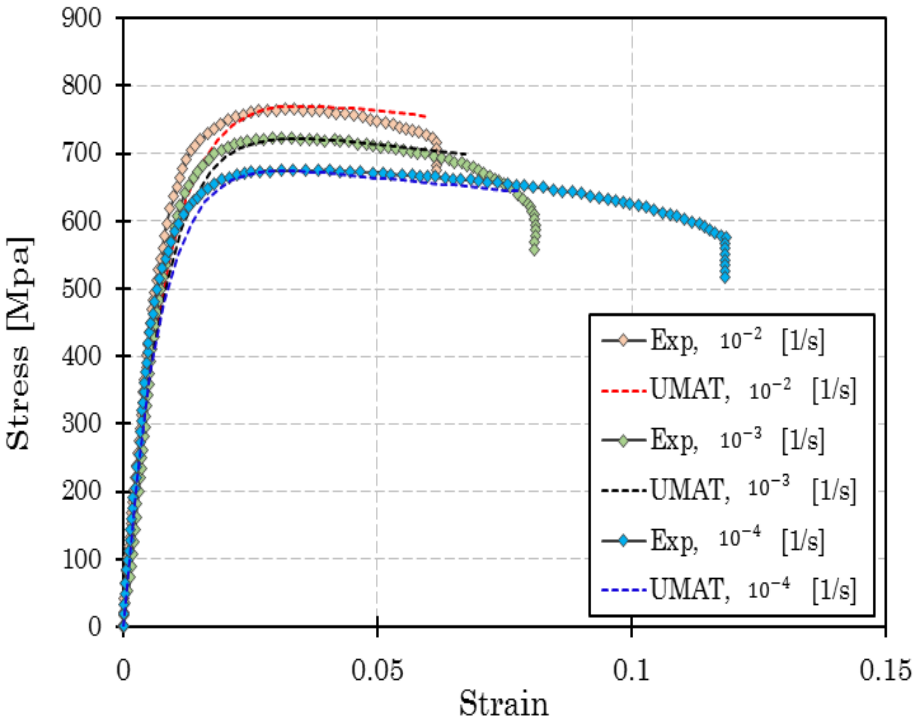


Figure 4-3. The comparison results between the simulated true stress-strain curves and the corresponding published data of Cu at RT with different strain rate [149].

The influence of temperature on the flow stress has been also examined at the elevated temperature with a constant strain rate. The comparison of thermo-mechanical FE and experimental results of the P91 steel at 600℃ and at a strain rate of $0.0005s^{-1}$ is presented. The contour plot shown in Figure 4-4 exhibits an axisymmetric effective plastic distribution, while Figure 4-5 shows a contour plot of the flow stress at failure for a strain rate of $0.0005s^{-1}$.

The total of dislocation density can be determined by assuming an initial of dislocation density of $\rho = 1.73 \times 10^{13}\ m^{-2}$. Figure 4-6 shows the contour plot of the total dislocation density. The evolution of dislocation density is obviously determined by the relative plastic strain at applied deformation conditions (constant strain rate and elevated temperature). It can be clearly seen that the value of saturated (total) dislocation density is to $1.38 \times 10^{14} m^{-2}$ at the centre of the specimen.

Figure 4-7 shows the simulated stress/strain curves obtained from the uniaxial tensile FE model, and an experimental tensile test carried out on P91 steel at 600℃. The FE data showed the same ultimate tensile strength as the experimental results. The experimental data are seen to fit well with the FE simulated curves, as shown in Figure 4-7. The change of dislocation structure, (a combination of the effect of strain and temperature), represents the microscopic behaviour of the material. These three factors could be separated by making a change of strain rate or temperature in the uniaxial tensile test.

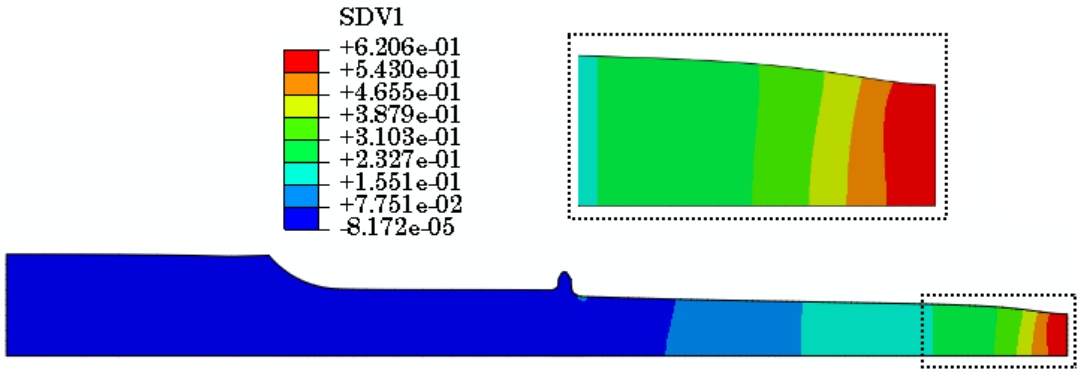


Figure 4-4. Contour plot of the effective plastic strain at failure for the P91 steel at 600ºC.

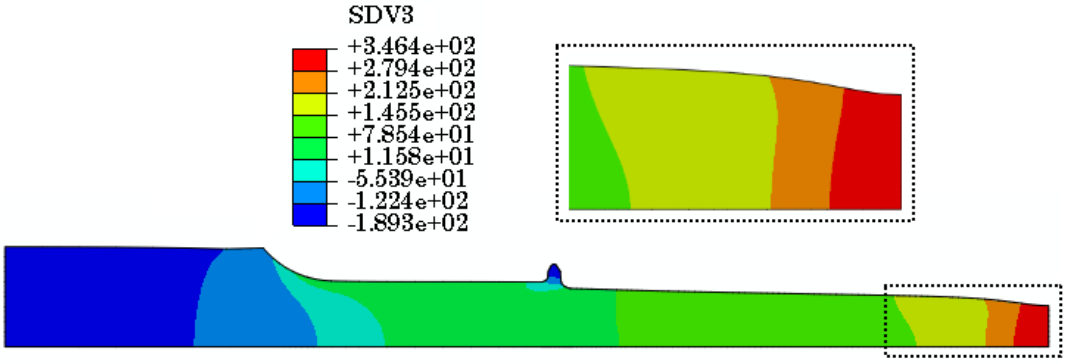


Figure 4-5. Contour plot of the flow stress at failure for the P91 steel at 600ºC.

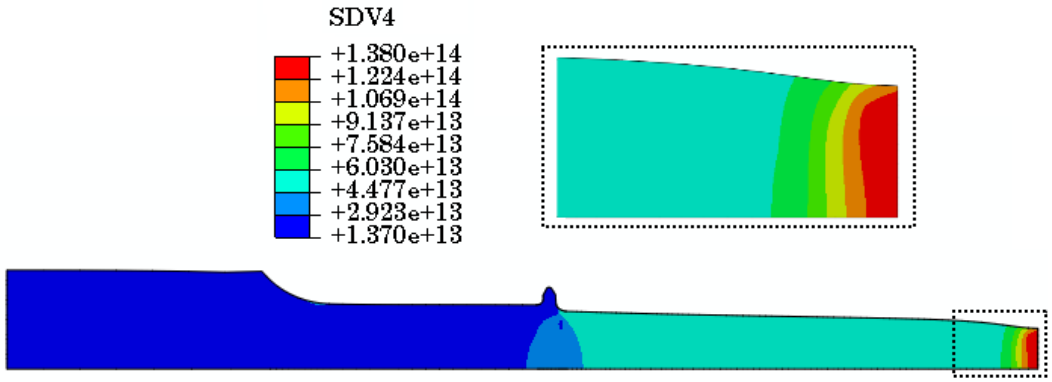


Figure 4-6. Contour plot of the total dislocation density at failure for the P91 steel at 600°C.

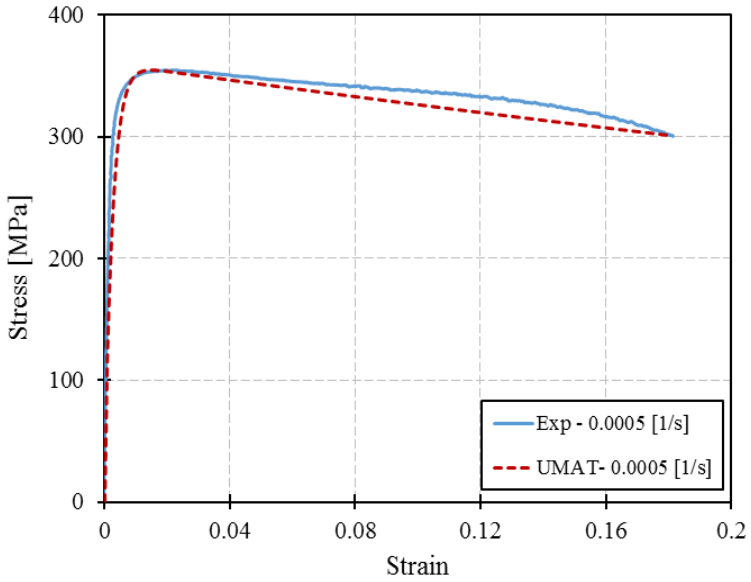


Figure 4-7. Experimental and numerical stress-strain curves for the P91 steel at 600°C.

Figures 4-8 shows the simulation dislocation density/strain curves for the P91 at the strain rate $10^{-4}s^{-1}$ and an isothermal temperature of 600°C. It can be seen that the total of dislocation density value of $\rho = 1.4 \times 10^{14}\ m^{-2}$.

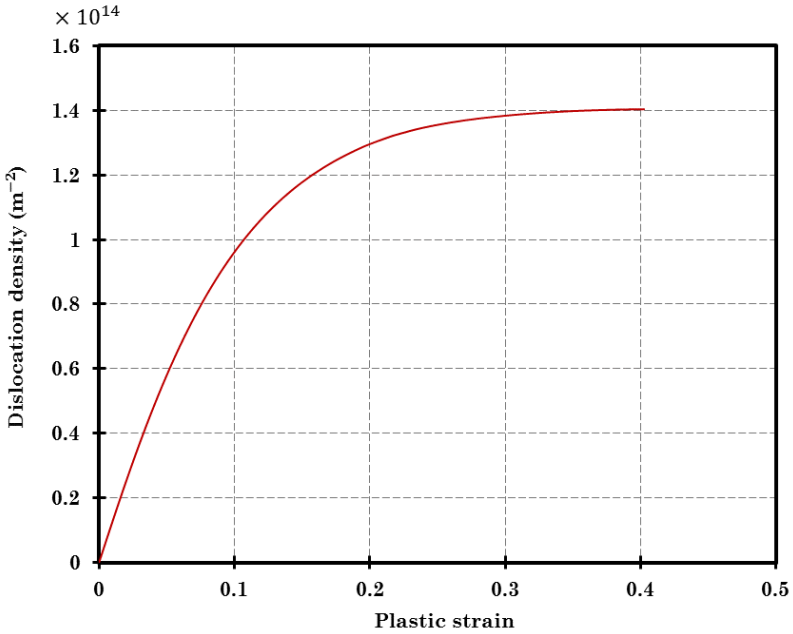


Figure 4-8. Total of dislocation density along with effective plastic strain for the P91 steel at 600℃.

4.6.2 Uniaxial Creep Behaviour

The strain-time curves for uniaxial creep test of 180, 170, 160MPa at 600ºC are shown in Figure 4-9 and of 150 and 140MPa at 600ºC are shown in Figure 4-10. The experimental creep results at 600ºC were used to compare with the corresponding FE results. The results obtained show excellent agreement with data is achieved of the constant stress of 140, 150, 160, 170, and 180MPa. The FE results for the 180MPa test predict much shorter time to failure. The unified mechanical model produces typical primary, secondary, and tertiary creep responses for all stress levels. The primary creep strain increases with stress. The minimum creep strain rate observed in the secondary creep regime increases as the stress increases. The amount and rate of tertiary creep strain increase with

stress. The current microstructural model approximates the hardening, softening, and steady-state behaviour undoubtedly well when compared to the capability of phenomenological constitutive models.

The evolution of dislocation density with respect to time for uniaxial creep test of 160, 170, and 180MPa at 600ºC is shown in Figure 4-11 and 140, 150MPa at 600ºC is shown in Figure 4-12. A systematic increase in the values of dislocation density with increasing applied loads has been observed for the P91 steel.

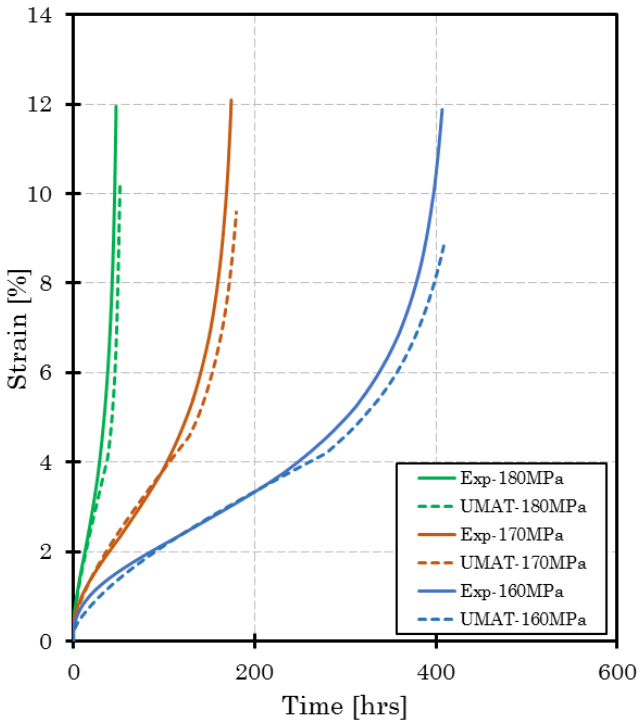


Figure 4-9. Experimental and calculated uniaxial creep curves for stresses at 160, 170 and 180MPa.

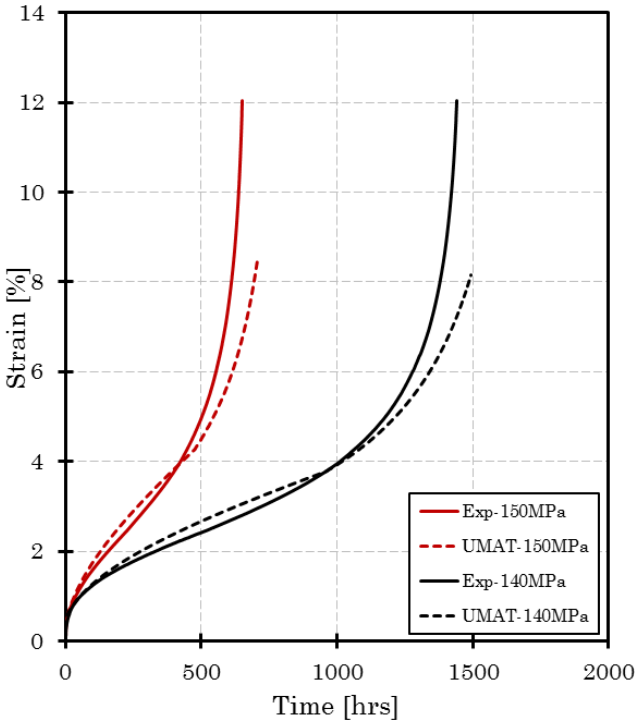


Figure 4-10. Experimental and calculated uniaxial creep curves for stresses at 140 and 150MPa.

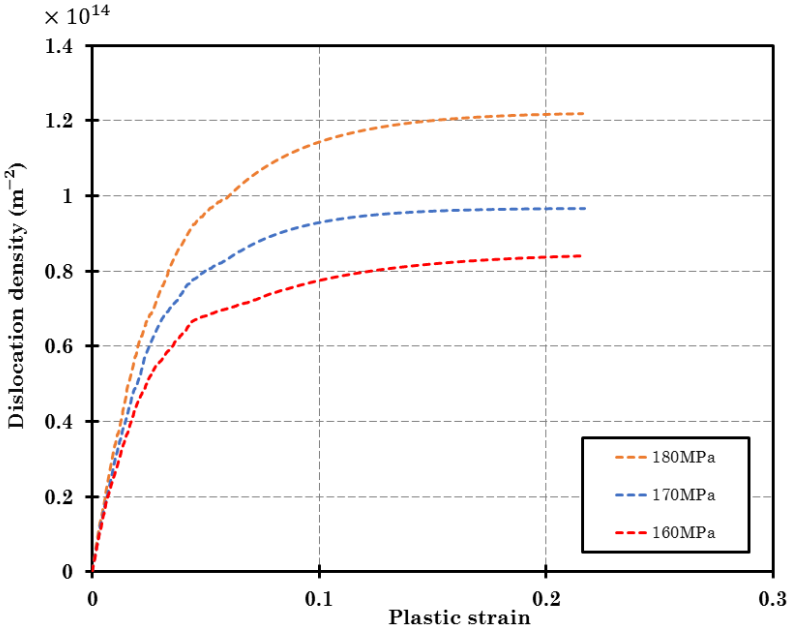


Figure 4-11. Influence of applied stress on dislocation density for constant stress tests at 160, 170 and 180MPa.

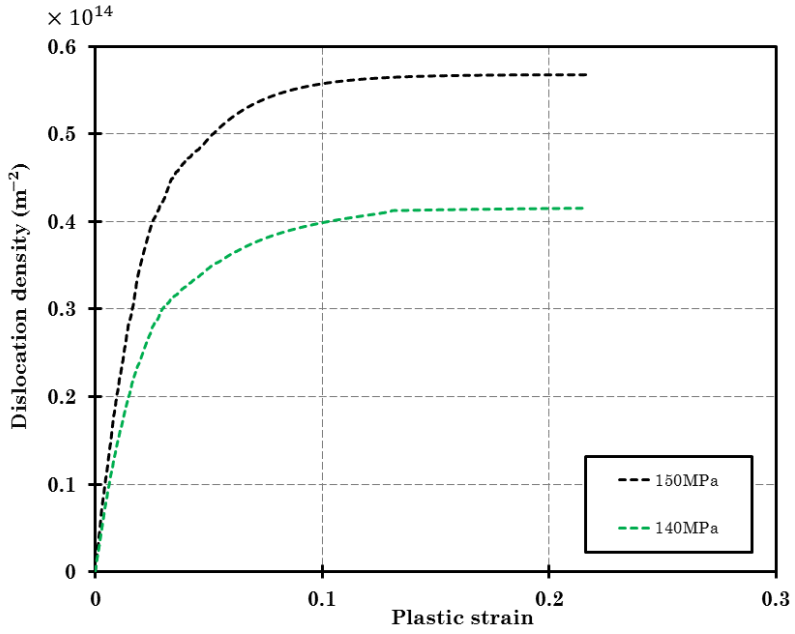


Figure 4-12. Influence of applied stress on dislocation density for constant stress tests at 140 and 150MPa.

Although the FE simulation results for dislocation density evolution at high temperature appear satisfactory, it is essential to validate them against experimental observations of dislocation density.

Figure 4-13 shows the minimum creep strain rate data for the P91 steel at 600℃ for the constant stress tests at 140, 150, 160, 170 and 180 MPa. Figure 4-14 shows the variation of the minimum strain rate $\dot{\varepsilon}_{min}$ versus the applied stress σ using logarithmic scales. A power law correlation between $\dot{\varepsilon}_{min}$ and σ was found and is represented by Equation (4-32), where $\dot{\varepsilon}_{min}$ is expressed in $\frac{1}{\text{hrs}}$ and σ in MPa.

$$\dot{\varepsilon}_{min} = 4.731 \times 10^{-33}\sigma^{13.831}. \quad (4\text{-}39)$$

Figure 4-15 shows the variation of the failure time t_f versus the applied stress σ. A power law correlation between t_f and σ was found and is represented by Equation (4-33), where t_f is expressed in hrs and σ in MPa.

$$t_f = 2.69 \times 10^{30} \sigma^{12.667}. \quad (4\text{-}40)$$

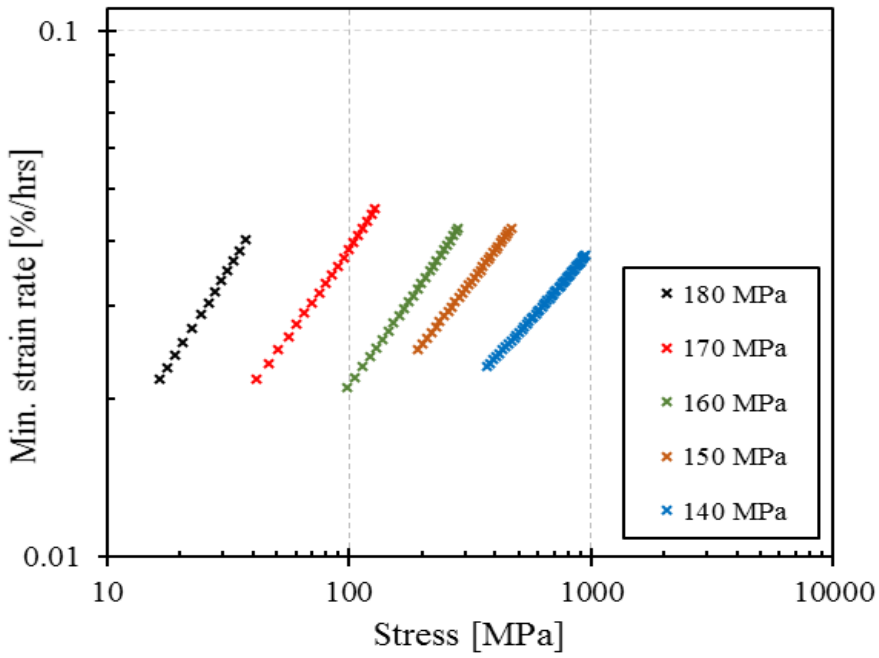


Figure 4-13. Variation of minimum strain rate versus applied stress.

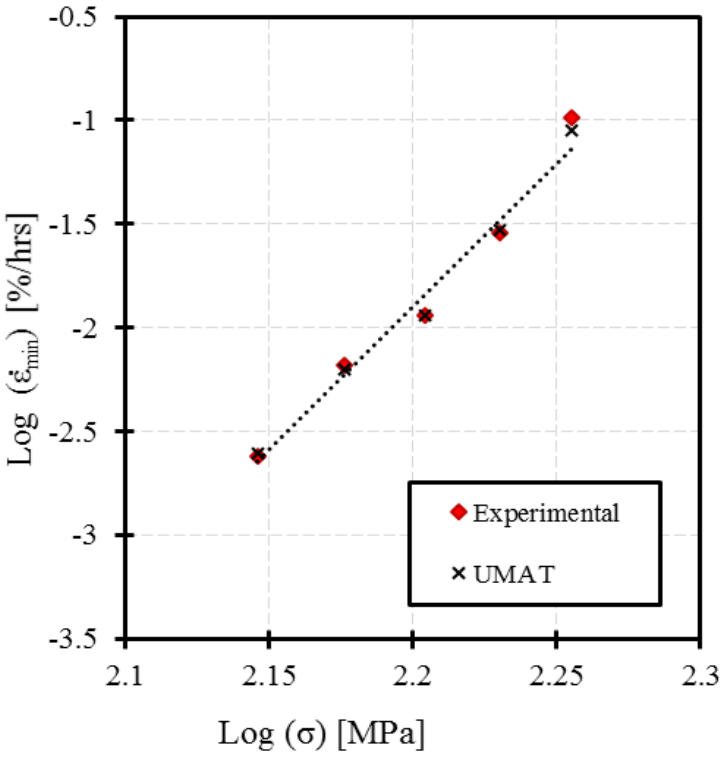


Figure 4-14. Variation of strain rate versus applied stress.

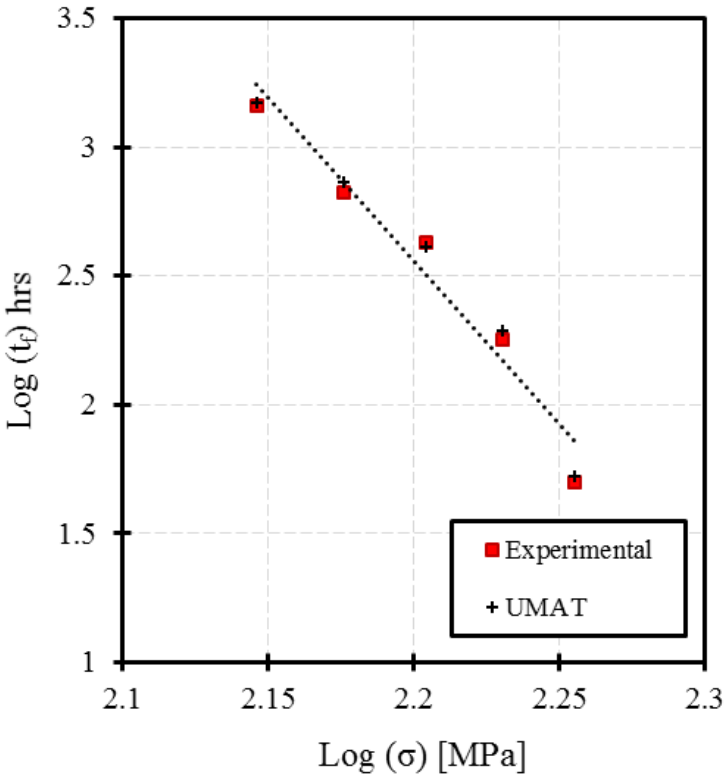


Figure 4-15. Variation of time to failure versus applied stress.

4.7 Concluding Remarks

In this chapter, a new numerically implicit, three-dimensional formulation of the KME model has been proposed. It has been implemented on the basis of the radial return mapping algorithm as an ABAQUS User Material. The FE results are compared to the tensile tests for a range of strain rates from $10^{-2}\,s^{-1}$ to $10^{-4}\,s^{-1}$ at room temperature for Cu and strain rate of $10^{-4}\,s^{-1}$ at 600°C for P91 steel. Good predictive ability is observed between experiments and simulations. It is evident that the pile-up of dislocations in the region close to a grain boundary is strongly related to strain hardening. The dislocation density increases gradually over time, eventually tending to a steady-state value. Therefore, the flow stress in the crystallite relies on the dislocation density evolution which is related to the strain rate and temperature. The model capability for structural analysis has been presented through numerical examples of monotonic loading. FE implementation of the present visco-plasticity framework results in a good tool to predict creep behaviour using microstructural features at elevated temperature. Within this approach, prediction of time to fracture is also of critical importance. The material model has been developed to capture of creep behaviour under constant stress through the evolution of dislocation density. These microstructural parameters can be used to predict failure.

CHAPTER 5:
HIGH TEMPERATURE DEFORMATION AND FRACTURE PROCESS DURING SPT TESTS

5.1 Introduction

In the last ten years, testing techniques using miniature samples have received ever-increasing attention from the electricity generation industry for situations where the amount of material used in the test is limited [70, 71]. Structural components such as those found in thermal power plants that operate under increased steam temperature and pressure conditions usually undergo creep and plasticity damage induced by volumetric inclusions such as voids and cracks.

One of the main strengthening mechanisms comes from Dislocation via (i) dislocation-dislocation interactions in which immobile dislocations were an obstacle to the mobile dislocations, (ii) strain hardening resulting from the rate of dislocation evolution/annihilation, (iii) the pile-ups of mobile dislocation at the grain boundary [150]. Precipitation hardening is final strengthening mechanisms in the P91 steel. The precipitates consist of carbides of mainly $Cr_{23}C_6$ type which is located at the prior austenite grain and packet boundaries, and MX type (M=V or Nb and X=N or C) which is found in the martensite laths interiors and martensite lath boundaries. The typical dimensions of the $Cr_{23}C_6$ carbides and the

MX solutes are approximately up to 100nm and 20nm respectively (miss ref.). The $Cr_{23}C_6$ particles can enhance the creep properties of the tempered P91 due to fixing mobile dislocation and sub-grain boundaries [151]. The small martensitic microstructure of P91 steel is stable and has a good creep and corrosion strength at a temperature up to 600°C. However, P91 components may encounter problems of degradation of properties results from the evolution of microstructure at the elevated temperature and the over-heating at a long service exposure time [151].

One of the critical reasons for a loss of strength for P91 steel under tensile conditions is work softening, which typically occurs in materials with a high initial dislocation density. Metallurgical changes of the initial martensitic lath microstructure produce a significant effect under tensile conditions. The process of lath martensitic recovery is produced by the growing size of the $Cr_{23}C_6$ and the MX type carbides. Coarsening of carbides and precipitation may mainly occur around grain boundary and in martensitic laths interiors respectively [152, 153]. Due to the complicated nature of the evolution of microstructural P91 steel [154, 155], this chapter describes the results of physical characterisation of the high-temperature deformation and fracture process of the P91 steel via SPTT at 600ºC. Disc specimens, 8 mm in diameter and 0.5 mm in thickness, were tested in a small punch test rig at 600°C using a constant displacement rate of 2 μm/s. Interrupted small punch tensile tests were performed to investigate the microstructural evolution in different deformation regimes. Another objective is to gain an insight into the relationship that may exist between the physical model behaviour and the underlying microscopic mechanisms (bulk deformation behaviour, microstructural evolution and grain structure change). A physical

characterisation of the deformed specimens was conducted via scanning electron microscopy and electron backscatter diffraction. The chapter is structured as follows: Section 2 describes the test material and experimental procedure where the small punch rig and SPTT are also described. The load-displacement and bulk deformation behaviour are presented in Section 3. Section 4 is devoted to the physical characterisation of plastic deformation process, including microstructural evolution, void progression and grain structure. The deformation regimes, the energy of plasticity and fracture mechanisms are discussed in Section 5. Finally, conclusions are given in Section 6.

5.2 Material and Experimental Procedure

5.2.1 The P91 Steel

In as-received states, the microstructure of the P91 steel is typically characterised to consist of a multi-scale architecture shown schematically in Figure 5-1. The average grain size of the austenite structure varies between 10 and 60 μm relying upon normalising heat treatment at the temperature range of 1030-1080°C [156]. The P91 material is then cooled rapidly to produce a distribution of chromium carbide, and an extremely high dislocation density [157]. Each prior austenitic grain consists of a few packets which result from the martensitic transformation due to a tempering heat treatment in the temperature range of 730-780°C for 1-2 hour. These packets include several blocks which have a typical dimension about 4 μm [158]. Such blocks are divided into martensitic laths that also arise from the martensitic transformation. The average width of martensitic laths is 0.535 μm [154]. The complex matrix structure, described above, results in the main

strengthening mechanism of the P91 material [150]. The further strength mechanism for the matrix microstructure is produced by high initial dislocation density and various precipitates.

As one of the key 9-12% Cr ferritic steels, P91 steel has high creep strength with good weldability and fracture toughness and has been extensively used all over the world for headers and steam pipes in ultra-supercritical plants [159]. In the present work, the P91 steel has been used to carry out the SPTT at 600°C. The chemical compositions, in wt. %, of the as-received P91 steel tabulated in Table 3-1, are also provided in [160, 161]. The as-received P91 steel was machined into a cylinder shape with diameter 8 mm and was then sliced into disc SPTT specimens with a thickness slightly larger than 0.5 mm using wire electro-discharge machining. The specimens were then ground down to a final thickness of 0.5 mm using 1200-grade silicon carbide papers.

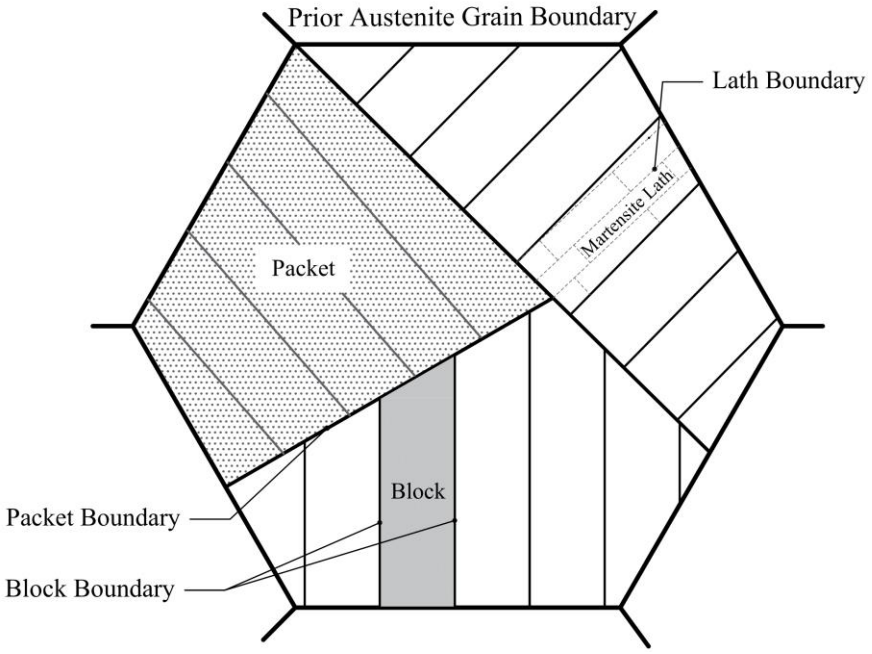


Figure 5-1. Scheme of the microstructural of the P91 steel.

5.2.2 The Small Punch Tensile Testing

A Tinius Olsen H5KS single column material testing machine was used to perform the SPTTs, see Figure 5-2. A 1.0 KN load cell, which has a loading accuracy of ± 0.5% of the applied load, is installed to measure the load transmitted to the specimen through a hemispherical punch head. The displacement of the punch was recorded as the average reading of two linear variable differential transformers, which have an accuracy of ± 0.01 mm, a resolution of 1 μm and a speed resolution of 1 μm/min. A constant displacement rate of 2 μm/s was applied to the punch and a backoff speed of 4 mm/s was applied when the specimen has failed or when the displacement of the punch has reached the setting values (for interrupted tests). The loading assembly of the small punch test rig is shown in Figure 5-3. The radius of the punch (2) is 1.04 mm, the receiving hole diameter of the die (7) and the holder (3) is 4 mm. The specimen (1) is clamped tightly by the

screw nut (4) and the holder (3) onto the die. The holder, which cannot rotate due to the locating pins (5), rests on top of the specimen and prevents the specimen from sliding. The rig, together with the specimen, is held at a constant temperature of 600 ± 1 °C by a furnace. A thermocouple (6) is positioned close to the top surface of the specimen to control and monitor the testing temperature.



Figure 5-2. The small punch testing machine with the furnace.

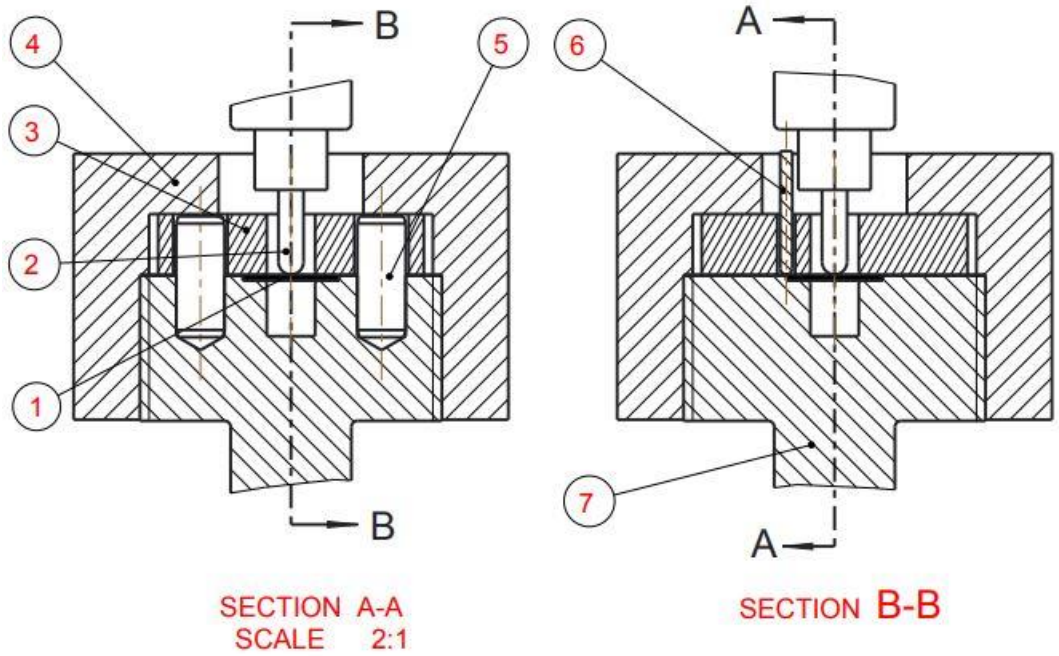


Figure 5-3. Detailed drawing of the rig, the part numbers are as follows:
1. Specimen, 2. Hemispherical punch, 3. Upper holder,
4. Screwing nut, 5. Locating pin, 6. Thermocouple, and 7. Die.

5.2.3 Microstructural Characterisation

The microstructures of the tested specimens were examined in a Zeiss field emission gun scanning electron microscope (SEM) operated at 20 kV. The morphology of the deformed P91 specimens was characterised using secondary electron (SE) imaging. Cross-sections of the deformed specimens were mounted in a conductive resin, successively ground and polished to 1 μm surface finish and were investigated using backscattered electron (BSE) imaging. The semi-quantitative energy dispersive X-ray spectroscopy (EDS) was utilised for phase identification. To elucidate the evolution of grain morphology during the SPTTs, SEM-based electron backscattered diffraction (EBSD) was employed in a FEI Quanta 250 SEM equipped with an EBSD detector (Oxford Nordlys Max2).

Samples for EBSD underwent a further polishing stage using colloidal silica suspension to achieve minimum surface deformation. The EBSD system was operated at an accelerating voltage of 20 kV with a specimen tilt angle of 70°. EBSD mappings were conducted in areas of 30 μm × 20 μm at a step size of 0.15 μm.

5.3 Mechanical Behaviour

5.3.1 Load-Displacement Curves and Macroscopic Interrupted Patterns

A schematic diagram of the applied force, F, and displacement, u, of SPTT for a ductile material is shown in Figure 5-4. According to Abendroth and Dymacek [162, 163], the F-u curve can be separated into six stages. Stage I represents the elastic deformation of the specimen. Stage II represents the transition between elastic and plastic deformation. The primary plastic deformation mechanism of material is based on the work-hardening property which is produced by the competition between variation and softening of structural parameters. The first conception, the evolution of microstructural parameters, could be occurring during stage III, while the second conception may be assumed to follow the first conception which is associated with stage IV. The damage variation also happens during this stage which leads to reducing in the thickness around the centre of the specimen. The crack initiation may begin during stage V, then crack degradation continues with the marginal decrease in F-u curve which is due to failure at stage VI [163].

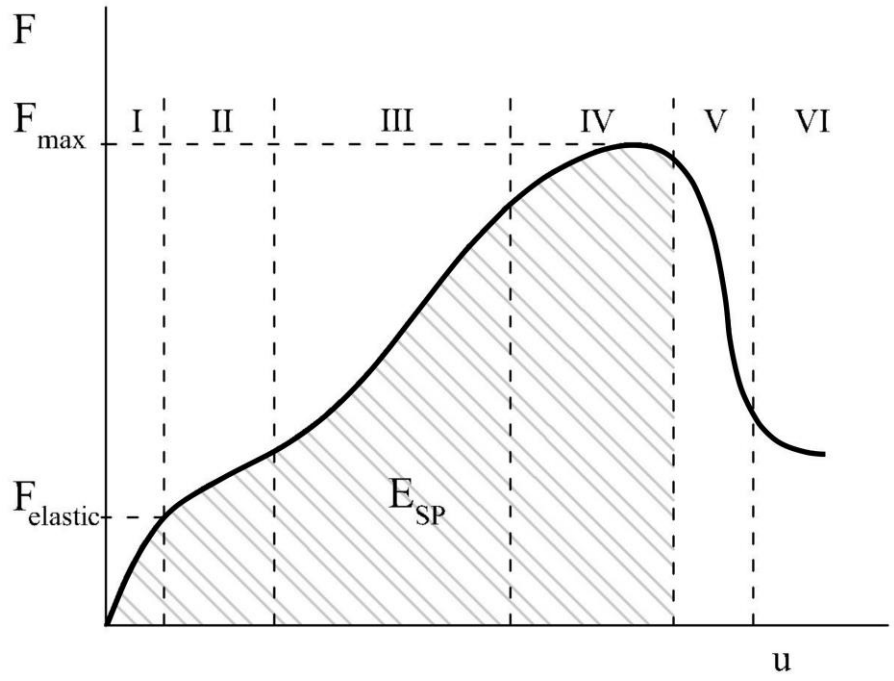


Figure 5-4. Schematic diagram of the SPTT load-displacement curve.

Thus, to investigate the physical nature of the deformation process and the fracture behaviour of the P91 steel at 600 °C, a series of interrupted SPTTs have been carried out. Firstly, two specimens are used to perform the repeated SPTTs for the whole stroke until fracture. The whole load-displacement curves obtained are shown in Figure 5-5. The maximum force, F_{max}, achieved is 634 N; this force is assumed to be related to the ultimate tensile stress σ_{ULT} at 600 °C. Another important parameter is the punch displacement at the maximum load, $u_{F_{max}}$, which is believed be related to the ductility of the P91 steel at 600°C. It is seen that the experimentally obtained whole load-displacement curves in Figure 5-5 are similar to the curve in Figure 5-4.

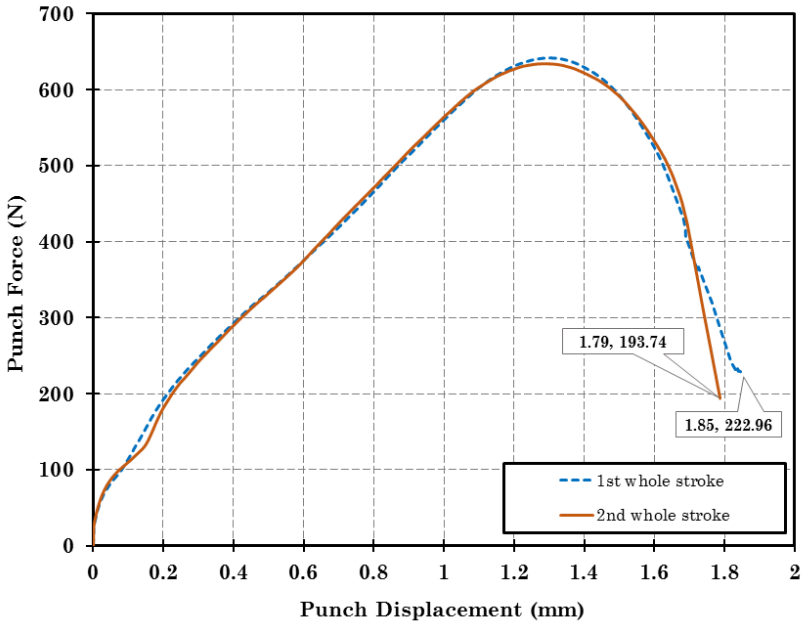


Figure 5-5. The punch load-displacement curves of the whole stroke till material failure.

To investigate the deformation mechanisms of P91 in SPTT, the key interrupted displacements of the punch were determined based on the schematic load-displacement diagram as shown in Figure 5-4. The main objective of interrupted SPTTs is to provide "In Situ" investigations into the evolution of microstructures and deformation mechanisms at each stage of the SPTT until fracture. Seven interrupted SPTTs were conducted on the P91 steel at 600 °C in Figures 5-6 to 5-12. The interrupted displacements are set as 0.26, 0.60, 1.00, 1.25, 1.50, 1.65 and 1.74 mm respectively to represent the six deformation regimes in Figure 5-4. 0.26 mm indicates the transition region from elastic deformation to plastic deformation. 0.6 mm was taken to represent the plastic deformation region. 1 mm shows the deformation region where the microstructural variations start to occur. 1.25 mm was selected to approximate the displacement at maximum load. 1.5 mm

was chosen as a displacement just after the maximum load to observe the development of damage. 1.65 mm which correlates with stage V in Figure 5-4 is used to study the mechanisms of void nucleation and crack initiation. Finally, 1.74 mm is assumed to be the displacement very close to fracture to investigate the fracture mechanism of P91 during SPTT. The microscopic iterrupted and fracture patterns obserevd for the P91 at 600℃ are shown in Figure 5-13.

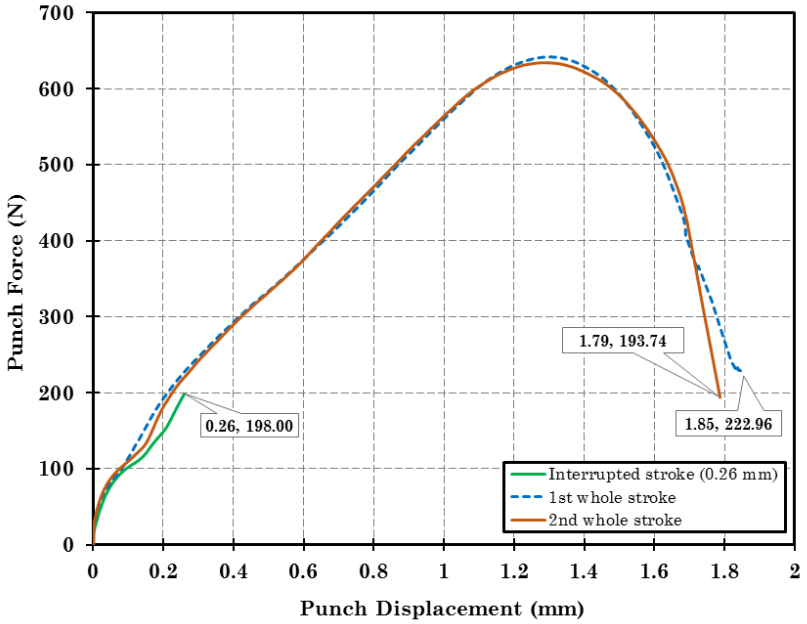


Figure 5-6. Interrupted stroke at 0.26 mm and whole stroke.

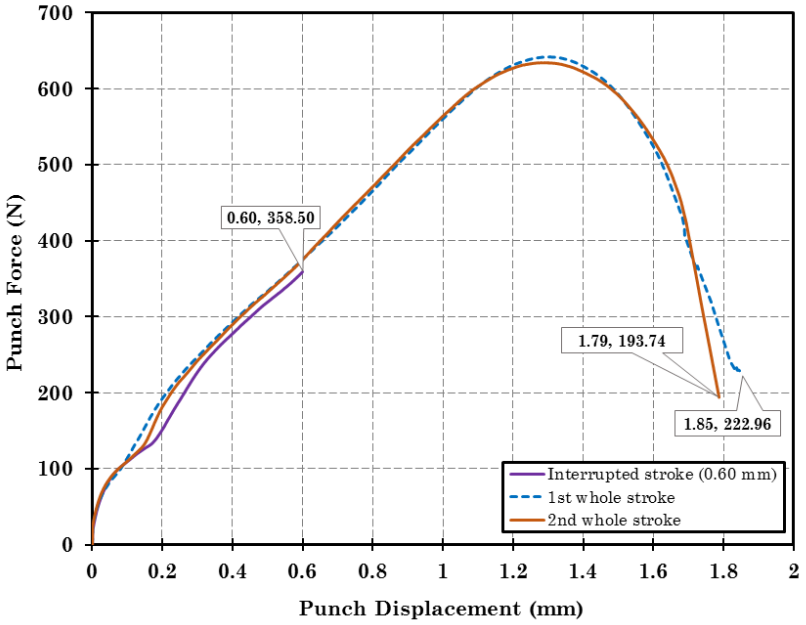


Figure 5-7. Interrupted stroke at 0.6 mm and whole stroke.

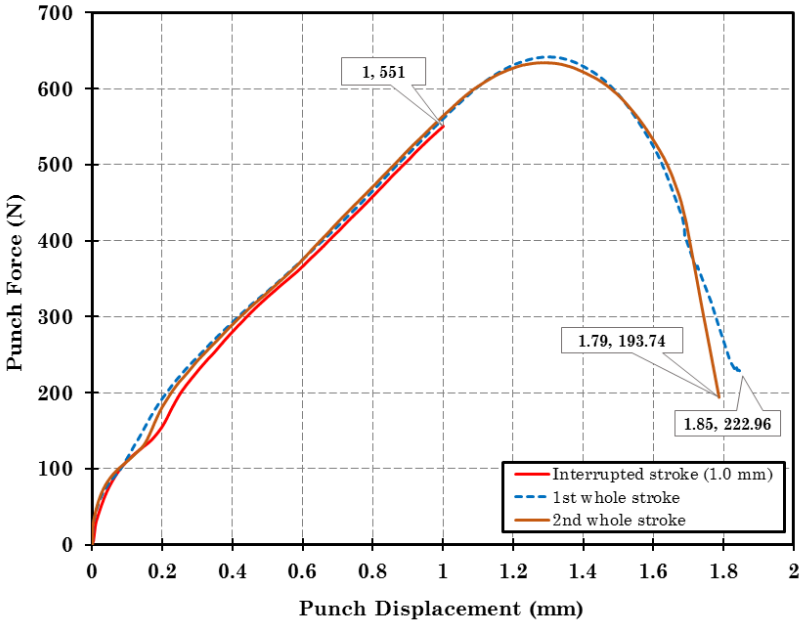


Figure 5-8. Interrupted stroke at 1.0 mm and whole stroke.

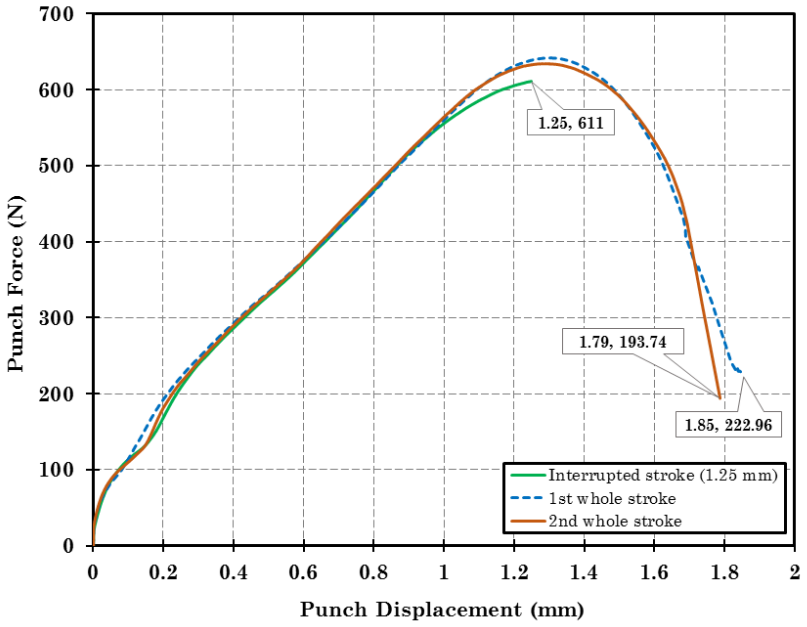


Figure 5-9. Interrupted stroke at 1.25 mm and whole stroke.

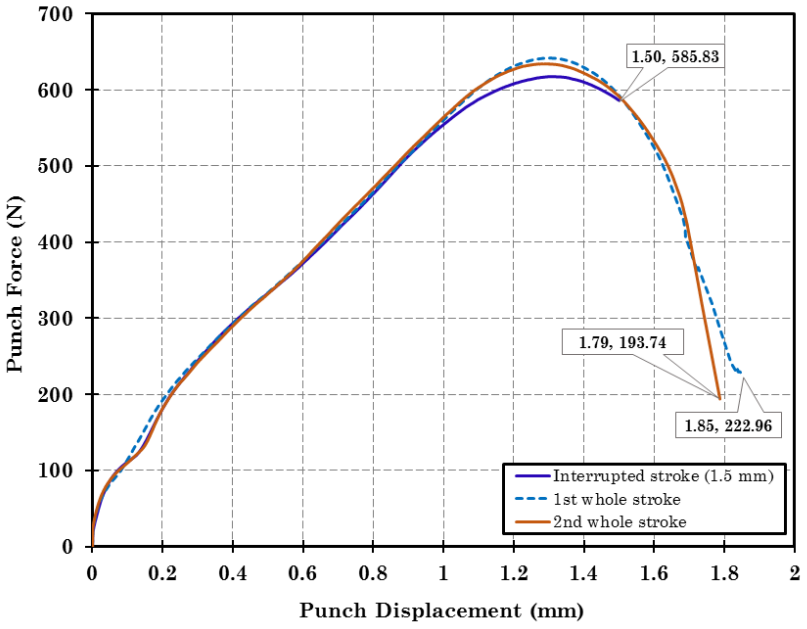


Figure 5-10. Interrupted stroke at 1.50 mm and whole stroke.

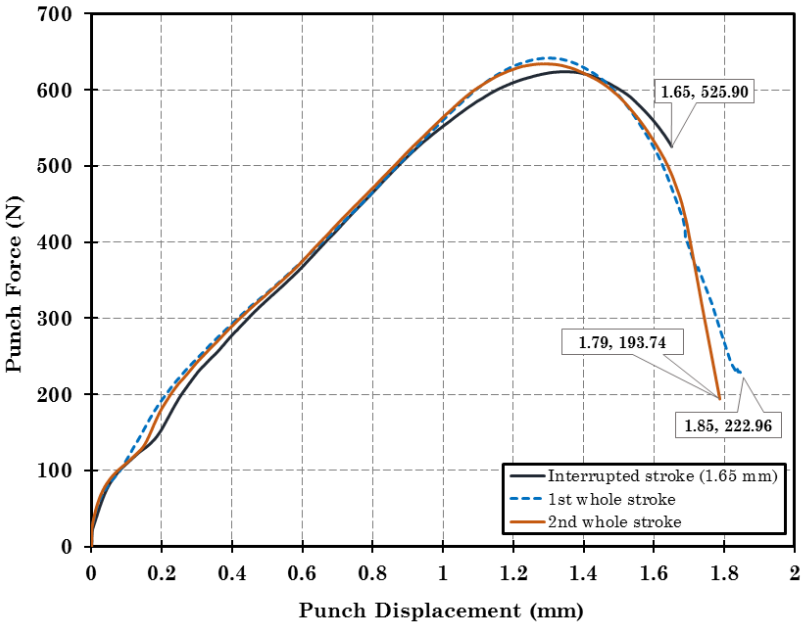


Figure 5-11. Interrupted stroke at 1.65 mm and whole stroke.

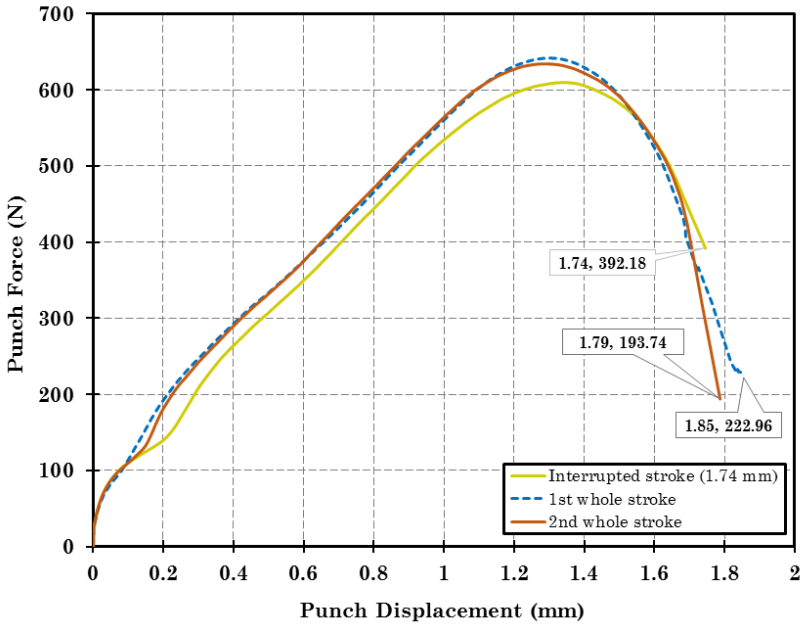


Figure 5-12. Interrupted stroke at 1.74 mm and whole stroke.

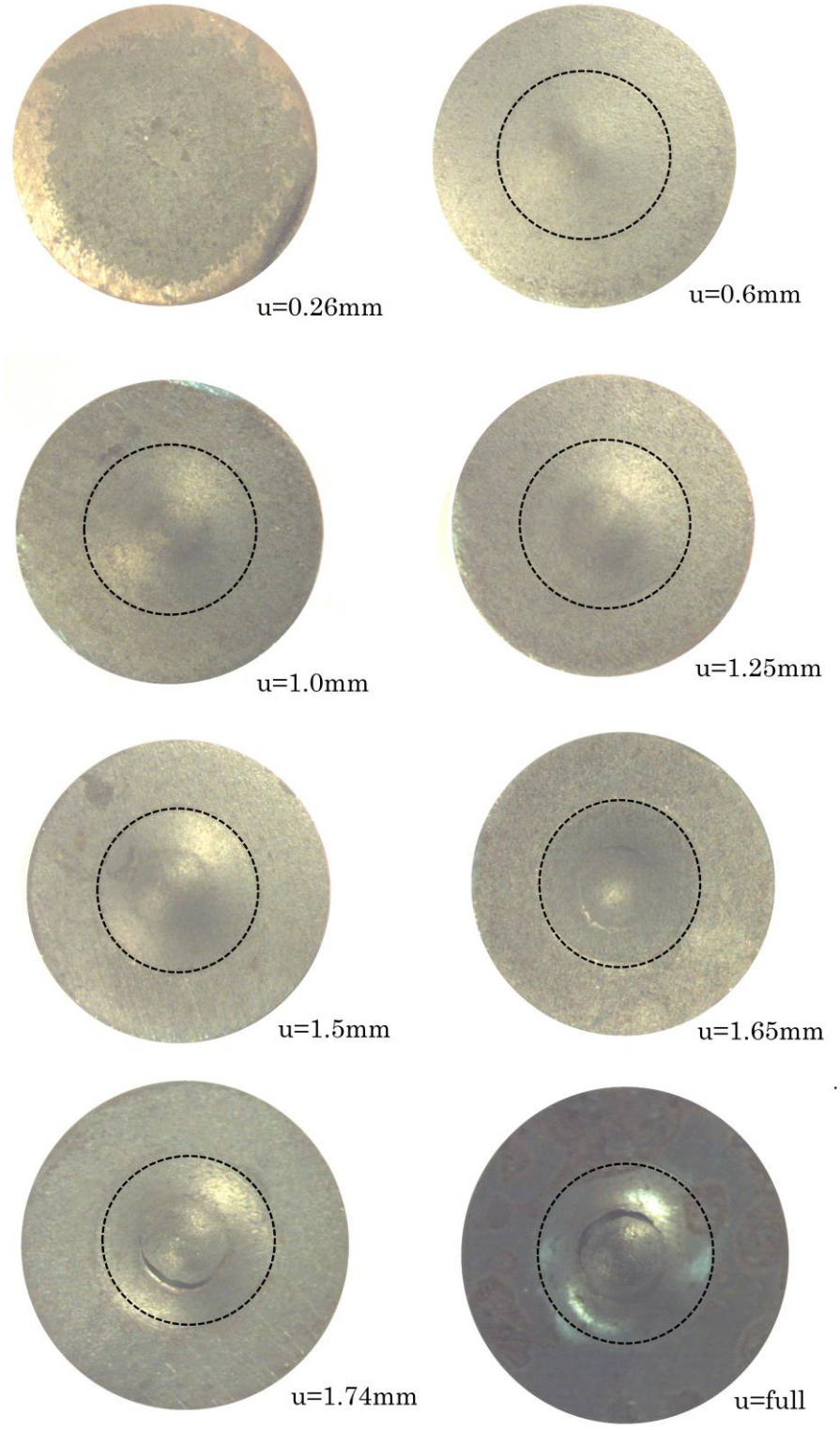


Figure 5-13. Tensile surfaces of The P91 steel following interrupted and fracture SPTT testing at 600℃.

5.3.2 Bulk Deformation Behaviour

The morphologies of the dome-shaped deformed P91 specimens are depicted in Figures 5-14 to 5-20 for displacements at 0.26 mm, 0.6 mm, 1 mm, 1.25 mm, 1.5mm, 1.65mm and 1.74mm respectively. At small displacement, 0.26 mm, the dome shape starts to form when the specimen is plastically deformed as shown in Figure 5-14a. It is noted from Figure 5-4 that 0.26 mm is in the transition region between elastic and plastic deformation. Thus, plastic deformation of the P91 specimen may have already occurred. As shown in Figure 5-14b some cracks are formed at the top of the dome shape. These cracks are likely to have resulted from the cracking of the brittle oxide layer on the specimen surface at 600 °C. The shape of the dome becomes more evident when the displacement increases to 0.6 mm, as shown in Figure 5-15a. Similar features can be seen on the deformed surface, where the size of the dome increases and more cracks are developed due to the increased plastic deformation in Figure 5-15b. It is noticed that the cracks in the oxide layer have propagated radially from the centre of the specimen. This is also the case for the punch displacements at 1 mm and 1.25 mm in Figures 5-16a and 5-17a. The radiation of the cracks in the oxide layer indicates that the specimen is probably subjected to a tension force which leads to the stretching of the P91 specimen. Since it has been reported that the P91 is ductile in this temperature regime, the large dome-shaped deformation of the specimen during the test is produced due to the high ductility of the material [164]. It is found that the oxides of P91 are mainly chromium and iron oxides by EDS analysis. These oxides, of approximately 5 μm in thickness, are believed to be brittle due to their nature as

ceramics. Thus cracking of the oxide layer occurs due to the tension force developed during the punching process.

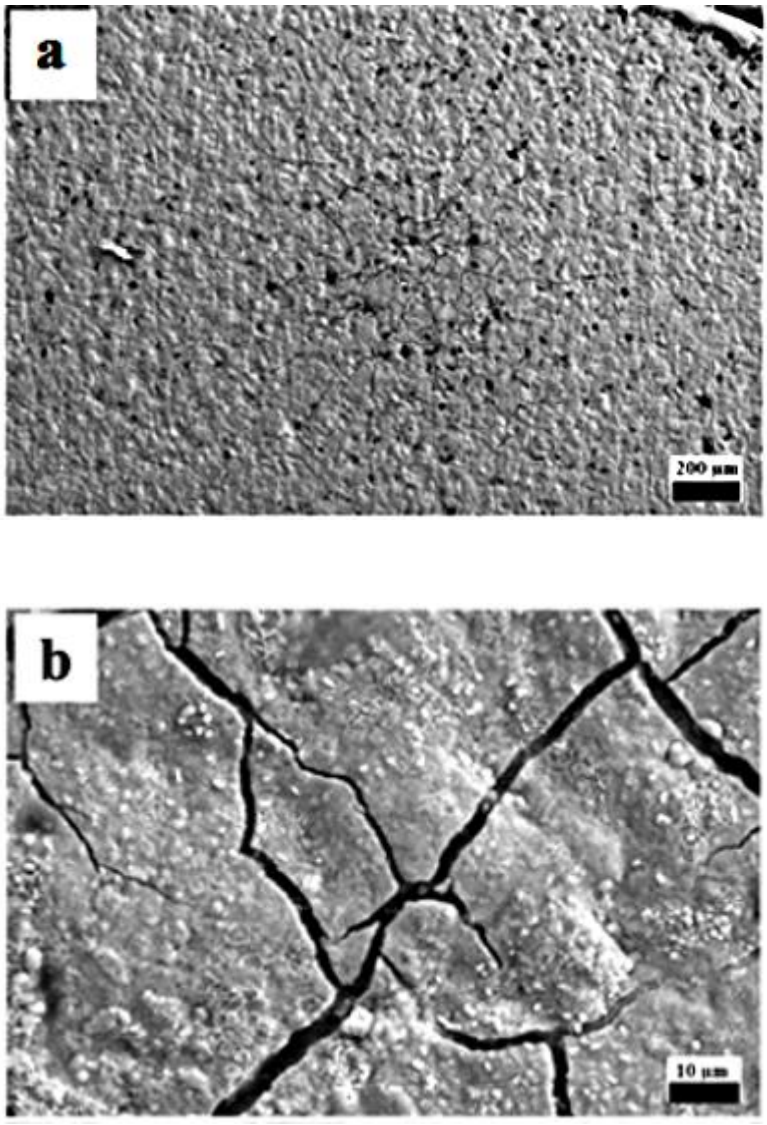


Figure 5-14. The morphology of the deformed P91 specimens at 0.26 mm shown in (a) low magnification image, (b) high magnification image.

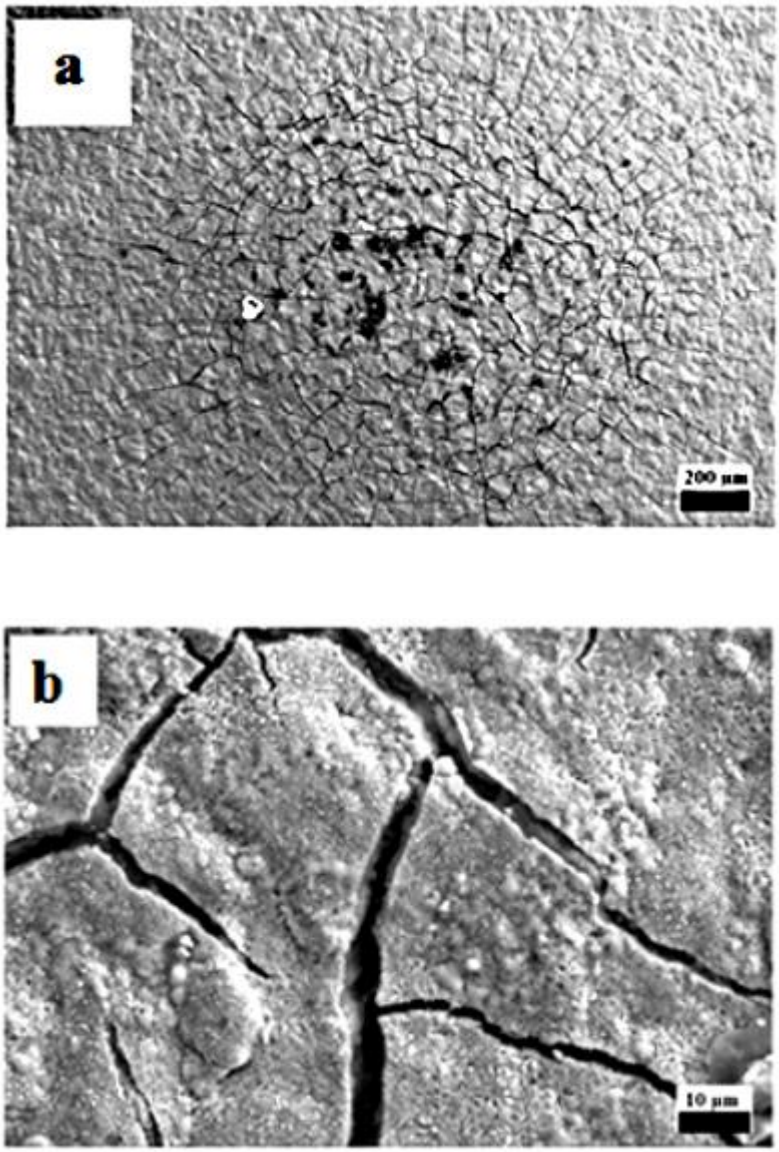


Figure 5-15. The morphology of the deformed P91 specimens at 0.6 mm shown in (a) low magnification image, (b) high magnification image.

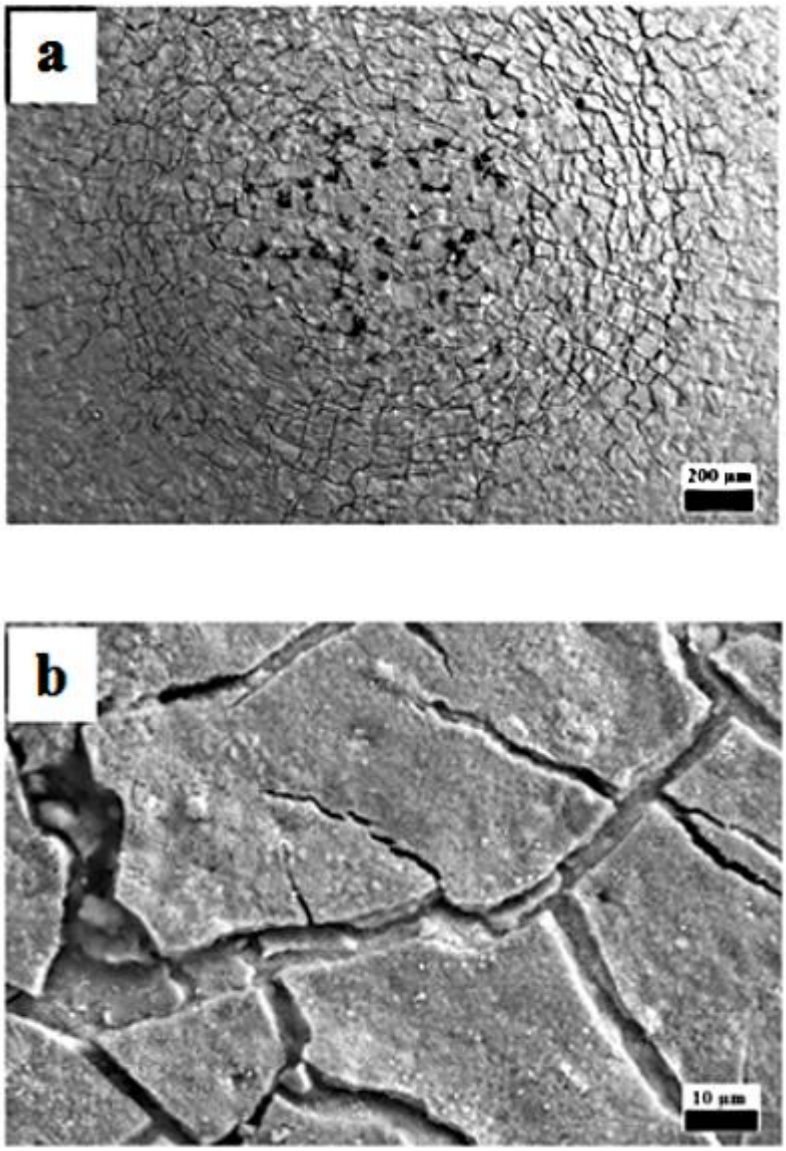


Figure 5-16. The morphology of the deformed P91 specimens at 1.0 mm shown in (a) low magnification image, (b) high magnification image.

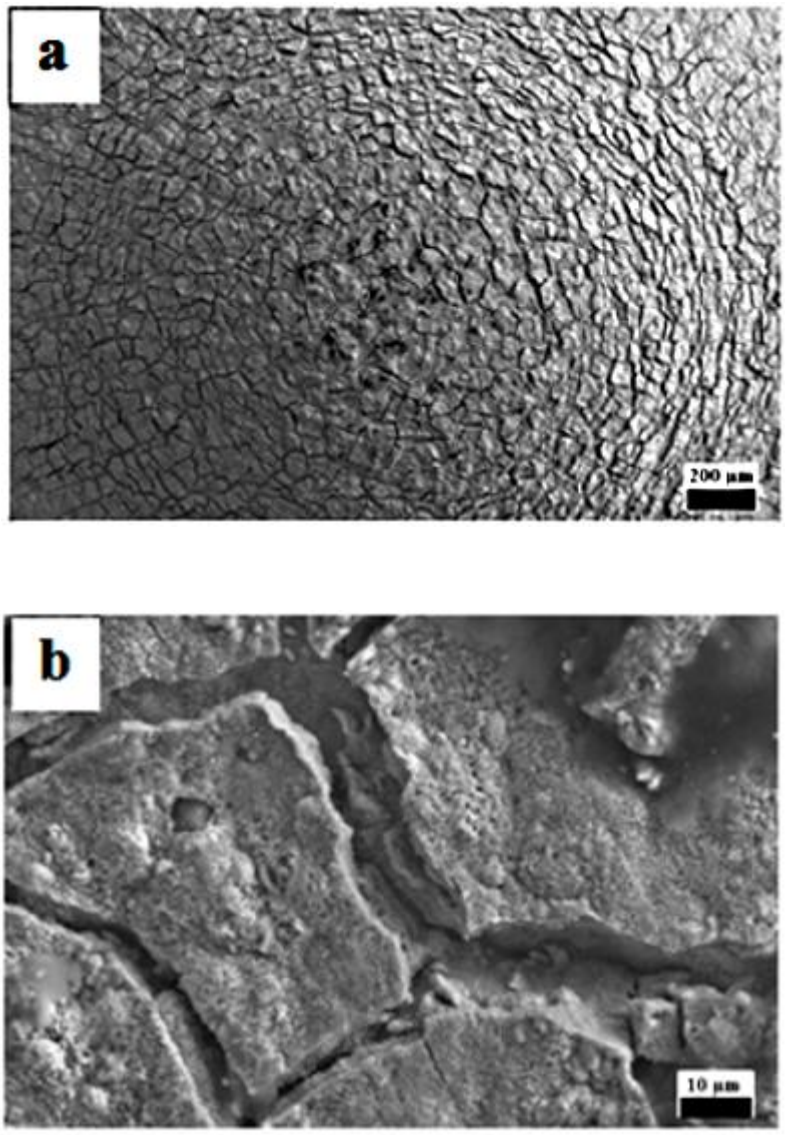


Figure 5-17. The morphology of the deformed P91 specimens at 1.25 mm shown in (a) low magnification image, (b) high magnification image.

In the Figures 5-18 to 5-20, the dome shape of the specimen remains the key feature of the deformed specimens. It can be seen that the size of the dome has increased significantly due to the large displacements. It is further noticed that some voids have developed in the dome-shaped specimens in Figures 5-18c and 5-19c. These areas are near the edge of contact between the punch and specimen. The shearing between the bending and tensile stresses leads to localised material necking and thinning around the edge of contact, causing a significant decrease in the load-carrying capacity of the specimens. The voids are developed at the highly strained regions of the specimens, as highlighted in Figures 5-18a and 5-19a. This gives the crack initiation sites within the specimens. At further displacement, 1.74 mm, the fracture of the dome-shaped specimen has occurred. The voids that are seen in Figures 5-18a and 5-19a correlate with the fracture sites in Figure 5-20a, showing that the fracture of the specimen occurs near the edge of contact. It can be seen from the fracture surface in Figure 5-20c that tearing has occurred and ductile dimples were formed due to the tension force developed within the specimen.

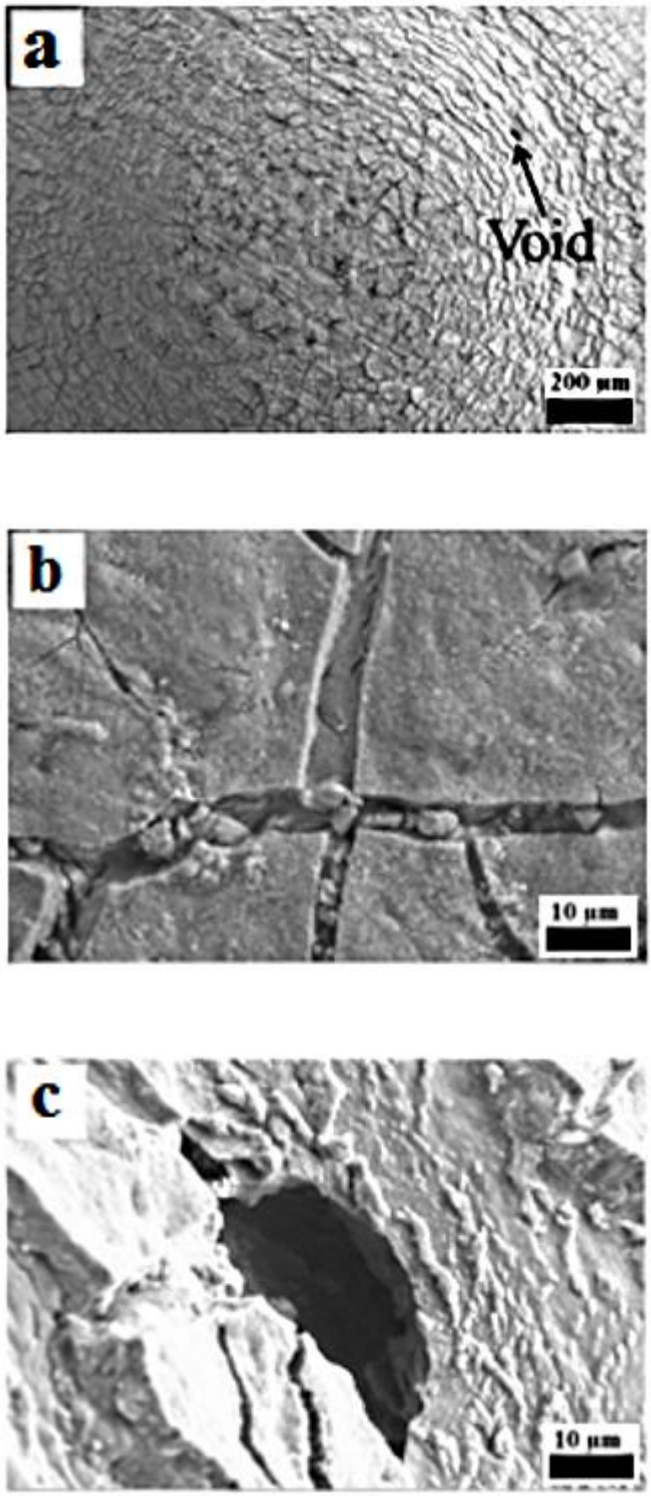


Figure 5-18. The morphology of the deformed P91 specimens at 1.5 mm shown in (a) low magnification image, (b) and (c) high magnification image.

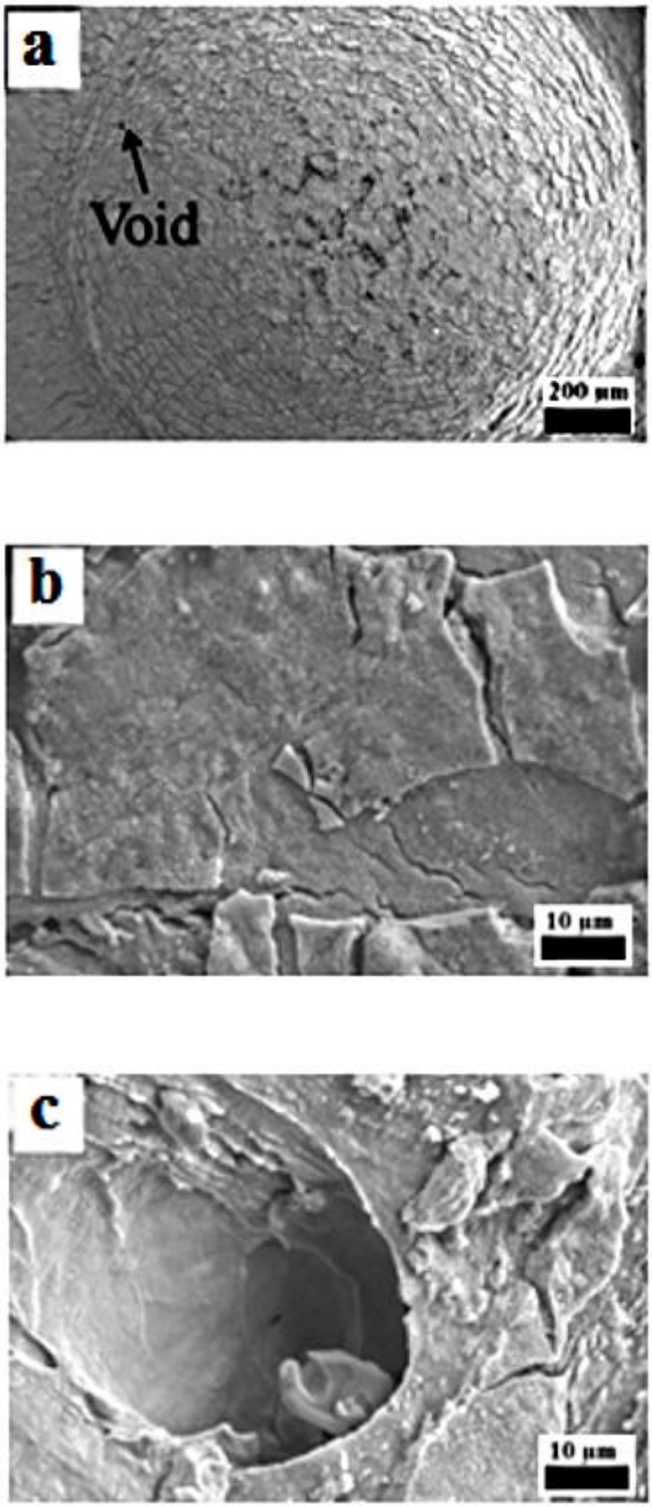


Figure 5-19. The morphology of the deformed P91 specimens at 1.65 mm shown in (a) low magnification image, (b) and (c) high magnification image.

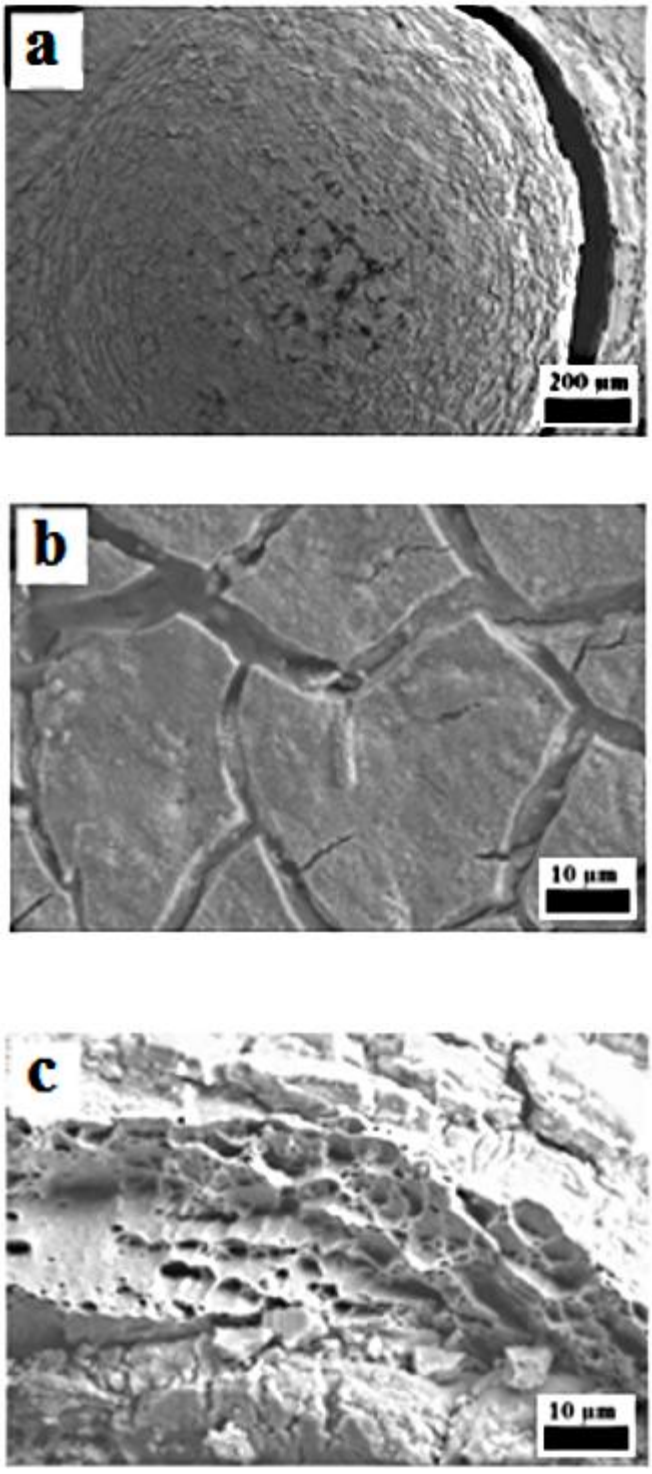


Figure 5-20. The morphology of the deformed P91 specimens at 1.74 mm shown in (a) low magnification image, (b) and (c) high magnification image.

5.4 Physical Characterization of the Deformation Process in SPTT

5.4.1 Microstructural Evolution

The cross-sectional microstructure of the above deformed P91 specimen is shown in Figures 5-21 to 5-24. The small deformation after a displacement of 0.26 mm in Figure 5-21a exhibits a good correlation with Figure 5-14a, i.e. the dome shape is about to form due to the punch movement. It can be seen that the thickness of the specimen remains uniform without obvious material thinning as shown in Figure 5-21a. The primary phase that can be seen is the prior austenitic phase in Figure 5-21b. No large voids have yet formed for a displacement of 0.26 mm. The dome shape becomes more evident when the deformation of the specimen increases. The alignment of the grains is not found in Figures 5-21b and 5-22b, but such evidence is seen at large punch displacements as shown in Figures 5-23b and 5-24b. This indicates that the grain alignment will tend to occur when the plastic deformation becomes dominant. The beginning of necking occurs, as shown in Figures 5-23a and 5-24a, due to the bending and stretching stress at the edge of contact between the punch and specimen.

Figures 5-25 to 5-27 show the cross-sectional microstructure of the P91 after achieving the maxium load. The dome shape has developed further due to the increased punch displacements. It is noticed that the necking and thinning at the edge of contact significantly progress in these specimens, where the thickness of the specimen has been further reduced, as shown in Figure 5-26a due to the ongoing bending and streching stresses under the bi-axial stress state.

Meanwhile, void nucleation and elongation are found as can be seen in Figure 5-25b. Due to the large plastic deformation arising from these punch displacements, the voids have been deformed into elongated shapes of which the long axis is pointing in the direction of the plastic flow. The phases also align with the plastic flow in Figures 5-25b and 5-26b. Moreover, it is found from Figure 5-26b that the austentic and martensitic phases have been elongated along the plastic flow direction due to the extensive plastic deformation at the edge of contact. A number of voids, approximately 3-5 μm across, are found in Figure 5-26b. The morphology of the voids has been further stretched and elongated. Figures 5-27a and 5-27b depict the microstructure of the fracture point at the edge of contact. It can be seen that the phases have also been elongated due to the large plastic deformation in Figure 5-27b. Some discrete and ellipsoidal voids are found in this region, especially close to the fracture site. This indicates that the fracture of the P91 specimen tends to occur in areas which are occupied with a greater density of voids. No clear evidence of crack propagation is noted. Noting that significant material necking and thinning have occurred during this stage, together with the void nucleation and elongation, it is possible that the thinning of the specimen at the edge of contact allows the coalescence of voids to occur, resulting in the fracture of the specimen. Eventually, the tearing of the material occurs, producing the rough fracture surface.

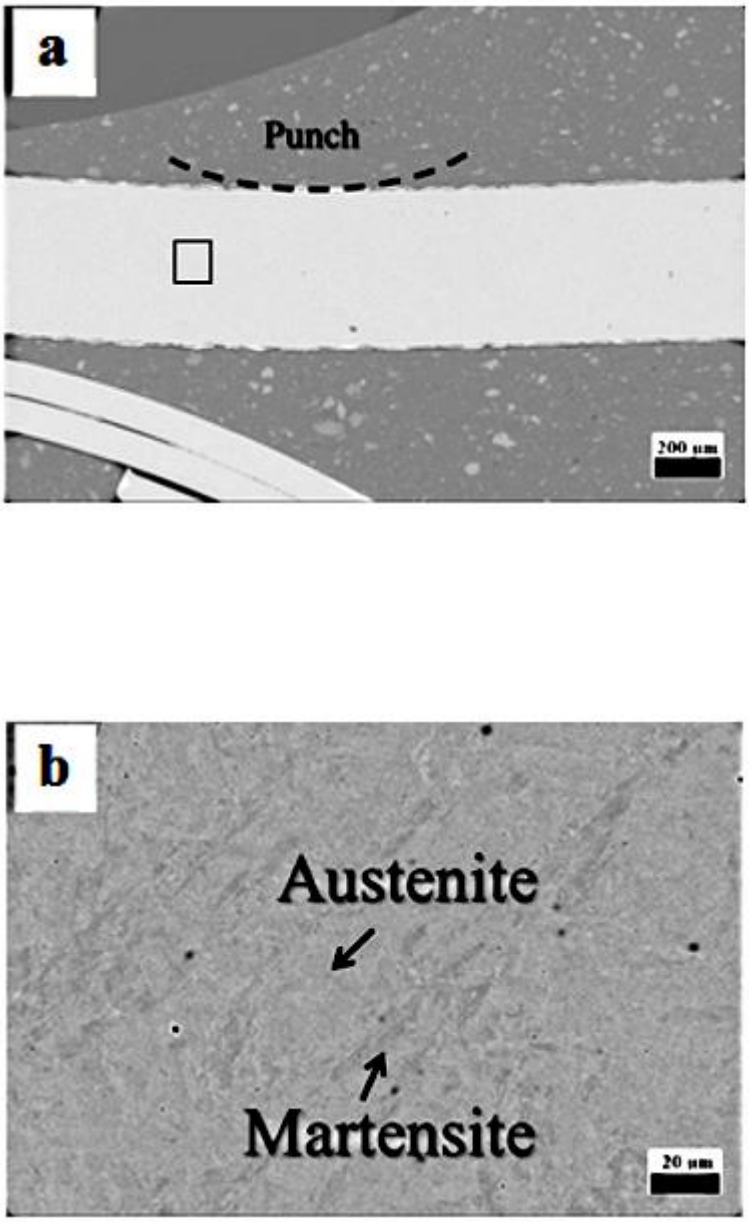


Figure 5-21. (a) The cross-sectional microstructure of the P91 specimen at interrupted displacements of 0.26 mm, where the black box outline the area shown in the higher magnification image (b).

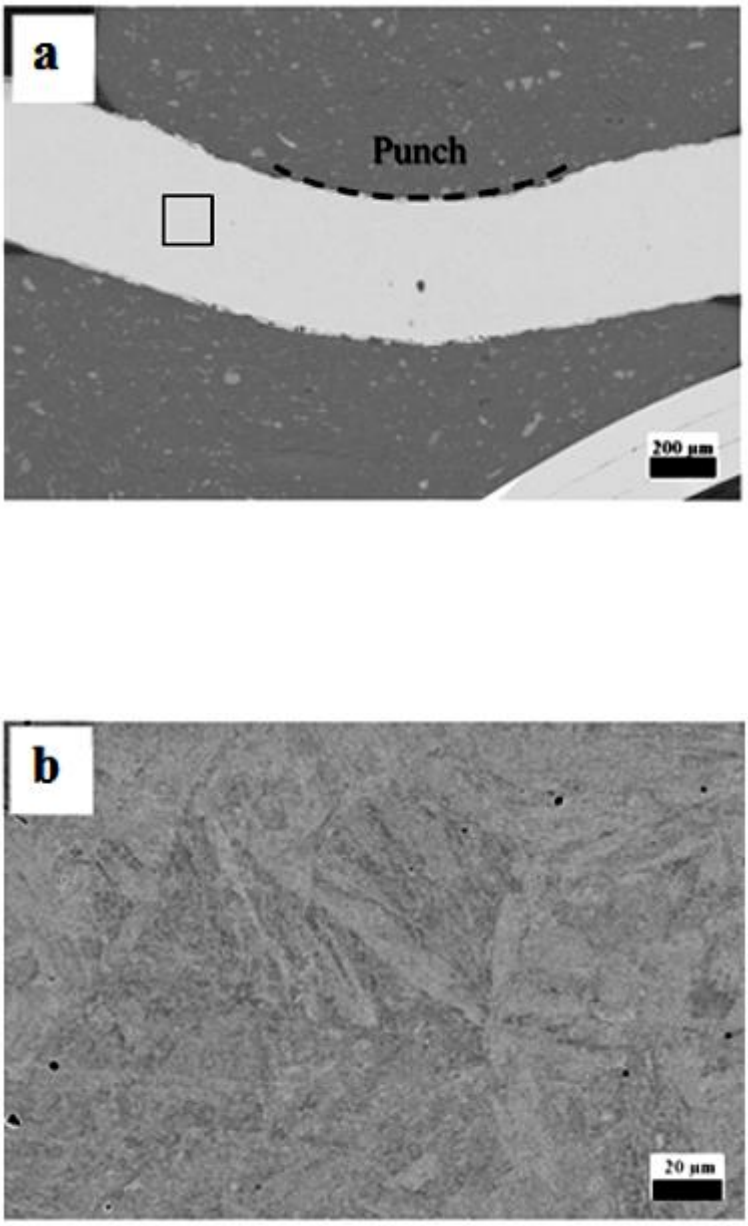


Figure 5-22. (a) The cross-sectional microstructure of the P91 specimen at interrupted displacements of 0.6 mm, where the black box outline the area shown in the higher magnification image (b).

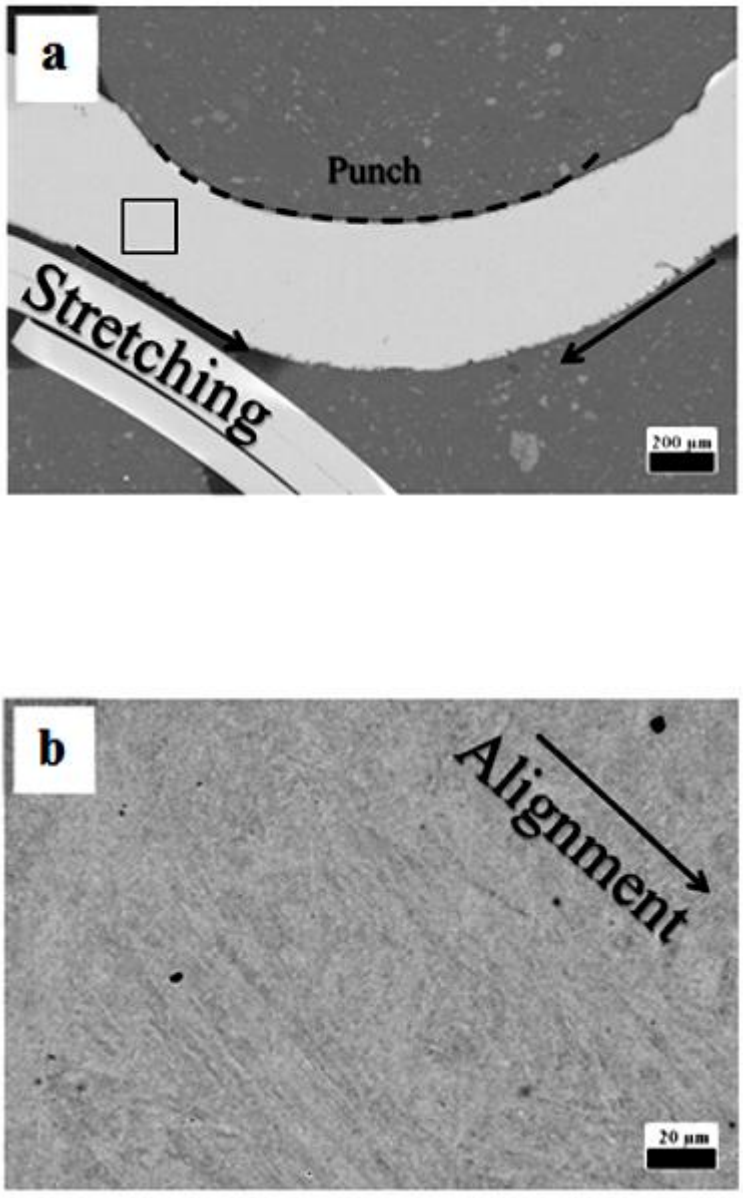


Figure 5-23. (a) The cross-sectional microstructure of the P91 specimen at interrupted displacements of 1.0 mm, where the black box outline the area shown in the higher magnification image (b).

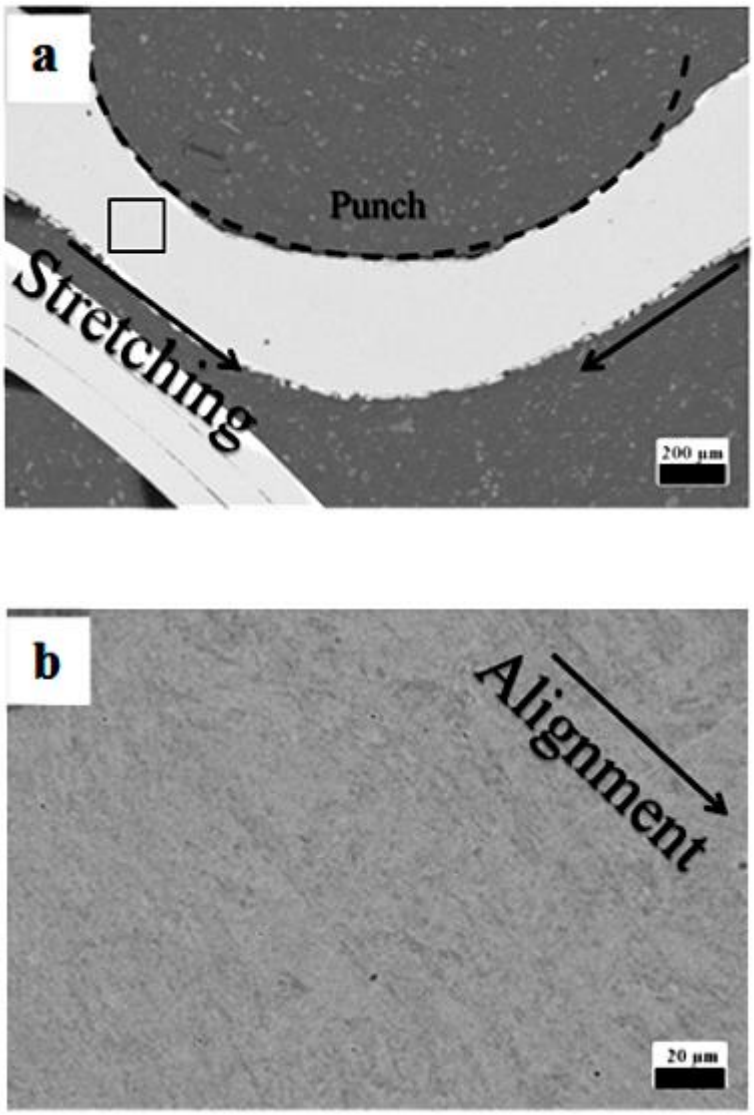


Figure 5-24. (a) The cross-sectional microstructure of the P91 specimen at interrupted displacements of 1.25 mm, where the black box outline the area shown in the higher magnification image (b).

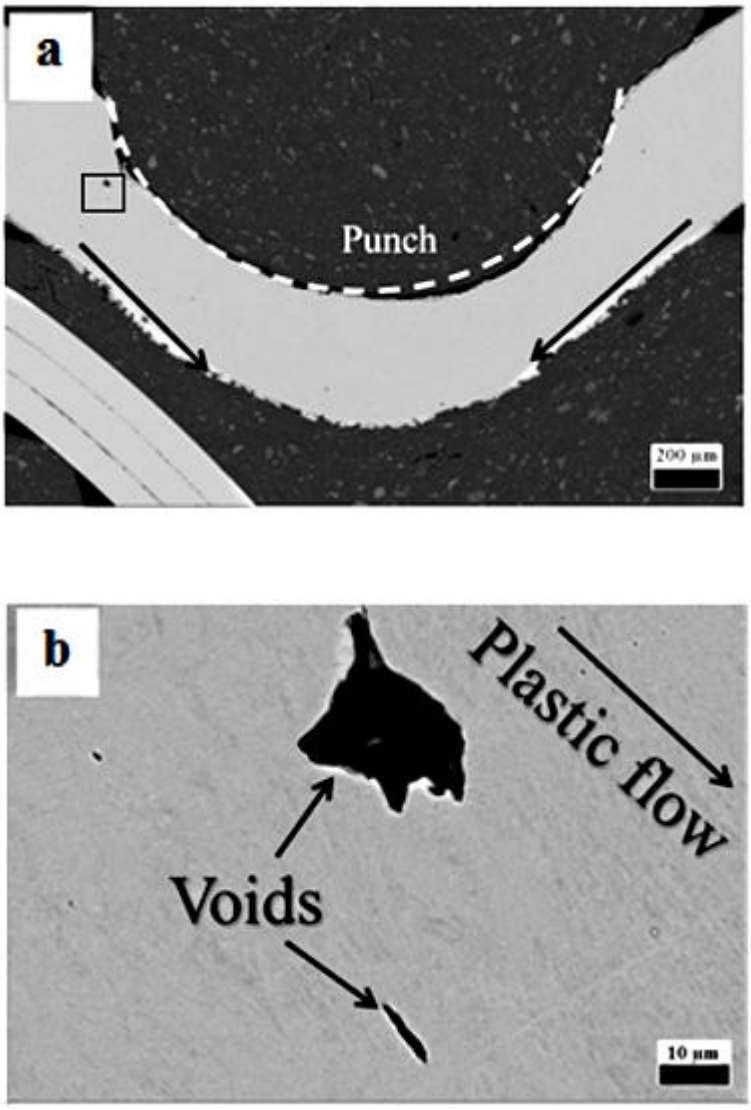


Figure 5-25. (a) The cross-sectional microstructure of the P91 specimen at interrupted displacements of 1.5 mm, where the black box outline the area shown in the higher magnification image (b).

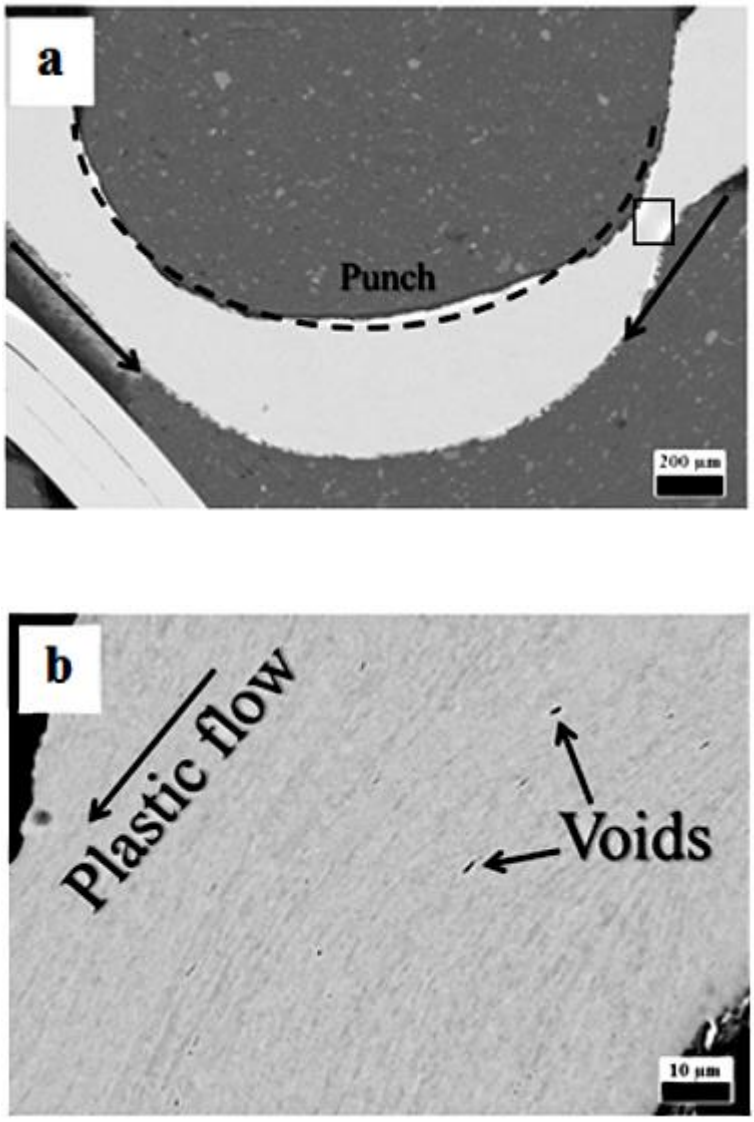


Figure 5-26. (a) The cross-sectional microstructure of the P91 specimen at interrupted displacements of 1.65 mm, where the black box outline the area shown in the higher magnification image (b).

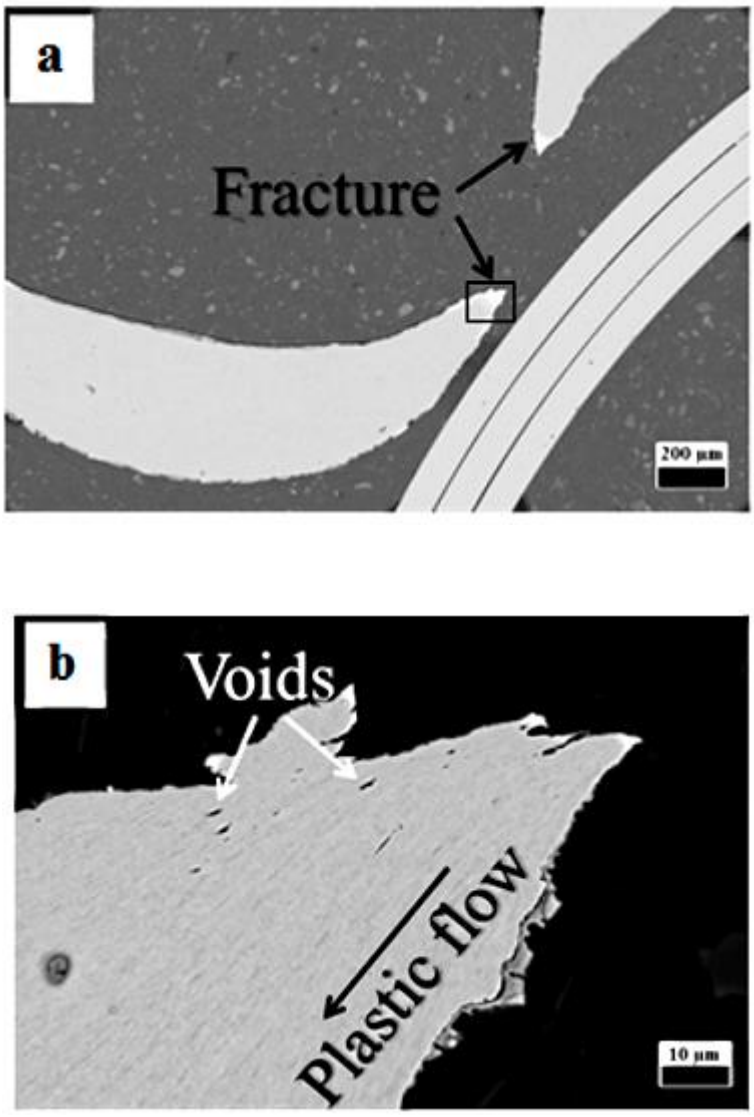


Figure 5-27. (a) The cross-sectional microstructure of the P91 specimen at interrupted displacements of 1.74 mm, where the black box outline the area shown in the higher magnification image (b).

5.4.2 Grain Structure Evolution

The electron backscatter diffraction (EBSD) sample is mechanically ground flat by emery grinding papers up to grade 4000. Diamond paste is also used to polish down to 1µm and then colloidal silicon 0.06µm suspension is used for final polishing. The EBSD investigations are carried out on field emission gun scanning electron microscopy JEOL 7100F (FEG-SEM). Figure 5-28 shows the EBSD mapping of as received the P91 steel.

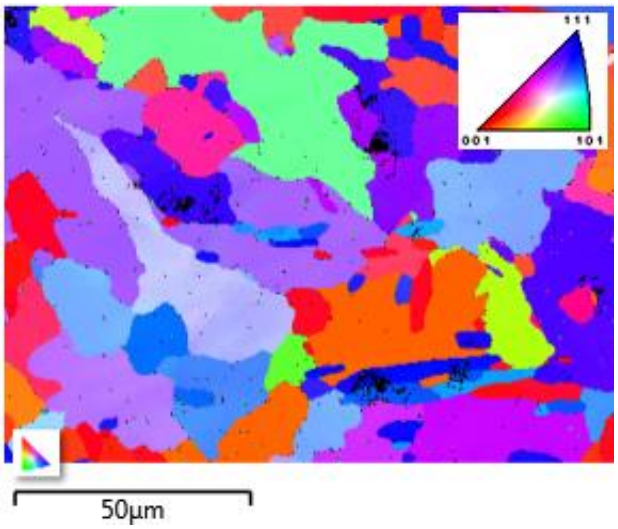


Figure 5-28. EBSD mappings of the as-received of the P91 steel.

EBSD investigation involving microstructural characterisation will be carried out on specimens for a range of punch displacements. These results will then be compared with results from the computational models. If confidence can be gained in them, then they may be used to predict the viscoplastic behaviour of P91 in service conditions. To further elucidate the deformation mechanisms of the P91 during SPTT, Figure 5-29 shows the EBSD mapping of regions near the edge of

contact for displacements at 0.26 and 0.6mm while Figure 5-30 shows at 1.0 and 1.25 mm. The P91 consists of prior austenitic grains and martensitic laths within the austenitic grains. The size of prior austenitic grains ranges from 30-60 μm while the size of the martensitic laths is within several microns. Since only a small displacement of 0.26 mm was imposed to the specimen in Figure 5-29a, the grains largely maintain their original distribution without aligning to the plastic flow. When the displacement increases to 0.6 mm, as shown in Figure 5-29b, the grains now start to align with the direction of the plastic flow. This is supported by the evidence that some grain boundaries exhibit an alignment as indicated by the arrow in Figure 5-29b. The alignment of the grains is likely to have resulted from the continuous plastic deformation when the punch displacement increases to 0.6 mm. Although the grain alignment has occurred by this stage, some grain boundaries still remain randomly distributed. Since 0.6 mm was chosen in the middle of the plastic deformation regime in Figure 5-4, the grain alignment has not yet become fully developed. When the displacement increases further to 1 and 1.25 mm, evidence of grain alignment can also be clearly seen in Figures 5-30a and 5-30b. No preferred grain orientation has yet been developed. It is noticed from Figures 5-30a and 5-30b that more martensitic laths are precipitated within the austenitic grains, in which the martensitic laths exhibit a small misorientation against each other, as indicated by the gradual orientation changes in the region of martensitic laths. It is further noticed that the alignment of the grain boundaries mainly occurs in the block boundaries within the prior austenitic grains. The majority of the grains retain their original morphology without significant grain deformation or elongation. This means that the grain

structure of the P91 specimen mainly undergoes grain boundary alignment along the direction of plastic flow.

Figure 5-31 shows the grain structure at the edge of contact for SPTT displacements at 1.5, 1.65 and 1.74 mm. Since the grain boundary alignment has already occurred in the previous deformation stages, the behaviour of the grains in this regime is dominated by the grain elongation. It can be seen that the aligned grains have been deformed along the deformation direction, particularly in Figures 5-31b and 5-31c. The blocks within the austenitic grains have been elongated. The martensitic laths are still observable within the prior austenitic grains. When displacements increase from 1.5 to 1.65 and 1.74 mm, the further elongation of the austenite grains is observed. Figure 5-32 shows the cross-sectional microstructure at the fracture point. It can be seen that the fracture site passed through the edge of contact where the specimen has become necked and thinned. Since the fracture process in SPTT occurred in a relatively short period, a significant number of cavities did not develop in the specimen. The voids that formed close to the fracture site have also become aligned with the plastic flow direction, and exhibit an elongated morphology. More voids are found around the fracture tip in Figure 5-32a. The void coalescence can further reduce the integrity of the specimen, leaving only limited bonding at the fracture site. This is consistent with the reduction in the specimen thickness as shown in Figure 5-26. It is shown from Figure 5-32b that the grains have become significantly elongated, with the majority of them becoming elongated along the plastic flow direction. The prior austenitic grains and the martensitic blocks have been stretched and elongated to form long, slim grains. The elongated grains allow more grain

boundary sliding to occur during the deformation stage. Since deformation and elongation of voids also occur at the edge of contact, failure at the fracture site occurs by tearing at the necking and thinning area.

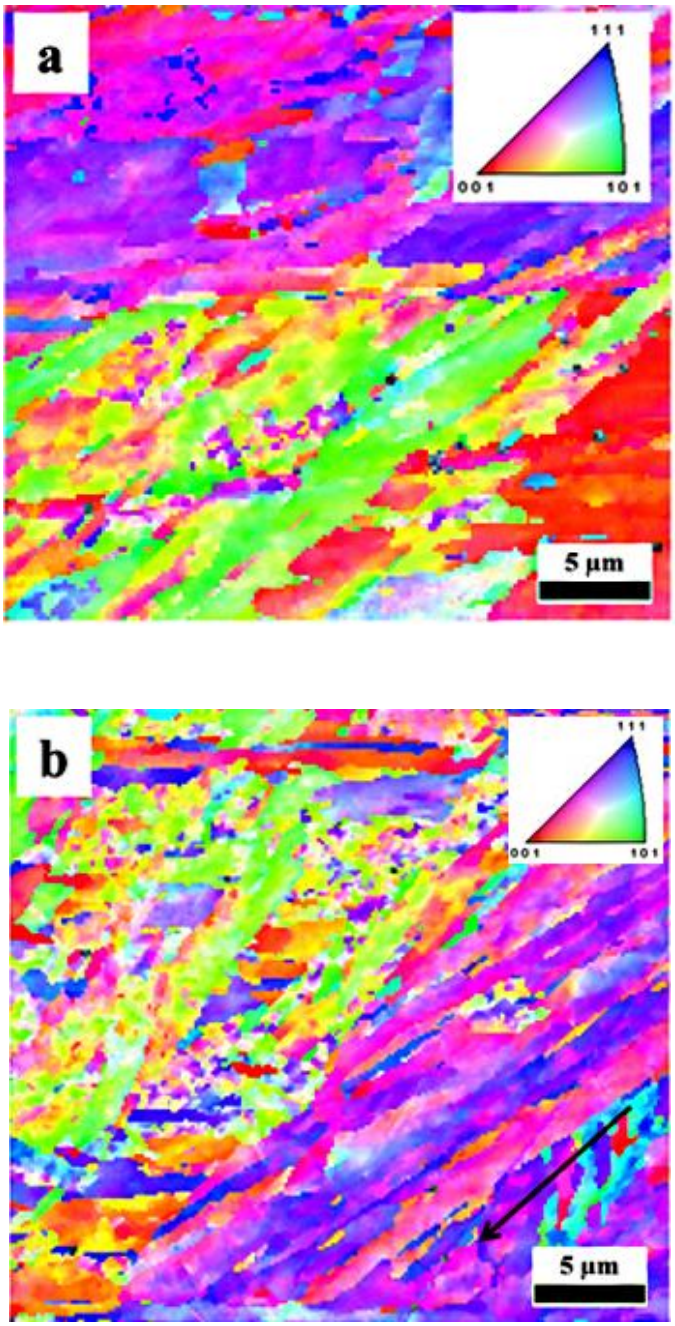


Figure 5-29. EBSD mappings of regions near the edge of contact for displacements of (a) 0.26 mm and (b) 0.6 mm.

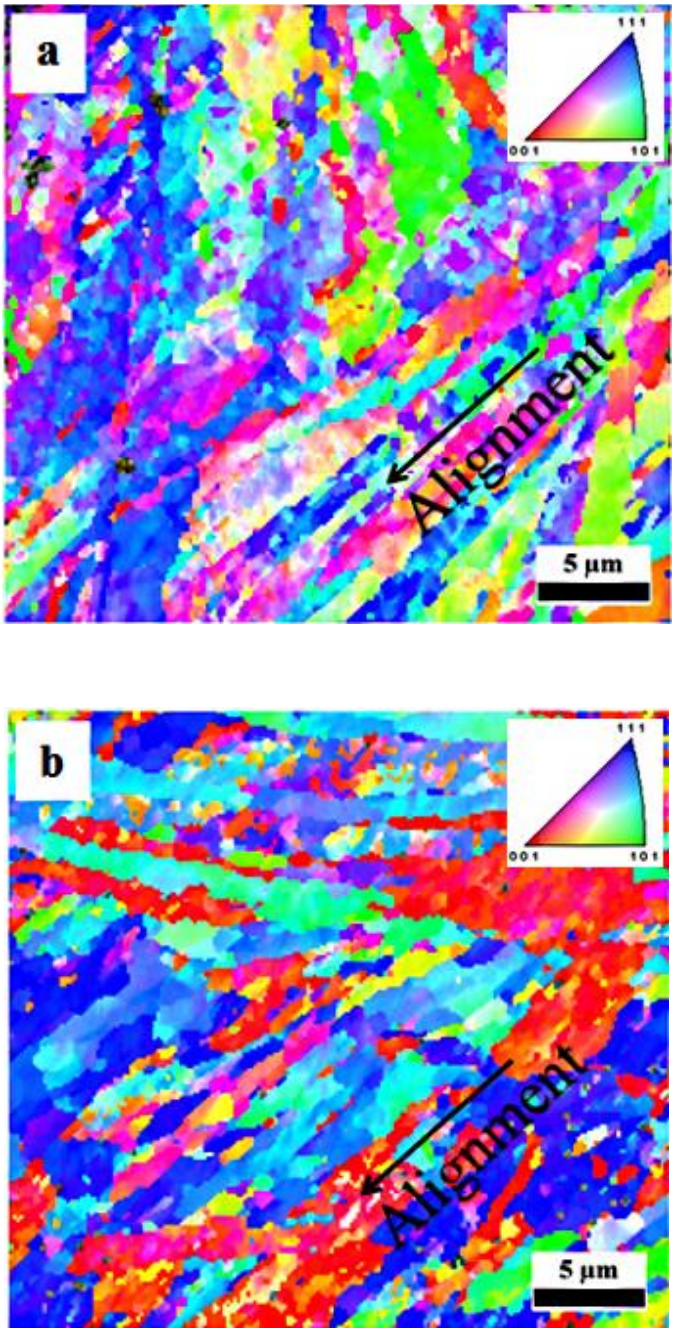


Figure 5-30. EBSD mappings of regions near the edge of contact for displacements of (a) 1.0 mm and (b) 1.25 mm.

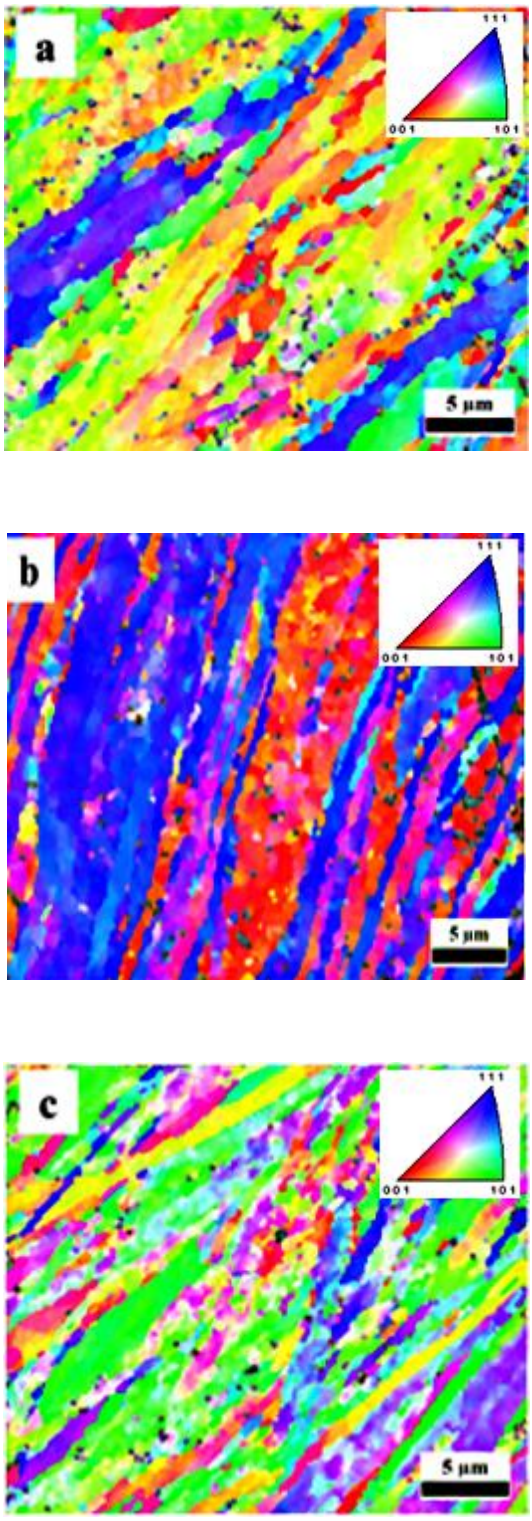


Figure 5-31. The grain structure at the edge of contact for SPTT displacements of (a) 1.5 mm, (b) 1.65 mm and (c) 1.74 mm.

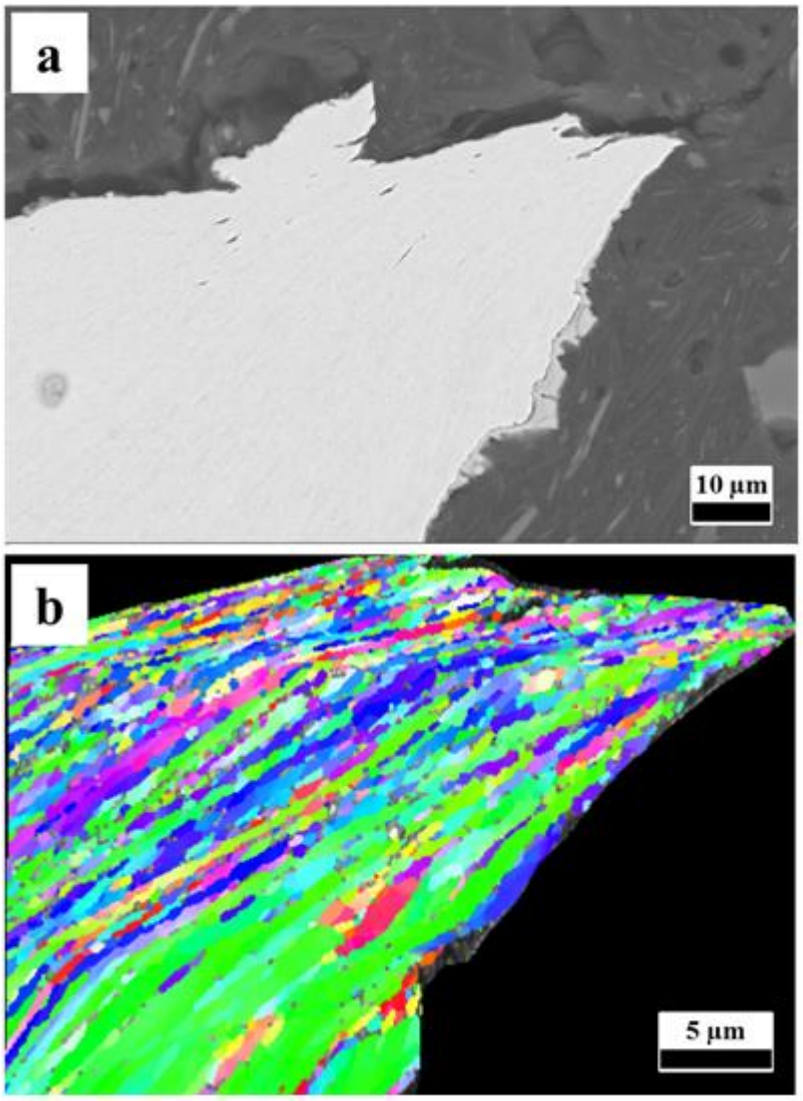


Figure 5-32. The cross-sectional microstructure at the fracture point.

5.5 Discussion

5.5.1 Deformation Regimes and Plasticity Energy

The fraction of deformation energy at different stages of SPTT is summarised in Figure 5-33. It can be seen that over 65% of the energy is consumed before the maximum load is reached. Since the continuous movement of the punch results in progressive material necking and thinning at the edge of contact, Figure 5-34 presents the evolution of the specimen thickness at the edge of contact. The minimum thickness at the edge of contact was taken to represent how the material thinning occurs during the SPTT. It can be seen that the significant material thinning primarily occurs after the maximum load is achieved. This behaviour is similar to that observed in uniaxial tensile testing in which the necking occurs after the ultimate tensile stress. The significant thinning at the edge of contact indicates that the specimen starts to fracture, which shows good consistency with Figure 5-26. To demonstrate the specimen response during the SPTT, Figure 5-35 gives the schematic diagram of deformation of the specimen at different stages, from the initial plastic deformation to the necking at failure. Stage II represents the transition zone from elastic to plastic deformation, in which plastic deformation occurs in the local contact zone between the punch tip and the specimen, stretching the material into the receiving die. Stage III represents homogeneous plastic deformation and the specimen thickness reduces uniformly in the deformation zone (as shown in Figures 5-14a, 5-15a and 5-16a and Figures 5-21a, 5-22a and 5-23a for punch displacements from 0.26 mm to 1.0 mm). The energy required for the initial elastic deformation (Stage I in Figure 5-33) is quite small (2.1%) but gradually increases with displacements in the plastic

deformation regimes. In Stage III, the energy consumed is more than 45% of the total energy, indicating that the P91 exhibits a good toughness. The thickness of specimen reduces at localised circular band near the contact edge between the punch and specimen in Stage IV (as shown in Figure 5-17a and Figure 5-24a), in which circumferential necking occurs and the energy consumed is around 20%, where the rate of energy decreases in this stage. It is possible that material thinning and void nucleation start to occur in this stage (Figure 5-24a), resulting in a decrease in plasticity deformation of the P91 specimen. In Stage V, the continuous plastic deformation and the on-going material necking and thinning lead to the formation of large voids near the edge of contact, as shown in Figures 5-18a and 5-19a and Figures 5-25a and 5-26a, in which the nucleation and elongation of voids lead to the void coalescence and the point necking occur in the circumferential necking area. Since the continuous necking and thinning occurs with the punch movement, the energy consumed is about 29% in this deformation regime. Finally, the material is torn when approaching the failure in Stage VI (as shown in Figure 5-20a and Figure 5-27a), in which the energy consumed is only 4.1% of the total energy due to the area at the contact edge reducing as failure is approached.

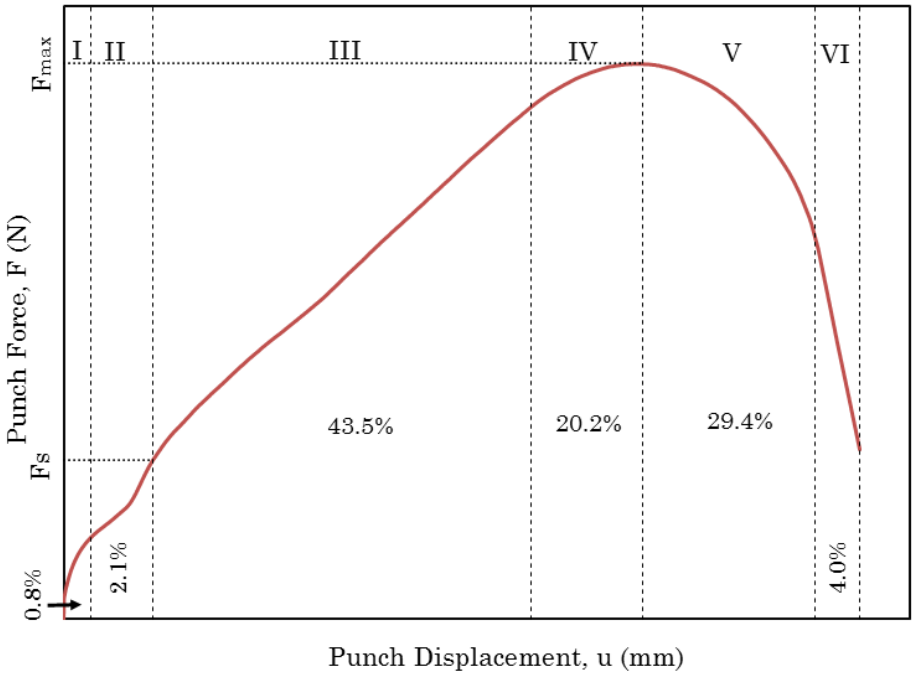


Figure 5-33. The deformation energy in different stages of the SPTT load-displacement curve for P91 at 600°C.

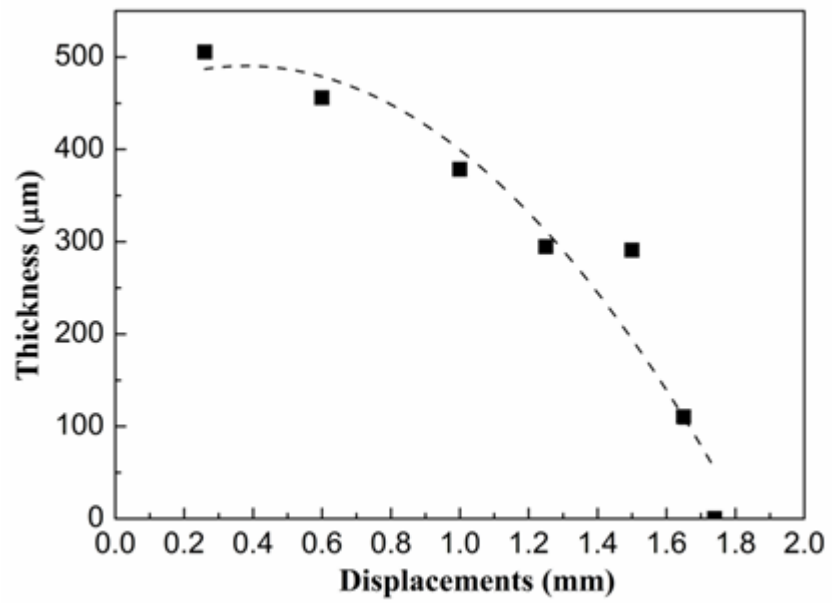


Figure 5-34. The evolution of specimen thickness at the edge of contact against displacements.

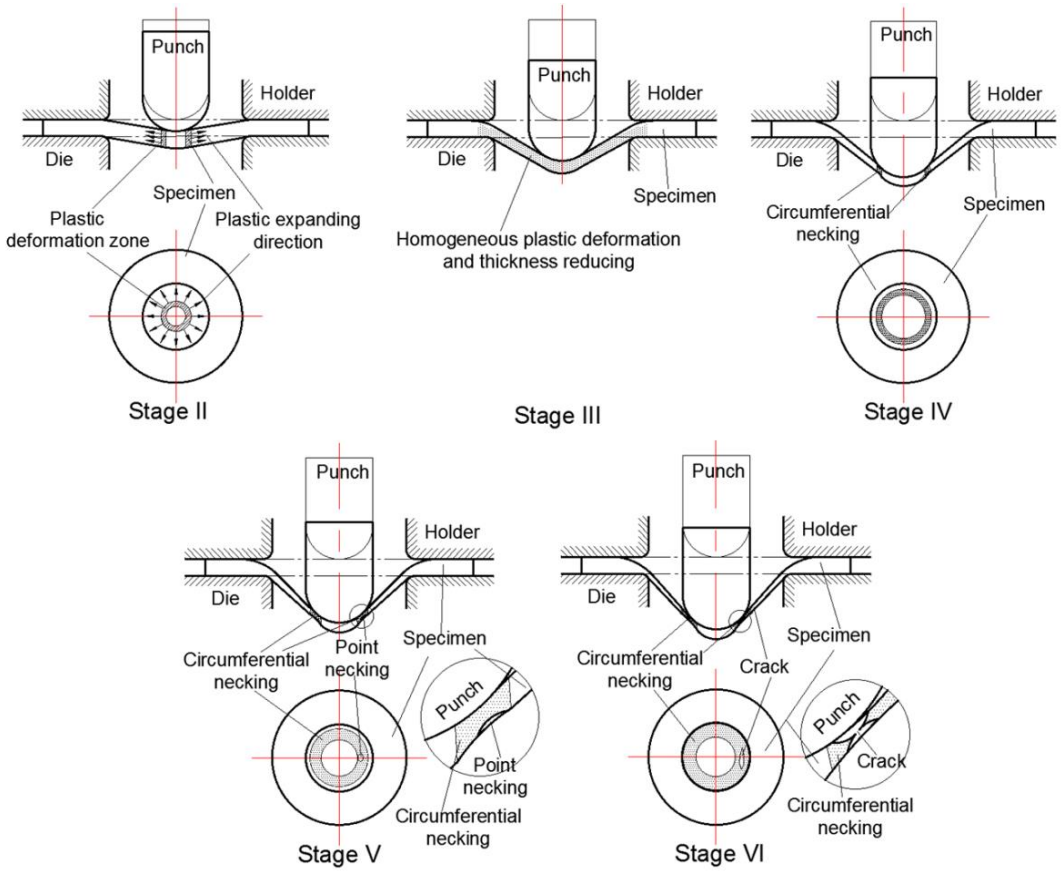


Figure 5-35. The schematic diagram of deformation mechanism of P91 in SPTT at different stages.

5.5.2 Deformation and Fracture Mechanisms

From Figures 5-29 to 5-31, it can be seen that the grain behaviour of the P91 during the SPTT can be divided into two regimes, namely grain boundary alignment before the maximum load (Stages I-IV in Figures 5-33 and 5-35) and grain elongation after the maximum load (Stages V-VI in Figures 5-33 and 5-35). This is schematically illustrated in Figure 5-36. Before achieving the maximum load, the P91 specimens gradually deform with the punch displacements. The "stiffening effect" of the specimen during SPTT allows the load that is required to further deform the specimen to increase (Stages II-III). During the SPTT, the regions along the edge of contact between the punch and specimen are subjected to the "stretching effect" when the punch starts to deform the specimen, leading to the circumferential necking (Stage IV). In the grain alignment stage, the martensitic blocks within the austenitic grains are aligned with the plastic flow from Figures 5-36a to 5-36b. This is evidenced by the alignment of the block boundaries in Figures 5-29 and 5-30. The morphology of the grains maintains the original morphology without significant changes to the grain orientations. This behaviour of grain alignment dominates the deformation mechanism in Stages II-IV. Meanwhile, the grain deformation and elongation occur after the maximum load in Stages V-VI. Since the grains have already been aligned along the plastic flow direction, the load required to further deform the sample decreases, as indeed seen in Figures 5-6 to 5-12. Although void nucleation is seen in Figure 5-26b, the number of voids is quite limited. Thus, in order for further punch displacements to occur, grain boundary sliding occurs along the aligned grain boundaries. During the grain boundary sliding, the martensitic blocks and the large prior

austenitic grains have also become elongated along the plastic flow direction, as seen in Figure 5-32b. Therefore, in the deformation stage after the maximum load (Stages V-VI), the deformation mechanism is realised by grain elongation and grain boundary sliding in Figure 5-36c.

Since the voids nucleation and coalescence occur during the SPTT, the size of the voids near the edge of contact is compared. The diameter is quoted for spherical or nearly spherical voids whilst the long axis is quoted for the ellipsoidal voids. It can be seen from Figure 5-26b that the diameter of the spherical voids is approximately 1 μm. The size of the voids does not change significantly before the maximum load. The small displacements of 0.26, 0.6 and 1 mm would not lead to the formation of the voids. When the displacements increase further, especially after the maximum load, small and discrete sub-micron voids start to become elongated. Since the localised shearing and stretching are believed to be effective in facilitating the growth of the voids during the SPTT, especially at larger displacements, the voids are subjected to the same stress state as the bulk material under the stretching effects during the SPTT. As a result, the voids are elongated to become ellipsoidal shapes, as seen in Figures 5-25b, 5-26b and 5-27b. The size of the voids is approximately 5 μm or even larger when the deformation of specimen increases to 1.74 mm as shown in Figure 5-27b. Some large voids are also developed during this stage, indicating a possible coalescence of the voids during the SPTT. Since it is noticed from Figures 5-21 to 5-27 that the voids have grown significantly after the maximum load, it is thus believed that the fracture mechanism consists of the void elongation and coalescence close to the fracture site in Figure 5-36d.

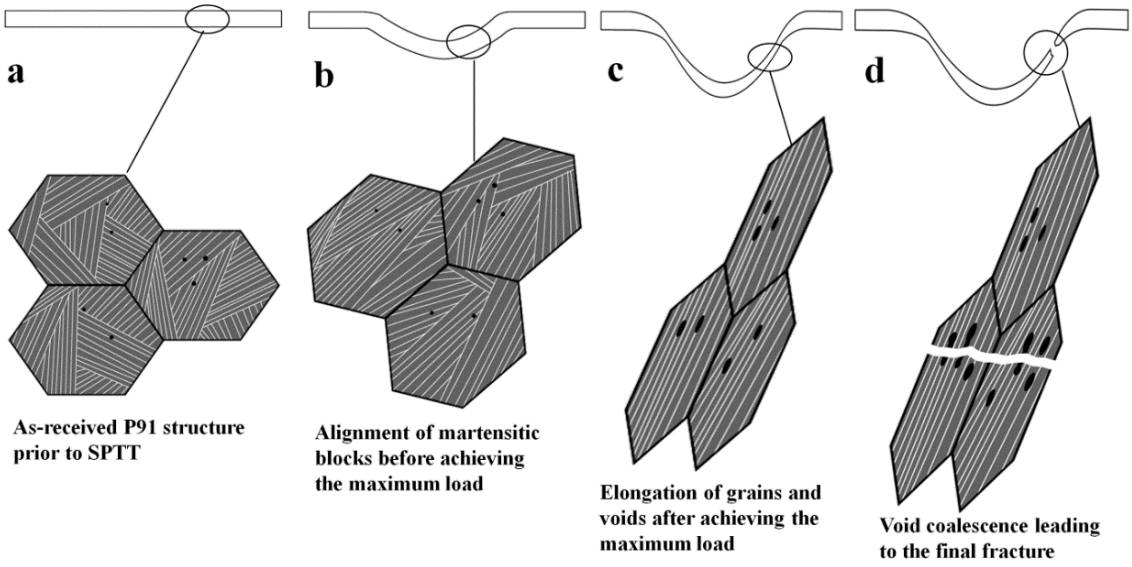


Figure 5-36. The schematic diagram of microstructure evolution and fracture mechanism of P91 during SPTT. (a) the as-received structure prior to SPTT, (b) the grain alignment, (c) the elongation of grains and voids and (d) the void coalescence that leads to fracture.

5.6 Conclusions

The interrupted small punch tensile tests of P91 were performed at 600 °C to investigate the deformation and fracture mechanisms. The bulk deformation behaviour and the microstructure evolution during the SPTTs were studied. The main conclusions are drawn as follows:

- The bulk deformation behaviour of the P91 during SPTT exhibits the typical six deformation regimes. It is found that over 65% of the plasticity energy is consumed before the maximum load. It is also found that the voids are likely to form after the maximum load is achieved, which indicates that the local cracking of the P91 specimen is starting to occur.
- From the microstructure evolution, it is shown that significant necking and thinning occur after the maximum load. Evidence of void nucleation is also found near the edge of contact where the specimen has been highly stressed. The voids are found to be aligned with the direction of plastic flow due to the "stretching effects" during the SPTT.
- It is shown from the grain structure evolution that the grains maintain their original morphology prior to achieving the maximum load in SPTT, but a tendency to align themselves along the stretching direction is observed. It is found that the punch displacements cause the martensitic blocks within the prior austenitic grains to align with plastic flow of the specimen during SPTT.
- After achieving the maximum load, the grains are deformed and elongated along the plastic flow direction. The elongated grains can result in grain

boundary sliding which tolerates further displacement in the fracture region. A number of voids are developed close to the fracture site and the voids have been developed into nearly ellipsoidal shapes. The fracture of the P91 specimen is believed to be a combination of void coalescence and tearing at the contact edge between the punch and specimen.

CHAPTER 6:
FE MODELLING OF DISLOCATION DENSITY AND GRAIN SIZE EFFECT ON SPTT

6.1 Introduction

In this study, the ABAQUS finite element (FE) simulation software was used to simulate the small punch tensile behaviour of the P91 steel at 600℃. The constitutive model of the steels was defined using UMAT subroutine which is compatible with ABAQUS. This chapter focuses on validating the performance of the developed based-dislocation viscoplasticity model by comparing the finite element simulation results with experimental data such as those obtained from the interrupted SPT tests at 600℃.

6.2 Development of Constitutive Model

A range of phenomenological material models for high-temperature application have been developed, i.e. the Chaboche unified power law [165, 12], the hyperbolic sine unified [38, 166, 167], and the two-layer viscoplasticity formulation [168] which allow a predictive model to be used to extrapolate experimental data. However, these approaches are focused only a portion of the bulk response of materials. In this PhD project, the new dislocation mechanisms of isotropic hardening are incorporated, involving mobile and immobile dislocation both within the lath

interiors and along boundaries. The developed viscoplastic model is applied to high temperature small punch tensile experiments which is described in Chapter 5.

6.2.1 Model Formulation

The material model was based on a limited set on main microstructural variables that represent a selection of the basic strengthening mechanisms in the P91 steel. The present work uses three internal variables instead of using one and two internal variables that are suggested by [169, 170] respectively. The viscoplastic constitutive equations can be presented as:

$$\dot{\varepsilon}^{vp} = \dot{\varepsilon}_o \left(\frac{\sigma_{eq}}{\sigma_f}\right)^m \tag{6-1}$$

The yield surface is defined by the equation

$$f = \sigma - \sigma_f \tag{6-2}$$

The function f determines the elastic domain when $f \leq 0$ and defines the visco-plastic domain when $f > 0$. The increment in effective accumulated plastic strain rate is

$$\dot{p} = \dot{\varepsilon}^{vp} \tag{6-3}$$

The main strengthening mechanisms presented in the current model are PAG size and martensitic lath hardening coupled with stress produced from the existence of the dislocation network inside a hierarchical grain structure, flow stress (σ_f) which has been introduced as

$$\sigma_f = \sigma_d + \sigma_b \tag{6-4}$$

Thus, the hardening rate is considered to be dependent on the evolution of dislocation density during mechanical loading and is represented as:

$$\sigma_d = \sigma_y + \alpha M b \mu \sqrt{\rho}, \tag{6-5}$$

where σ_y is initial yield stress. The PAG size and the martensitic lath width are suggested to enter the problem via two aspects. The dislocations piled up in the vicinity of the packet and lath boundaries will both result in work hardening providing an isotropic hardening contribution previously described in later forms of KME models, contributing to the production of back stress that provides the kinematic hardening component. The back stress caused by stopped dislocations at the packet and lath boundary will prevent the movement of similar dislocations. In its basic formulation, this back stress may be described as,

$$\sigma_b = M b \mu n \left(\frac{1}{L_e}\right) \tag{6-6}$$

Combining Equations (6-5) and (6-6) into (6-4), the flow stress is given by

$$\sigma_f = \left[\sigma_y + \alpha M b \mu \sqrt{\rho} + M b \mu \left(\frac{1}{D} + \frac{1}{\delta}\right)\right] n \left(1 - \frac{n}{n_o}\right) \tag{6-7}$$

The evolution of flow stress form can be expressed as

$$\dot{\sigma}_f = \left[\sigma_y + \alpha M b \mu \frac{\dot{\rho}}{2\sqrt{\rho}} - M b \mu \left(\frac{\dot{D}}{D^2} + \frac{\dot{\delta}}{\delta^2}\right)\right] \dot{n} \left(1 - \frac{\dot{n}}{n_o}\right) \tag{6-8}$$

6.2.2 Evolution of Dislocation Density

The dislocations, whose evolution is presented here, are assumed to form three different populations: (i) mobile dislocations, ρ_m, (ii) immobile dislocations in PAGs and lath interiors, ρ_f, and (iii) immobile dislocations at PAGs and lath boundary, ρ_w, so that the evolution equation for three dislocation densities is defined as:

$$\rho = \rho_m + (1 - f_w)\rho_f + f_w\rho_w \tag{6-9}$$

where f_w is the volume fraction of the PAGs and lath boundary regions. The boundary dislocations can be divided into two groups ($\rho_w = \rho_{ws} + \rho_{wg}$), where ρ_{ws} is the statistical boundary dislocations and ρ_{wg} is the GNDs that improve misorientation across the PAGs and lath boundary. Two competing mechanisms describe the evolution of mobile dislocations: storage and recovery. The storage term can be defined in terms of shear strain increment; the Orowan form is used as [171]:

$$\dot{\rho}_m = \frac{\dot{\gamma}^{pl}}{bL_e} \tag{6-10}$$

where $\dot{\gamma}^{pl}$ shear slip rate and L_e is the mean free path moved by mobile dislocation before it is stopped or annihilated. The Taylor model is used to describe relation between microscopic shear slip rate $\dot{\gamma}^{pl}$ and the macroscopic plastic strain rate $\dot{\varepsilon}^{pl}$ as:

$$\dot{\gamma}^{pl} n = \dot{p} M \tag{6-11}$$

where n is the number of dislocations piled up at the boundaries.

The important strengthening mechanisms of P91 steel is produced by the hierarchical microstructure described above, as shown in Figure 5-1. During the inelastic deformation of P91 steel, in addition to the PAG boundaries, the martensitic lath widths act as additional barriers for dislocations movement, producing more sources of dislocation growth in the material. This action is included in the equations utilizing material parameter L_e which is modified as:

$$\frac{1}{L_e} = \frac{1}{D} + \frac{1}{\delta} \tag{6-12}$$

where D is the average of PAG size of P91 and δ is martensitic lath width. This modification leads to enhancement of the storage evolution term (Equations (6-10) and (6-11)) by adding the PAG size (D) and martensitic lath width (δ) effect,

$$\dot{\rho}_m = \frac{\dot{p}M}{nb}\left(\frac{1}{\dot{D}} + \frac{1}{\dot{\delta}}\right) \tag{6-13}$$

According to Sinclair et al. [172], the dislocation of opposite sign is not reaching to the same area on the slip system (no screening effects), the storage of mobile dislocations in terms of strain increment can be extended as:

$$\dot{\rho}_m = \dot{p}M\left(\frac{1-\dot{n}/n_o}{b}\left(\frac{1}{\dot{D}} + \frac{1}{\dot{\delta}}\right)\right) \tag{6-14}$$

The corrective term $(1 - n/n_o)$ accounts for the fixed number of dislocations that arrive at the boundary.

The overall variation of mobile dislocations is determined by concurrent effects: storage and recovery term. The storage of mobile dislocation is presented using the Orowan form above. To include recovery mechanism, one can recognise the consumption of stored mobile dislocations, which involves the dislocations leaving the glide planes on which they are stored at solid obstacles. The annihilation process is provided either by climb of edge dislocations or by cross slip of screw dislocations. Following the work of Kocks and Mecking, the action of recovery can be represented as thermal activation through the parameter (k_2) which is termed as the thermal recovery constant

$$k_2 = k_{20}(\dot{\varepsilon}^{vp}/\dot{\varepsilon}_o)^{-1/q} \tag{6-15}$$

Here k_{20} is a constant, the temperature dependence is represented by the parameter (q) [173]. Cheong and Busso [174] have determined the probability of a dislocation consumption event via the critical area for the annihilation of mobile dislocation using relation $P = 0.5A\rho_m$. Roters et.al. [175] have concluded that the mechanisms of static recovery of dislocation density mainly are accounted by three events: (i) mutual consumption of two mobile dislocations, (ii) the formation of immobile locked configurations and (iii) dipole dislocation formation. The present study extends the Kocks approach of thermal recovery and includes the mechanisms of athermal consumption of mobile dislocation of [175, 174]. The extended equation of evolution of mobile dislocation density can be presented as

$$\dot{\rho}_m = \dot{p}M\left(\frac{1-\dot{n}/n_o}{b}\left(\frac{1}{\dot{D}}+\frac{1}{\delta}\right) - \left(2d_{dip} + \left(\frac{\dot{n}}{n_o-\dot{n}}\right)4d_{lock} + d_e\right)\frac{1+k_2}{b}\rho_m\right) \tag{6-16}$$

where d_{dip} dipole formation, d_{lock} locked configurations and d_e the critical distances for loss of mobile dislocations due to annihilation. In parallel to Equation (6-14), we also passed the corrective term $(1 - n/n_o)$ in to Equation (6-16). The evolution of n can be expressed as

$$\dot{n} = \frac{M\gamma}{b}\left(1 - \frac{\dot{n}}{n_o}\right)\dot{p} \tag{6-17}$$

where γ is the mean spacing between slip bands and n_o is the critical value of dislocations piled up at the boundaries. According to the second mechanism, explained above, the evolution of immobile dislocations in PAGs and lath interiors, ρ_f, accounts for the consumption of mobile dislocations result from the formation of immobile locked configuration and climb dislocations action respectively [150, 176].

$$\dot{\rho}_f = 4\dot{p}M\left(1 - \frac{\dot{n}}{n_o}\right)\frac{d_{lock}}{b}\left(\frac{\dot{n}}{n_o - \dot{n}}\right)\dot{\rho}_m - m_{cl}\mu b^2\dot{\rho}_f^2 \tag{6-18}$$

where m_{cl} is the rate of climb dislocations movement. The immobile dislocations at PAGs and lath boundary, ρ_w, can be given by

$$\rho_{wg} = \left(\frac{1}{D} + \frac{1}{\delta}\right)^2 \tag{6-19}$$

and then the rate of the immobile dislocations at PAGs and lath boundary

$$\dot{\rho}_{wg} = 2\left(\frac{\dot{D}}{D^3} + \frac{\dot{\delta}}{\delta^3}\right) \tag{6-20}$$

6.2.3 Growth of the PAG Size and Lath Microstructure

Two mechanisms are presented in this work to simulate the growth of PAG size and martensitic lath respectively. The growth of PAG size is presented here to involve both static growth size (time-dependent growth resulting from the elevated temperature) and a plastic strain dependent due to applied mechanical load. The evolution change of grain size in terms of plastic strain can be expressed as,

$$\dot{D} = \zeta_D \exp(-Q_D/RT) D^{-\alpha_D} + \frac{1}{\alpha b a \rho} \dot{p} \tag{6-21}$$

where α_D is a material parameter, ζ_D is a static PAG growth size, Q_D is the activation energy for PAG size growth, R is the gas constant and a is unit cell constant.

The evolution of martensitic lath width can be given by differential equation:

$$\dot{\delta} = (\zeta_\delta \exp(-Q_\delta/RT) + \omega_\delta \dot{p}) \delta^{-\alpha_\delta} \tag{6-22}$$

where α_δ is a material parameter, ζ_δ is a static lath growth size, Q_δ is the activation energy for lath growth and ω_δ is a dynamic lath growth constant.

6.3 UMAT Implementation

The implicit integration approach has been carried out to obtain the increment in effective plastic strain. According to Dunne and Petrinic, the von Mises equivalent stress, σ, has been represented as a function of the trial stress and the increment of effective plastic strain rate as follows [38]

$$\sigma_{eq} = \sigma_{eq}^{(trial)} - 3\mu\Delta p \tag{6-23}$$

where the von Mises equivalent trial stress, $\sigma_{eq}^{(trial)}$, is defined as

$$\sigma_{eq}^{(trial)} = \left[\frac{3}{2}\, \mathcal{S}_{ij}^{(trial)} \mathcal{S}_{ij}^{(trial)}\right]^{1/2} \tag{6-24}$$

Thus, the increment in effective accumulated plastic strain-rate given in Equation (6-3) may be rewritten as follows

$$\dot{p} = \phi(\Delta p, \rho, D, \delta, n) = \dot{\varepsilon}_o \left(\frac{\sigma_{eq}^{(trial)} - 3\mu\Delta p}{\left[\alpha M b \mu\sqrt{\rho} + M b \mu\left(\frac{1}{D} + \frac{1}{\delta}\right)\right] n\left(1 - \frac{n}{n_o}\right) + \sigma_y}\right)^m \tag{6-25}$$

In order to be applicable to the Newton iterative approach, the Equation (6-25) can be written in an incremental form as

$$\psi(\Delta p, \rho, D, \delta, n) = \Delta p - \phi(\Delta p, \rho, D, \delta, n)\Delta t = 0 \tag{6-26}$$

Implementing the Newton iterative method then yields

$$\psi + \frac{\partial \psi}{\partial \Delta p} d\Delta p + \frac{\partial \psi}{\partial \rho} d\rho + \frac{\partial \psi}{\partial D} dD + \frac{\partial \psi}{\partial \delta} d\delta + \frac{\partial \psi}{\partial n} dn = 0 \tag{6-27}$$

Thus, calculating the partial derivatives and rearranging Equation (6-27) to describe the iterative increment in effective plastic strain gives

$$d\Delta p = \frac{\frac{\Delta p}{\Delta t} - \dot{\varepsilon}_o \left(\frac{\sigma_{eq}^{(trial)} - 3\mu\Delta p}{\left[\alpha M b \mu\sqrt{\rho} + M b \mu\left(\frac{1}{D} + \frac{1}{\delta}\right)\right] n\left(1 - \frac{n}{n_o}\right) + \sigma_y}\right)^m}{\frac{1}{\Delta t} - \left(\frac{\partial \psi}{\partial \Delta p} d\Delta p + \frac{\partial \psi}{\partial \rho} d\rho + \frac{\partial \psi}{\partial D} dD + \frac{\partial \psi}{\partial \delta} d\delta + \frac{\partial \psi}{\partial n} dn\right)} \tag{6-28}$$

And the increment in effective plastic strain yields

$$\Delta p = \Delta p + d\Delta p \tag{6-29}$$

The internal variable, Δp, is updated at each increment until convergence is obtained. The tolerance within the current study is set as 1×10^{-12} and convergence is checked against the term ψ, where the iterative scheme will end when the term, ψ, is less than the tolerance.

The improved model was also implemented within a UMAT user material subroutine via the commercial finite element code ABAQUS. A flowchart showing the essential procedures within UMAT is depicted in Figure 6-1. The increment in plastic strain and stress tensor is calculated using the flow rule of Equation (4-24b) and Equation (4-24d), respectively. For more details on the implementation of 3D stress space, see Section 4.3 in Chapter 4.

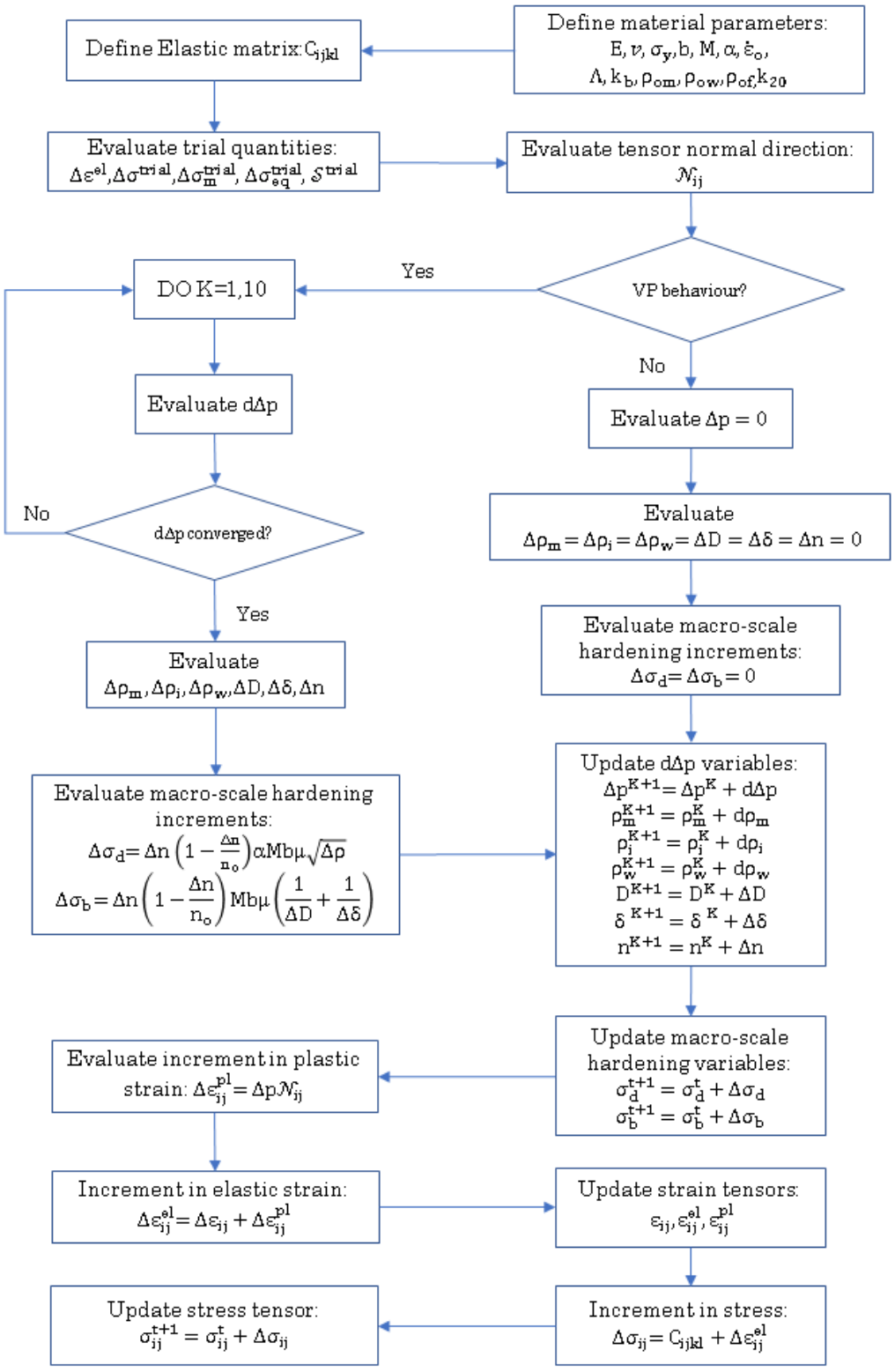


Figure 6-1. Flow chart describing the main processes in the UMAT user material subroutine.

6.4 Determination of Material Parameters

The material parameters within this study can be divided into three main groups, namely: (i) elastic material parameters such as Young's modulus, E, Poisson's ratio, v, and initial yield stress, σ_y, (ii) the viscoplasticity material parameters, $\dot{\varepsilon}_o$ and m, and (iii) the microstructural material parameters, related to the evolution of dislocation density and the grain and lath structure.

The elastic parameter, v, has been taken as a constant value of 0.3 throughout the current study although it is a temperature dependent parameter. The elastic parameters E and σ_y were taken from Ref. [165]. The viscoplasticity material parameter, $\dot{\varepsilon}_o$, was taken from Ref. [64] while the parameter m was obtained from $\frac{\Lambda}{Tk_b}$ where the constant, Λ, is assumed to be equal to 5.0 for steel, T is the temperature and k_b is the Boltzmann constant [177]. The elastic-viscoplasticity material parameters for The P91 steel at 600℃ presented in Table 6-1. As P91 steel consists of FCC crystals, the Taylor factor is 2.9, and the magnitude of the Burgers vector is 0.248nm. The specific microstructural material parameters related to (i) dislocation densities, (ii) evolution of PAGs size and (iii) evolution of the martensitic laths are presented below. The microstructural material constants utilized here are listed in Table 6-2. The initial mean size for the P91 PAGs has been obtained from measurements using EBSD which has been determined to be equal to 50μm , shown in Figure 5-28. Similarly, the initial lath martensitic width of the P91 steel has been obtained from Ref. [150]. The volume fraction has been defined as follow [178].

$$f_w = 3t_w/(D + \delta) \quad (6\text{-}30)$$

where t_w is the cell wall thickness which has been assigned as a constant value of 100b [138]. The P91 steel has an initial overall dislocation density with limit values between $1.6 \times 10^{13} m^{-2}$ and $7.5 \times 10^{13} m^{-2}$ identified for heat treatment process on steel using TEM [179, 3]. The initial yield stress values for the P91 steel at different temperatures have been presented by Aziz as shown in Table 6-3 [165]. These values provided to Equations (6-4) to calibrate the material constant α and the initial dislocation density, ρ_o. The calibrated initial value of ρ_o lies between $1.0 \times 10^{13} m^{-2}$ and $5.5 \times 10^{13} m^{-2}$ and α lies within the range 0.3-0.7. According to Magnusson and Sandstrom, the initial immobile dislocations in PAGs and lath interiors, ρ_{of}, has been appointed to low value of $1 \times 10^{11} m^{-2}$ [138]. The initial density of immobile dislocations at PAGs and the lath boundary, ρ_w, of the 'as-received' material is generally 10% less than the overall dislocations [180], so that the initial value of immobile dislocation density, ρ_{ow}, for both the PAGs and the lath boundaries is taken to be $0.9\rho_o$.

Table 6-1. The elastic-viscoplastic material parameters at 600℃ [165, 177].

T (℃)	E (GPa)	σ_y(MPa)	v	$\dot{\varepsilon}_o$ (s^{-1})	Λ
600	139.4	80	0.3	1	5.0

Table 6-2. Microstructural material constants [136, 138, 150].

Parameter	Value	Parameter	Value
ρ_o	$1.0 \times 10^{13} m^{-2}$	t_w	100 b
ρ_{ow}	$0.9\rho_o$	n_o	6
δ_o	0.7μm	d_{dip}	7b
b	0.248nm	d_{lock}	b
α	0.5	d_e	6b
M	2.9	γ	2.002
k_{20}	22	m_{cl}	2×10^{-3}
α_D	2.002	ω_D	2.5×10^{-9}
ζ_D	1.0×10^{-18}	α_δ	2.002
Q_D	303KJ/mol	ζ_δ	1.0×10^{-18}
a	1.0	Q_δ	303KJ/mol
D_o	50 μm	ω_δ	2.5×10^{-9}

Table 6-3. The initial constants of the viscoplasticity model for P91 at different temperatures [165].

T (℃)	E (GPa)	σ_y(MPa)
400	197.5	96
500	181.3	90
600	139.4	80

6.5 Results and Discussion

The objective of the finite element simulation of the SPT specimen is to validate the multiaxial behaviour of the developed dislocation-based viscoplasticity model. The SP rig, as shown in Figure 4-11, is represented by an axisymmetric model as given in Figure 4-12. The type of element mesh and boundary conditions on the SPT model have been described in Chapter 4. The FE simulation were carried out with displacement-controlled condition of the P91 steel at 600℃. The effects of five primary micro-structural variables, i.e. (i) the initial mobile dislocations density (ii) the initial immobile dislocations in PAGs and lath interiors (iii) the initial immobile dislocations at PAGs and lath boundary (iv) initial PAGs size and (v) initial lath width on predicted plastic strain-range have been studied.

6.5.1 FE Simulation of the SPTT

To achieve the universal small punch tensile responses from FE simulation and experimental investigation, the modified dislocation based viscoplastic model were interrupted after a set of punch displacement intervals (0.26, 1.0, 1.25, 1.5,1.65 and 1.74mm) to help conclude the complex and evolving micro-mechanical states that was developed during small punch tensile test. The FE simulation results of the SPT of displacement rate of 2 μm/sec at 600℃ are shown in Figures 6-2 to 6-9. The maximum principal strains (red contour) are located at lower surface of specimen when beginning of punch movement, i.e. 0.26, 1.0 and 1.25mm, as shown in Figure 6-2. Figure 6-3 shows the contour plots of the maximum principal strain at puncher displacement of 1.5, 1.65 and 1.74mm.

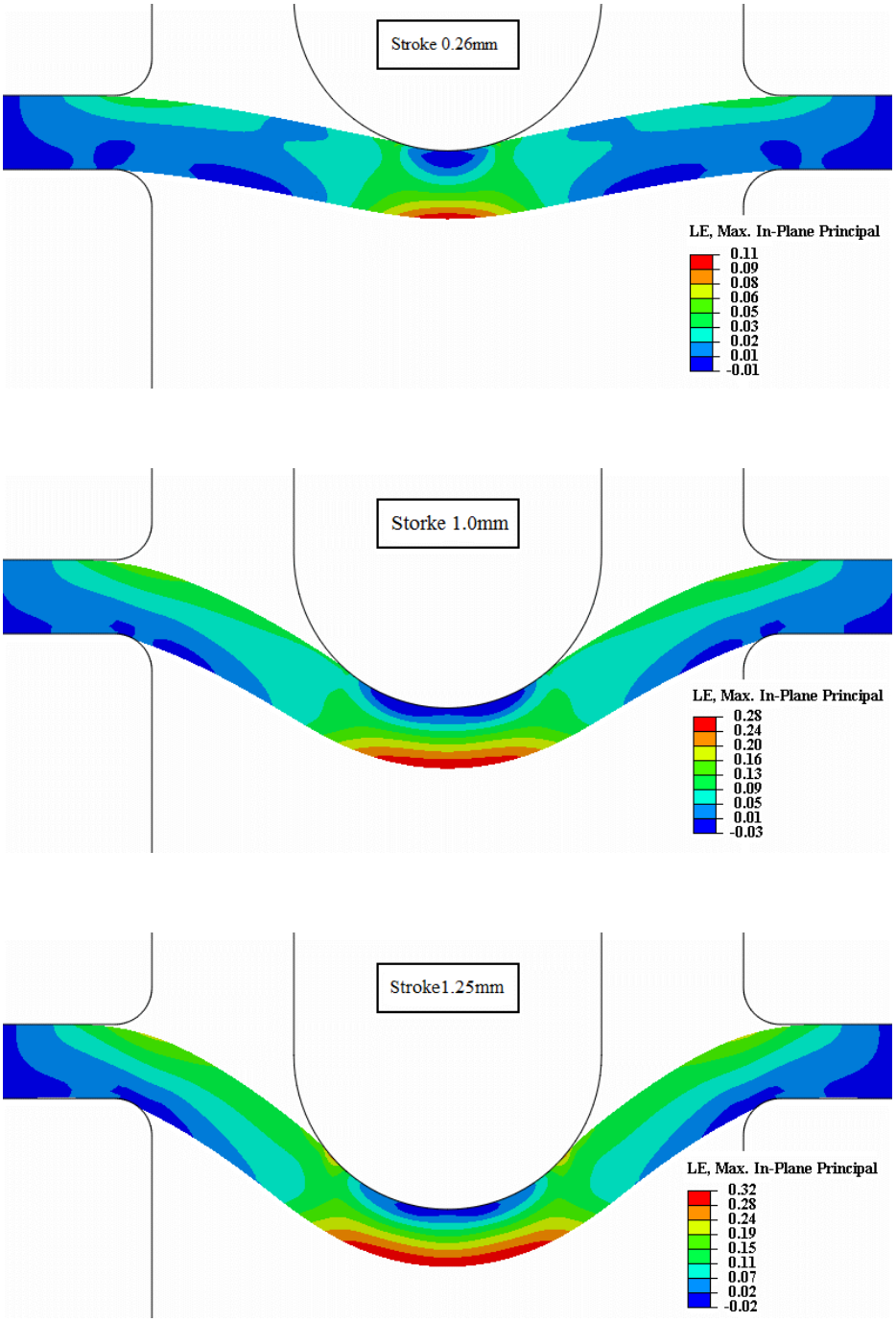


Figure 6-2. Maximum principal strains at a Puncher displacements of 0.26, 1.0 and 1.25mm.

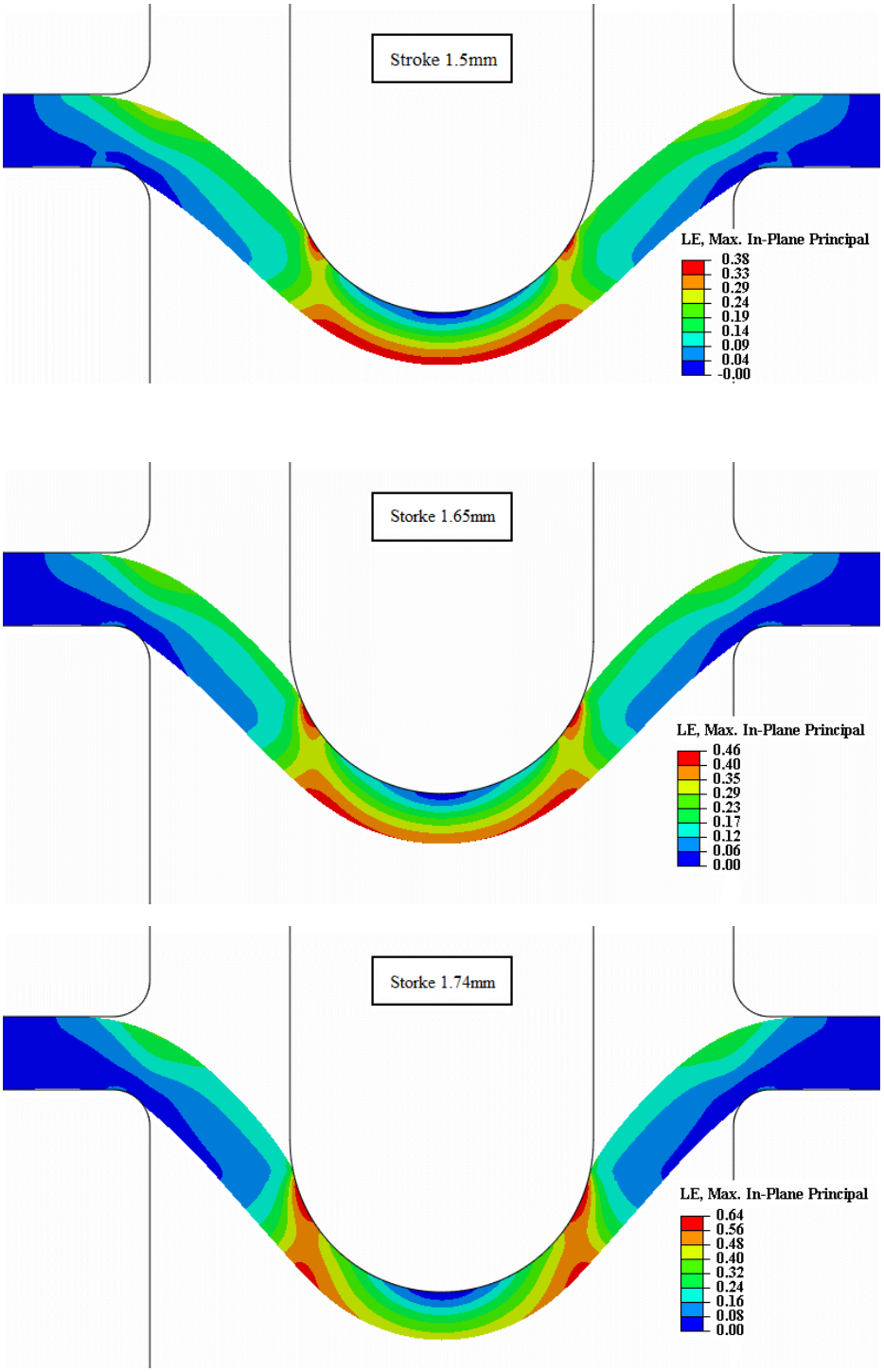


Figure 6-3. Maximum principal strains at a Puncher displacements of 1.5, 1.65 and 1.74mm.

The contour plots of the FE simulation show that the high strain locations were founded near the bottom surface of the specimen and near the contact edge between the punch with top surface of specimen. This strain evolution through the small punch tensile test is compatible with that reported in the literature [119, 120]. The evolution of the peak strain is not identical in both surfaces, i.e. the top and bottom surface of specimen, as a result of different plastic mechanisms, bending and stretching, in the various elements of specimen as well as the effect of the contact. The elements in the region close to support die exhibit a plastic resistance effect and the strain level at this area (blue contour) becomes low. It should be noted that the strains regions pointed in Figures 6-2 and 6-3 are in agreement with the area of the specimen where voids growth and cracks initiation were formed during the interrupted small punch tensile tests presented in Chapter 5.

We have presented a detailed definition of the dislocation development upon athermal storage, thermal recovery and static recovery, see Equations 6-12 and 6-14, of P91 steel. The evolving of dislocation densities at temperature 600℃ is shown in Figures 6-3 and 6-4. The contour plots show the developing dislocation density field exhibits the same trend upon beginning of punch movement and there is a high compression stress field in the punch contact region which leads to localised dislocation density and then flow stress. In the region close to bottom surface, which is described by the high strain field, the dislocation density (red contour) occurs in that area at the beginning of punch movement, i.e. 0.26, 1.0 and 1.25mm, as shown in Figure 6-4. The punch-specimen contact region increases as the punch moves more, and as a result, the evolution of dislocation

densities pointed to propagate further from the lower surface of the specimen, i.e. stroke puncher of 1.5, 1.65 and 1.74mm as depicted in Figure 6-5. In the region close to upper die, top surface of specimen, the evolution densities occurs at the beginning of stroke punch of 1.5mm, as a result of bending deformation at this area. When the punch stroke increases from 1.5 to 1.65mm and then 1.74mm, the dislocation field arises at the region close to the punch-specimen contact interface and then moves from this area to the lower surface of specimen. The global densities of the specimen is related to the maximum principal strain fields, which show values around $33.3 \times 10^{13}\ \mathrm{m}^{-2}$ in the annular region close to punch-specimen contact edge.

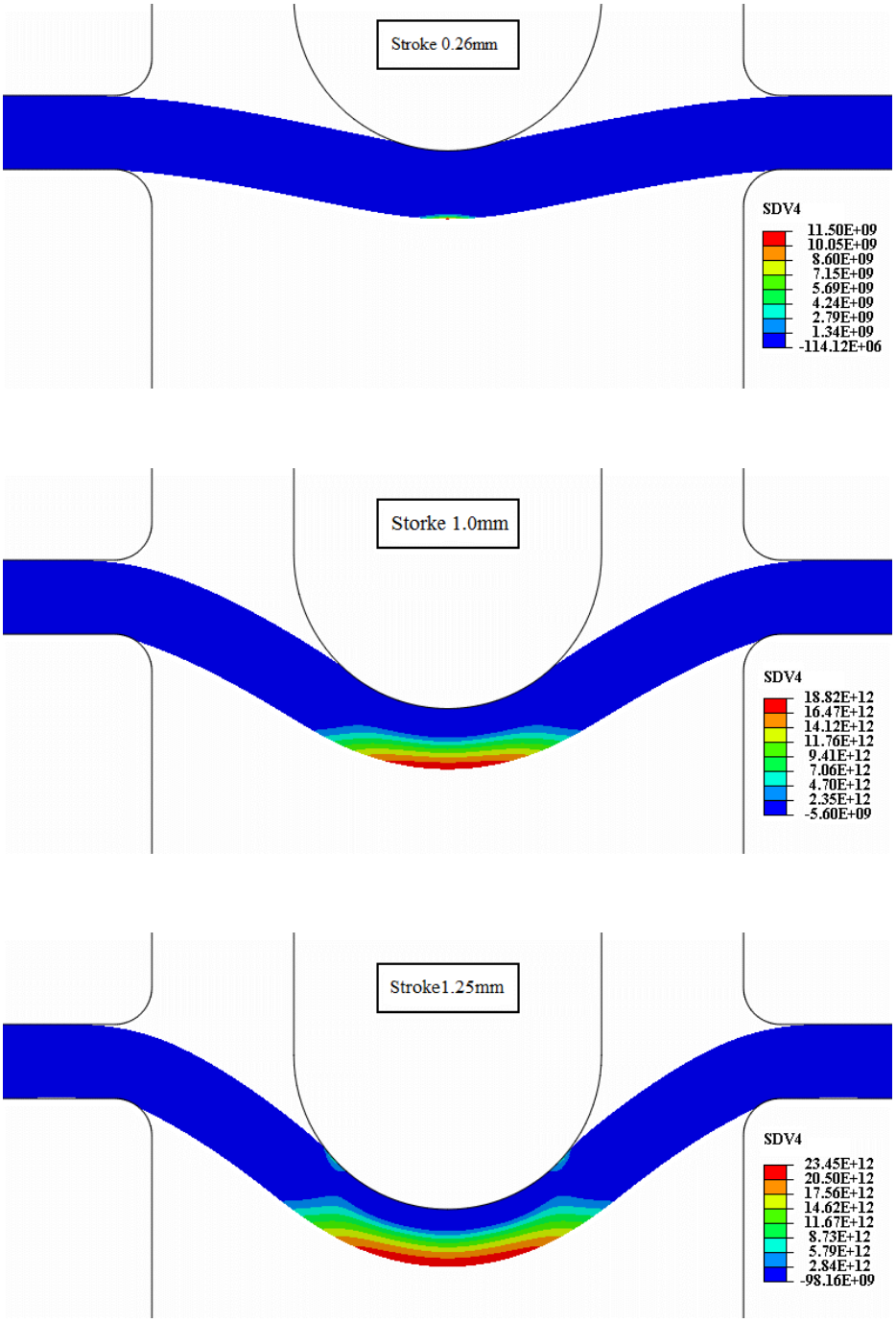


Figure 6-4. The evolution of dislocation densities (SDV4) at a Puncher displacements of 0.26, 1.0 and 1.25mm.

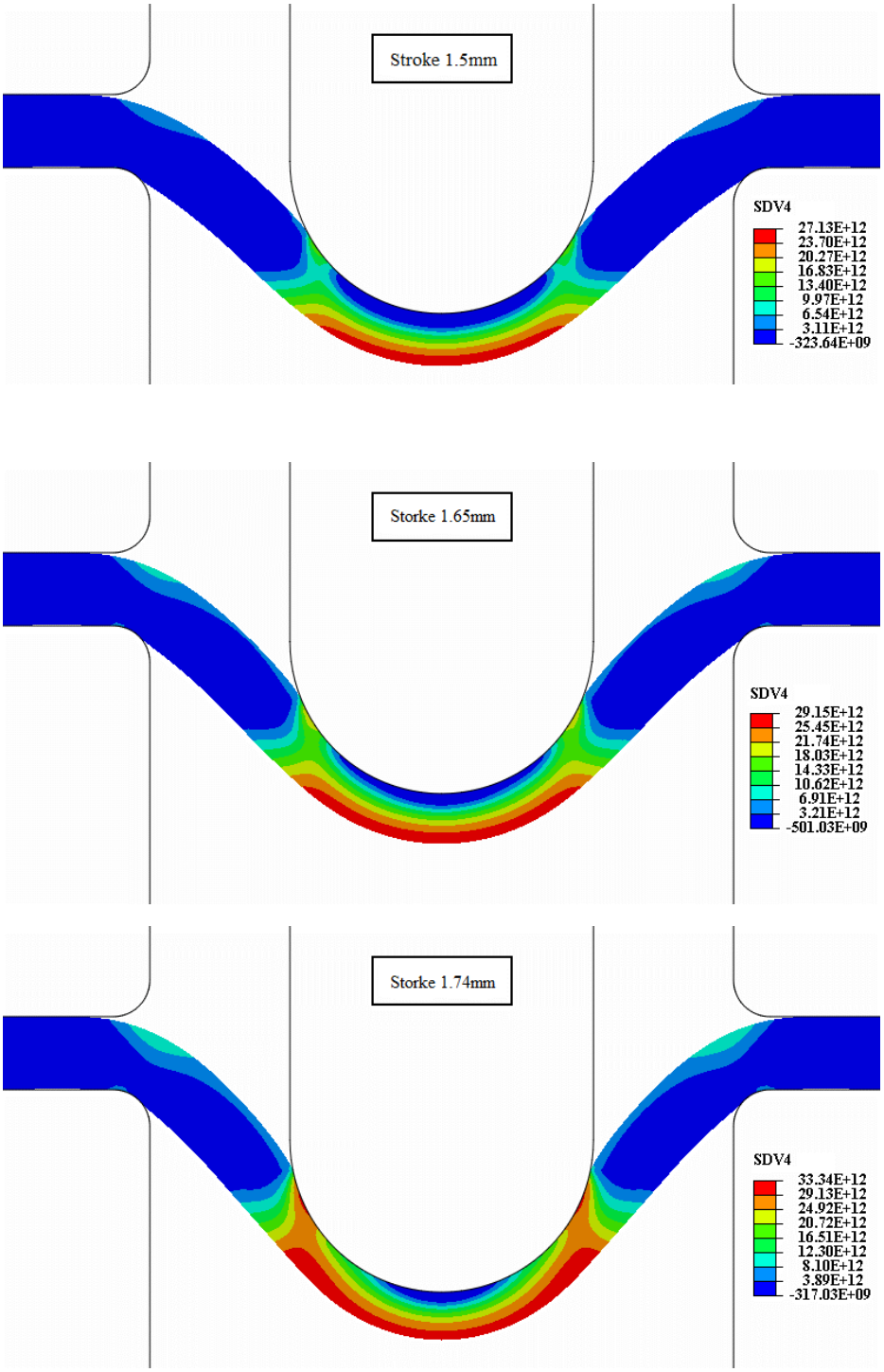


Figure 6-5. The evolution of dislocation densities (SDV4) at a Puncher displacements of 1.5, 1.65 and 1.74mm.

Figures 6-6 and 6-7 show the contour plots of equivalent stress distribution of the specimen during the SPTT. The equivalent stresses are usually peak at the beginning of loading because elastic-plastic deformation is initially dominant at the lower surface of specimen i.e. punch stroke of 0.26mm. The central region of the specimen is described by the minimum bending stiffness because the centre of specimen locates at the maximum distance from the holder and support dies. It can be seen in Figure 6-6 that when punch reached the stroke of 1.0mm, the stresses (blue contour) of the specimen decreased because the von Mises stresses in this area are compression stresses. However, as depicted in Figures 6-8 and 6-9, with the increase of punch displacement, the U1 displacements in the top surface of specimen with the decrease of stresses also decreased. As puncher further proceeds, the specimen develops into conical in shape, and "membrane stretching" at the annular region of the lower surface of specimen becomes dominate mechanism. Meanwhile, the von Mises stresses in the opposite surface (lower surface) of specimen which promoted the evolution of voids is increased. The increase of punch displacement, the U1 displacements in the lower surface of specimen which confirmed the increase of stresses are decreased too, as shown in Figures 6-8 and 6-9. From Figures 6-6 and 6-7, it can be seen that the von Mises stresses first increased at stroke of 0.26, 1mm then decreased at stroke of 1.25mm and then increased again at stroke of 1.5, 165 and 1.74mm with the punch displacement increased.

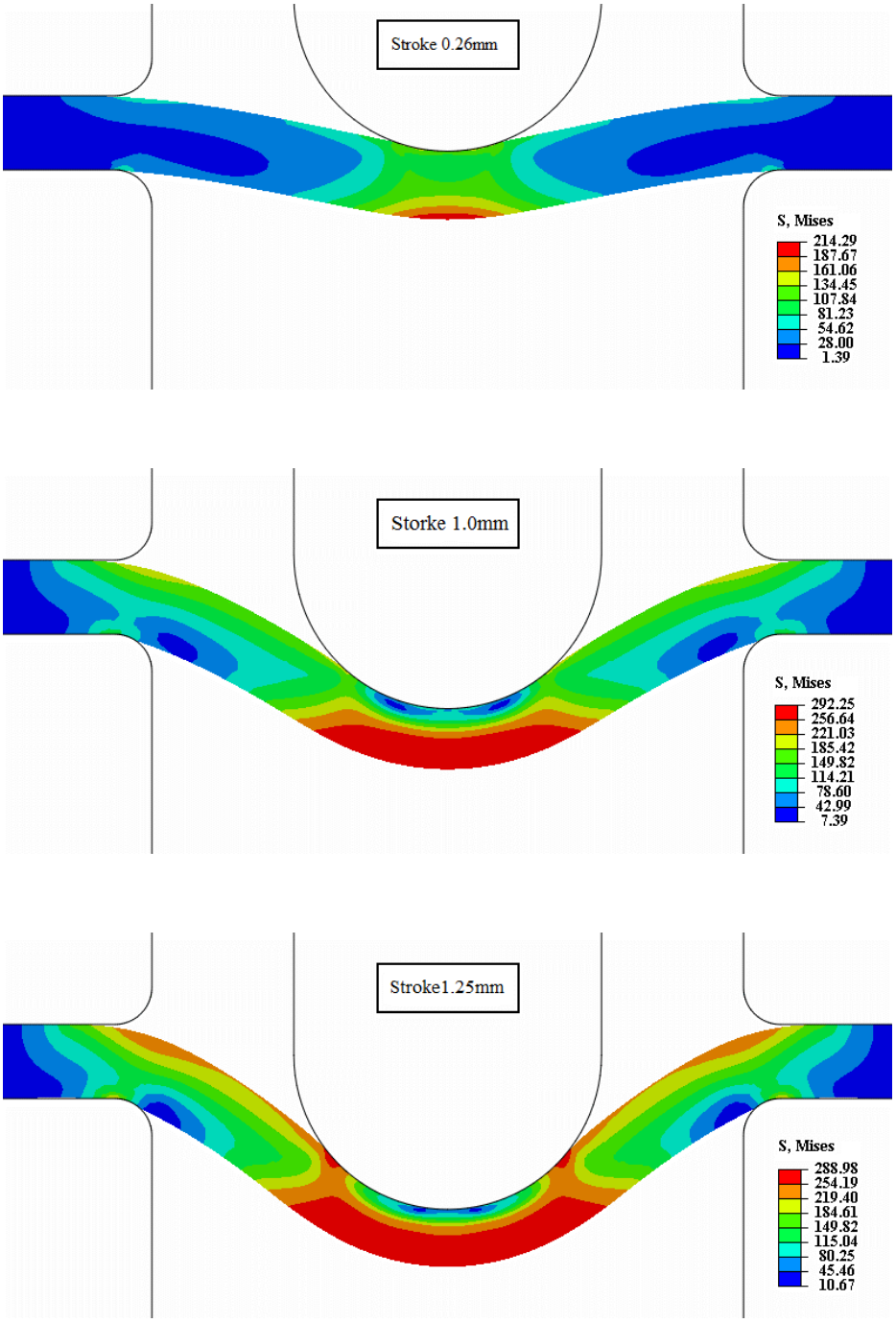


Figure 6-6. Mises stresses at a Puncher displacements of 0.26, 1.0 and 1.25mm.

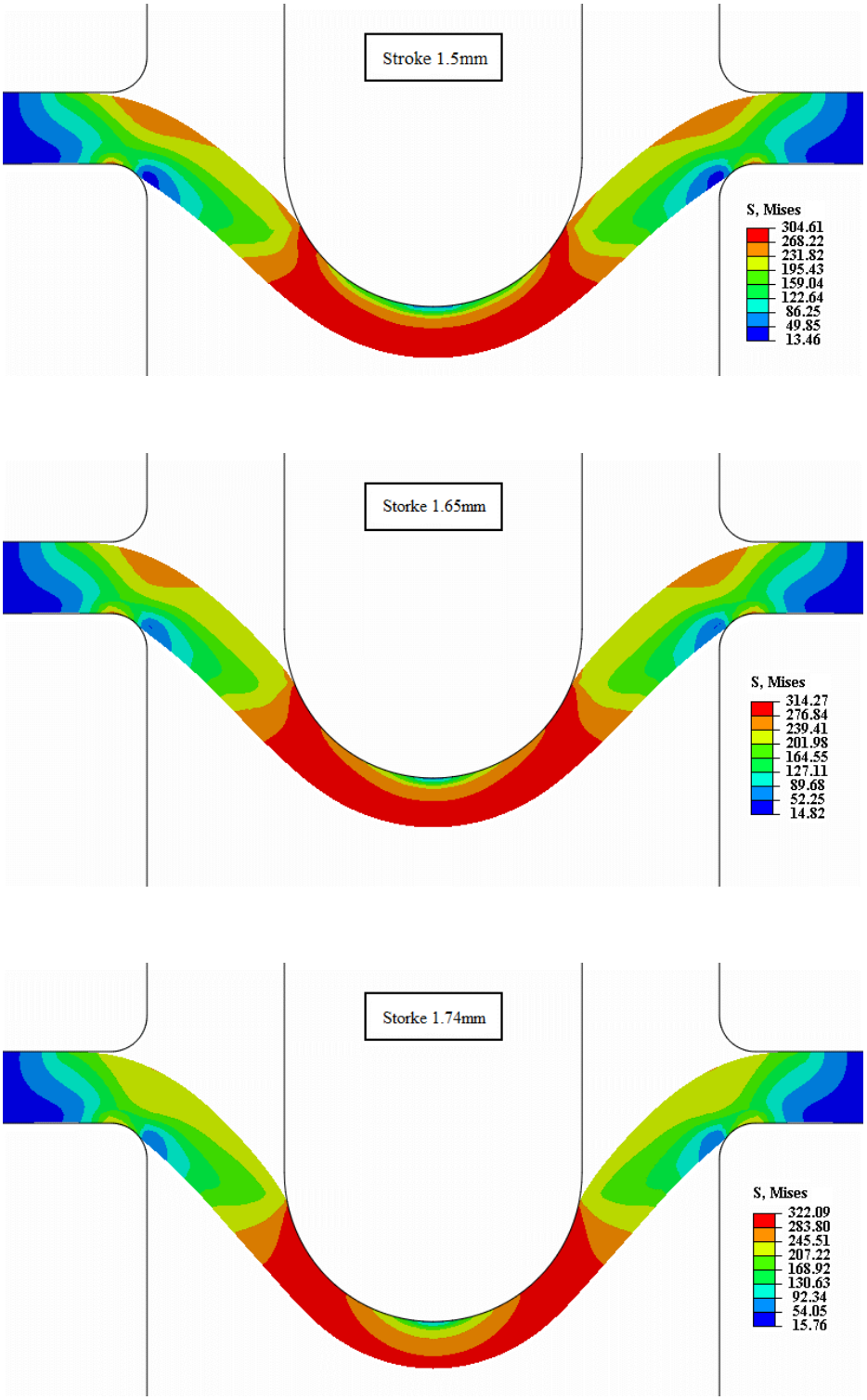


Figure 6-7. Mises stresses at a Puncher displacements of 1.5, 1.65 and 1.74mm.

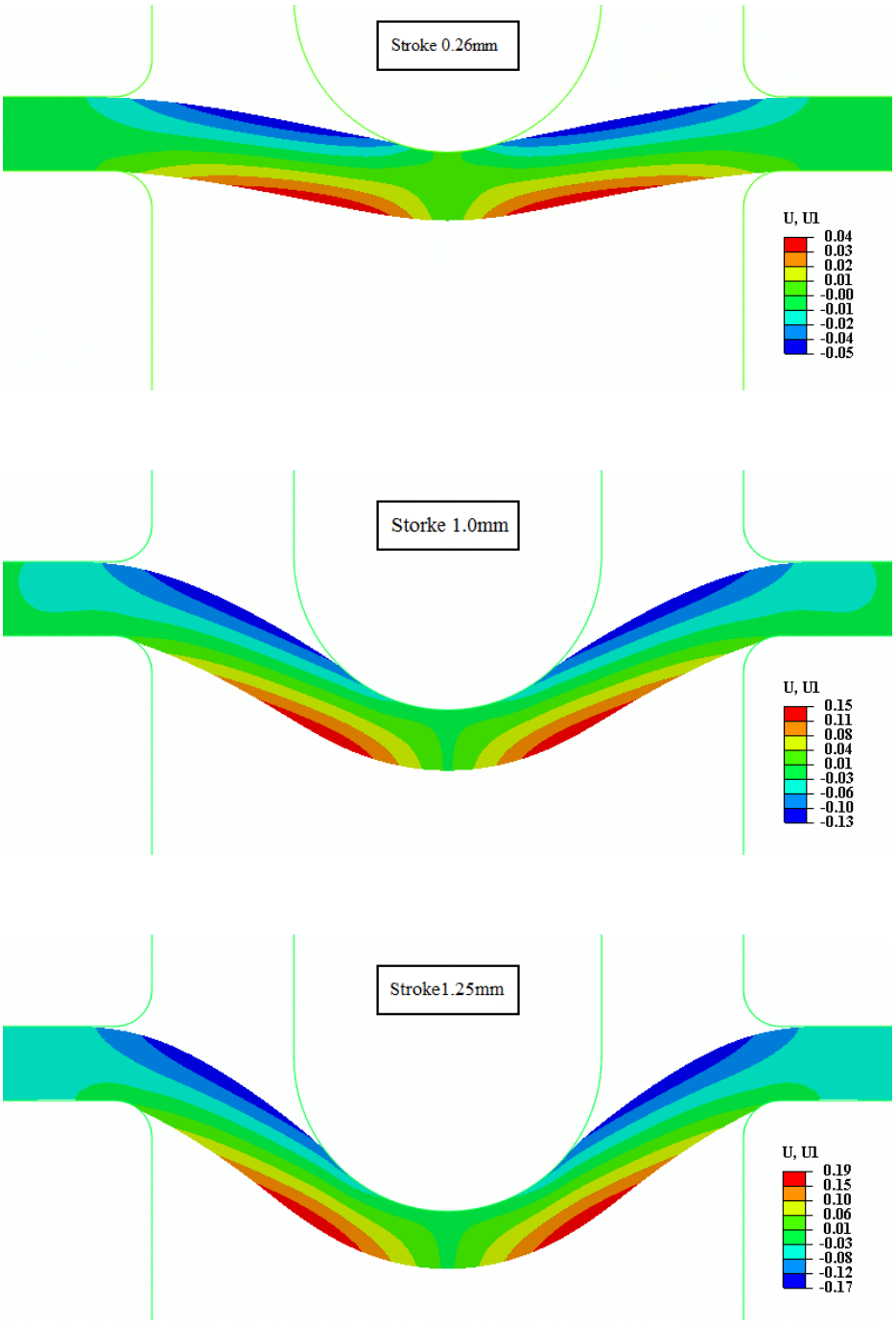


Figure 6-8. The x-axis (U1) displacement at a Puncher displacements of 0.26, 1.0 and 1.25mm.

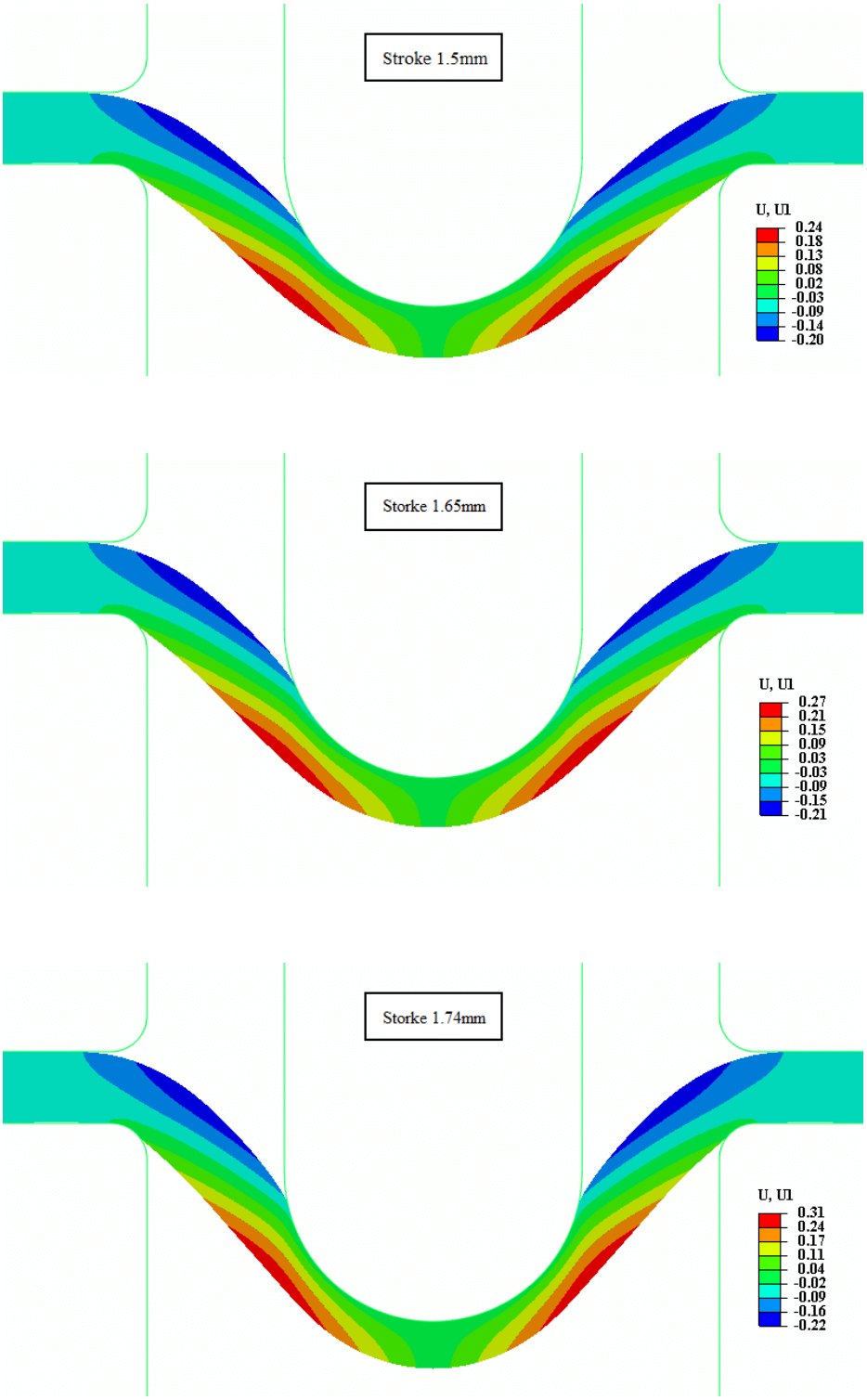


Figure 6-9. The x-axis (U1) displacement at a Puncher displacements of 1.5, 1.65 and 1.74mm.

6.5.1.1 The Evolution of Microstructure

The comparison between the deformed shape predicted by FE and the morphology of the dome-shaped deformed P91 specimens, is shown in Figure 6-10 for punch displacement of 1.0mm, 1.25mm and Figure 6-11 for punch displacement of 1.5mm and 1.65mm respectively. Good agreement is observed between FE and experiments, i.e. the dome shape is very similar for both FE and experiment. At a puncher displacement of 1mm, it can be seen that the FE of specimen thickness remains the same without the observed thinning as shown in Figure 6-10. The FE dome shape has developed further, at puncher displacement of 1.25mm in Figure 6-10, due to the increase of the puncher displacement. It can be noticed that the thinning occurs in the FE plot and also through the microstructure of specimen. In Figure 6-11, the dome shape has extended further due to the further increase of puncher displacement, i.e. 1.5mm. It can be seen that the highly strained area has extended through the lower surface of the specimen within the thinned region The extension of the dome shape becomes more obvious when the puncher moves to 1.65mm. It is noted that the highly strain area moves toward the edge of contact between specimen and puncher. Further highly strain area is also developed at the contact point between the specimen and puncher. Both highly strain regions, shown by the red contour at 1.65mm, are subjected to the thinning and necking as observed experimental at a puncher displacement of 1.65mm. As Figures 6-8 and 6-9, the U1 displacement is indicated to stretched and elongated region in which the plastic flow locates. It can be seen that the region near to the lower surface of specimen is subjected to “tensile effect”, due to U1 displacement, when the puncher continues to deform the discs. This behaviour means that the

evolution of dislocation of the P91 specimen mainly increases along the direction of plastic flow, which is in agreement with Equation (6-4). The elongated grains, as depicted in Figures 5-23 to 5-27, allow more pile up of mobile dislocations at the grain boundary and sliding of immobile densities across the PAGs and lath boundaries. Since high strain and dislocation values also occur at the lower surface of specimen, stretching effect area, nucleation of voids, thinning and the fracture site develop in this area.

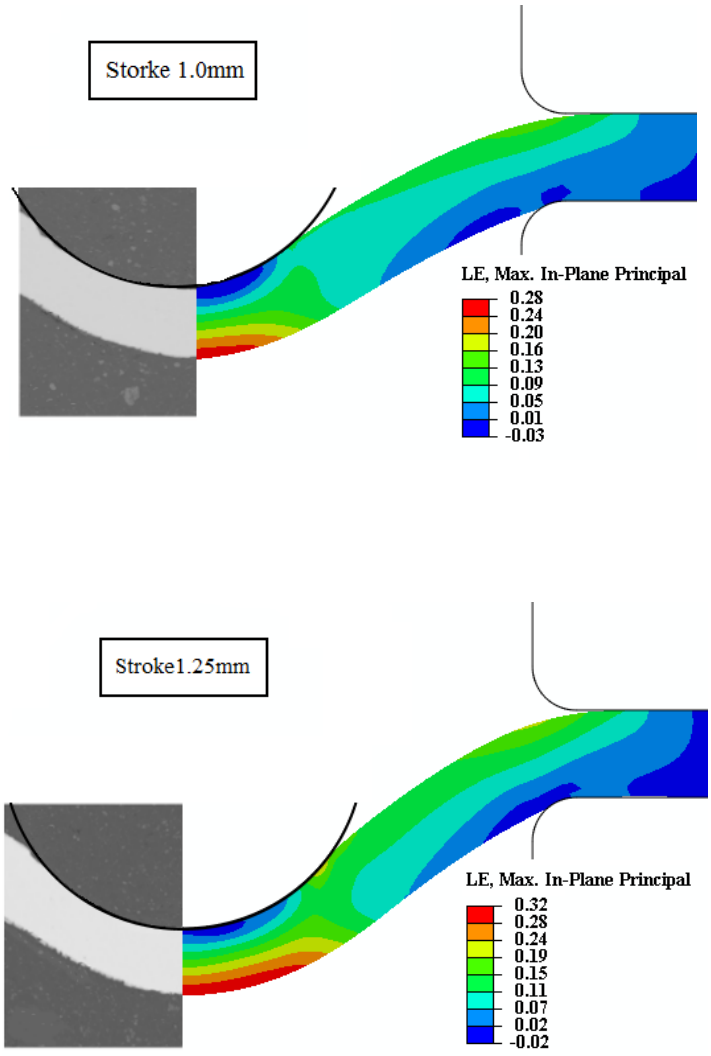


Figure 6-10. Contour plot of strain and SEM images of SPTT at interrupted displacements of 1.0 and 1.25mm for the P91 steel at 600℃.

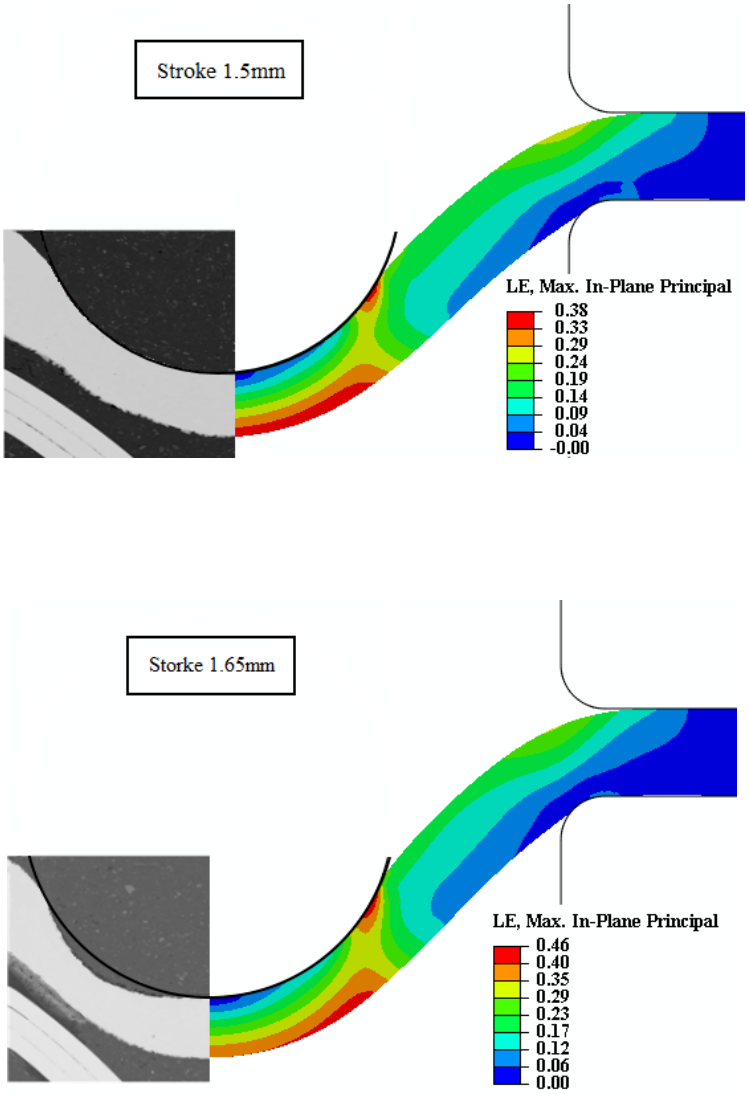


Figure 6-11. Contour plot of strain and SEM images of SPTT at interrupted displacements of 1.5 and 1.65mm for the P91 steel at 600℃.

6.5.1.2 Bulk Deformation

The comparison between the predicted and experimental deflected shapes of deformed P91 specimens are shown in Figures 6-12 to 6-15 for punch displacement at 1.25mm, 1.5mm, 1.65mm and 1.74mm respectively. At puncher displacement of 1.25, i.e. Figure 6-12, the FE dome shape develops progressively. It can be noted from this shape, the maximum strain value is concentrated at the central of the specimen. Cracks may occur at the highly strain region (red contour). These cracks are clearly observed, as brittle cracks in the oxide layer, in the morphology of deformed P91 discs as depicted in Figure 6-12. The shape of the FE dome becomes more evident when the puncher displacement increases to 1.5mm as shown in Figure 6-13. It can be seen that the size of dome shape increases more and the region of highly strain is extended. More surface cracks may develop within the highly strain region (red contour in Figure 6-13) which is in agreement with that was observed in Chapter 5, i.e. Figure 5-18. The comparison between FE contours and the dome-shaped deformed P91 specimen for punch displacement at 1.65mm is shown in Figures 6-14. The predicted shape dome has increased due to the further large puncher displacement. Highly strained region has extended more at the edge of contact between specimen and puncher which leads to the initiation of necking and thinning, due to the nucleation of voids, as depicted in Figure 6-14 and Figure 5-19. Figure 6-15 shows the comparison between FE contours and the dome-shaped deformed P91 specimen for punch displacement at 1.74mm. The predicted shape dome shape of discs is increased due to the large puncher displacement. It can be seen that the highly strain region has moved from the central of specimen (yellow contour) to

around the edge contact between specimen and puncher (red contour). The fracture of the dome shape has occurred at this region as depicted in Figure 6-15.

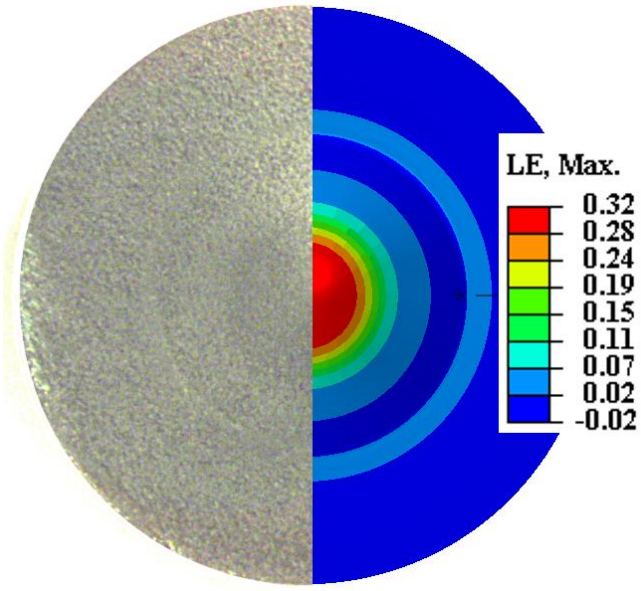


Figure 6-12. The comparison between FE result and the dome-shaped deformed P91 specimen for punch displacement of 1.25mm.

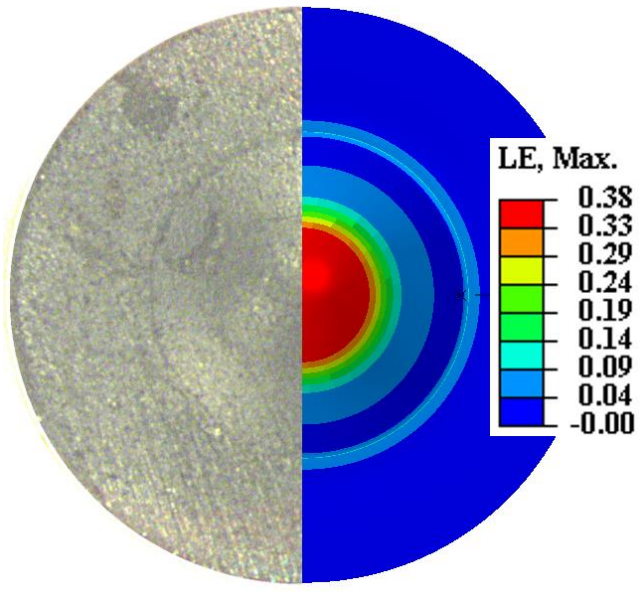


Figure 6-13. The comparison between FE result and the dome-shaped deformed P91 specimen for punch displacement of 1.5mm.

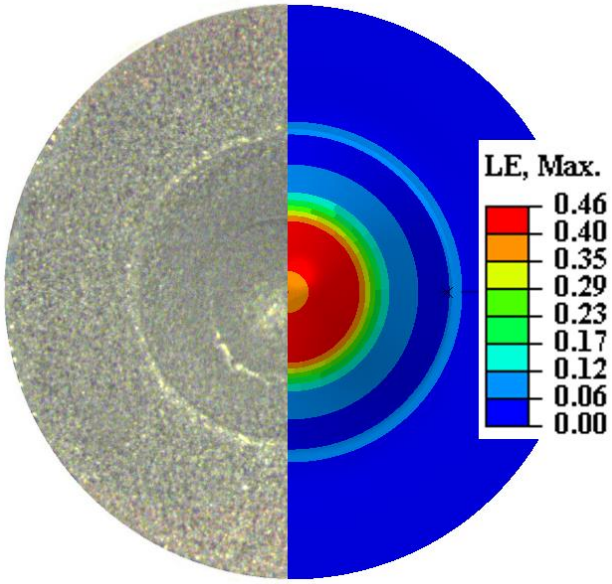


Figure 6-14. The comparison between FE result and the dome-shaped deformed P91 specimen for punch displacement of 1.65mm.

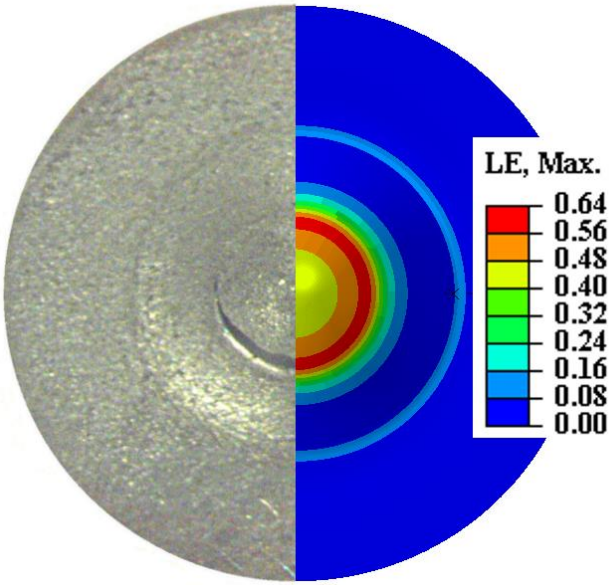


Figure 6-15. The comparison between FE result and the dome-shaped deformed P91 specimen for punch displacement of 1.74mm.

6.5.2 Small Punch Tensile Curves

The load-displacement curves obtained from experiment and FE simulation are shown in Figure 6-16. The FE result of force shows good agreement with corresponding of the experimental curves. Best fit of FE results with the experimental data using a friction coefficient of 0.2 has been described in [181, 88]. FE simulation of SPT were performed with various initial micro-structural parameters of the P91 at 600℃. They are characterized by initial PAGs size D_0 and martensitic lath width δ_o. The effect of initial PAGs size and lath width on the punch load level is shown in Figure 6-17. The maximal force value ranged from about 700N, for $D_0 = 50\mu m$ and $\delta_o = 7\mu m$, to about 800N, when $D_0 = 35\mu m$ and $\delta_o = 6\mu m$. Therefore, the effect of the initial PAGs size and lath width are significant in the FE simulation of SPTTs. The influence of initial PAGs size and lath width on the evolution of dislocation density during small punch tensile FE simulation of the P91 is reported in the Figure 6-18. This figure shows the variation of evolving dislocation density curves of different initial values of PAGs size and lath width under the punch displacement of $2\ \mu ms^{-1}$. The dislocation density increases from about $4 \times 10^{13}\ m^{-2}$, the final stage, of $D_0 = 50\mu m$ and $\delta_o = 7\mu m$ to about $5.5 \times 10^{13}\ m^{-2}$ when $D_0 = 35\mu m$ and $\delta_o = 6\mu m$. It can be seen from Figure 6-18, that with the decrease of the micro-structure parameters, the peak dislocation density on the dislocation-plastic increased significantly and the displacement of peak load changed too. Thus, the multiaxial stress and then voids changed significantly too. From Figures 6-17 and 6-18, it can be seen that the force-displacement and the evolution of dislocation density responses of the FE simulated curves (and the tested force-displacement curves) are not always

overlapping in the beginning of the curve. The effect of friction coefficient, μ_f, on the small punch tensile output is presented by considering the effect of friction on the stress field of the specimen is constant. The influence of friction coefficient on the FE force results is shown in Figure 6-19. It can be seen from this figure that with the increase of friction coefficient, the maximum load on the force-displacement curve increased. Friction forces induce a local stress field which prevents the relative universal movement of the puncher and specimen. Friction between the specimen, the holder die, support die and the punch has almost no influence on the force-displacement response until nearly of 0.2 punch displacement. The effect of friction coefficient on the force-displacement curves only around the peak load. The effect of friction coefficient on the FE dislocation density results shown in Figure 6-20. In the same manner, it can be seen that with the increase of friction coefficient, the peak dislocation density on the dislocation-strain curves increased with significant change in the punch displacement. For given friction coefficients in this study, 0.2, 0.3 and 0.4, when the friction coefficient increase, the friction forces field arises as well. In turn, the value of bending moment arises that opposing the universal plastic deformation of the specimen. The rate of puncher displacement decreases as a result of this action that leads to increase in the punch force and dislocation density.

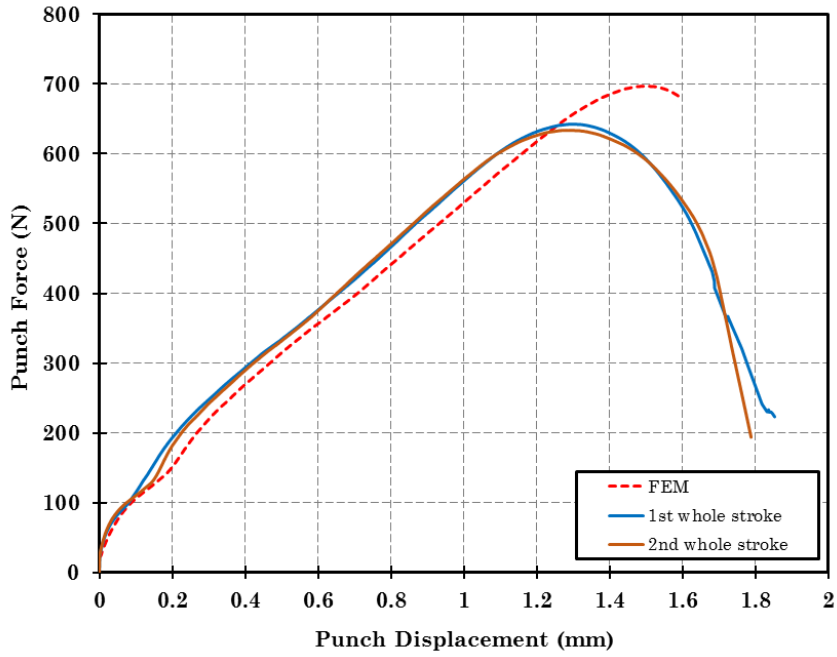


Figure 6-16. Comparison of FE model with experimental data.

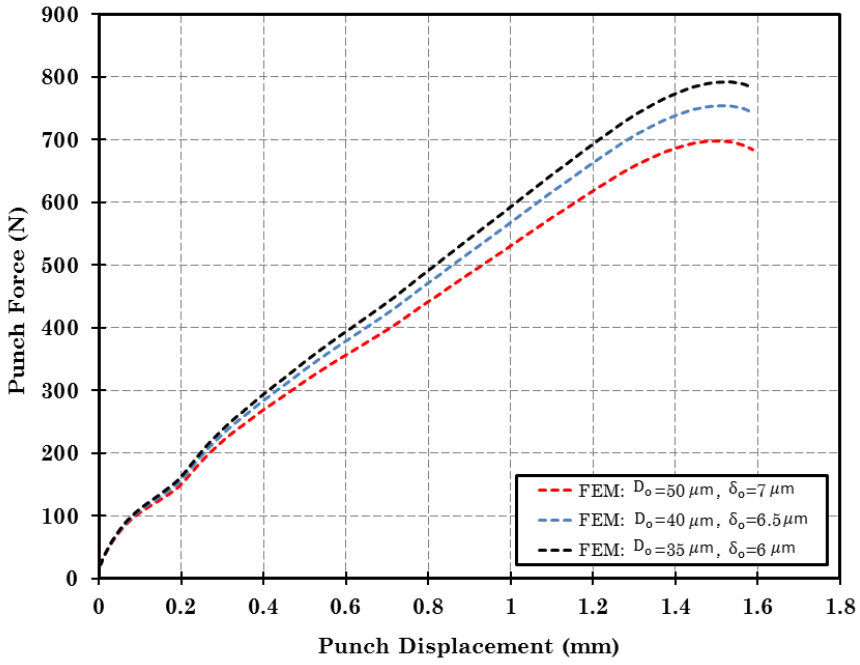


Figure 6-17. Plot of punch force versus punch displacement for various initial PAGs size and lath width.

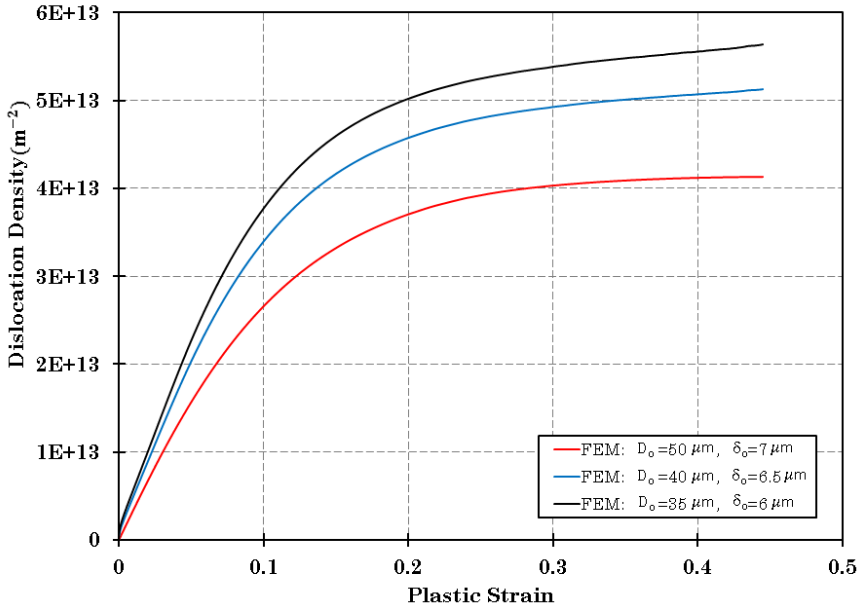


Figure 6-18. Plot of dislocation density versus plastic strain for various initial PAGs size and lath width.

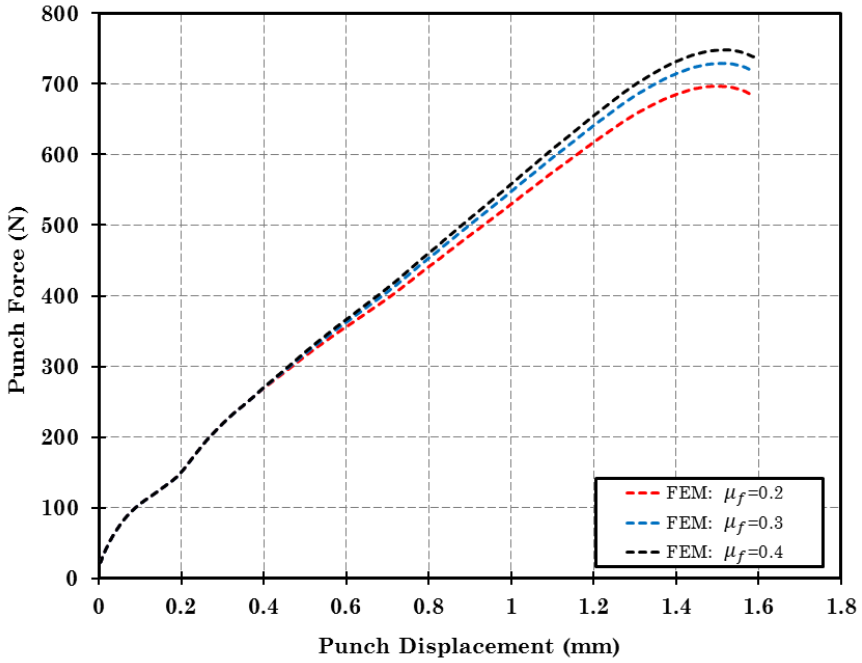


Figure 6-19. Plot of punch force versus punch displacement for various friction coefficient.

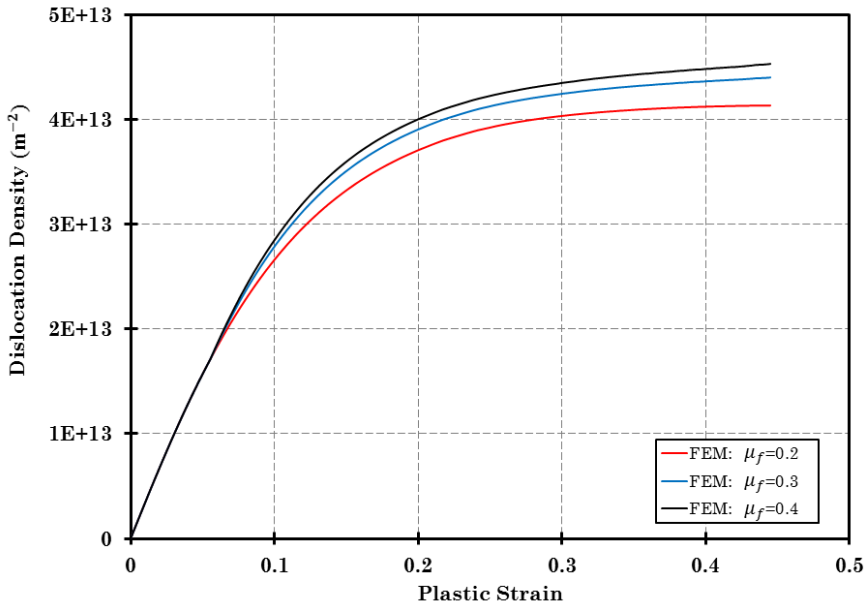


Figure 6-20. Plot of dislocation density versus plastic strain for various friction coefficient.

6.6 Conclusion

Developed visco-plastic FE simulation model based dislocation density and grain size of a small punch tensile specimen has been carried out for the P91 at 600℃. A dislocation-based visco-plastic model is developed to account for the essential strength mechanisms during the plastic deformation at high temperature, including (i) increase in overall dislocation density, and (ii) a coarsening of the PAGs size and lath martensitic width in the microstructure of P91 steel. The results of FE simulation showed that the friction coefficient varies over the contact surface between punch and specimen impact on the small punch tensile results. The results of FE simulation also showed that the initial of micro-structural variables play an influential role on the small punch tensile results. The friction linearly increase the punch load and dislocation density. Good

agreement between the experimental results generated through small punch tensile tests with FE simulation. The FE results reported in the present Chapter are valid for the interpretation of mechanical and microstructural properties of experimental SPT tests under high temperature conditions. Dislocation densities, the PAGs size and lath martensitic width and the friction coefficient can interact and strongly effect on the macroscopic degradation of the material at high stress and elevated temperature conditions.

CHAPTER 7:
CONCLUSIONS AND FUTURE WORK

7.1 Conclusions

- In Chapter 3, the viscoplasticity based dislocation density model for the P91 steel has been developed at 600°C. This model was predicted the micromechanical behaviour of materials under monotonic loading using the finite element method, following an implicit formulation. The constitutive model concentrates on the rate of change of dislocation density as the key to representing visco-plastic deformation. A general stress-strain algorithm is used in the implementation of the material model into a finite element code (UMAT). The computational methodology is based on the radial return mapping algorithm. This model is applied to high temperature uniaxial tensile of strain rate of $10^{-4}\,s^{-1}$ and uniaxial creep experiments of 140, 150, 160, 170, 180MPa of the P91 steel at 600°C. The material constants were initially used from the previous literature. The constants give good predictions of the stress-strain behaviour in tensile conditions. The model also gives reasonably good predictions of strain-time curves for creep tests that mentioned above.

- In Chapter 4, the creep based on initial microstructural variables of dislocation density model for the P91 steel has been developed at 600°C. The user material subroutine (UMAT) is coded to implement the developed creep model via ABAQUS software. This model is applied to high temperature uniaxial creep experiments of 140, 150, 160, 170, 180MPa of the P91 steel at 600°C, and applied to high temperature small punch creep (SPC) experiments of punch load of 25, 28, 30, 34, 40Kg of the P91 steel at 600°C. The predicted finite element results of SPC and uniaxial creep have a good agreement with the corresponding experimental tests. The main advantage of developed creep model is the capability to determine the creep model parameters from utilizing microstructure information in addition to uniaxial creep data. The significant effect of friction coefficient on the creep behaviour was observed in these simulations. The maximum equivalent strain was observed within an annular zone on the underside of the specimen and this weakest location did not change even though the timescales to reach failure varied greatly across the different loading cases.

- In Chapter 5, the microstructural evolution and physical fracture mechanism have been investigated during small punch tensile tests of the P91 steel at 600°C. Disc specimens, 8 mm in diameter and 0.5 mm in thickness, were tested in a small punch test rig at 600°C using a constant displacement rate of 2 μm/s. Interrupted small punch tensile tests were performed to investigate the microstructural evolution in

different deformation regimes. Physical characterisation of the deformed specimens was conducted via scanning electron microscopy and electron backscatter diffraction. Morphology analysis of the deformed specimens showed that voids were formed near the edge of contact between the punch and specimen at large displacements. Cross-sectional microstructure analysis revealed that thinning and circumferential necking started to occur at the edge of contact before the maximum load was reached, and then significant point necking occurred in the circumferential necking area after the maximum load. The voids formed during the tests become physically elongated to align with the plastic flow within the specimen. Alignment of grains occurred in the plastic deformation direction, before achieving the maximum small punch load. It was further found that the aligned grains become elongated and oriented due to the large plastic deformation prior to fracture.

- In Chapter 6, the finite element simulation using a visco-plastic developed model based on the dislocation density, PAGs size and martensitic lath width using ABAQUS software combined with a UMAT material subroutine. This model is applied to high temperature small punch tensile tests (SPTT) of punch displacement rate of 2 μm/s of the P91 steel at 600°C. The results of FE simulation also showed that the initial values of micro-structural variables play an influential role in the small punch tensile results. Reasonably good agreement was found between the experimental results generated through small

punch tensile tests with FE simulation. The FE results reported are valid for the interpretation of mechanical and microstructural properties of experimental SPT tests under high temperature conditions.

7.2 Future work

This work was aimed to develop the viscoplastic and creep models based on and understanding different features of the P91 steel at elevated temperature, but some issues still remain obvious. Further improvement of several aspects in this research may lead to improve the accuracy of the FE results and more understand of the microstructure behaviour. Thus, some suggested work can be further achieved in order to develop and enhance the current research in the future as follows:

- The finite element prediction of the P91 could be extended to include combined isotropic softening and kinematic hardening under thermo-mechanical fatigue condition at high temperature. The microstructural investigation using the transmission electron microscope (TEM) of the interrupted cyclic tests specimens should be further studied by focussing on the dislocation density evolution. The statistically determined data, such as the grain orientation, should be also studied by using the electron microscope with electron backscattered diffraction (EBSD) capability to support the research finding quantitatively. However, this work is more relevant to specific research on the metallurgy of the P91 steels.

- A further microstructural characterization could include SPCT with wide applied load range at a range of high temperatures, compared with the corresponding dislocation density viscoplastic model in order to investigate the creep coupling with plastic deformation.

- The finite element implementation could be extended to include material damage behaviour to predict the micro-mechanical properties at elevated temperature. Further experiments on small punch creep and tensile specimens should be undertaken in order to improve the understanding of the creep and stress-strain behaviour in the miniature specimen and predict fracture mechanism in real components of power plant.

- Implementation of more experimental tests could be carried out to improve the understanding the stress-strain and creep behaviour using SP techniques of power plant components.

- The material parameters could be determined using a suitable optimisation strategy to fit the simulated experimental observations to the physical measurements.

- Transmission electron microscope (TEM) measurements could be undertaken upon the interrupted SPTT specimens to investigate the evolution of dislocation density as the tests progress.

REFERENCES

[1] Jackson, G.A. Influence of Microstructure on the Mechanical Properties of Thermally Sprayed Nicocraly Coatings Determined by Small Punch Testing. University of Nottingham, 2018.

[2] Ali, B.S. Development of Non-Destructive Small Specimen Creep Testing Techniques. University of Nottingham, 2014.

[3] Ennis, P. and Czyrska-Filemonowicz, A. Recent Advances in Creep-Resistant Steels for Power Plant Applications. *Sadhana* **2003**, *28,* 709-730.

[4] Shibli, A. and Starr, F. Some Aspects of Plant and Research Experience in the Use of New High Strength Martensitic Steel P91. *International journal of pressure vessels and piping* **2007**, *84,* 114-122.

[5] Brett, S. Service Experience of Weld Cracking in Crmov Steam Pipework Systems. In Second International Conference on Integrity of High Temperature Welds, London, 2003.

[6] Shibli, A. Performance of Modern High Strength Steels (P91, P92) in High Temperature Plant. In ASME 2007 Pressure Vessels and Piping Conference, 2007.

[7] Hyde, T.; Sun, W. and Williams, J. Creep Analysis of Pressurized Circumferential Pipe Weldments—a Review. *The Journal of Strain Analysis for Engineering Design* **2003**, *38,* 1-27.

[8] Hyde, T.; Becker, A.; Sun, W. and Williams, J. Finite-Element Creep Damage Analyses of P91 Pipes. *International journal of pressure vessels and piping* **2006**, *83,* 853-863.

[9] Hayhurst, R.; Mustata, R. and Hayhurst, D. Creep Constitutive Equations for Parent, Type Iv, R-Haz, Cg-Haz and Weld Material in the Range 565–

640 C for Cr–Mo–V Weldments. *International Journal of Pressure Vessels and Piping* **2005**, *82,* 137-144.

[10] Hayhurst, D.; Lin, J. and Hayhurst, R. Failure in Notched Tension Bars Due to High-Temperature Creep: Interaction between Nucleation Controlled Cavity Growth and Continuum Cavity Growth. *International Journal of Solids and Structures* **2008**, *45,* 2233-2250.

[11] Yaghi, A.; Hyde, T.; Becker, A. and Sun, W. Finite Element Simulation of Welding and Residual Stresses in a P91 Steel Pipe Incorporating Solid-State Phase Transformation and Post-Weld Heat Treatment. *The Journal of Strain Analysis for Engineering Design* **2008**, *43,* 275-293.

[12] Chaboche, J. and Rousselier, G. On the Plastic and Viscoplastic Constitutive Equations—Part I: Rules Developed with Internal Variable Concept. *Journal of Pressure Vessel Technology* **1983**, *105,* 153-158.

[13] Yaguchi, M.; Yamamoto, M. and Ogata, T. A Viscoplastic Constitutive Model for Nickel-Base Superalloy, Part 2: Modeling under Anisothermal Conditions. *International Journal of Plasticity* **2002**, *18,* 1111-1131.

[14] Penny, R.K. and Marriott, D.L. *Design for Creep*; Springer Science & Business Media, 2012.

[15] Betten, J. *Creep Mechanics*; Springer Science & Business Media, 2008.

[16] Hurst, R.; Bicego, V. and Foulds, J. Small Punch Testing for Creep: Progress in Europe. In ASME 2007 Pressure Vessels and Piping Conference, 2007.

[17] Stewart, C. A Hybrid Constitutive Model for Creep, Fatigue, and Creep-Fatigue Damage. 2013.

[18] Webster, G. and Ainsworth, R., High Temperature Component Life Assessment, Chapman and Hall, London. UK, **1994**.

[19] Naumenko, K. Modeling of High-Temperature Creep for Structural Analysis Applications. **2018**.

[20] Andrade, E.N.d.C. The Flow in Metals under Large Constant Stresses. *Proceedings of the Royal Society of London. Series A, Containing Papers of a Mathematical and Physical Character* **1914**, *90,* 329-342.

[21] Odqvist, F.K. and Hult, J. *Kriechfestigkeit Metallischer Werkstoffe*; Springer-Verlag, 2013.

[22] Dorn, J.E. Some Fundamental Experiments on High Temperature Creep. *Journal of the Mechanics and Physics of Solids* **1955**, *3,* 85-116.

[23] Garofalo, F. *Fundamentals of Creep and Creep-Rupture in Metals*; Macmillan, 1965.

[24] KACHANOV, L.M. Time of the Rupture Process under Creep Conditions, Izy Akad. *Nank SSR Otd Tech Nauk* **1958**, *8,* 26-31.

[25] Dieter, G. *Mechanical Metallurgy" Mcgraw-Hill Book Company (Uk) Limited*; ISBN-0-070-100406-8, 1988.

[26] Rabotnov, Y.N. Creep Problems in Structural Members. **1969**.

[27] Kachanov, L. The Theory of Creep (National Lending Library for Sciences and Technology). *Bostion Spa, Yorkshire* **1967**.

[28] Evans, R.W. and Wilshire, B. Creep of Metals and Alloys. **1985**.

[29] Prager, M. Development of the Mpc Omega Method for Life Assessment in the Creep Range. *Journal of Pressure Vessel Technology* **1995**, *117*.

[30] Lakki, A.; Herzog, R.; Weller, M.; Schubert, H.; Reetz, C.; Görke, O.; Kilo, M. and Borchardt, G. Mechanical Loss, Creep, Diffusion and Ionic Conductivity of Zro2-8 Mol% Y2o3 Polycrystals. *Journal of the European Ceramic Society* **2000**, *20,* 285-296.

[31] Chokshi, A.H. An Analysis of Creep Deformation in Nanocrystalline Materials. *Scripta materialia* **1996**, *34,* 1905-1910.

[32] Berbenni, S.; Favier, V. and Berveiller, M. Impact of the Grain Size Distribution on the Yield Stress of Heterogeneous Materials. *International Journal of Plasticity* **2007**, *23,* 114-142.

[33] Fournier, B.; Dalle, F.; Sauzay, M.; Longour, J.; Salvi, M.; Caës, C.; Tournié, I.; Giroux, P.-F. and Kim, S.-H. Comparison of Various 9–12% Cr Steels under Fatigue and Creep-Fatigue Loadings at High Temperature. *Materials Science and Engineering: A* **2011**, *528,* 6934-6945.

[34] Hansen, N. Hall–Petch Relation and Boundary Strengthening. *Scripta Materialia* **2004**, *51,* 801-806.

[35] Indrawan, I.; Rahardjo, H. and Leong, E.C. Effects of Coarse-Grained Materials on Properties of Residual Soil. *Engineering Geology* **2006**, *82,* 154-164.

[36] Callister, W.D. and Rethwisch, D.G. *Materials Science and Engineering: An Introduction*; John Wiley & Sons New York, 2007.

[37] Brooks, C.R. and Choudhury, A. *Failure Analysis of Engineering Materials*; McGraw-Hill New York, 2002.

[38] Dunne, F. and Petrinic, N. *Introduction to Computational Plasticity*, 2nd ed.; Oxford University Press: New York, USA, 2005.

[39] Hill, R. *The Mathematical Theory of Plasticity*; Oxford university press, 1998.

[40] Kelly, P. *Solid Mechanics Part Ii*, 2013.

[41] Levy, M. Extrait Du Mémoire Sur Les Équations Générales Des Mouvements Intérieurs Des Corps Solides Ductiles Au Delà Des Limites Où L'élasticité Pourrait Les Ramener À Leur Premier État; Présenté Le

20 Juin 1870. *Journal de mathématiques pures et appliquées* **1871**, *16,* 369-372.

[42] Levy, M. Comptes Rendus De L'académie Des Sciences Paris. **1870**.

[43] Mises, R.v. Nachrichten Von Der Gesellschaft Der Wissenschaften Zu Göttingen. *Mathematisch-Physikalische Klasse* **1913**, *582,* 1913.

[44] Betten, J. Generalization of Nonlinear Material Laws Found in Experiments to Multiaxial States of Stress. *Eur J Mech-A/Solids* **1989**, *8,* 325-339.

[45] Chaboche, J. A Review of Some Plasticity and Viscoplasticity Constitutive Theories. *Int. J. Plasticity* **2008**, *24,* 1642-1693.

[46] de Souza Neto, E.A.; Peric, D. and Owen, D.R. *Computational Methods for Plasticity: Theory and Applications*; John Wiley & Sons, 2011.

[47] Mroz, Z. On the Description of Anisotropic Workhardening. *Journal of the Mechanics and Physics of Solids* **1967**, *15,* 163-175.

[48] Lemaitre, J. and Chaboche, J.-L. *Mechanics of Solid Materials*; Cambridge university press, 1994.

[49] Jacek, J.S., Plasticity and Creep: Theory, Examples, and Problems. London: CRC Press, **1993**.

[50] Chun, B.; Jinn, J. and Lee, J. Modeling the Bauschinger Effect for Sheet Metals, Part I: Theory. *International Journal of Plasticity* **2002**, *18,* 571-595.

[51] Prager, W. Recent Developments in the Mathematical Theory of Plasticity. *Journal of applied physics* **1949**, *20,* 235-241.

[52] Avanzini, A. Mechanical Characterization and Finite Element Modelling of Cyclic Stress–Strain Behaviour of Ultra High Molecular Weight Polyethylene. *Materials & Design* **2008**, *29,* 330-343.

[53] Frederick, C.O. and Armstrong, P. A Mathematical Representation of the Multiaxial Bauschinger Effect. *Materials at High Temperatures* **2007**, *24,* 1-26.

[54] Shang, J.; Leen, S. and Hyde, T. Finite-Element-Based Methodology for Predicting the Thermo-Mechanical Behaviour of Superplastic Forming Tools. *Proceedings of the Institution of Mechanical Engineers, Part L: Journal of Materials: Design and Applications* **2006**, *220,* 113-123.

[55] Krempl, E. Viscoplastic Models for High Temperature Applications. *International Journal of Solids and Structures* **2000**, *37,* 279-291.

[56] Lemaitre, J. Handbook of Materials Behavior Models, in Handbook of Materials Behavior Models. **2001**.

[57] Chaboche, J.-L. Constitutive Equations for Cyclic Plasticity and Cyclic Viscoplasticity. *International journal of plasticity* **1989**, *5,* 247-302.

[58] Kocks, U. Laws for Work-Hardening and Low-Temperature Creep. *J. Eng. Mater. Tech.* **1976**, *98,* 76-85.

[59] Mecking, H. and Kocks, U. Kinetics of Flow and Strain-Hardening. *Acta. Metall. Mater.* **1981**, *29,* 1865-1875.

[60] Estrin, Y. and Mecking, H. A Unified Phenomenological Description of Work Hardening and Creep Based on One-Parameter Models. *Acta. Metall. Mater.* **1984**, *32,* 57-70.

[61] Estrin, Y. Dislocation Theory Based Constitutive Modelling: Foundations and Applications. *J. Mater. Process Tech.* **1998**, *80,* 33-39.

[62] Voce, E. The Relationship between Stress and Strain for Homogeneous Deformation. *J. Inst. Met.* **1948**, *74,* 537-562.

[63] Voce, E. A Practical Strain-Hardening Function. *Metallurgia* **1955**, *51,* 219-226.

[64] Domkin, K. Constitutive Models Based on Dislocation Density: Formulation and Implementation into Finite Element Codes. Ph.D thesis, Luleå University of Technology, Sweden, 2005.

[65] Dunlop, J.; Bréchet, Y.; Legras, L. and Estrin, Y. Dislocation Density-Based Modelling of Plastic Deformation of Zircaloy-4. *Mater. Sci. Eng. A* **2007**, *443,* 77-86.

[66] Barlat, F.; Glazov, M.; Brem, J. and Lege, D. A Simple Model for Dislocation Behavior, Strain and Strain Rate Hardening Evolution in Deforming Aluminum Alloys. *Int. J. Plasticity* **2002**, *18,* 919-939.

[67] Kalidindi, S.R. Modeling the Strain Hardening Response of Low Sfe Fcc Alloys. *Int. J. Plasticity* **1998**, *14,* 1265-1277.

[68] Capolungo, L.; Jochum, C.; Cherkaoui, M. and Qu, J. Homogenization Method for Strength and Inelastic Behavior of Nanocrystalline Materials. *Int. J. Plasticity* **2005**, *21,* 67-82.

[69] Wu, Y.; Zhou, J.; Dong, S.; Hu, A.; Wang, L. and Pang, X. Constitutive Modeling for Strain Rate-Dependent Behaviors of Nanocrystalline Materials Based on Dislocation Density Evolution and Strain Gradient. *J. Mater. Res.* **2014**, *29,* 2982-2993.

[70] Morris, A.; Cacciapuoti, B. and Sun, W. The Role of Small Specimen Creep Testing within a Life Assessment Framework for High Temperature Power Plant. *Int. Mater. Rev.* **2018**, *63,* 102-137.

[71] Hyde, T.H.; Sun, W. and Williams, J.A. Requirements for and Use of Miniature Test Specimens to Provide Mechanical and Creep Properties of Materials: A Review. *Int. Mater. Rev.* **2007**, *52,* 213-255.

[72] Hyde, T.H. and Sun, W. A Novel, High-Sensitivity, Small Specimen Creep Test. *J Strain Anal Eng.* **2009**, *44,* 171-185.

[73] Rouse, J.; Cortellino, F.; Sun, W.; Hyde, T.H. and Shingledecker, J. Small Punch Creep Testing: Review on Modelling and Data Interpretation. *Mater Sci Tech.* **2013**, *29,* 1328-1345.

[74] Cortellino, F.; Rouse, J.; Cacciapuoti, B.; Sun, W. and Hyde, T.H. Experimental and Numerical Analysis of Initial Plasticity in P91 Steel Small Punch Creep Samples. *Exp Mech.* **2017***,* 1-20.

[75] Dymáček, P. and Milička, K. Small Punch Testing and Its Numerical Simulations under Constant Deflection Force Conditions. *Strength Mater+* **2008**, *40,* 24-27.

[76] Dymáček, P. Recent Developments in Small Punch Testing: Applications at Elevated Temperatures. *Theor Appl Fract Mec.* **2016**, *86,* 25-33.

[77] Parker, J. and James, J. Disc-Bend Creep Deformation Behaviour of 0. 5 Cr 0. 5 Mo 0. 25 V Low Alloy Steel. *Creep and fracture of engineering materials and structures* **1993***,* 651-660.

[78] Zhou, Z.; Zheng, Y.; Ling, X.; Hu, R. and Zhou, J. A Study on Influence Factors of Small Punch Creep Test by Experimental Investigation and Finite Element Analysis. *Materials Science and Engineering: A* **2010**, *527,* 2784-2789.

[79] Komazaki, S.-i. Evaluation of Creep Rupture Strength of High Nitrogen Ferritic Heat-Resistant Steels Using Small Punch Creep Testing Technique. *Materials Science and Engineering: A* **2016**, *676,* 100-108.

[80] Moreno, M. Application of Small Punch Testing on the Mechanical and Microstructural Characterizations of P91 Steel at Room Temperature. *International Journal of Pressure Vessels and Piping* **2016**, *142,* 1-9.

[81] Chen, H. Mechanical and Chemical Behaviour of Thermally Sprayed Conicraly Bond Coats. Ph. D Thesis, Department of Mechanical, Materials and Manufacturing …, 2015.

[82] Hyde, T.; Stoyanov, M.; Sun, W. and Hyde, C.J. On the Interpretation of Results from Small Punch Creep Tests. *The Journal of Strain Analysis for Engineering Design* **2010**, *45,* 141-164.

[83] Kobayashi, K.-i.; Kajihara, I.; Koyama, H. and Stratford, G.C. Deformation and Fracture Mode During Small Punch Creep Tests. *Journal of Solid Mechanics and Materials Engineering* **2010**, *4,* 75-86.

[84] Chakrabarty, J. A Theory of Stretch Forming over Hemispherical Punch Heads. *International Journal of Mechanical Sciences* **1970**, *12,* 315-325.

[85] Yang, Z. and Wang, Z.-w. Relationship between Strain and Central Deflection in Small Punch Creep Specimens. *International Journal of Pressure Vessels and Piping* **2003**, *80,* 397-404.

[86] Li, Y.; Sun, M. and Zhang, C. Practical Approach to Determine Creep Properties from Small Punch Test. In Proceedings of the 2nd International Conference SSTT, Ostrava, Czech Republic, 2012.

[87] Agreement, C.W., Small Punch Test Method for Metallic Materials. CEN Brussels, Belgium, **2006**.

[88] Simonovski, I.; Holmström, S. and Bruchhausen, M. Small Punch Tensile Testing of Curved Specimens: Finite Element Analysis and Experiment. *International Journal of Mechanical Sciences* **2017**, *120,* 204-213.

[89] García, T.; Rodríguez, C.; Belzunce, F. and Suárez, C. Estimation of the Mechanical Properties of Metallic Materials by Means of the Small Punch Test. *Journal of alloys and compounds* **2014**, *582,* 708-717.

[90] Kachanov, L. *Introduction to Continuum Damage Mechanics*; Springer Science & Business Media: USA, 2013.

[91] Li, Y. An Analytic Approach for Interpreting Creep Curves from Small Punch Tests. In Proc. 3rd. Conference 'Advances in material technology for fossil power plants', Swansea, 2001.

[92] Abendroth, M. Fem Analysis of Small Punch Tests. *Key Eng Mat.* **2017**, *734,* 23-36.

[93] Manahan, M.; Browning, A.; Argon, A. and Harling, O. Miniaturized Disk Bend Test Technique Development and Application. In The Use of Small-Scale Specimens for Testing Irradiated Material, ASTM International, New Mexico, 1986.

[94] Shibli, I.; Holdsworth, S. and Merckling, G. Creep and Fracture in High Temperature Components: Design and Life Assessment Issues. In ECCC Creep Conference, London, UK, 2005.

[95] Evans, R. and Evans, M. Numerical Modelling of Small Disc Creep Test. *Mater Sci Tech.* **2006**, *22,* 1155-1162.

[96] Evans, M. and Wang, D. Optimizing the Sensitivity of the Small-Disc Creep Test to Damage and Test Conditions. *J Strain Anal Eng.* **2007**, *42,* 389-409.

[97] Dymáček, P. and Milička, K. Creep Small-Punch Testing and Its Numerical Simulations. *Materials Science and Engineering: A* **2009**, *510,* 444-449.

[98] Guan, K.-s.; Xu, T.; Zhang, X.-c. and Wang, Z.-w. Effect of Microdefects on Load-Deflection of Small Punch Test by Experimental Investigation and Finite Element Analysis. *International Journal of Pressure Vessels and Piping* **2013**, *110,* 14-16.

[99] Huang, F.H.; Hamilton, M.L. and Wire, G.L. Bend Testing for Miniature Disks. *Nuclear Technology* **1982**, *57,* 234-242.

[100] Manahan, M.; Argon, A. and Harling, O. The Development of a Miniaturized Disk Bend Test for the Determination of Postirradiation Mechanical Properties. *Journal of Nuclear Materials* **1981**, *104,* 1545-1550.

[101] Baik, J.-M.; Buck, O. and Kameda, J. Small Punch Test Evaluation of Intergranular Embrittlement of an Alloy Steel. *Scripta Metallurgica* **1983**, *17,* 1443-1447.

[102] Lucas, G.; Okada, A. and Kiritani, M. Parametric Analysis of the Disc Bend Test. *Journal of Nuclear Materials* **1986**, *141,* 532-535.

[103] Li, H.; Chen, F. and Ardell, A. A Simple, Versatile Miniaturized Disk-Bend Test Apparatus for Quantitative Yield-Stress Measurements. *Metallurgical Transactions A* **1991**, *22,* 2061-2068.

[104] Blagoeva, D. and Hurst, R. Application of the Cen (European Committee for Standardization) Small Punch Creep Testing Code of Practice to a Representative Repair Welded P91 Pipe. *Mater. Sci. Eng. : A* **2009**, *510,* 219-223.

[105] Panayotou, N.; Puigh, R. and Opperman, E. Miniature Specimen Tensile Data for High Energy Neutron Source Experiments. *J. Nucl. Mater.* **1981**, *104,* 1523-1526.

[106] Madia, M.; Foletti, S.; Torsello, G. and Cammi, A. On the Applicability of the Small Punch Test to the Characterization of the 1crmov Aged Steel: Mechanical Testing and Numerical Analysis. *Eng. Fail. Anal.* **2013**, *34,* 189-203.

[107] Lucas, G. The Development of Small Specimen Mechanical Test Techniques. *J. Nucl. Mater.* **1983**, *117,* 327-339.

[108] Ha, J.S. and Fleury, E. Small Punch Tests on Steels for Steam Power Plant (I). *Ksme Int. J.* **1998**, *12,* 818.

[109] Rodríguez, C.; Fernández, M.; Cabezas, J.; García, T. and Belzunce, F. The Use of the Small Punch Test to Solve Practical Engineering Problems. *Theor. Appl. Fract. Mec.* **2016**, *86,* 109-116.

[110] Rodríguez, C.; García, J.; Cárdenas, E.; Belzunce, F. and Betegón, C. Mechanical Properties Characterization of Heat-Affected Zone Using the Small Punch Test. *Weld. J.* **2009**, *88,* 188-192.

[111] Fernández, M.; Rodríguez, C.; Belzunce, F. and García, T. Use of Small Punch Test to Estimate the Mechanical Properties of Powder Metallurgy Products Employed in the Automotive Industry. *Powder Metall.* **2015**, *58,* 171-177.

[112] Shindo, Y.; Yamaguchi, Y. and Horiguchi, K. Small Punch Testing for Determining the Cryogenic Fracture Properties of 304 and 316 Austenitic Stainless Steels in a High Magnetic Field. *Cryogenics* **2004**, *44,* 789-792.

[113] Mao, X. and Takahashi, H. Development of a Further-Miniaturized Specimen of 3mm Diameter for Tem Disk (Ø 3mm) Small Punch Tests. *J. Nucl. Mater.* **1987**, *150,* 42-52.

[114] Bulloch, J. A Study Concerning Material Fracture Toughness and Some Small Punch Test Data for Low Alloy Steels. *Eng. Fail. Anal.* **2004**, *11,* 635-653.

[115] Cuesta, I. and Alegre, J. Determination of the Fracture Toughness by Applying a Structural Integrity Approach to Pre-Cracked Small Punch Test Specimens. *Eng. Fract. Mech.* **2011**, *78,* 289-300.

[116] Xu, Y. and Guan, K. Evaluation of Fracture Toughness by Notched Small Punch Tests with Weibull Stress Method. *Mater. Design* **2013**, *51,* 605-611.

[117] Cuesta, I.; Rodriquez, C.; Belzunce, F. and Alegre, J. Analysis of Different Techniques for Obtaining Pre-Cracked/Notched Small Punch Test Specimens. *Eng. Fail. Anal.* **2011**, *18,* 2282-2287.

[118] Manahan, M.P. A New Postirradiation Mechanical Behavior Test—the Miniaturized Disk Bend Test. *Nuclear Technology* **1983**, *63,* 295-315.

[119] Coleman, M.; Alshehri, H.; Banik, R.; Harrison, W. and Birosca, S. Deformation Mechanisms of In713c Nickel Based Superalloy During Small Punch Testing. *Materials Science and Engineering: A* **2016**, *650,* 422-431.

[120] Chang, Y.S.; Kim, J.M.; Choi, J.B.; Kim, Y.J.; Kim, M.C. and Lee, B.S. Derivation of Ductile Fracture Resistance by Use of Small Punch Specimens. *Engineering Fracture Mechanics* **2008**, *75,* 3413-3427.

[121] Abendroth, M. and Kuna, M. Identification of Ductile Damage and Fracture Parameters from the Small Punch Test Using Neural Networks. *Engineering fracture mechanics* **2006**, *73,* 710-725.

[122] Lancaster, R.J.; Illsley, H.W.; Davies, G.R.; Jeffs, S.P. and Baxter, G.J. Modelling the Small Punch Tensile Behaviour of an Aerospace Alloy. *Materials Science and Technology* **2017**, *33,* 1065-1073.

[123] Abe, F.; Kern, T.-U. and Viswanathan, R. *Creep-Resistant Steels*; Elsevier, 2008.

[124] Findeisen, A.; Klatt, M. and Krautz, H.J. Examination of the Corrosion Behaviour of Selected Power Plant Materials under Various Operating Conditions. *Chemie der Erde-Geochemistry* **2010**, *70,* 193-199.

[125] Tanner, D.; Becker, A. and Hyde, T. High Temperature Life Prediction of a Welded In718 Component. In Journal of Physics: Conference Series, 2009.

[126] Giroux, P.-F.; Dalle, F.; Sauzay, M.; Malaplate, J.; Fournier, B. and Gourgues-Lorenzon, A.-F. Mechanical and Microstructural Stability of P92 Steel under Uniaxial Tension at High Temperature. *Materials Science and Engineering: A* **2010**, *527,* 3984-3993.

[127] Hyde, T.; Becker, A.; Song, Y. and Sun, W. Failure Estimation of Tig Butt-Welded Inco718 Sheets at 620 C under Creep and Plasticity Conditions. *Computational materials science* **2006**, *35,* 35-41.

[128] Tanner, D.W. Life Assessment of Welded Inconel 718 at High Temperature. University of Nottingham, 2009.

[129] Haarmann, K.; Vaillant, J.; Vandenberghe, B.; Bendick, W. and Arbab, A. The T91/P91 Book. *Vallourec & Mannesmann Tubes* **2002**, *19992002*.

[130] Arbab, A.; Bendick, W.; Haarmann, K.; Vaillant, J. and Vandenberghe, B., The T91/P91 Book. Vallourec and Mannesmann Tubes, **2002**.

[131] Igarashi, M., Alloy Design Philosophy of Creep-Resistant Steels, in *Creep-Resistant Steels*Elsevier. 2008. 539-572,

[132] Vaillant, J.; Vandenberghe, B.; Hahn, B.; Heuser, H. and Jochum, C. T/P23, 24, 911 and 92: New Grades for Advanced Coal-Fired Power Plants—Properties and Experience. *International Journal of Pressure Vessels and Piping* **2008**, *85,* 38-46.

[133] Bendick, W.; Cipolla, L.; Gabrel, J. and Hald, J. New Eccc Assessment of Creep Rupture Strength for Steel Grade X10crmovnb9-1 (Grade 91). *International Journal of Pressure Vessels and Piping* **2010**, *87,* 304-309.

[134] Swindeman, R.; Santella, M.; Maziasz, P.; Roberts, B. and Coleman, K. Issues in Replacing Cr–Mo Steels and Stainless Steels with 9cr–1mo–V Steel. *International Journal of Pressure Vessels and Piping* **2004**, *81,* 507-512.

[135] Richardot, D.; Vaillant, J.; Arbab, A. and Bendick, W. The T92/P92 Book. *Vallourec & Mannesmann Tubes* **2000**.

[136] Maruyama, K.; Sawada, K. and Koike, J.-i. Strengthening Mechanisms of Creep Resistant Tempered Martensitic Steel. *ISIJ international* **2001**, *41,* 641-653.

[137] Esposito, L. and Bonora, N. A Primary Creep Model for Class M Materials. *Materials Science and Engineering: A* **2011**, *528,* 5496-5501.

[138] Magnusson, H. and Sandström, R. Creep Strain Modeling of 9 to 12 Pct Cr Steels Based on Microstructure Evolution. *Metallurgical and materials transactions A* **2007**, *38,* 2033-2039.

[139] Spigarelli, S. and Quadrini, E. Analysis of the Creep Behaviour of Modified P91 (9cr–1mo–Nbv) Welds. *Materials & design* **2002**, *23,* 547-552.

[140] Spigarelli, S. Microstructure-Based Assessment of Creep Rupture Strength in 9cr Steels. *International Journal of Pressure Vessels and Piping* **2013**, *101,* 64-71.

[141] Thompson, A., Work Hardening in Tension and Fatigue, in *Aime, New York*. 1977. 89-126,

[142] Estrin, Y., Dislocation-Density-Related Constitutive Modelling, in *(Ed. Krausz, A.S. And Krausz, K.), 'Unified Plastic Constitutive Laws of Deformation',*Academic Press limited: London. 1996. 69-106, 0-12-425970.

[143] Rezania, M.; Taiebat, M. and Poletti, E. A Viscoplastic Saniclay Model for Natural Soft Soils. *Comput Geotech* **2016**, *73,* 128-141.

[144] ABAQUS, Analysis User's Manual Version 6.14. Hibbitt, Karlsson and Sorensen, Inc.: Pawtucket, USA, **2014**.

[145] Benaarbia, A.; Rae, Y. and Sun, W. Unified Viscoplasticity Modelling and Its Application to Fatigue-Creep Behaviour of Gas Turbine Rotor. *Int J Mech Sci.* **2018**, *136,* 36-49.

[146] Al-Abedy, H.; Jones, A. and Sun, W. Fe Modelling of Small Punch Creep Test Using Kocks-Mecking-Estrin Model. In '5th Internationl Small Sample test Techniques Conference', Wales, UK, 2018.

[147] Cortellino, F.; Sun, W.; Hyde, T.H. and Shingledecker, J. The Effects of Geometrical Inaccuracies of the Experimental Set-up on Small Punch Creep Test Results. *J Strain Anal Eng.* **2014**, *49,* 571-582.

[148] Sauzay, M.; Fournier, B.; Mottot, M.; Pineau, A. and Monnet, I. Cyclic Softening of Martensitic Steels at High Temperature—Experiments and Physically Based Modelling. *Mater. Sci. Eng. A* **2008**, *483,* 410-414.

[149] Cheng, S.; Ma, E.; Wang, Y.; Kecskes, L.; Youssef, K.; Koch, C.; Trociewitz, U. and Han, K. Tensile Properties of in Situ Consolidated Nanocrystalline Cu. *Acta. Metall. Mater.* **2005**, *53,* 1521-1533.

[150] Barrett, R.; O'Donoghue, P. and Leen, S. A Dislocation-Based Model for High Temperature Cyclic Viscoplasticity of 9–12cr Steels. *Comp. Mater. Sci.* **2014**, *92,* 286-297.

[151] Pandey, C.; Giri, A. and Mahapatra, M. Evolution of Phases in P91 Steel in Various Heat Treatment Conditions and Their Effect on Microstructure Stability and Mechanical Properties. *Mater. Sci. Eng. : A* **2016**, *664,* 58-74.

[152] An, L.; Xu, Q.; Xu, D. and Lu, Z. Review of Creep Deformation and Rupture Mechanism of P91 Alloy for the Development of Creep Damage Constitutive Equations under Low Stress Level. In The 10th International Conference on Science Computing, USA 2013.

[153] Gaffard, V.; Besson, J. and Gourgues-Lorenzon, A.-F. Creep Failure Model of a Tempered Martensitic Stainless Steel Integrating Multiple Deformation and Damage Mechanisms. *Int. J. Fract.* **2005**, *133,* 139-166.

[154] Panait, C.G.; Zielińska-Lipiec, A.; Koziel, T.; Czyrska-Filemonowicz, A.; Gourgues-Lorenzon, A.-F. and Bendick, W. Evolution of Dislocation Density, Size of Subgrains and Mx-Type Precipitates in a P91 Steel During Creep and During Thermal Ageing at 600 C for More Than 100,000 H. *Mater. Sci. Eng. : A* **2010**, *527,* 4062-4069.

[155] Abe, F.; Taneike, M. and Sawada, K. Alloy Design of Creep Resistant 9cr Steel Using a Dispersion of Nano-Sized Carbonitrides. *Int. J. Pres. Ves. Pip.* **2007**, *84,* 3-12.

[156] Fournier, B.; Sauzay, M.; Barcelo, F.; Rauch, E.; Renault, A.; Cozzika, T.; Dupuy, L. and Pineau, A. Creep-Fatigue Interactions in a 9 Pct Cr-1 Pct Mo Martensitic Steel: Part Ii. Microstructural Evolutions. *Metall. Mater. Trans. A* **2009**, *40,* 330-341.

[157] Shankar, V.; Valsan, M.; Rao, K.B.S.; Kannan, R.; Mannan, S. and Pathak, S. Low Cycle Fatigue Behavior and Microstructural Evolution of Modified 9cr–1mo Ferritic Steel. *Mater. Sci. Eng. : A* **2006**, *437,* 413-422.

[158] Sauzay, M.; Fournier, B.; Mottot, M.; Pineau, A. and Monnet, I. Cyclic Softening of Martensitic Steels at High Temperature—Experiments and Physically Based Modelling. *Mater. Sci. Eng. : A* **2008**, *483,* 410-414.

[159] Viswanathan, R.; Henry, J.F.; Tanzosh, J.; Stanko, G.; Shingledecker, J.; Vitalis, B. and Purgert, R. Us Program on Materials Technology for Ultra-Supercritical Coal Power Plants. *J Mater Eng Perform* **2005**, *14,* 281-292 DOI: 10.1361/10599490524039.

[160] Saad, A.A.; Hyde, T.; Sun, W.; Hyde, C.J. and Tanner, D.W. Characterization of Viscoplasticity Behaviour of P91 and P92 Power Plant Steels. *Int. J. Pres. Ves. Pip.* **2013**, *111,* 246-252.

[161] Benaarbia, A.; Rouse, J.P. and Sun, W. A Thermodynamically-Based Viscoelastic-Viscoplastic Model for the High Temperature Cyclic Behaviour of 9–12% Cr Steels. *Int. J. Plasticity* **2018**.

[162] Dymáček, P. Recent Developments in Small Punch Testing: Applications at Elevated Temperatures. *Theor. Appl. Fract. Mec.* **2016**, *86,* 25-33.

[163] Abendroth, M. Fem Analysis of Small Punch Tests. *Key Eng. Mat.* **2017**, *734,* 23-36.

[164] Cacciapuoti, B.; Sun, W. and McCartney, D.G. A Study on the Evolution of the Contact Angle of Small Punch Creep Test of Ductile Materials. *Int. J. Pressure Vessels Piping* **2016**, *145,* 60-74 DOI: https://doi.org/10.1016/j.ijpvp.2016.06.002.

[165] Saad, A.A. Cyclic Plasticity and Creep of Power Plant Materials. Ph.D thesis, University of Nottingham, 2012.

[166] Barrett, R.A.; O'Donoghue, P. and Leen, S.B. An Improved Unified Viscoplastic Constitutive Model for Strain-Rate Sensitivity in High Temperature Fatigue. *International Journal of Fatigue* **2013**, *48,* 192-204.

[167] Barrett, R.A.; Farragher, T.; O'Dowd, N.; O'Donoghue, P. and Leen, S. Multiaxial Cyclic Viscoplasticity Model for High Temperature Fatigue of P91 Steel. *Materials Science and Technology* **2014**, *30,* 67-74.

[168] Farragher, T.P.; Scully, S.; O'Dowd, N. and Leen, S. Development of Life Assessment Procedures for Power Plant Headers Operated under Flexible Loading Scenarios. *International Journal of Fatigue* **2013**, *49,* 50-61.

[169] Estrin, Y. A Versatile Unified Constitutive Model Based on Dislocation Density Evolution. *High Temperature Constitutive Modelling-Theory and Application* **1991***,* 65-83.

[170] Braasch, H. and Estrin, Y. Parameter Identification for a Two-Internal Variable Constitutive Model Using the Evolution Strategy. In Parameter identification for a two-internal variable constitutive model using the evolution strategy, 1993.

[171] Orowan, E. Problems of Plastic Gliding. *Proceedings of the Physical Society* **1940**, *52,* 8.

[172] Sinclair, C.; Poole, W. and Bréchet, Y. A Model for the Grain Size Dependent Work Hardening of Copper. *Scripta Materialia* **2006**, *55,* 739-742.

[173] Kocks, U., Unified Constitutive Equations for Creep and Plasticity Ed Ak Miller. New York: Elsevier, **1987**.

[174] Cheong, K.-S. and Busso, E.P. Discrete Dislocation Density Modelling of Single Phase Fcc Polycrystal Aggregates. *Acta Materialia* **2004**, *52,* 5665-5675.

[175] Roters, F.; Raabe, D. and Gottstein, G. Work Hardening in Heterogeneous Alloys—a Microstructural Approach Based on Three Internal State Variables. *Acta materialia* **2000**, *48,* 4181-4189.

[176] Magnusson, H. and Sandström, R. The Role of Dislocation Climb across Particles at Creep Conditions in 9 to 12 Pct Cr Steels. *Metallurgical and Materials Transactions A* **2007**, *38,* 2428-2434.

[177] Kocks, U. Laws for Work-Hardening and Low-Temperature Creep. *Journal of Engineering Materials and Technology* **1976**, *98,* 76-85.

[178] Collini, L. and Bonardi, A. A Micromechanical Model of the Evolution of Stress and Strain Fields in Ultrafine-Grained Metal Structures under Tension. *The Journal of Strain Analysis for Engineering Design* **2013**, *48,* 91-102.

[179] Sauzay, M.; Fournier, B.; Mottot, M.; Pineau, A. and Monnet, I. Cyclic Softening of Martensitic Steels at High Temperature—Experiments and Physically Based Modelling. *Materials Science and Engineering: A* **2008**, *483,* 410-414.

[180] Pešička, J.; Kužel, R.; Dronhofer, A. and Eggeler, G. The Evolution of Dislocation Density During Heat Treatment and Creep of Tempered Martensite Ferritic Steels. *Acta Materialia* **2003**, *51,* 4847-4862.

[181] Haroush, S.; Priel, E.; Moreno, D.; Busiba, A.; Silverman, I.; Turgeman, A.; Shneck, R. and Gelbstein, Y. Evaluation of the Mechanical Properties of Ss-316l Thin Foils by Small Punch Testing and Finite Element Analysis. *Materials & Design* **2015**, *83,* 75-84.

APPENDIX A:

MATERIAL JACOBIAN MATRIX CALCULATION

The rate-based Hooke's law (the relationship between $\dot{\sigma}_{ij}$ the Cauchy stress rate and $\dot{\varepsilon}^{e}_{kl}$ the elastic strain rate) takes the following form

$$\dot{\sigma}_{ij} = C^{e}_{ijkl}\, \dot{\varepsilon}^{e}_{kl} \ , \tag{A.1}$$

where C^{e}_{ijkl} is the elastic stiffness matrix.

The material constitutive response (the relationship between $\dot{\sigma}_{ij}$ the Cauchy stress and $\dot{\varepsilon}_{kl}$ the total strain rate) is

$$\dot{\sigma}_{ij} = C_{ijkl}\, \dot{\varepsilon}_{kl} \ , \tag{A.2}$$

where C_{ijkl} is the total stiffness matrix better known as the "material Jacobian matrix". Mathematical manipulation furnishes

$$\dot{\sigma}_{ij} = C_{ijkl}\, \dot{\varepsilon}_{kl} \ , \tag{A.3}$$

$$\dot{\sigma}_{ij} = C^{e}_{ijkl}\, \dot{\varepsilon}^{e}_{kl} + C^{cr}_{ijkl}\, \dot{\varepsilon}^{cr}_{kl} \quad , \text{and } C_{ijkl} = C^{e}_{ijkl} + C^{cr}_{ijkl}. \tag{A.4}$$

Above demonstrates that C_{ijkl} the material Jacobian matrix can be decomposed into elastic and creep stiffness matrices, C^{e}_{ijkl} and C^{cr}_{ijkl} respectively. The material Jacobian matrix is a vital part of the equilibrium equations used in FEM.

$$C_{ijkl} = \frac{\partial \Delta \sigma_{ij}}{\partial \Delta \varepsilon_{ij}} \tag{A.5}$$

where $\partial \Delta \sigma_{ij}$ is the change in the i^{th} stress at the end of the time increment caused by the jth strain, $\partial \Delta \varepsilon_{ij}$. A closed-form solution to C^{e}_{ijkl} the elastic stiffness matrix always exists. A closed-form solution to C^{cr}_{ijkl} the creep stiffness matrix may or may not exist. If a closed-form solution exists, it greatly reduces computational costs.

The creep strain rate is

$$\dot{\varepsilon}^{cr}_{ij} = \frac{3}{2} \dot{\varepsilon}_o \, \hat{\sigma}_{so}^{-p} \tilde{\sigma}^{p-1} S_{ij} \tag{A.6}$$

Following the same process for Equation A.4,

$$\frac{d\varepsilon^{cr}_{ij}}{dt} = \frac{3}{2} \dot{\varepsilon}_o \, \hat{\sigma}_{so}^{-p} \tilde{\sigma}^{p-1} S_{ij} \tag{A.7}$$

$$\int_{\varepsilon^{cr}_{ijo}}^{\varepsilon^{cr}_{ijo}+\Delta\varepsilon^{cr}_{ij}} d\varepsilon^{cr}_{ij} = \int_{t_o}^{t_o+\Delta t} \frac{3}{2} \dot{\varepsilon}_o \, \hat{\sigma}_{so}^{-p} \tilde{\sigma}^{p-1} S_{ij} dt \tag{A.8}$$

$$\Delta\varepsilon^{cr}_{ij} = \frac{3}{2} \dot{\varepsilon}_o \, \hat{\sigma}_{so}^{-p} \tilde{\sigma}^{p-1} S_{ij} \Big|_{t_o+\Delta t} \Delta t \tag{A.9}$$

From differentiation of Equation A.9, this term can be expressed as

$$\frac{\partial \Delta \varepsilon^{cr}_{ij}}{\partial \Delta \sigma_{kl}} = \frac{3}{2} \dot{\varepsilon}_o \, \hat{\sigma}_{so}^{-p} \left[(p-1) \tilde{\sigma}^{p-2} \frac{\partial \sigma}{\partial \Delta \sigma_{kl}} S_{ij} + \tilde{\sigma}^{p-1} \frac{\partial S_{ij}}{\partial \Delta \sigma_{kl}} \right] \Delta t \tag{A.10}$$

where $\tilde{\sigma}$ is the equivalent stress at each phase, calculated as

$$\tilde{\sigma} = \sqrt{\frac{3}{2} S_{rs} S_{rs}} \tag{A.11}$$

By differentiation of Equation A.11, $\frac{\partial \sigma}{\partial \Delta \sigma_{kl}}$ is obtained as needed in Equation A.10,

$$\frac{\partial \sigma}{\partial \Delta \sigma_{kl}} = \frac{1}{2} \left(\frac{3}{2} S_{rs} S_{rs} \right)^{\frac{-1}{2}} \frac{3}{2} 2 S_{pq} \frac{\partial S_{pq}}{\partial \Delta \sigma_{kl}} \Big|_{t_o + \Delta t} = \frac{3}{2\tilde{\sigma}} S_{pq} \frac{\partial S_{pq}}{\partial \Delta \sigma_{kl}} \Big|_{t_o + \Delta t} \tag{A.12}$$

Equation A.12 can be rewritten in an alternative way, identifying the two tensors that compose its right hand side term,

$$\frac{\partial \tilde{\sigma}}{\partial \Delta \sigma_{kl}} = \frac{\partial \tilde{\sigma}}{\partial S_{pq}} \frac{\partial S_{pq}}{\partial \Delta \sigma_{kl}} \Big|_{t_o + \Delta t} \tag{A.13}$$

where

$$\frac{\partial \tilde{\sigma}}{\partial S_{pq}} = \frac{3}{2\sigma} S_{pq} \Big|_{t_o + \Delta t} \tag{A.14}$$

Equation A.13 can be substituted back into Equation A.10 giving

$$\frac{\partial \Delta \varepsilon_{ij}^{cr}}{\partial \Delta \sigma_{kl}} = \frac{3}{2} \dot{\varepsilon}_o \, \hat{\sigma}_{so}^{-p} \left[(p-1) \tilde{\sigma}^{p-2} \frac{\partial \tilde{\sigma}}{\partial S_{pq}} \frac{\partial S_{pq}}{\partial \Delta \sigma_{kl}} S_{ij} + \tilde{\sigma}^{p-1} \frac{\partial S_{pq}}{\partial \Delta \sigma_{kl}} \right] \Big|_{t_o + \Delta t} \Delta t \tag{A.15}$$

which can be expressed, making use of Kronecker's delta, as

$$\frac{\partial \Delta \varepsilon_{ij}^{cr}}{\partial \Delta \sigma_{kl}} = \frac{3}{2} \dot{\varepsilon}_o \, \hat{\sigma}_{so}^{-p} \left[(p-1) \tilde{\sigma}^{p-2} \frac{\partial \tilde{\sigma}}{\partial S_{pq}} \frac{\partial S_{pq}}{\partial \Delta \sigma_{kl}} S_{ij} + \tilde{\sigma}^{p-1} \delta_{ip} \delta_{jq} \frac{\partial S_{pq}}{\partial \Delta \sigma_{kl}} \right] \Big|_{t_o + \Delta t} \Delta t \tag{A.16}$$

$\frac{\partial S_{pq}}{\partial \Delta\sigma_{kl}}$ can be extracted as a common factor to both terms in brackets in Equation A.16, giving as a result

$$\frac{\partial \Delta\varepsilon_{ij}^{cr}}{\partial \Delta\sigma_{kl}} = \frac{3}{2}\dot{\varepsilon}_o\, \hat{\sigma}_{so}^{-p}\Delta t\left[(p-1)\tilde{\sigma}^{p-2}\frac{\partial \tilde{\sigma}}{\partial S_{pq}}S_{ij} + \tilde{\sigma}^{p-1}\delta_{ip}\delta_{jq}\right]\frac{\partial S_{pq}}{\partial \Delta\sigma_{kl}}\Big|_{t_o+\Delta t} \qquad (A.17)$$

$\frac{\partial \Delta\varepsilon_{ij}^{cr}}{\partial \Delta\sigma_{kl}}\Big|_{t_o+\Delta t}$ requires the tensor $\frac{\partial \tilde{\sigma}}{\partial S_{pq}}\Big|_{t_o+\Delta t}$ for its calculation, which is obtained using Equation A.14, so the only remaining unknown tensor is $\frac{\partial S_{pq}}{\partial \Delta\sigma_{kl}}\Big|_{t_o+\Delta t}$. The deviatoric stress tensor for a given phase, $S_{pq}\big|_{t_o+\Delta t}$, is calculated as

$$S_{pq}\big|_{t_o+\Delta t} = \left(\sigma_{pq}\big|_{t_o} + \Delta\sigma_{pq}\right) - \frac{1}{3}\left(\sigma_{uu}\big|_{t_o} + \Delta\sigma_{uu}\right)\delta_{pq} \qquad (A.18)$$

Derivation Equation A.18,

$$\frac{\partial S_{pq}}{\partial \Delta\sigma_{kl}}\Big|_{t_o+\Delta t} = \frac{\partial \Delta\sigma_{pq}}{\partial \Delta\sigma_{kl}} - \frac{1}{3}\,\delta_{pq}\delta_{kl} = \delta_{pk}\delta_{ql} - \frac{1}{3}\,\delta_{pq}\delta_{kl} \qquad (A.19)$$

All the terms needed for the calculation of $\frac{\partial \Delta\varepsilon_{ij}^{cr}}{\partial \Delta\sigma_{kl}}$ has been obtained through Equations A.6 – A.19. Inverting the creep stiffness matrix, C_{ijkl}^{cr}, will furnish the creep compliance matrix, S_{ijkl}^{cr}, as follows

$$S_{ijkl}^{cr} = \left(C_{ijkl}^{cr}\right)^{-1} = \frac{\partial \Delta\varepsilon_{ij}^{cr}}{\partial \Delta\sigma_{kl}} \qquad (A.20)$$

The matrix was simplified to the following

$$S_{ijkl}^{cr} = \frac{3}{2}\dot{\varepsilon}_o\, \hat{\sigma}_{so}^{-p}\Delta t\left[(p-1)\tilde{\sigma}^{p-2}\frac{\partial\tilde{\sigma}}{\partial S_{pq}}S_{ij} + \tilde{\sigma}^{p-1}\delta_{ip}\delta_{jq}\right]\frac{\partial S_{pq}}{\partial\Delta\sigma_{kl}}\Big|_{t_o+\Delta t} \quad (A.21)$$